Groundwater and geotechnical controls on landslide mechanisms of coastal cliffs formed in glacial till

SASIWIMOL NAWAWITPHISIT

How to cite:

NAWAWITPHISIT, SASIWIMOL (2014) Groundwater and geotechnical controls on landslide mechanisms of coastal cliffs formed in glacial till. Doctoral thesis, Durham University.

Groundwater and geotechnical controls on landslide mechanisms of coastal cliffs formed in glacial till

SASIWIMOL NAWAWITPHISIT

THESIS SUBMITTED FOR THE DEGREE OF
DOCTOR OF PHILOSOPHY

Department of Geography
University of Durham

2014

ABSTRACT

Landslides behave in a complex manner especially in terms of the relationship between groundwater variation and the mechanisms of movement; a relationship that remains poorly understood. The aim of this research is to improve the understanding of landslide movement patterns for coastal cliffs. The objectives are (1) to understand controls on landslide initiation; (2) to evaluate landslide movement patterns so as to explain the development to failure and their mechanisms; and (3) to investigate the hysteresis relationship between groundwater and displacement rate.

Field monitoring has been undertaken at Upgang, a cliff formed in glacial till in North Yorkshire, UK (54.29° N and 0.38° W) for 30 months between 2010 and 2012. The monitored section extends 250 m along the coast and is 30 m high. The characteristics of the cliff face and its deformation over time were monitored monthly by terrestrial laser scanning. The landslide complex displays seasonal movements, associated with rotational failures, sliding and deterioration of the failed mass into a complex of mudslides. Movement is dominated both by groundwater variations resulting from precipitation, and marine cutting of the cliff toe. Data from a reactivating landslide, situated at the upper till section of the cliff, was selected to characterise post-failure change. The high spatial and temporal resolutions of the monitoring undertaken in this research allow these processes to be better understood. Uniquely, this study combines three detailed datasets including terrestrial laser scanning, in-situ monitoring and rigorous laboratory testing to explore the controls on the nature and style of landslide movement.

The results demonstrate that reactivation of the landslide occurred in phases of accelerated (0.2 – 6.27 mm/hr), slow (< 0.2 mm/hr) and negligible movements, which were found to be influenced by the fluctuation of groundwater. A complex relationship has been found at the reactive shallow landslide, where the onset of accelerated movements corresponds to an increase in groundwater at the landslide base. Two types of hysteresis patterns, both clockwise (Strain hardening) and anti-clockwise (Strain softening), relating groundwater and displacement rate, were observed. The key controlling mechanism appears to be plastic deformation. The varied velocities are dependent on the stress state controlled by both rate of change in groundwater and absolute groundwater level. The intensity of rainfall has a significant effect on the style of movement. The results have wider implications for understanding the controls on landslide movement in coastal cliffs and reactivation landslides.

Key words: glacial till, reactivation, hysteresis, strain hardening, strain softening, plastic deformation

Declaration

I hereby declare that this thesis is my own work and effort and where other sources of information have been used, they have been acknowledged. No portion of the work referred to in the thesis has been submitted in support of an application for another degree or qualification of this or any other learning institutes.

Statement of Copyright

Acknowledgements

Yes! I have come a long way, both literally and metaphorically, in completing this thesis! This journey would not have been possible without the numerous helpful souls who supported me in each and every single step (no matter how tiny) I took to reach here!

My utmost gratitude goes to my supervisors, Professor Dave Petley and Dr. Nick Rosser for their guidance and patience throughout my years in Durham. This thesis would not have been possible without your insightful comments. Thank you for all the helpful discussions and for always making time for me despite your busy schedules. Dave has provided timely support from various remote locations around the world. Nick is always supportive and encouraging. I am grateful to him for his insightful advice at every stage of fieldwork, from choice of instruments to digging of samples and laser scanning. Both supervisors have contributed significantly to technical and analytical aspects of my research. Moreover, I would like to say thank to Nick and Dave for bringing me to the 11th International & 2nd North American Symposium on Landslide, in Banff, Canada (June 2012). The conference was where I made my first international presentation.

I am thankful to the lecturers and staff, both in Durham and elsewhere (too many to mention), who have in one way or another assisted me in overcoming the multiple challenges in the course of completing this thesis. My sincere thanks to Professor Alexander Densmore and Dr. Jeff Warburton who have shown interest in my research topic and helped shape what follows in this thesis. I am also grateful to Dr. Matthew Brain, who has always been friendly and supportive.

The Department of Geography in beautiful Durham is a great place to be. I thank Veronica Crooks, Frank Davies, Alison George, Mervyn Brown, Kathryn Melvin, Matin D. West, Jean Swales, Michele L. Allan, and Paul West for creating such a friendly and warm environment. I will cherish our wonderful moments in the Manley Room. Cheers to my Ustinov College flatmates, Linyao, Granville, Wariya, Yujing, Chen Chen, and Jiacheng for creating such a lovely living environment. I will fondly remember those ‘flat party’ days.

Not forgetting colleagues in the department who have supported me throughout my fieldwork process. In particular, my earnest thanks go to Dr. Michael Lim, Dr. John Barlow, Dr. Kuo-Lung Wang, Dr. Tim Lane, Dr. Samantha J. Waugh and Jitendra Thakur. Many thanks to Chris Longley for helping with my fieldwork, and for always being willing to help with sample collection. I would also like to acknowledge the kind support rendered by the manager of Whitby Golf Course, Mr. Tony Mason, for granting the team access to the cliff.

'Writing up' this thesis was indeed a monumental task for me. I thank Louise Rayne, Dr. Emma C. Norman, Jack Willams, Siobhan Whadcoat, Rachel Carr, Jayne Sellick, Hannah Bickerdike, Dr. Wasana La-orngplew, Pimpunyawat Tummuangpak, Dr. Karuntarat Boonyawat, Dr.Prapaiwan Sunwong and Dr. Namphon Khampilang for cheering me on right from the start. Your encouragement and support have made this process less painful.

I sincerely acknowledge the Thai Royal Scholarship (Ministry of Science and Technology Scholarship) for funding my PhD in Durham.

I am hugely indebted to my mother and other family members for their unfailing love and support. Thank you for your understanding and patience. Words alone cannot express my gratitude and appreciation towards each of you.

To Dr. J.J. Zhang, your labour of love in editing earlier versions of this thesis, and your unconditional support despite having to deal with different time zones means the most to me. This thesis is for you!

Last but not least, I extend my heartfelt gratitude to those whom I have inadvertently missed. Thank you!

SASIWIMOL NAWAWITPHISIT, OCTOBER 2013

Table of Contents

List of Tables

Chapter 2 Literature review

Chapter 3 Field site and research methods

Chapter 4 Monitoring coastal landslides

Chapter 5 Landslide movement dynamics

Chapter 6 Control of groundwater on landslide movement

Chapter 7 Discussion

List of Figures

Chapter 1 Introduction

Chapter 2 Literature review

Chapter 3 Field site and research methods

Chapter 4 Monitoring coastal landslides

Chapter 5 Landslide movement dynamics

Chapter 6 Control of groundwater on landslide movement

Chapter 7 Discussion

List of Notations

The following symbols (BSI, 1990a; Head, 1998) and notations have been used in the thesis, with the term and the international system (SI) of Units defined where appropriate. An asterisk indicates no unit, multiple units or dimensionless.

Symbol	**Description**	**Unit**
AMSL	Above mean sea level	*
aD	Axial displacement	mm
BPS	Back Pressured Shear box	*
ρ_{wet}	Bulk density	mg/m^3
PZU, PZM, PZL	Casagrande piezometers	*
S1 to S5	Compact string potentiometer extensometer	*
DIS	Drained initial shear	*
ρ_{dry}	Dry density	mg/m^3
c’	Effective cohesion	kPa
ϕ’	Effective frictional angle	°
σ'	Effective stress	kPa
Gw	Groundwater level	m
U1	Hessle till or weathered till	*
e_i	Initial void ratio	*
Δ	Inverse velocity	hr/µs
LL	Liquid limit	%
LoI	Loss on ignition	%
τ_{max}	Maximum horizontal shear stress	kPa
PL	Plastic limit	%
PI	Plasticity Index	%
PWP	Pore water pressure	kPa
PPR	Pore water pressure reinflation test	*
σ'_c	Pre-consolidation pressure	kPa
Δp	Rate of change in pore water pressure	µkPa/hr
M	Sand and gravel beds	*
sD	Shear displacement	mm
τ	Shear stress	kPa
L1	Skipsea till	*
G_s	Specific gravity	*
Std	Standard deviation of the mean	*
TLS	Terrestrial Laser Scanning	*
σ	Total stress	kPa
VBW 1 to 5	Vibrating-wire extensometers	*
e	Void ratio	*
U2	Withernsea till	*

Chapter 1 Introduction

1.1 Landslides in a global context: justification and research motivations

Landslides are one of the most destructive natural geological hazards on earth (Brabb, 1991). In total, 2,620 fatal landslides were recorded worldwide between A.D. 2004 and 2010, causing a total of 32,322 recorded fatalities (Petley, 2012). The temporal occurrence of fata landslides in this data set appears to indicate a rising trend. Despite the damaging effects of landslides to both lives and properties, knowledge on landslides mechanisms is surprisingly lacking. As such, this thesis seeks to contribute to this genre of research in the hope of gaining a better understanding on the nature and characteristics of landslide movements. It is hoped that through a more in-depth and rigorous understanding of landslide mechanisms, a model will be developed to improve the predictability of landslide occurrence and movement.

Landslides can be categorized into ‘first-time’ or ‘reactivated’. First-time landslides are often characterized by high velocities, and have a greater chance of generating fatalities (Cascini, et al., 2005). Conversely, reactivated landslides commonly cause greater economic damage and, sometimes, temporary or permanent evacuation of large zones. Therefore, forecasting the behaviour of these phenomena represents an important issue for an adequate management. Investigating the mechanisms of landslide displacement is crucial for understanding and potentially forecasting future landslide behaviour.

Reactivated landslides, which are mostly slow-moving failures, are often classified as earth slides and creeping landslides (Varnes, 1978). Such landslides cause substantial levels of damage both to structures and to infrastructure (Cascini et al. 2005). According to the geotechnical characterization of slope movement (Fell et al., 2000), slow-moving landslides are phenomena in which movement occurs along one or several pre-existing slip surfaces. The post failure behaviour exhibit either active or occasional reactivation movement (Leroueil, 1996). Such landslides generally display seasonal variation at the rate of movement that is controlled, both in the accelerating and decelerating phases, by groundwater fluctuations (Massey, 2010; Massey et al., 2013). Occasional reactivations refer to larger episodic movement that is controlled by high rates of change in groundwater, exaggerated by antecedent rainfall conditions.

This study is motivated by the desire to address two limitations in contemporary landslides research. Firstly, at present, monitoring or detection of landslide activity is based primarily on information provided by aerial/satellite images and Geographic Information System (GIS). However, such techniques are not applicable to near vertical surface such as a cliff face. This leads to the first research question of the thesis: What methods are available to better capture landslide activity on steep slopes?

Besides the limitations of aerial/satellite images and GIS techniques in monitoring/detecting landslides, there is also an apparent lack of knowledge in terms of landslides mechanisms. In other words, most research focuses on the triggering factors of a landslide without probing the inner-workings governing initiation, and cessation of movement (Allison and Brusden, 1990; Angeli et al., 2000; Corominas et al., 2000; Lee and Clark, 2002 and Picarelli, 2007). Therefore, the second research question asks what the underlying landslide movement mechanisms are.

1.2 Research aim and objectives

In response to the research questions, the aim of this research project is to improve the understanding of landslide movement patterns by conducting both field monitoring and laboratory tests on a coastal cliff formed in glacial till. The study area is located at Upgang Beach, which is on the coast North of Whitby, North Yorkshire, at 54.29° North and 0.38° West (Figure 1.1). The area extends for *c.* 250 m of the coastline. The terrain at the top of the cliff is relatively flat, dropping away to the North towards the North Sea. The cliff is approximately 30 m in height. There is Whitby Golf Club and Sandsend Road (A174) positioned approximately 200 m inland from the cliff edge.

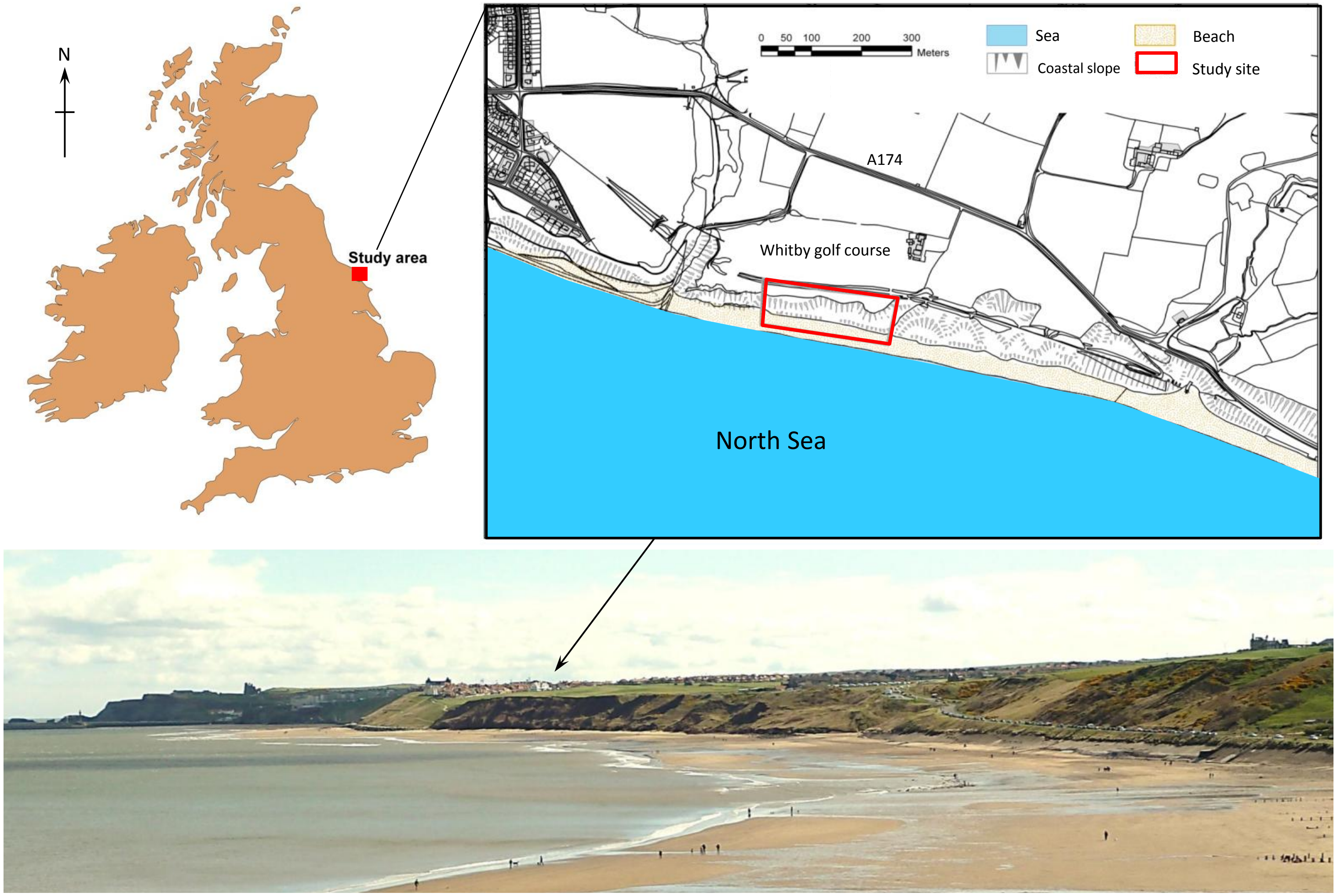

Figure 1.1 Location of the study area (red outline) at Upgang cliff, North Yorkshire, UK showing the coastal slope, beach terrain and constructions. Note: Photograph taken in 2012 by Chris Longley.

The objectives of this research are to:

1. Develop techniques to measure the spatial and temporal patterns of landslide movement using a combination of in situ field monitoring and laboratory tests.
2. Understand controls on landslide initiation focusing on rainfall-induced changes in groundwater;
3. Evaluate the mechanisms of reactivated movements using field monitoring data;
4. Examine the deformation of reactivation using reinflation tests to replicate field failure conditions;
5. Investigate the relationship between displacement rate and groundwater level in governing the varied displacement velocities.

1.3 Scope of the study

To enhance the understanding of the mechanisms of landslide movement, field monitoring and laboratory testing approaches were established. 250 m of the Upgang cliff was monitored. Monitoring systems were designed to cover the cliff face using a terrestrial laser scanning while a specific landslide area was chosen (see Chapter 3) to capture the landslide movement, groundwater and rainfall (Objective 1). This study focuses on a reactivated landslide that is associated with antecedent rainfall controlled groundwater changes (Objective 2). As indicated by the field monitoring data, increasing groundwater is a key landslide triggering mechanism in rainfall-induced landslides in which groundwater increases above a triggering threshold leading to landslide movements. Field monitoring provided information on the types of movement deformation, patterns of landslide movement and controls on landslide (Objective 3). Conversely, laboratory testing allowed patterns of landslide deformation to be understood through the Saito approach (Δ-t space analyses) (Petley et al., 2002) (Objective 4). Finally, the hysteresis relationship between the landslide displacement rate and the groundwater level was investigated (Objective 5).

1.4 Thesis structure

The thesis has been subdivided into eight chapters, which are briefly outlined below:

Chapter 1 provides an introduction to the research, its context and justification of this thesis. The chapter identifies the aim, key objectives and scope of the study and describes the thesis structure.

Chapter 2 presents a detailed review of the recent state of knowledge on the mechanisms of landslide, which includes three main themes:
1) Landslide definitions and classification systems, and the significance and role of material deformation;
2) A review of the literature focusing on landslide dynamics including monitoring landslide morphology techniques, engineering property of till; landslide movement patterns and the patterns of relationship between groundwater and displacement rates;
3) The underlying mechanisms of landslide including reinflation testing, landslide behaviours in terms of the Δ-t space technique, dilative behaviour and creep deformation.

Chapter 3 briefly introduces the study area and outlines the methodologies developed; the field monitoring record of displacement, groundwater and rainfall; the method used to investigate the spatial and temporal distribution of landslides through a series of terrestrial laser scanner (TLS) datasets; and the method used to undertake laboratory tests, including material properties and reinflation testing.

Chapter 4 provides an analysis of the TLS datasets, which are used to investigate the spatial and temporal distribution of landslides across the cliff, and their association with rainfall and marine activity. The chapter also discusses landslide failures that are associated with different failure mechanisms, and the reworking of failed material and the continued removal of fresh material from the cliff.

Chapter 5 offers a discussion on the landslide movement dynamics observed from March 2011 to December 2012. The analysis provides an overall characteristic of recorded monitoring results and seeks to identify landslide deformation patterns based on rate of landslide displacement. Two main movement deformation patterns are addressed, namely accelerated and slow movements. Factors affecting movement patterns (precipitation and groundwater level) are also examined.

Chapter 6 gives an analysis of the laboratory testing used in this study, including physical properties, strain-controlled compression by the back pressured shear box (BPS) and the stress-controlled reinflation tests (PPR). The chapter further describes the response of the sediment to increasing pore water pressure using field monitoring data of accelerated periods.

Chapter 7 discusses the data described in chapters 4, 5 and 6 by drawing upon and synthesising the results in order to gain a better understanding of landslide mechanisms in shallow landslides. By assessing the landslide patterns, one can better calibrate the landslide movement behaviour observed in the laboratory testing.

Chapter 8 concludes the thesis by highlighting the principal findings, limitations of this study and recommendations for further research.

Chapter 2 Literature review

2.1 The fundamentals of landslide processes

The fundamentals of landslide processes can be discussed in terms of:

- The definition and classification of landslides;
- Principles of slope stability;
- Material deformation behaviour;
- Failure processes of slope movements

These will be discussed in the following sections. The general landslide definition and classification are defined based on Cruden (1996) and Cruden and Varnes (1996), respectively. The factor of safety is a principle of slope stability, is described as the relationship between shear stress and shear strength, which are the key strength and stress operating within a slope. The basics of material behaviour and ductile and brittle deformation are introduced. Finally, the failure of landslide is addressed in terms of slope movements including pre, progressive and post failure stages.

2.1.1 Definition and classification of landslides

Landslides are defined as the movement of mass of rock, debris, or earth (soil) down a slope under the influence of gravity (Cruden, 1991). Landslides are classified and described based upon three key elements: the types of movement, the types of material and the rate of movement (Varnes, 1978). The classification proposed by Varnes (1978) is most widely accepted and utilised (Table 2.1). The five main landslide types include falls, topples, slides, spreads, or flows, which can occur in rock debris (> 20% gravel and coarse grains) and earth material (<20% gravel and coarse grains) (Jakob and Hungr, 2005). The rate of movement range from ‘extremely slow’ (< 16 mm/yr) to ‘extremely rapid’ (> 5m/sec) (Table 2.2 from Cruden and Varnes, 1996). This study is concerned with a complex type of landslide that is formed from multiple shallow landslides, including rotational slides and translational slides, earth flows and topples.

Table 2.1 A classification of landslide movement (Varnes, 1978)

MOVEMENT TYPES		**MATERIAL TYPES**		
		BEDROCK	**ENGINEERING SOILS**	
			Predominately coarse > 20 % gravel and coarse grain	Predominately fine < 20 % gravel and coarse grain
FALLS		Rock fall	Debris fall	Earth fall
TROPPLES		Rock topple	Debris topple	Earth topple
SLIDE	ROTATIONAL	Rock slide	Debris slide	Earth slide
	TRANSLATION			
LATERAL SPREADS		Rock spread	Debris spread	Earth spread
FLOWS		Rock flow (Deep creep)	Debris flow	Earth flow
			(Soil creep)	
COMPLEX		combination of two or more principle types of movement		

Table 2.2 The rate of movement scale as proposed by Cruden & Varnes (1996)

VELOCITY CLASS	**DESCRIPTION**	**VELOCITY**	**TYPICAL VELOCITY**	**PROBABLE DESSTRUCTIVE SIGNIFICANCE**
7	Extremely Rapid	5×10^{3}	5 m/sec	Catastrophe of major violence; buildings destroyed by impact of displaced material; many deaths; escape unlikely.
6	Very Rapid	5×10^{1}	3 m/min	Some lives lost; velocity too great to permit all persons to escape
5	Rapid	5×10^{-1}	1.8 m/hr	Escape evacuation possible; structures, possessions, and equipment destroyed
4	Moderate	5×10^{-3}	13 m/month	Some temporary and insensitive structures can be temporarily maintained
3	Slow	5×10^{-5}	1.6 m/year	Remedial construction can be undertaken during movement; insensitive structures can be maintained with frequency maintenance work if total movement is not large during a particular acceleration phase
2	Very Slow	5×10^{-7}	16 mm/year	Some permanent structures undamaged by movement
1	Extremely Slow	$< 5 \times 10^{-7}$	< 16 mm/year	Imperceptible without instruments; construction possible with precautions.

2.1.2 Principles of slope stability

Landslides initiate when shear stress is greater than the shear resistance of the material (Terzaghi, 1950). Their relative relationship is expressed as a ratio of shear resistance (shear strength, τ_f) to shear stress (τ), known as the factor of safety (F) (Figure 2.1). The failure will occur when the shear stress are exactly equal to the shear strength F=1 (Craig, 2004); The slope is in a condition for failure when F <1, and is likely to be stable when F >1.

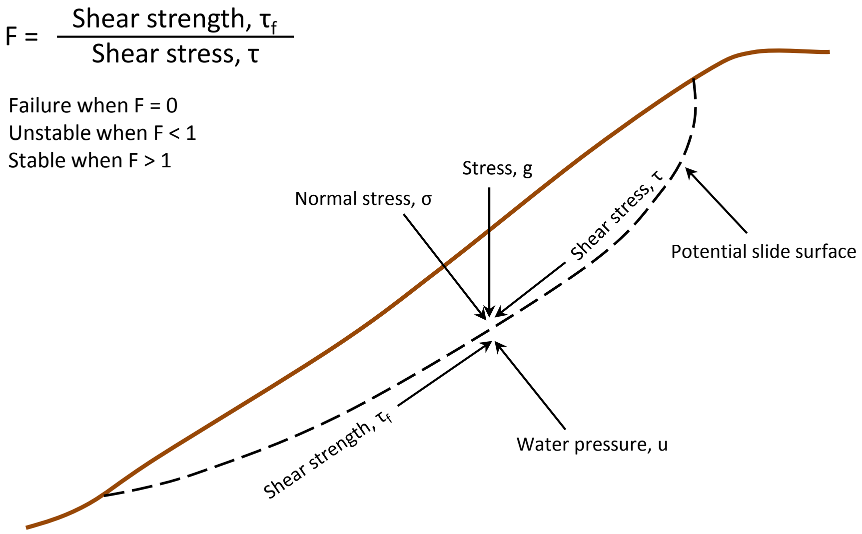

Figure 2.1 The relationship between shear stress and shear strength expressed as a ratio of shear strength to shear stress, known as the factor of safety (Modified from Selby, 1993)

Petley et al., (2005a) proposed a model to explain the development of progressive failure in cohesive materials. The Four stages of development of the failure are illustrated in the model and each stage is shown in terms of the change in the factor of safety through time (Figure 2.2). In the first stage (Figure 2.2: A), the variation of the factor of safety of the slope through time (the F fluctuates) is caused by variations of pore water pressures. When a critical factor of safety is reached, it resulted in the growth of micro-cracks. The slope undergoes a small amount of creep-type displacement, through strains are small (Petley et al., 2005a). In the second stage (Figure 2.2: B), the microcracks grow to a high density and start to interact and coalesce after reaching a critical strain leading to the formation of the shear surface within the shear zone. The factor of safety drops further as the strength of the material decreases from the peak to residual strength. This causes microcrack coalescence and development of the shear surface. This stage is the secondary creep (Varnes, 1978), as characterized by small movements of the landslide mass. The failure surface is not fully developed at this stage. In the third stage (Figure 2.2: C), rapid growth of the shear surface is facilitated by the hyperbolic increase in shear stress transferred to the unsheared materials within the shear zone. The factor of safety drops rapidly through time. In this stage, the shear stress exceeds the shear strength leading to a catastrophic acceleration to failure. This point is the tertiary creep and it is characterised by linearity in 1/velocity (Δ)-t space. However, changes in pore pressure have little influence in the rupture-surface development process, which is primarily controlled by crack growth (Petley et al., 2005a). The final failure is when factor of safety equals unity (Figure 2.2: D). The landslide occurs and the rate of movement becomes dependent upon processes other than cracking, including smoothing and polishing of the shear plane, downslope geometry, pore water pressure fluctuation and fragmentation (Petley et al., 2005a). The failure occurred by a fully-developed shear plane surface just before Δ = 0.

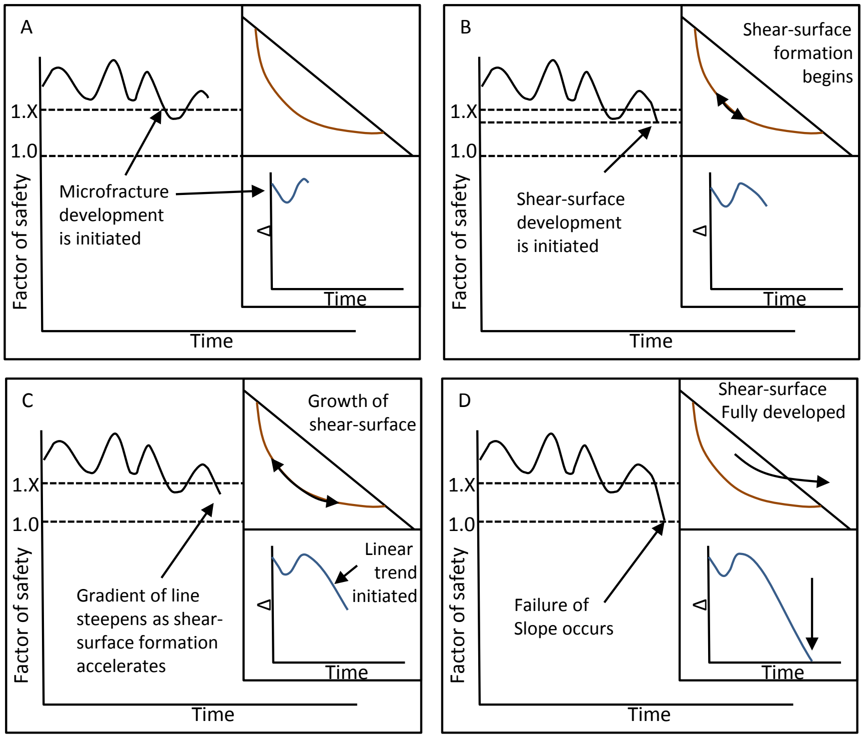

Figure 2.2 Development of progressive failure in cohesive landslide presented using the factor of safety through time with shear surface formation and strains in Δ-t space (source: Petley et al., 2005a).

In this research, the Upgang landslide, which is a reactivated landslide, may be viewed as a movement in the post-failure stage acting to rebalance the forces within a slope from an unstable to a more stable state. To understand landslide failure conditions and their mechanisms, knowledge of the key strength and stress operating within a slope is needed. The shear strength of a soil is expressed by the Mohr Coulomb relationship as a linear function of the normal effective stress (σ') on the plane at the same point (Craig, 2004). The Coulomb shear strength equation indicates that slope resistance mainly comes from the effective cohesion (c′) and the angle of internal friction ($\o'$), which in turn depends on the normal stress (σ_n). The effective shear strength of soil is given by the Coulomb equation as:

$$\tau_f = c' + (\sigma_n - u) \tan \o' \qquad \text{Equation 2.1}$$

where τ_f is the effective shear strength at any point in the soil; c' is the effective cohesion, σ_n is the total normal stress, u is the pore water pressure, $\o'$ is the effective angle of internal friction.

The shear strength of a slope can be assessed in terms of effective major (σ_1') and minor (σ_3') principal stresses of soil at the failure point. A stress state can be represented either by a point with coordinates τ and σ' or by a Mohr circle defined by the effective principal stresses σ_1' and σ_3'. Stress points and Mohr circles representing stress states at failure are shown in Figure 2.3.

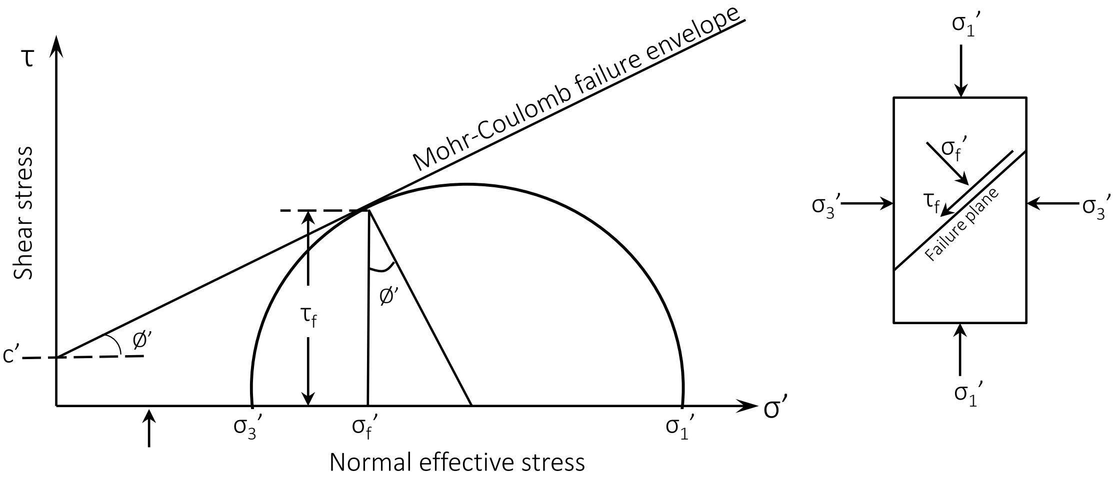

Figure 2.3 Mohr-Coulomb failure criterion (after, Craig 2004)

The Mohr Coulomb failure criterion is a typical method to represent states of stress of material at failure. The resultant Coulomb shear strength of material indicates the effective cohesion (c’) and the angle of internal friction (ø’). However, the Mohr Coulomb failure criterions do not address the strains prior to failure, especially when the displacement accelerates as failure develops (the pre-failure) or when reactivation occurs (post-failure) (Cristescu et al., 2002; Quinn et al., 2010; Ng, 2007).

For shallow landslides, failures occur when a critical combination of shear stress and effective normal stress develops (Craig, 2004). The effects of cohesion (Sidle and Ochiai, 2006) and pore water pressure (u) are large. This is because the safety factor (f) of a slope decreases at greater depths in the soil profile and approaches $\tan\phi/\tan\beta$ in deep soil. However, when the soil is deep, the effects of cohesion and pore water pressure become small, while the effect of slope inclination and internal friction angle become large (Sidle and Ochiai, 2006). Therefore, in terms of the factor of safety (F) this can be expressed as:

$$F = c' + (\gamma z\cos^2\beta - u)\tan\phi' / \gamma z\sin\beta\cos\beta \qquad \text{Equation 2. 2}$$

$$u = \gamma_w m z\cos^2\beta \qquad \text{Equation 2. 3}$$

Thus,

$$F = c' + (\gamma - m\gamma_w) z\cos^2\beta\tan\phi' / \gamma z\sin\beta\cos\beta \qquad \text{Equation 2. 4}$$

Where γ is the unit weight of the soil at the natural moisture content, γw is the unit weight of water, m is a fraction of the soil thickness above the plane, β is the slope angle, u is the pore water pressure at depth z and z is the soil depth

On a natural soil slope (based on the Equation 2.4, the triggering mechanism of shallow landslides is attributed to increases of pore water pressure. This has been termed “hydrological triggering” by Terlien (1998). Although the shear stress is approximately constant, the increase of pore pressure reduces the normal effective stress of the slope materials acting on a potential shear surface.

2.1.3 Material deformation behaviour

The underlying mechanisms for landslide movements can be explained in more detail with reference to the typical stress-strain behaviour of material at different levels of effective stresses (Figure 2.4) (Petley and Allison, 1997). In general, brittle deformation is represented by a catastrophic failure that occurs rapidly. This type of deformation is characterised by fracture. Conversely, ductile deformation is often related to continual creep movement or sliding on existing planes of weakness (Petley and Allison, 1997; Hungr et al., 2005). Ductile deformation is associated with shear fracture, promoted by shear stresses, and occurs as a result of extensive slip on an active slip plane.

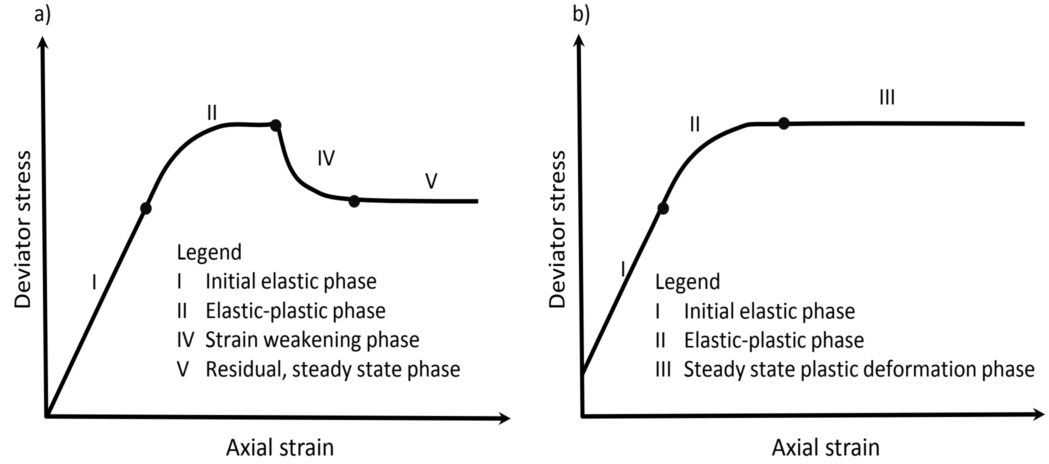

Figure 2.4 Stress-strain curves showing deformation patterns of materials: (a) brittle deformation; (b) ductile deformation (after Petley and Allison, 1997).

Both brittle and ductile deformation undergo a combination of elastic and plastic deformation as can be seen in stage I (initial elastic phase) and stage II (Elastic-plastic phase) (Figure 2.4). However, in a brittle material continued loading will cause failure as strength decreases and strain localises (strain-weakening), causing a shear zone or surface to develop (stage IV). Therefore, displacement will occur across the shear surface while the stress reaches a steady residual value (stage V) (Petley and Allison, 1997). Conversely, for a ductile material, after the yield point, the stress remains constant due to internal restructuring of the material in which the strain cannot localize to form a shear surface and as a result the material is not able to sustain the increase in load. Consequently, the material is dominated by plastic behaviour (Stage III) (Petley and Allison, 1997). However, the ductile concept applies to homogenous material that behaves in a perfectly plastic manner. Most natural soft sediments are not purely ductile meaning that the materials can experience both ductile and brittle deformation. For instance, London clay undergoes ductile-brittle deformation (Petley and Allison, 1997) at very high effective stress states (i.e. in very deep of landslide) as can been seen in Figure 2.5.

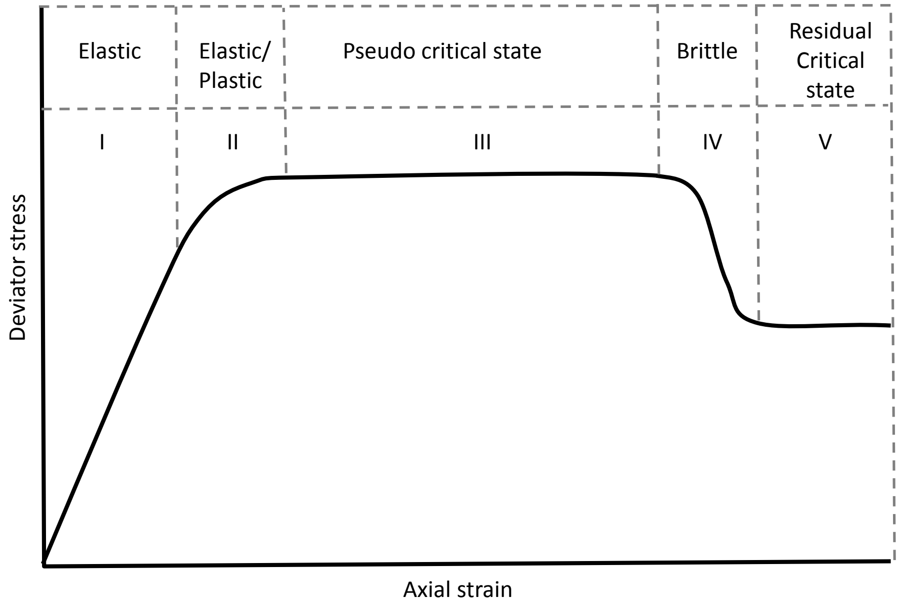

Deformation phase		Description
I	Elastic	There is an initial elastic response to loading and at this point all strains are recoverable.
II	Elastic-plastic	At the initiation of yield, interparticle bonding begins to break down. The sample starts to accumulate plastic or irrecoverable strain in addition to elastic strain.
III	Pseudo critical state	As deformation continues, the sample enters a phase of plastic or purely irrecoverable deformation. The main deformation mechanism is the growth of a multitude of pervasive microcracks. Deformation is effectively in a stable state at constant deviatoric stress. Pore pressures in the sample are constant, suggesting that any dilation that is occurring in the sample during the growth of microcracks is being balanced by compaction elsewhere.
IV	Brittle	The continuing growth and coalescence of the microcracks eventually leads to the formation of a continuous fracture or shear surface across the sample. At this point brittle failure has effectively occurred. The strength of the sample is no longer determined by the properties of the intact material but by the friction across the shear plane. As the shear plane develops and becomes smoothed, the sample undergoes strain-weakening.
V	Residual critical state	Strain-weakening ends with the development of a complete, smooth, polished shear plane and associated damage zone (Petley *et al*., 1994). The sample is now at a stable state in which deformation can continue without any further change in either the stress regime or strain in the sample.

Figure 2.5 An idealised stress-strain curve illustrating the characteristics of deformation in the translational regime (redrawn from Petley and Allison, 1997)

2.1.4 Failure processes of slope movements

Patterns of landslide movement provide an insight into the processes occurring in the basal deformation zone (Terzaghi, 1950; Petley et al., 2002). Slope movements can be classified into four stages of failure, namely pre-failure; post-failure; either occasional reactivation or active landslide (Leroueil et al., 1996) (Figure 2.6). Stage one includes both a pre-failure and a progressive failure state. Pre-failure occurs when the slope has developed strain throughout, but is essentially intact. Eventually, in a brittle material, the onset of failure is characterized by the formation of a continuous surface of rupture (e.g. a shear band) through the slope (Fell et al., 2000). This is true only of brittle failures. However, ductile failures do not have shear surfaces. The post failure stages - stages two, three and four - include movement of the material in the landslide immediately after failure until it stops (Fell et al., 2000). Stages three and four (occasional reactivation and active landslides) refer to those bodies that have experienced failure and are still moving (Urciouli et al., 2007) and where the body slides along one or several pre-existing shear surfaces (Fell et al., 2000). These two stages can be termed ‘the reactivation stage’ (Fell et al., 2000). A reactivated landslide is one in which the shearing resistance on the failure surface is everywhere reduced to the residual strength (Skempton 1985; Brooker and Peck, 1993). This reactivation can be occasional or continuous with seasonal (or longer period) variations in the rate of movement (Fell et al., 2000).

In the case of coastal landslides, reactivation of the landslide delivers further sediment to the toe of the cliff. The strength mobilized in reactivation is the residual strength and movements generally corresponding to the sliding of rigid blocks of material over a pre-existing basal shear surface (Lee and Clark, 2002). As the residual strength belong approximately a lower boundary condition, the soil is not influenced by strain softening and behaves closely to that of rigid plastic or elastic-plastic material (Lee and Clark, 2002; Moore, 1991; Moore and Brunsden, 1996). Residual strength is, however, a dynamic property, with increases or decreases in strength occurring as a result of changes in environmental factors such as increasing pore water pressure (Moore, 1991; Moore and Brunsden, 1996).

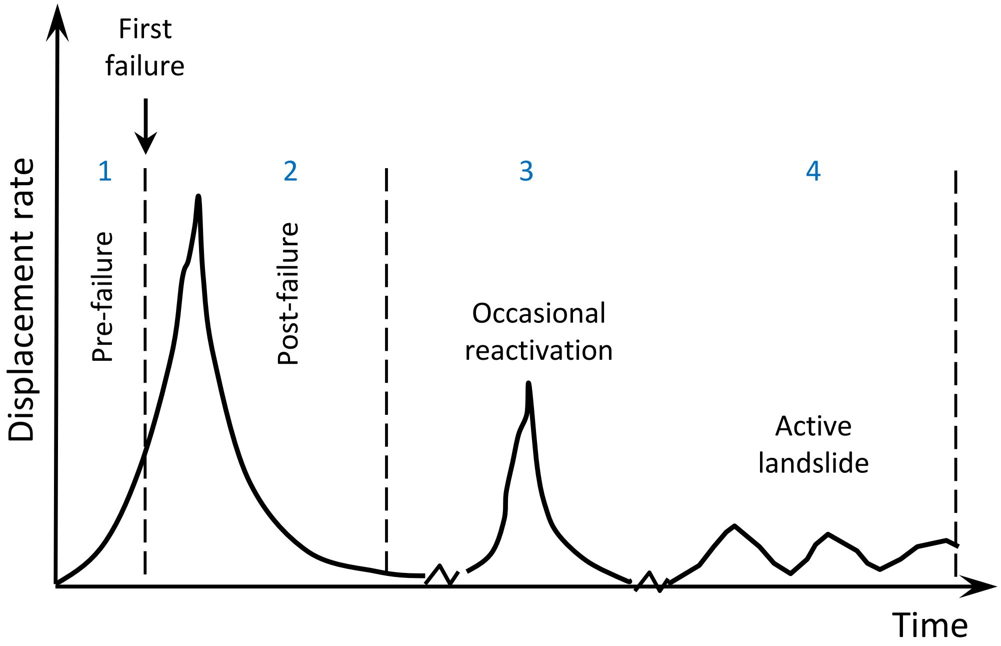

Figure 2.6 Conceptual diagram of progressive landslide development and post-failures stages presenting by displacement and displacement rate (adapted from Varnes, 1983 and Leroueil, 1996)

However, the mechanisms of a reactivated landslide are not completely clear. A reactiviated landslide is often associated with increases of pore water pressure (Picarelli and Viggiani, 1988) and the mobilized shear strength is closely related to the residual strength (Fenelli and Picarelli, 1986). In some cases, this can be related to morphodynamic position within landslide and the movement characteristics changes, as was the case in the Tessina landslide in Italy (Petley et al., 2005b). Seismic forces caused by an earthquake may also lead to reactivated landslides (or of course to first time failures) (D’Elia et al., 1986). With the fundamentals of landslide processes covered, the next section moves on to discuss existing techniques from which landslide dynamics are captured.

2.2 Landslide dynamics

2.2.1 Capturing landslide dynamics

Capturing of the dynamics of landslide-prone slopes can provide immediate notification of landslide activity, as well as high-quality datasets for understanding the initiation and movement of landslides. Monitoring of deformation of structures and ground surface displacements during landslides can be accomplished by using different types of systems and techniques. These techniques include remote sensing, and geotechnical or instrumentation for capturing the spatial and temporal patterns of landslide movements at both coarse and fine scales.

For instance, several remote sensing techniques have been used for an improved understanding of landslide processes. Such techniques include both aerial/satellite and terrestrial options (e.g. Differential Global Positioning System (dGPS), aerial photo, InSAR and LiDAR). Both airborne LiDAR and Terrestrial Laser Scanning (TLS) have been particularly effective for quantifying change (e.g. Rosser et al., 2005; Quinn et al., 2009; Quinn et al., 2010; Massey, 2010). However, InSAR and airborne LiDAR are costly and also take time to implement and repeat (Massey, 2010). Conversely, TLS or ground-based LiDAR surveys can be implemented more rapidly and provide a high accuracy mapping as well as the determination of surface changes over time via repeat measurements (e.g. Hobbs et al., 2002; Poulton et al., 2006; Quinn, 2009).

In the case of coastal landslides, vertical cliff faces are difficult to capture from above as they need to be viewed at an oblique angle. Whilst most research has focused on the recession rate or volumetric retreat, this study attempts to characterise change across the cliff face based on geomorphological cliff behaviour. This is related to a range of mass movement and soil erosion processes, which occur in a sequence of distinctive morphodynamic zones (Brunsden and Jones, 1980). Four zones, in descending order of elevation, are identified in Figure 2.7 and Table 2.3.

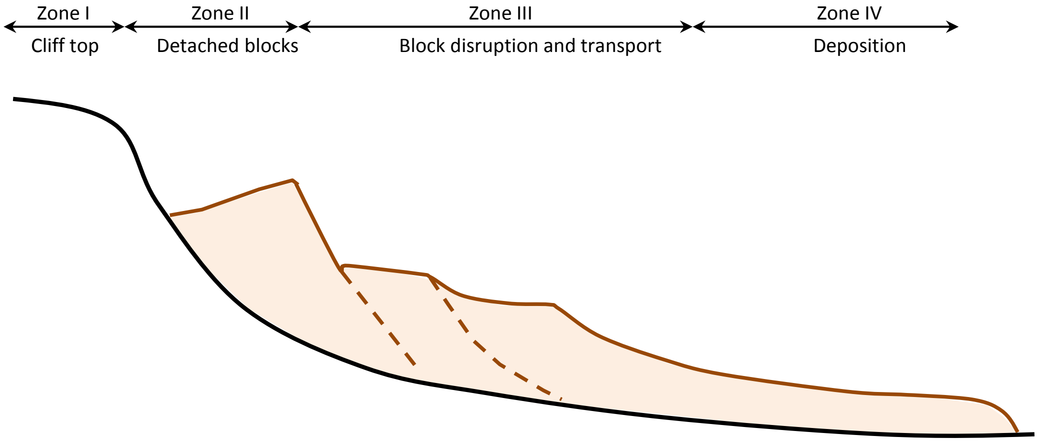

Figure 2.1 Schematic cliff behaviour unit morphodynamic zones (I-IV) in soft-rock cliff: Zone I – cliff top: intact zone; Zone II – detached blocks: a steep landslide scar fronted by a talus slope which passes onto a sequence of detached blocks. Zone III – block disruption and transport: the detached blocks are transported downslope. Zone IV – deposition: marine influence (Redrawn from Brunsden and Jones, 1980)

Table 2.3 A sequence of distinctive morphodynamic zones (Source from Brunsden and Jones, 1980)

Morphodynamic zones		Movement processes
Zone I	Cliff top	This zone is largely unaffected by mass movement
Zone II	detached blocks	This zone may comprise a steep landslide scar fronted by a talus slope which passes onto a sequence of detached blocks. These blocks often appear largely intact and may have been tilted forwards or backwards during their detachment from the cliff top. The scarp slopes can be prone to both surface erosion and seepage erosion
Zone III	block disruption and transport	This zone is where the detached blocks are broken down by small-scale mass movement processes and surface erosion, and transported downslope
Zone IV	deposition	This zone often comprises single or overlapping lobes of debris at the base of the cliff. It is common for marine erosion of the debris lobes to leave a lag deposit of coarse material and boulders on the foreshore

Nevertheless, the temporal resolution of the TLS approach is limited, making it difficult to link movement to the cause. Thus, geotechnical instrumentation continues to be used to provide insights into the dynamics of landslide movement and the nature of the hydrologic triggers. Instruments include extensometers, inclinometers, tensionmeters, piezometers and rain gauges. Such monitoring has been used extensively for rainfall-induced shallow landslides in particular (e.g. Allison and Brusden, 1990; Angeli et al., 2000; Corominas et al., 2000; Lee and Clark, 2002; Picarelli, 2007; Petley et al., 2005b; Iverson 2005 and Reid et al., 2008). Corominas et al. (2005) demonstrated that displacements observed in borehole wired extensometers have recorded an immediate response to rainfall episodes. However, Kasperski et al. (2010) however suggested that instrument monitoring cannot provide a full continuous spatial view of displacements. As such, the landslide process can be understood better by a combination of TLS, which can provide high-resolution monitoring for whole landslide areas, and geotechnical instrument monitoring, which can characterise the dynamic behaviour and hydrologic conditions triggering at high temporal resolutions. This research attempts to improve the understanding of landslide activities and their processes by linking the different scales of the spatial and temporal patterns of landslide movements.

2.2.2 Landslide movement patterns

The techniques described above can be used to determine the patterns of landslide movement, based on velocities and displacements (e.g. Van Asch, 1984; Allison and Brunsden, 1990; Petley et al., 2005b; Massey et al., 2013). For example, Van Asch (1984) identified displacement of landslide blocks of clay material in the French Alps using Inclinometer measurements. He suggested that before initial slope failure, movement can be very slow as creep processes dominate. The creep movements are probably an outward sign of the development of progressive failure within the slope above the eventual slip surface (Saito, 1965; Skempton and Hutchinson, 1969).

A different movement pattern, as ductile deformation proposed by Allison and Brunsden (1990) separated mudslide movement patterns on the Isle of Purbeck into four components: 1) small ‘stick slip’ movements; 2) gradual or graded slip; 3) rapid ‘surges’ and 4) unexplained ‘random movements’. The four post failure movement types are related to a characteristic pattern of groundwater fluctuation (Table 2.4 and Figure 2.8). However, these patterns are limited by the relatively low spatial coverage of the instruments (Petley et al., 2005b).

On the other hand, Petley et al., (2005b) identified four patterns of landslide movement (which they termed Types I, II, III and IV) in Tertiary Flysch deposits, on the Tessina landslide in Italy by linking movement patterns with the landside process and geomorphological setting(Table 2.5 and Figure 2.9). According to the classifications of both Allison and Brunsden (1990) and Petley (2005b) a transition behaviour, which is attributed to the seasonal fluctuations of pore water pressure, can be identified. For instance, landslide movement patterns may develop from ‘stick slip’ to ‘graded’ and then ‘surge’ (Allison and Brunsden, 1990) or from Type I to Type IV (Petley, 2005b).

Recently, Massey et al. (2013) proposed three main types of movements for the Utiku landslide, New Zealand using horizontal cGPS time-series data, namely: ‘faster motion’ ‘slower motion’ and ‘cyclic motion’ (Figure 2.10). The Utiku landslide comprise a large-scale translational mass movement in weakly consolidated Neogene materials (i.e. silt, fine sandstones and sady siltstone). All motions can be classified as slow in the Cruden and Varnes (1996) classification. All these studies suggest that comparatively fast motions occurred in short periods of a few days to a few weeks, whereas the slower motions last many months to years and cyclic motions and typically display a seasonal cycle.

As mentioned above, the movement patterns of reactivated landslides are typically controlled by hydrological triggers, with an increase of pore water pressure leading to landslide reactivation. However, complex landslides respond to groundwater conditions, probably controlled by the landslide material and geomorphology. However, at present these are poorly understood.

Table 2. 4 Patterns of mudslide movement in relation to pore water pressure, in the Wealden Beds of the Isle of Purbeck, Dorset (extracted from Allison and Brunsden, 1990 and modified by Ng, 2007)

Movement type	Displacement characteristics	Related pore water pressures (PWP)
1) Stick slip	Small individual spatial movement < 1 cm, relatively slow or gradual rises. Total displacement up to 8 cm	Slowly rising PWP
	Separated by varying time interval with zero displacement	Slowly declining PWP
2) Graded slip	Larger gradual spatial movements over proportionally shorter time periods with maximum downslope movement of 35 cm over 17 hrs	Gradual rise in PWP at the start of movement and a more rapid increase by 0.3-0.4 in 2 hrs.
3) Surge	Large spatial displacements of 3 m over short time periods of approximately 20 minutes	Highest rate of increasing in PWP of 1.5 m in less than 10 minutes
4) Random	Small, irregular slip through space and time	Related to other factors, such as internal deformation with mudslide, effects of plasticity, seasonal cycles and gravitational forces

Table 2.5 Patterns of landslide movement in relation to pore water pressures for the Tessina landslide, Italy (extracted from Petley et al., 2005b and modified Ng, 2007)

Movement type	Displacement characteristics	Related pore water pressures (PWP)
1) Type I	Very slow movements at less than 1 mm/day; consist of slow creep	Increase in velocity associated with wetter wintter months
2) Type II	Low velocity movements 2-3 mm/day	Gradual rise in PWP
	Typical block movements; highly variable movement rate	Faster movements occur during months with high groundwater levels
3) Type III	Movement rates at 10 mm/day; creep occurs at similar, continuous rates	Relatively small seasonal fluctuations
4) Type IV	Episodic, very rapid movements. Movements initiated rapidly and terminates abruptly, but static in between movement events	Periods of reactivation associated with wetter winter months when PWP are seasonally high
	Peak rates more than 1-2 m/day	

a) Multiple (stick slip) movement

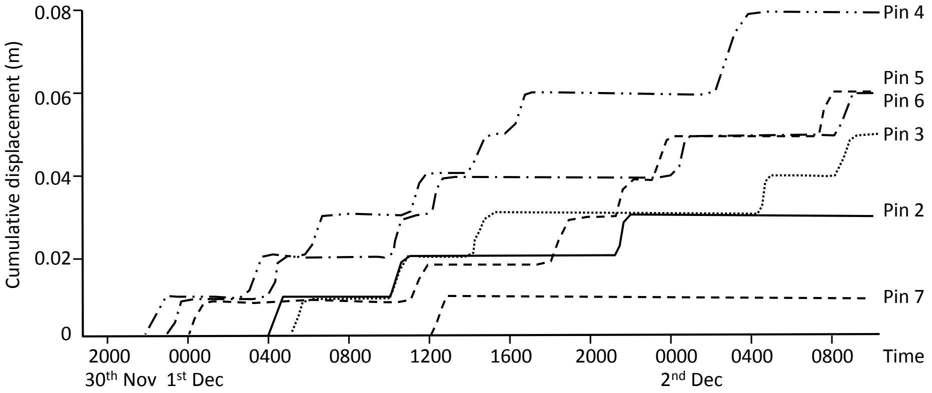

b) Gradual or graded slip

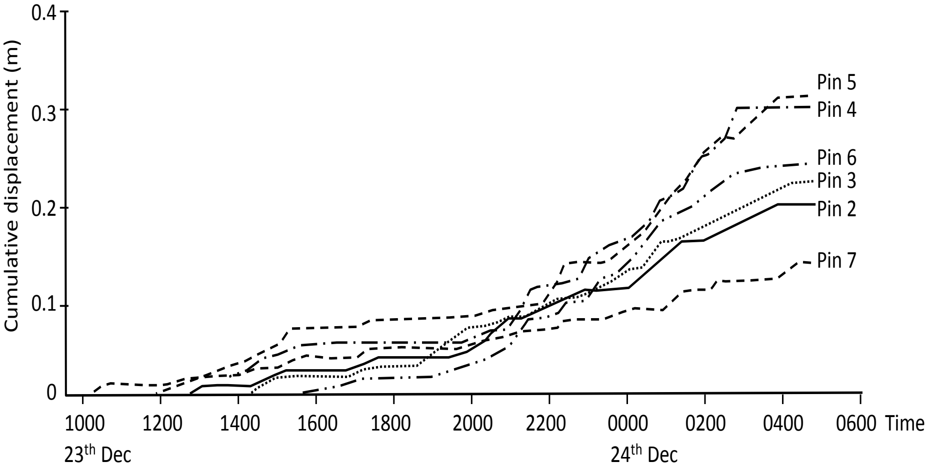

c) Rapid 'surge' movement

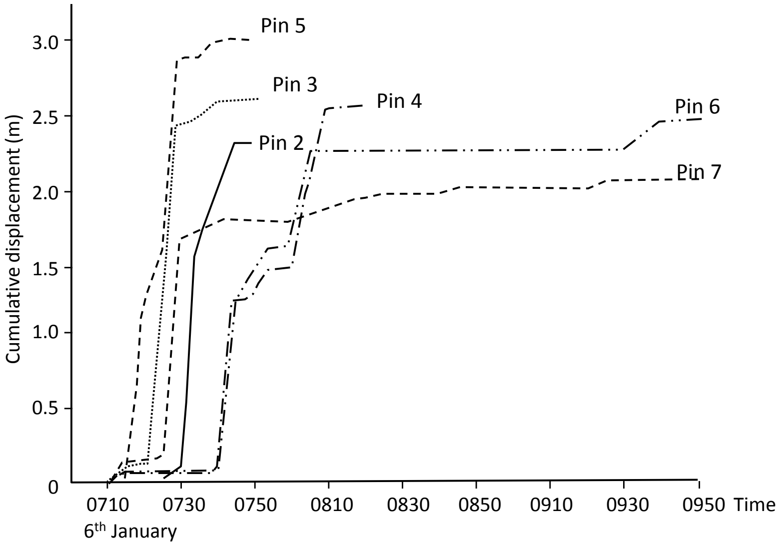

Figure 2. 2 Landslide displacement patterns (Redrawn from Allison and Brunsden, 1990)

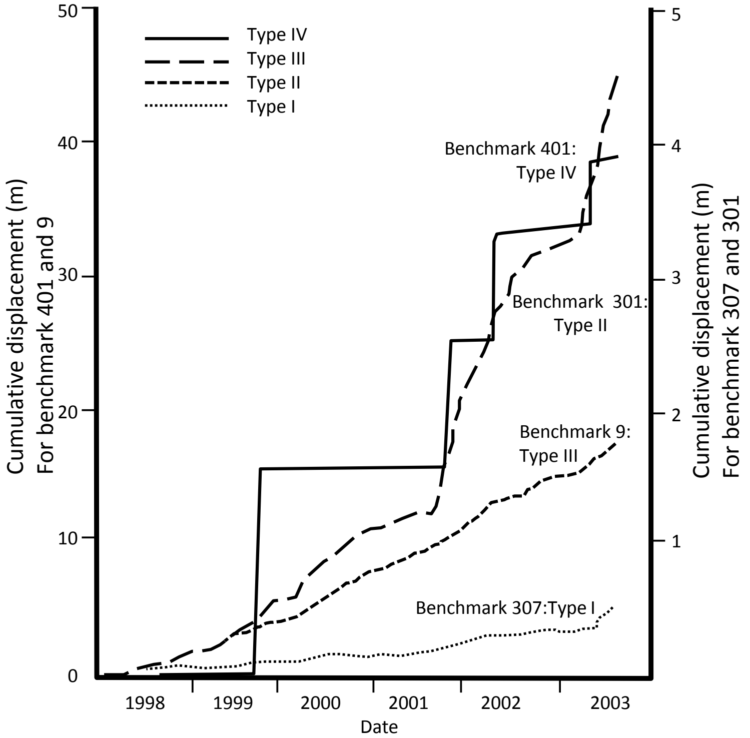

Figure 2.3 Schematic representation of the movement types in Tessina landslide, Italy (redrawn from Petley et al., 2005b)

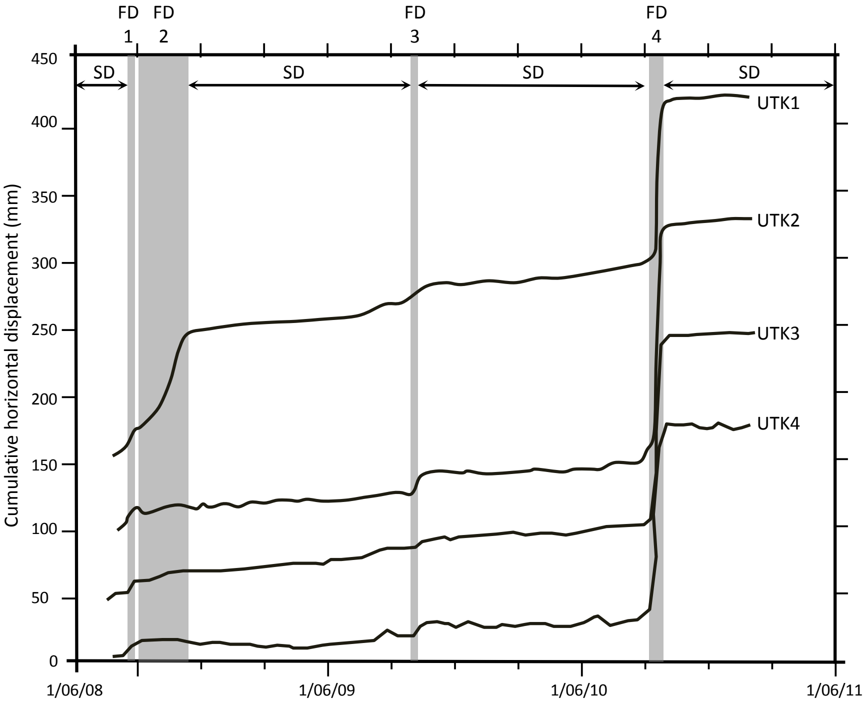

Figure 2.4 Daily filtered cumulative horizontal displacement of cGPs station located on the Utiku landslide, plotted along their main displacement bearings: FD-fast displacement periods, SD-slow displacement periods. Note: the cumulative displacement cGPS time all originate at zero and have been offset from zero for presentation purpose (redrawn from Massey et al., 2013).

2.2.3 The relationship between displacement rate and groundwater level (pore water pressure)

The movement patterns illustrated in Figure 2.11 show complex relationships between displacement rate and groundwater (pore water pressure) conditions. Several studies have found that there is a hysteresis relationship between these factors (see for example, Bertini et al., 1986; Corominas et al., 2005; Gonzalez et al., 2008; Matsuura et al., 2008; Van Asch et al., 2007 and Massey et al., 2013) (Figure 2.11). Examples include:

- Bertini et al. (1986), who examined the movement of the Fosso san Martino landslide in Central Italy, which consists of a narrow stratum of weathered bedrock overlaid by a clayey silt colluvium cover. They suggest different velocities for the rising and lowering limb of the piezometer levels (Figure 2.11: e).

- Corominas et al. (2005) and Gonzalez et al. (2008), who studied the Vallcebre landslide complex in the Eastern Pyrenees, Spain, which comprises of a set of shale, gypsum and claystone. They suggest the role of the viscous component as an explanation to the hysteresis relationship of movement patterns, and the ‘reversible behaviour’ of velocities, assuming that velocities in the rising limb are lesser than velocities in the lowering limb (Figure 2.11: d).

- Matsuura et al. (2008), who also found a similar pattern of hysteresis based on the Tertiary materials, Japan (i.e. soft clay, silt and rough fragments of broken stone) (Figure 2.11: c1, c2). One type of the hysteresis curve bulged upward when pore water pressure rose sharply and the displacement response was delayed. On the other hand, when pore pressure dropped sharply, displacement rate decreased gradually.

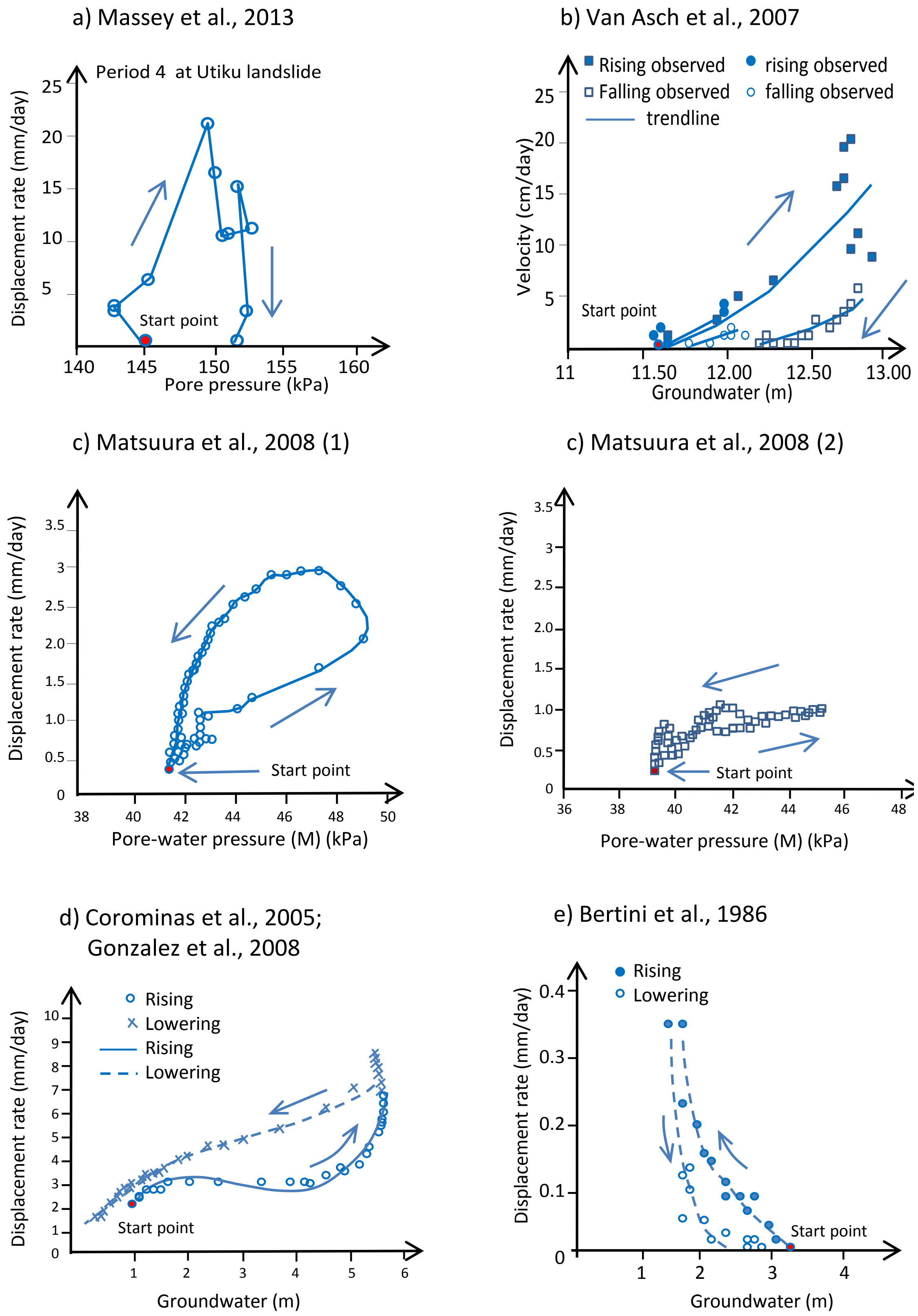

a) Massey et al., 2013

b) Van Asch et al., 2007

c) Matsuura et al., 2008 (1)

c) Matsuura et al., 2008 (2)

d) Corominas et al., 2005; Gonzalez et al., 2008

e) Bertini et al., 1986

Figure 2.5 Hysteresis relationship between groundwater/pore water pressure and displacement rate

- Conversely, Van Asch et al. (2007), who described a hysteresis relationship for the La Valette landslide in the French Alps, which consists of marl and argillaceous morainic materials, The research showed that during rising limbs of groundwater the material seems to have lower intrinsic viscosities and a lower dependency on excess shear stress than during falling limbs(Figure 2.11: b). Van Asch et al. (2007) also suggest that during movement excess pore pressure, both positive and negative, may develop due to compression and extension, and that this may result in viscosity before they dissipate (e.g. Iverson, 1985; Angeli et al., 1996; Corominas et al., 2005).

- Massey et al. (2013), who (found a similar pattern of hysteresis on the Utiku landslide, New Zealand Figure 2.11: a), which slides on thin clay layers within a mudstone, observing an initial rapid increase in displacement rate to peak values as pore water pressure increased. However, even as post-peak displacement rates decreased, pore water pressure either remained constant, or in some cases actually increased. Massey et al., (2013) suggested that this could be explained by rate-induced changes in shear strength of the slip surface (i.e. a dynamic rather than static frictional resistance), caused by a rearrangement of the clay particle bonds during shearing.

To summarise, two hysteresis patterns in the relationship between groundwater and landslide velocity have been observed (Table 2.6). Most clay matrix materials show a “clockwise” hysteresis relationship (i.e. Van Asch et al., 2007 and Massey et al., 2013), whilst the “anti-clockwise” pattern is observed in brittle materials (i.e. Bertini et al., 1986; Corominas et al., 2005; Gonzalez et al., 2008; Matsuura et al., 2008). This implies that the relationship between these factors is related to the deformation characteristics of the materials.

Table 2.6 A summary of relationships between landslide displacement and groundwater/pore water pressure in different landslides

Hysteresis patterns	Where/Name	Landslide materials	References
Clockwise	a) The translational Utiku landslide, New Zealand	Clay layers within the Taihape mudstone	Massey et al., 2013
	b) The La Valette landslide complex in the French Alps (Middle part- a translational slide)	Strongly remoulded Terres Noires mixed with morainic deposits. The matrix is a sandy silt with a considerable clay fraction in which larger fragment (stone, gravel) are incorporated	Van Asch et al., 2007
Anti-clockwise	c) The Fosso San Martino landslide, Central Italy	A narrow stratum of weathered bedrock overlaid by a clayey silt colluvial cover in which the sliding mass moves essentially as a rigid body	Bertini et al., 1986
	d) The translational Vallcebre landslide in the Eastern Pyrenees, Spain	A set of shale, gypsum and claystone	Corominas et al., 2005; Gonzalez et al., 2008
	e) The reactive landslide for debris at the coast of Japan	The Tertiary material (i.e. soft clay, silt and rough fragments of broken stone). The general properties of these rocks make them prone to clay formation by hydration and weathering due to weak cementation.	Matsuura et al., 2008

2.3 Material properties and mechanisms of landslide movement

2.3.1 Engineering properties of tills

Factors of relevance to glacial till slope stability include the depth to and the dip of rockhead, the presence of ancient failure surfaces and the presence or otherwise of associated glacial properties (Trenter, 1999). Previous studies suggest that landslides in glacial till are typically complex (32% frequency), debris flow (28%), planar (26%), rotational (8%) and multiple-rotational landslides (4%) (Trenter, 1999).

The glacial till of North-east England is considered to have been formed during the late Devensian age of the Quaternary period (Bell and Forster, 1991, Clarke et al., 1998, Bell, 2002 and Catt, 2007). The tills at Upgang cliff can be referred to as the Hessel till, the Withernsea till (the Upper section of the cliff) and the Skipsea till (the lower section of the cliff). Clarke et al.(1998) suggested that the upper till is a weathered unit (Upper till/unit 1). The position of the Hessle till on the plasticity chart also suggests that it is weathered material (Bell, 2002). The physical properties and direct shear test results are summarised in Table 2.7 (Bell and Forster, 1991; Bell, 2002). Bell (2002) found that most samples of Hessle till produced barrel-shaped failures, suggesting the materials are not predominantly cohesive. Moreover, this material has a greater range in strength than that of the Skipsea or Withernsea till because the Hessle till is the weathered derivative of these two tills (Table 2.7). Higher angles of friction are found in the Skipsea till, probably due to the large proportions of sand-silt.

Table 2.7 Classification data of glacial tills. Note: natural moisture content (MC), plastic limit (PL), liquid limit (LL), plasticity index (PI), liquidity index (LI), consistency index (CI), and activity (A). Note: Liquid limit L = low plasticity, less than 35%; I = intermediate plasticity, 35-50%; H = high plasticity, 50-70% (Anon,1999). Consistency index: VS = very stiff, above 1; S = stiff, 0.75-1; F = firm 0.5-0.75. Activity: I inactive, less than 0.75; N = normal, 0.75-1.25; A = active, over 1.25: c: cohesion in kPa from Direct shear; ϕ: angle of friction from Direct shear testing (source from Bell and Forster, 1991 and Bell, 2002)

Tills	MC%	PL%	LL%	PI%	LI	CI	A	c	ϕ°
Hessel Till (Dimlington, Hornesea)									
Max	26.6	26	53 (H)	32.0	0.072	1.147 (VS)	2.10 (A)	30	25
Min	18.5	20	38 (I)	17.0	-0.019	0.794 (S)	0.96 (N)	16	16
Mean	22.6	22	47 (I)	25.0	0.044	0.972 (S)	1.24 (N)	20	24
Withernsea Till (Dimlington)									
Max	19.3	21	39 (I)	20.0	-0.276	1.016 (VS)	1.21 (N)	38	30
Min	12.3	15	22 (L)	12.0	-0.095	0.828 (S)	0.72 (I)	21	20
Mean	16.9	18	34(L)	17.0	-0.164	0.986 (S)	0.93 (N)	36	24
Skipsea Till (Dimlington)									
Max	18.2	19	36(I)	18.0	-0.294	1.288 (VS)	0.67 (I)	45	38
Min	13.5	14	20(L)	9.0	-0.044	0.978 (S)	0.51 (I)	25	20
Mean	15.5	16	30(L)	14.0	-0.188	1.108 (VS)	0.56 (I)	27	26
Basement Till (Dimlongton)									
Max	20.4	23	42(I)	22.0	-0.158	1.081 (VS)	0.59 (I)	47	34
Min	15.6	16	28(L)	12.0	-0.032	0.984 (S)	0.53 (I)	23	20
Mean	17.0	20	36(I)	19.0	-0.127	1.009 (VS)	0.55 (I)	29	24

With regards to the shear strength parameters of the glacial till (c and ø), these factors are derived from conventional direct shear tests. However, these methods do not replicate the stress condition in the natural slope, as most landslide failures occur as a result of increasing pore pressures acting within the slope. As such, conventional geotechnical methods may not be suitable to define the true failure envelope in a slope. Thus, the pore water reinflation testing can be used to overcome this deficiency. This will be discussed in more details in section 2.3.2.

2.3.2 Pore pressure reinflation testing

Pore pressure reinflation (PPR) testing is helpful to gain a better understanding of the underlying mechanisms of landslides by simulating the field stress conditions. The simulated failure processes caused by increasing pore pressures were initially identified by Bishop and Henkel (1962) and later progressed by Brand (1981) with the development of the field stress path concept (Figure 2.12). The key concept is increasing pore water pressure at a constant total normal stress and constant shear stress. This testing procedure is able to replicate the most realistic field conditions for most rainfall- and groundwater-induced landslides (Carey, 2011). Several studies have adopted this general testing concept (e.g. Anderson and Sitar, 1995; Zhu and Anderson, 1998; Dai et al., 1999; Petley et al., 2002; Ng, 2007; Carey, 2011).

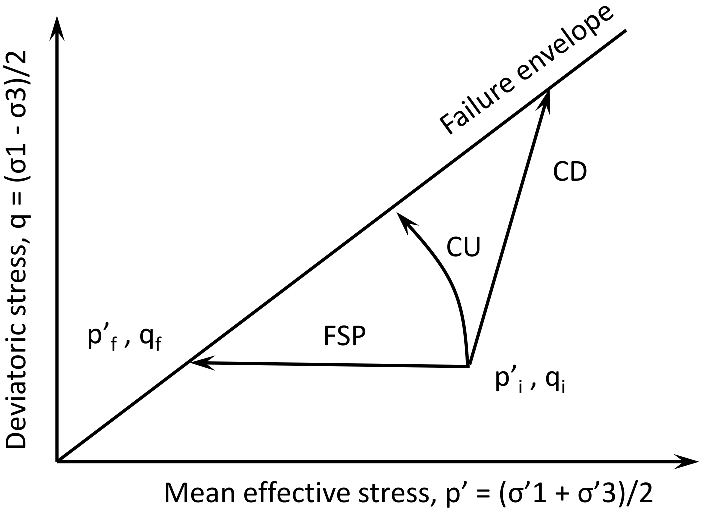

Figure 2.6 Conceptual diagram of field stress path (FSP), compared with consolidated undrained (CU) and consolidated drained (CD) stress paths (after Brand, 1981; Ng, 2007)

Petley et al. (2002) advanced the understanding of progressive landslide failure in cohesive material using conventional isotropic consolidation and undrained shear tests. Their key concept is to consolidate a sample isotropically and then subject it to undrained shear until a predetermined proportion of its peak deviatoric stress. At this point the deviatoric stress is held constant and the effective stress is reduced through pore water pressure inflation until the sample fails. As a consequence, two distinct patterns of movement styles are plotted in 1/v (Δ) - t space (Table 2.8). The first style has a linear trend in a plot of Δ-t space. The linear trend represents brittle failure and the development of a singular shear surface. The second style has an asymptotic trend in a plot of Δ-t space associated with ductile or sliding on an existing surface (Petley et al., 2002; Kilburn and Petley, 2003). The asymptotic trend is associated with slow or continual movements, known as creep, as is evident during accelerating phases for rainfall-induced landslides (Petley et al., 2002). In real slopes the accelerated processes may continue for a few days or longer, which can be individual or a repeating period of acceleration punctuated by periods of inactivity (Massey, 2010; Massey et al., 2013). Examples of reactivated slides are characterised by an asymptotic trend in Δ-t space as shown in Figure 2.13.

In this research, PPR testing has been used by adapting the process of simulating to the conditions within a hydrologically-triggered landslide. Constant shear stresses, which are based on 80% of shear strength (Petley et al., 2005a) have been applied using variable effective normal stresses with a combination of a range of pore water pressure inflation rates. The various rates of increasing pore water pressure will be designed by reference to the field monitoring data in order to simulate field stress conditions. Consequently, the result of the reinflation testing can be used to explain the underlying mechanisms of progressive landslide failures on pre-existing slip surfaces.

Table 2. 8 Summary of the Δ-t analyses and their implications on landslide behaviour (source: Ng, 2007)

Landslide movement patterns	Type I	Type II
Landslide acceleration behaviour (1/velocity against time)	Linear trend 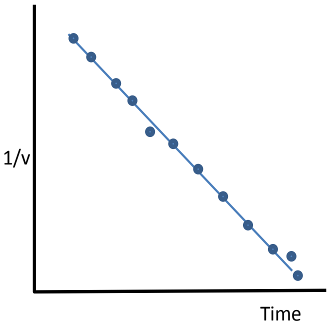 Bulk movement accelerates linearly with time	Asymptotic trend 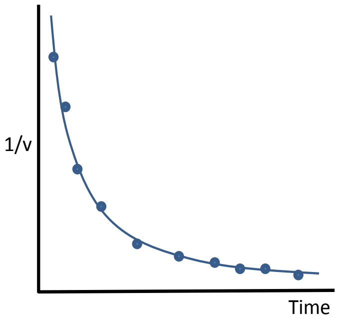 Bulk movement accelerates exponentially with time
Dominant basal deformation process	• Crack propagation/growth • New cracks join together (micro-cracking process) • Development of discrete shear/rupture surface • Shear surface generation • Brittle failure mechanisms	• Crack nucleation • New cracks remain isolated • Sliding on existing planes of weakness • Reactivation of existing landslide systems • Ductile deformation processes
Material behaviour Stress-strain relationship	• Brittle • Commonly occurs in bonded or cemented material at relatively low confining pressure	• Ductile/plastic/non-brittle • Shown by materials with little or no interparticle bonding at high confining pressures
Failure	• First-time failure • Catastrophic • Sudden and rapid displacement	• Landslide reactivation • Non catastrophic/not intrinsically dangerous • Continual slow, creep-like movement

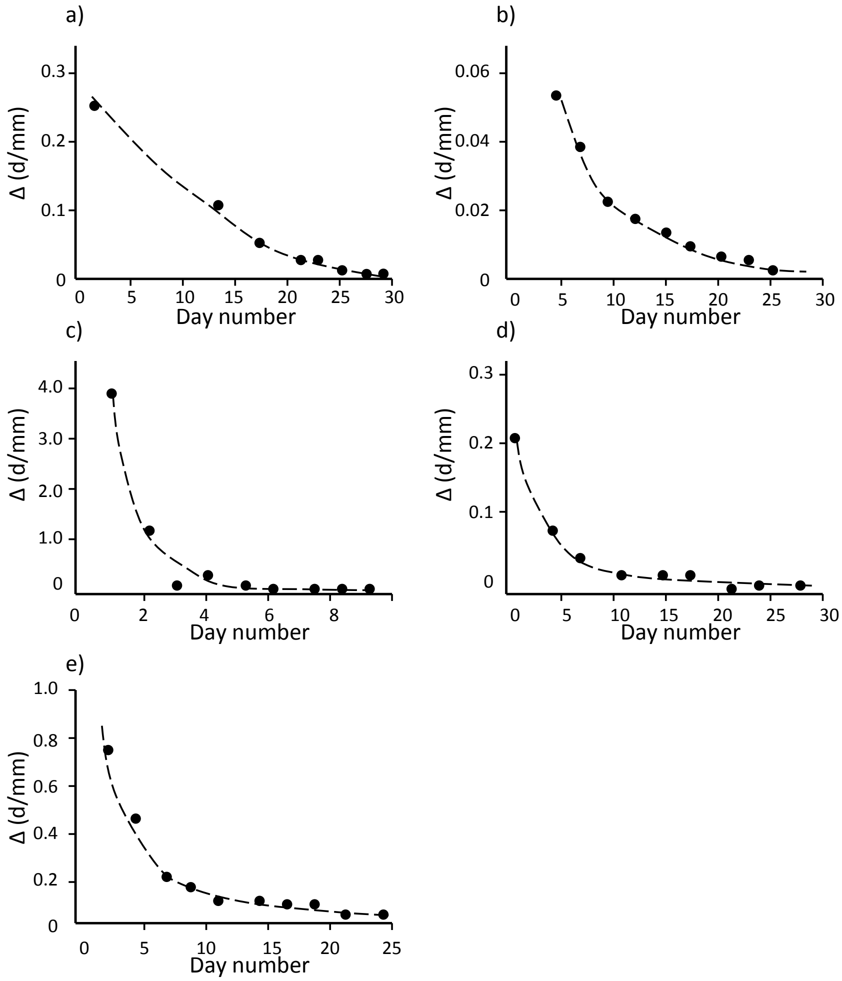

Figure 2.7 Examples of reactivated landslides presented by an asymptotic trends in term of Δ-t space: a) Failure of Giau Pass landslide in Italy (Angeli et al., 1989); b) Abbotsford landslide, New Zealand (Salt, 1985); c) Tessina landslide, Italy (Consiglio N Consiglio Nazionale delle Richerche, 2001); d) Cleveland Corral landslide in Californai (U.S.Geological Survey, 2002); e) Kunimi landslide in Japan (Shuzui, 2001) (Source from Petley et al., 2002)

2.3.3 Dilative behaviour

Dilative behaviour can be observed in most reinflation tests (e.g. Dai et al., 1999; Gabet and Mudd, 2006; Ng, 2007). The key mechanism of dilation involves the rearrangement of soil particles (Terzaghi et al., 1996; Craig, 2004). For instance, Ng (2007) and Ng and Petley(2009) used a range of pore water pressure inflation rates in linear, stepped and logarithmic forms on weathered volcanic slopes on Lantau Island, Hong Kong. The result of these tests has been used to develop an understanding of the inter-particle movements within the samples in shallow plastic landslides. The dilative behaviour has been defined as three stages in terms of void ratio and mean effective stress relationship (Figure 2.14). The Type 1 to Type 3 patterns of dilative behaviour during the increasing pore water pressure suggest three different inter-particle movements occurring within the soil samples, characterised as “push and climb”, “localised slide” and “generalised slide” respectively (Figure 2.14). The transition from Type 1 to Type 3 is likely to be associated with the increasing volume of pore fluid that reduces the contacts between soil particles facilitated by the constant shear.

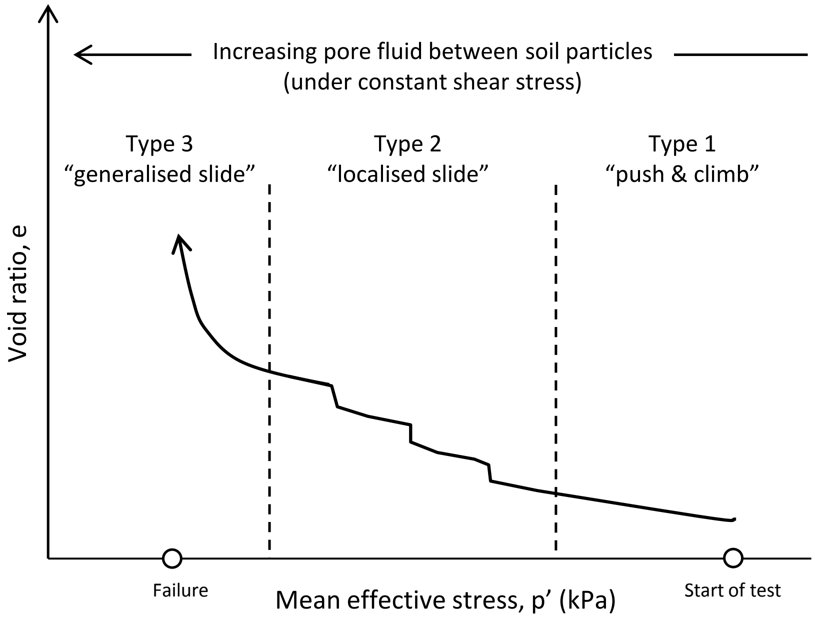

Figure 2.8 Explanation of dilative e-p’ relationship in terms of inter-particle movement within the soil samples during reinflation test: Type 1 (push and climb), Type 2 (localised slide) and Type 3 (generalised slide) (redrawn from Ng, 2007)

Type 1 ‘push and climb’ appears to have been mainly due to the increased amounts of pore fluid in the sample rather than shear deformation. However, relative inter-particle movements are limited due to strong interlocking with the other particles under high mean effective stress (Figure 2.14: type 1).

Type 2 ‘localised slide’ – particles begin to slide past each other in the direction of shear. The movements are still being restricted and blocked by the interlocked particles. The dilatant contributed by shear deformation becomes increasingly dominant over volumetric deformation (Figure 2.14: type 2).

Type 3 ‘generalised slip’ represents failure as the highly non-linear pattern is possibly related to plastic strain. Most particles are aligned and more free to slide pass each other. The sliding may also propagate due to stress transfer between particles. The dilatant behaviour is mainly controlled by shear deformation (Figure 2.14: type 3). Moreover, Ng (2007) suggests that the dilatant behaviours are likely to be associated with permeability due to the increasing volume of pore fluid.

In unsaturated soil, permeability can be controlled by precipitation and the water retention capacity of the soil (Selby, 1993). In terms of the permeability of clay tills, permeability is considered to be controlled by the macro-structure of the clay, rather than by the micro-structure, and the majority of the water migrates through the inter-clod spaces rather than through the denser or harder clods themselves (Figure 2.15). With further compaction and with increasing water content, the clods are broken down and remoulded, producing a more uniform but less permeable clay soil (Elsbury et al., 1990; Benson et al, 1999; Murray et al., 1992 and Wright et al. 1996). Hossain (1996) explored the permeability of undisturbed fissured west central Scotland tills using fixed-wall Rowe cells and flexible-wall Triaxial cells. He suggested that permeability is strongly dependent upon effective stress (Figure 2.16).

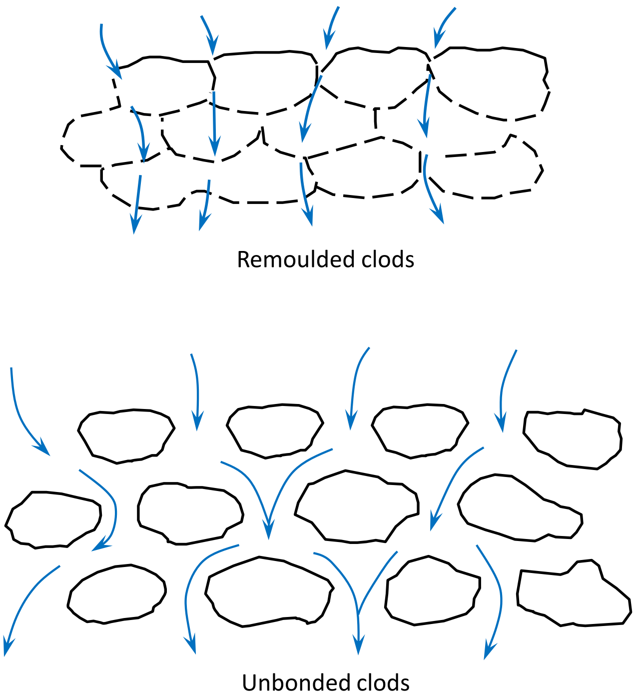

Figure 2.9 Influence of soil clods on permeability of compact clay. Note: arrows indicate direction of permeant flow (redrawn from Elsbury et al., 1990)

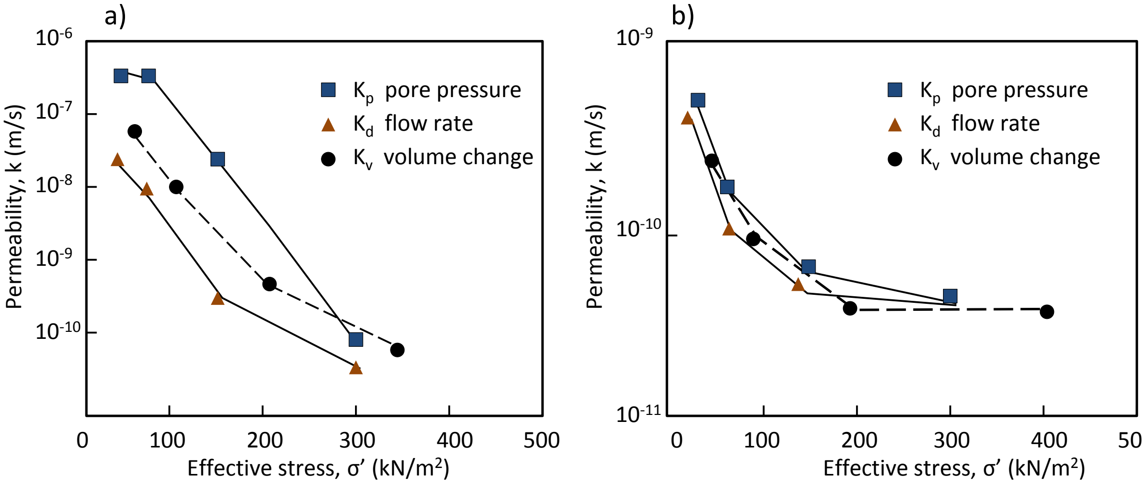

Figure 2.10 Plots of variation of permeability against effective stress for fissured Scottish till: a) Rowe cell tests; b) Triaxial cell tests (sourced from Hossain, 1996).

2.3.4 Creep deformation

In geotechnical terminology, pre-failure deformation mechanisms are usually referred to as creep, which is a continual deformation under sustained load (Varnes, 1983). The process of creep has been defined as occurring in three states (Figure 2.17). Primary creep occurs immediately after an increase in stress and is characterised by a decreasing strain rate. The secondary creep phase consists of deformation at a constant strain rate. The tertiary creep phase shows an accelerating strain rate, generally leading to creep rupture or failure (Fell et al., 2002). Varnes (1982) and others have taken note of the short periods of secondary creep, and the possibility that it is due to the concurrent processes of primary and tertiary creep. Moreover, the secondary creep behaviour is similar to plastic deformation, in which plastic strain increases at a constant rate after reaching the yield stress when the stress is constant (Summerfield, 1991). The fundamental differences and similarities between plastic and creep deformation on the basis of time under constant stress state are shown in Figure 2.18. These three stages of creep are for pre-failure and progressive failure and their mechanisms can be explained by brittle (stage 1) and plastic deformation (stage 2) and Tertiary creep to rupture (stage 3) is brittle.

However, the post-failure creep behaviour, which involves small renewals of failure on a pre-existing slip surface, is still unclear. Creep in this case is defined as a steady movement of the soil mass under in the direction of low shear stresses (Van Asch, 1984). According to Sidle and Ochiai (2006), creep is caused by slow viscoplastic deformation of the rock and soil. In a few cases, creep has been thoroughly monitored because large changes in stress occurred within a slope. The deformation of slope progresses slowly by changes in groundwater levels and weathering processes (Shimokawa, 1980; Jungerius and De Jong, 1989; Moeyersons, 1989).

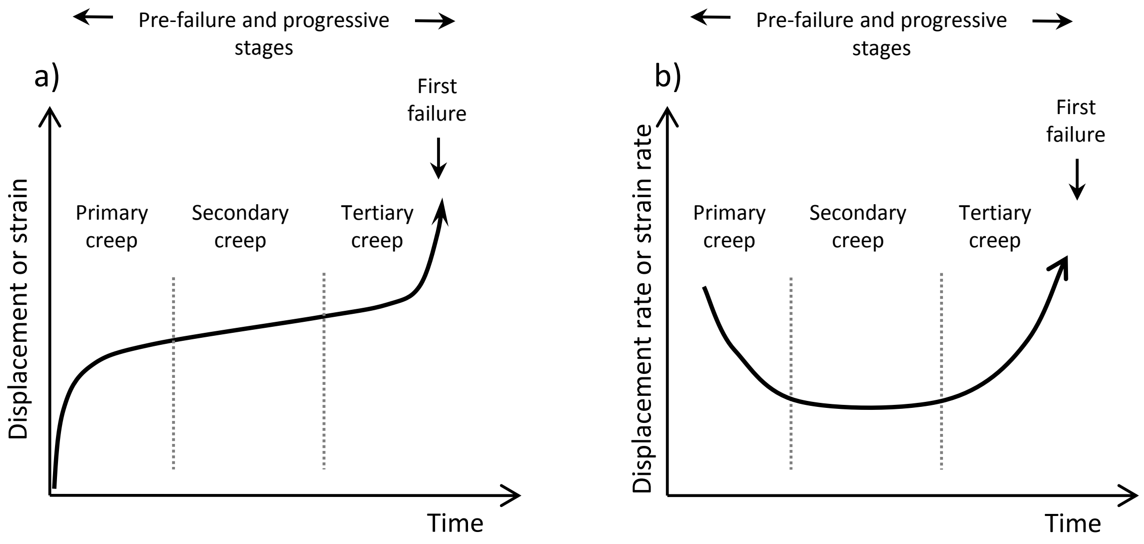

Figure 2.11 Diagrammatic representation of creep behaviours for pre-failure and progressive stages including three phases of creep at constant stress. a) plot of displacement against time; b) plot of displacement rate against time

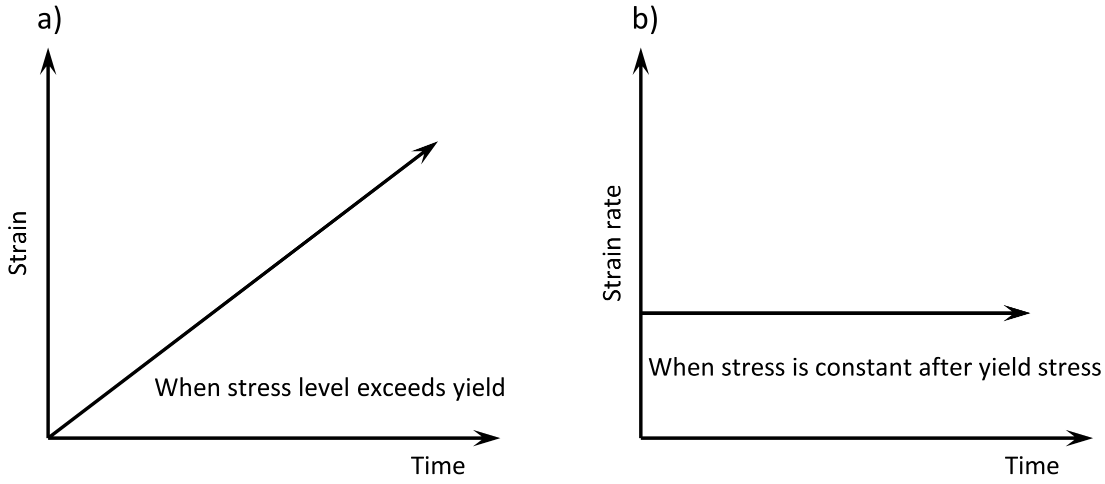

Figure 2.12 Plastic deformation at constant stress (after Summerfield; Ng, 2007)

2.4 Chapter summary

This chapter has reviewed the literature on landslides based on three themes: the fundamentals of landslide processes; landslide dynamics; and material property and mechanisms of landside. The literature review has identified the current gaps in landslide studies including:

1. Understanding of landslide morphology: most studies have used remote sensing techniques to investigate a coastal landslide. However, the temporal resolutions of such techniques are limited, making it difficult to link movement to the cause. Alternatively, geotechnical instrument based monitoring has been used to provide insights into the dynamics of landslide movements and hydrologic triggers to detect landslide activity. This research attempts to improve the understanding of landslide activities and their processes by linking the different scales of the spatial and temporal patterns of landslide movements.
2. Post-failure creep involves small renewals of failure on a pre-existing slip surface. Only two stages of post failure are mentioned – 'occasional reactivation' and 'active landslide'. However, these two patterns are insufficient to understand the landslide movement patterns during post failure creep.
3. A reactivated landslide is often associated with an increase of pore water pressure and the mobilized shear strength is closely related to the residual strength. However, the mechanisms of a reactivated landslide are not completely clear.
4. The relationship between pore pressure (groundwater) and landslide displacement rate is complicated by the complex landslide hydrogeology, particularly material property. The understanding of the hysteresis relationship between these two factors is still poor.

Chapter 3 Field site and research methods

This chapter describes the field site and methods used in this study. This background is later combined with field data and laboratory data to understand landslide mechanisms and their processes. Terrestrial laser scanning (TLS), the in-situ instrumentation and laboratory testing are described, including field set-up, data collection and processing techniques.

3.1 Study site

3.1.1 Rationale for site selection

The selection of the study site was based on the following criteria:

I. Representativeness - the study site should represent the characteristics of a small and shallow reactivated landslides complex under coastal environments, which is typically triggered by precipitation and marine activity (e.g. Clark et al., 1991; Quinn et al., 2009; Quinn et al., 2010; Brown et al., 2012). In particular, this research focused on the upper part of the landslide complex, which is influenced by changes in groundwater conditions and affects slope stability. Also, the weathered glacial till layer, which has the highest level of activity of rainfall-induced landslides has been considered.

II. Activity - only a reactivated landslide that is currently active should be selected, bearing in mind the short-duration of monitoring with regards to the very slow to slow movement rates of the slope

III. Accessibility - the selected landslides had to be accessible in consideration of safety of the field workers during equipment installation, collection and transportation of the soil samples feasible.

3.1.2 Climate

The climate at Whitby is Cfb in the Koeppen-Geiger classification, and is characterised by warm summers (June - August) with the warmest month lower than 22°C and four or more months above 10°C on average (Figure 3.1). Rainfall varies little from summer to winter (mean monthly rainfall: 48-50 mm), except for spring (March - May), which has less rainfall (mean monthly rainfall: 40 mm). These data for Whitby cover the 50-year period from 1961 to 2012 and are provided by the UK's National Weather Service MIDAS data, Met Office.

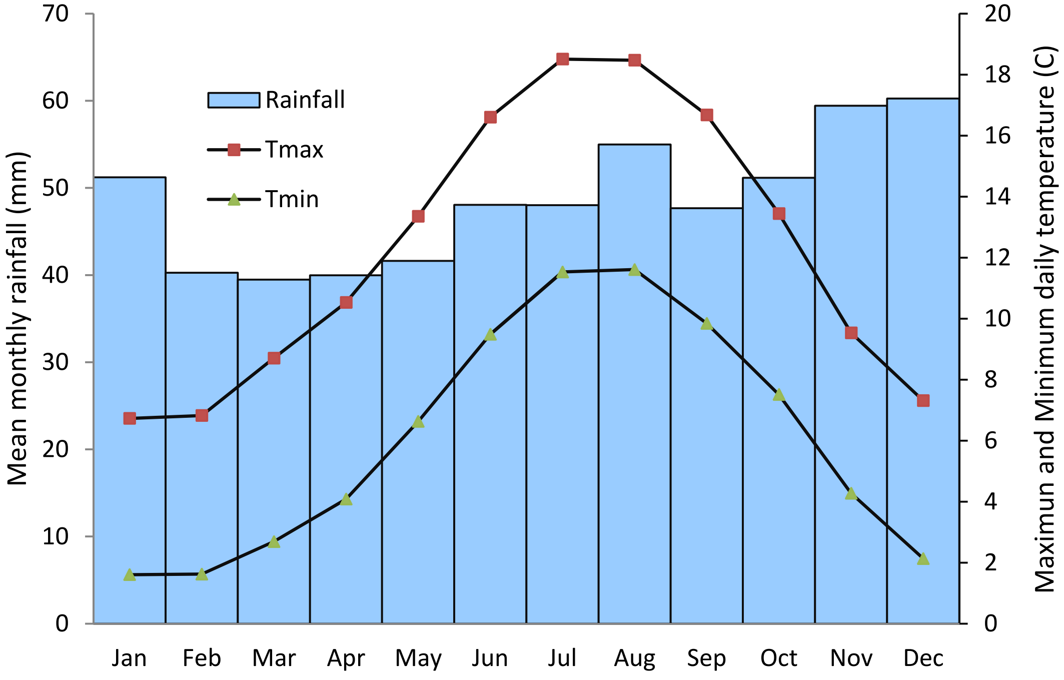

Figure 3.1 Whitby mean monthly rainfall and temperature trends for the 50-year period from 1961 to 2012, provided by the UK's National Weather Service MIDAS data, Met Office.

Focusing on the monitoring period, monthly rainfall at the study site in both 2011 and 2012 were plotted as shown in Figure 3.2. The total rainfall from January to December 2011 was approximately 565 mm with high amount of rainfall between January and February before the weather became very dry in March. Rainfall increased again between spring-summer (March - August 2011; 6 months) before the weather became drier towards winter (surface temperature was the warmest recorded in the UK over the past decade). Conversely, cumulative rainfall reached 430 mm during the wet period in 2012, which started from late spring and lasted through to winter (April – December 2012; 9 months). The marked differences in rainfall month to month imply strong landslide dynamics.

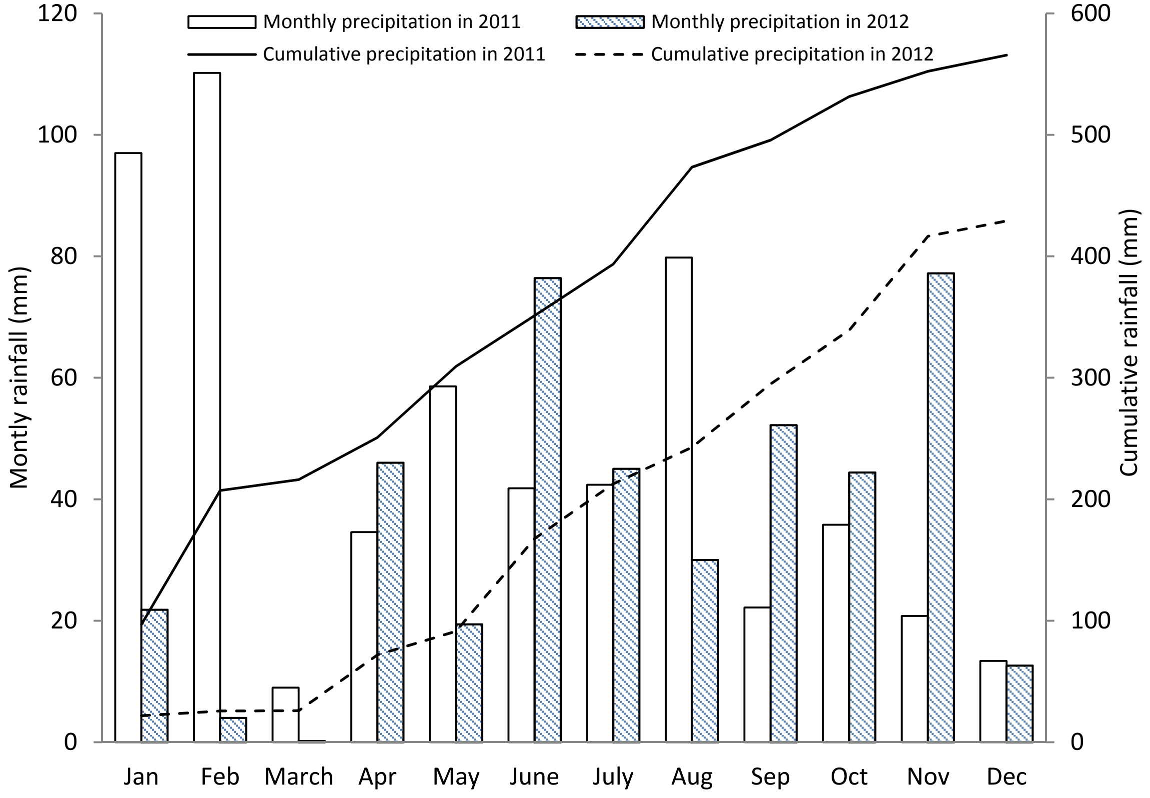

Figure 3.2 An overall pattern of monthly precipitation in 2011 and 2012 based on rainfall data from the Met office at Whitby.

3.1.3 General characteristics of glacial till at Upgang

The site is prone to landslides distributed across the cliff slope with a variety of landslide types such as rotational/translational slides, mudslides/mudflows, blockfalls, topples and gullies, as can be seen in Figure 3.3. This activity has been observed by Clark (1991) who suggests that the slope material, composed of glacial deposited tills, is vulnerable to deformation by triggering factors including precipitation, groundwater and undercutting. However, there is no evidence to identify when landsliding began although an active landslide complex is shown in a 1:2,500 Ordnance Survey Maps in 1892. The erosion rate of the glacial cliff averages about 25 m per century (Agar, 1960).

The study site is comprised of glacial till originating from the Devensian glacial stage of the Late Pleistocene (Table 3.1). In generally, this is an upper till separated from a lower till by discontinuous layers of sand, gravel and lacustrine clays (Clark et al., 1991; 2008). In this study, the cliff was separated into three sections namely, ‘upper’, ‘middle’ and ‘lower’ in order to link the characteristics of landslides to the local geology (Figure 3.4). The upper section of the cliff consists of weathered mottled orange / brown / grey upper till overlying a reddish brown matrix-supported till. More specifically, the upper section is composed of two layers of lithology namely weathered till or Unit 1 in the classification of Clark et al. (2008), which contributes to highly active shallow landslides, and Withernsea or LFA4 in the classification of Roberts et al. (2012) or Unit 2 in the classification of Clark et al. (2008), which exhibits stepped morphology with layers of landslide material from the weathered till layer resting on top. The middle section of the cliff is steep slope with laminated fine clay and sand, silts, sand and gravel layers. The fluvio-glacial sand layer can be referred to LFA3 in the classification of Roberts et al. (2012). The lower section consists of brown matrix supported till and can be referred to as Skipsea till or LFA2, which overlies grey clast supported till. The grey clast supported till can be referred to as Basement till or LFA1 or Unit 3 in the classification of Clark et al. (2008), which is subhorizontally bedded Liassic shale, occasionally exhibiting folding. The lower section also shows a stepped profile with layers of mobilised materials resting on top. Two triggering factors, rainfall and marine activity, significantly influence the lower section of the cliff slope.

Table 3. 1 Characteristics of the glacial till at the Upgang cliff

Site section	Symbol	Lithostratigraphy	Description	Cliff conditions	Approximately depth (m)	Schematic cross section (source: Roberts et al., 2013)
Upper	U1	Weathered till/Unit1	Brown/orange/grey matrix supported till	The majority of the cliff is influenced by highly active shallow landslides	2 - 3	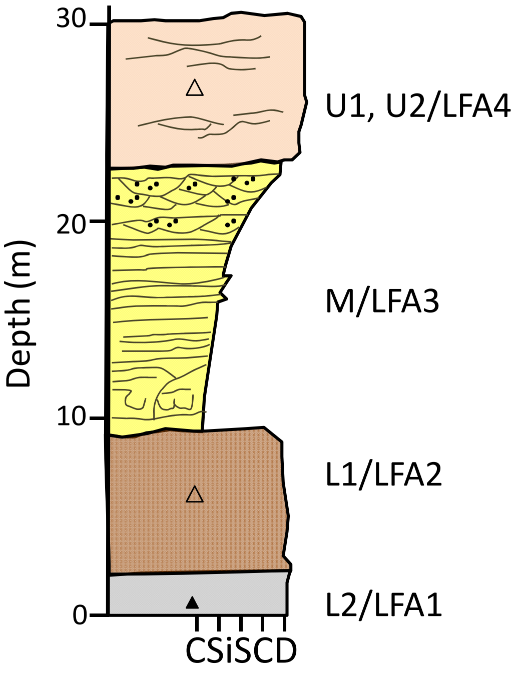
	U2	Withernsea till/ LFA4/ Unit2	Reddish Brown, matrix supported till	Stepped profile with layers of landslide material from the weathered till resting on top	3 - 8	
Middle	M	LFA3	Laminated fine sand, silt and clay	Steep slope of exposed sand	2 - 10	
Lower	L1	Skipsea till/ LFA2	Brown matrix support till	Stepped profile with layers of previously landslide material resting on the Skipsea till	3 - 9	
	L2	Basement till/ LFA1/ Unit3	Grey clast supported till	A tabular geometry with 1 - 1.5 m height, highly weathered	1 - 1.5	

Note: Depth or thickness is only observed from exposed thickness of the cliff; it is not the total unit thickness.

1. Upper section of the cliff

Shallow landslides (i.e. mudslides, slip plane < 3 m below ground level) and stepped morphology with reactive shallow landslide resting on the Withernsea till/LFA4

2. Middle section of the cliff

Steep exposed sand and gravel layer, Block fall/flow often found here

3. Lower section of the cliff

Block falls and gullies formed by action of running water

Figure 3.3 Characteristics of glacial till at the Upgang cliff and landslide features of the upper section (1), middle section (2) and lower section of the cliff (3)

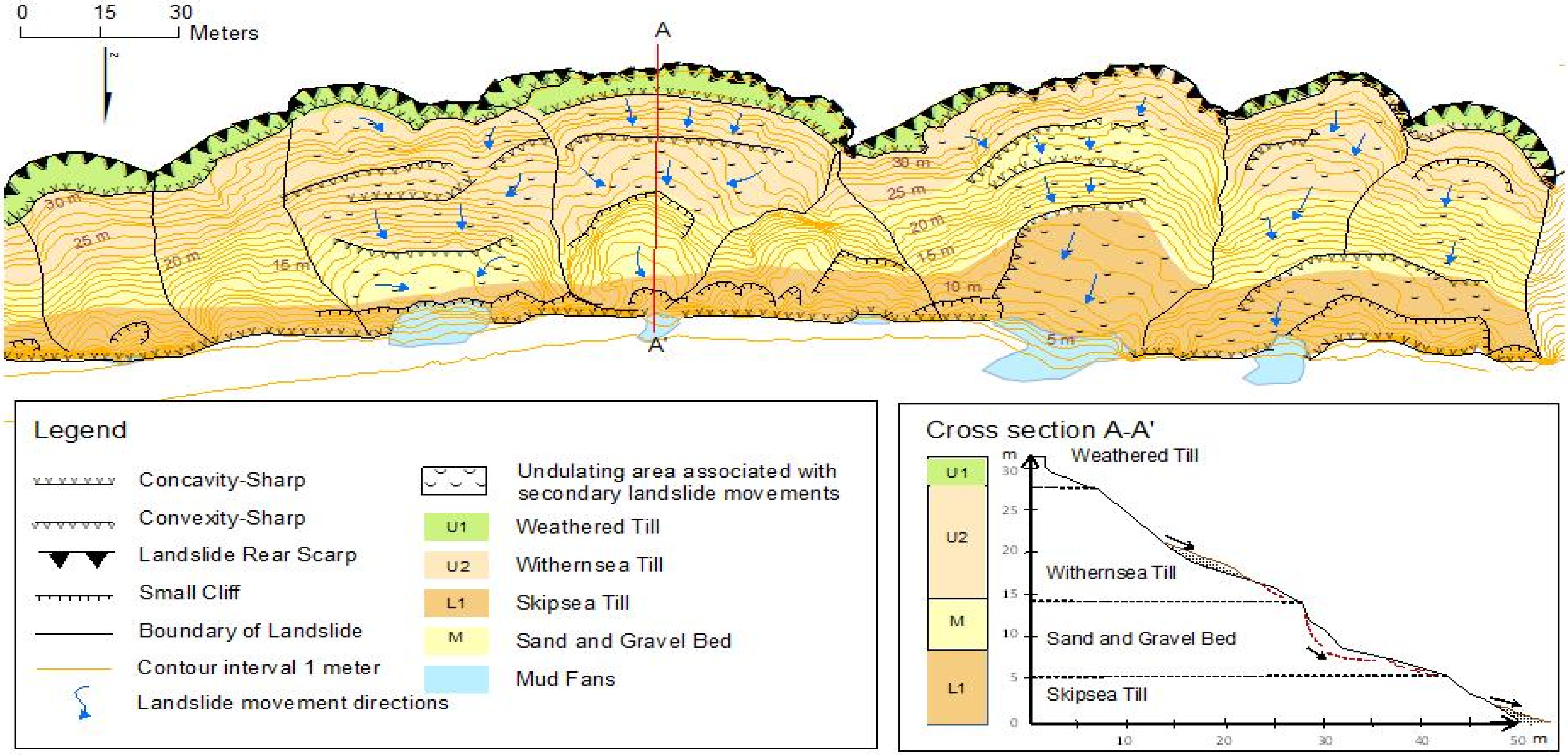

Figure 3.4 A geomorphological map of the study site. Note: contour information were extracted from TLS data in 2012.

3.2 Site investigation

Fieldwork was conducted between July 2010 and December 2012, with detailed monitoring using surveying techniques between March 2011 and December 2012 in order to improve the understanding of coastal cliff behaviour and processes. The period of monitoring and data capture is summarised in Table 3.2. A combination of in-situ instrumentation, terrestrial laser scanning and laboratory testing was employed. The fieldwork aims to capture the spatial and temporal distribution of landsliding in both coarse whole slope and fine local scales. The terrestrial laser scanning (TLS) has been demonstrated to be capable of capturing high-resolution topography, which collected repeatedly over time can provide a measurement of cliff change and landslide movement (Rosser et al., 2007; Quinn et al., 2009; and Norman, 2012). Geotechnical instruments have also been widely used to record detailed characteristics, in particular high temporal and spatial resolution monitoring of slope movement and hydrological factors (e.g. Van Asch, 1984; Allison and Brunsden, 1990; Petley et al., 2005b; Massey et al., 2013). Conversely, laboratory tests can be used to explore the physical properties and shear strength parameters of the slope materials (again – examples, or references). These methods, and subsequently the data collected, are significant in exploring deformation, landslide mechanisms and controls. The rest of this chapter discusses each method in detail.

Table 3.2 The period of monitoring data from all instruments, including Casagrande piezometers (PZU, PZM and PZL), vibrating-wire extensometers (VBW1, VBW2, VBW3, VBW4 and VBW5), string extensometers (S1, S2, S3, S4 and S5), tipping bucket rain gauge and the laser scanner (TLS) (Trimble and RIEGL VZ1000). Monitoring frequnecy: TLS – monthly; continous in-situ monitoring at 15 minutes intervals; and monthly site visits. Note: * the main site; ** broken instrument; No data- no displacement data for two and half months.

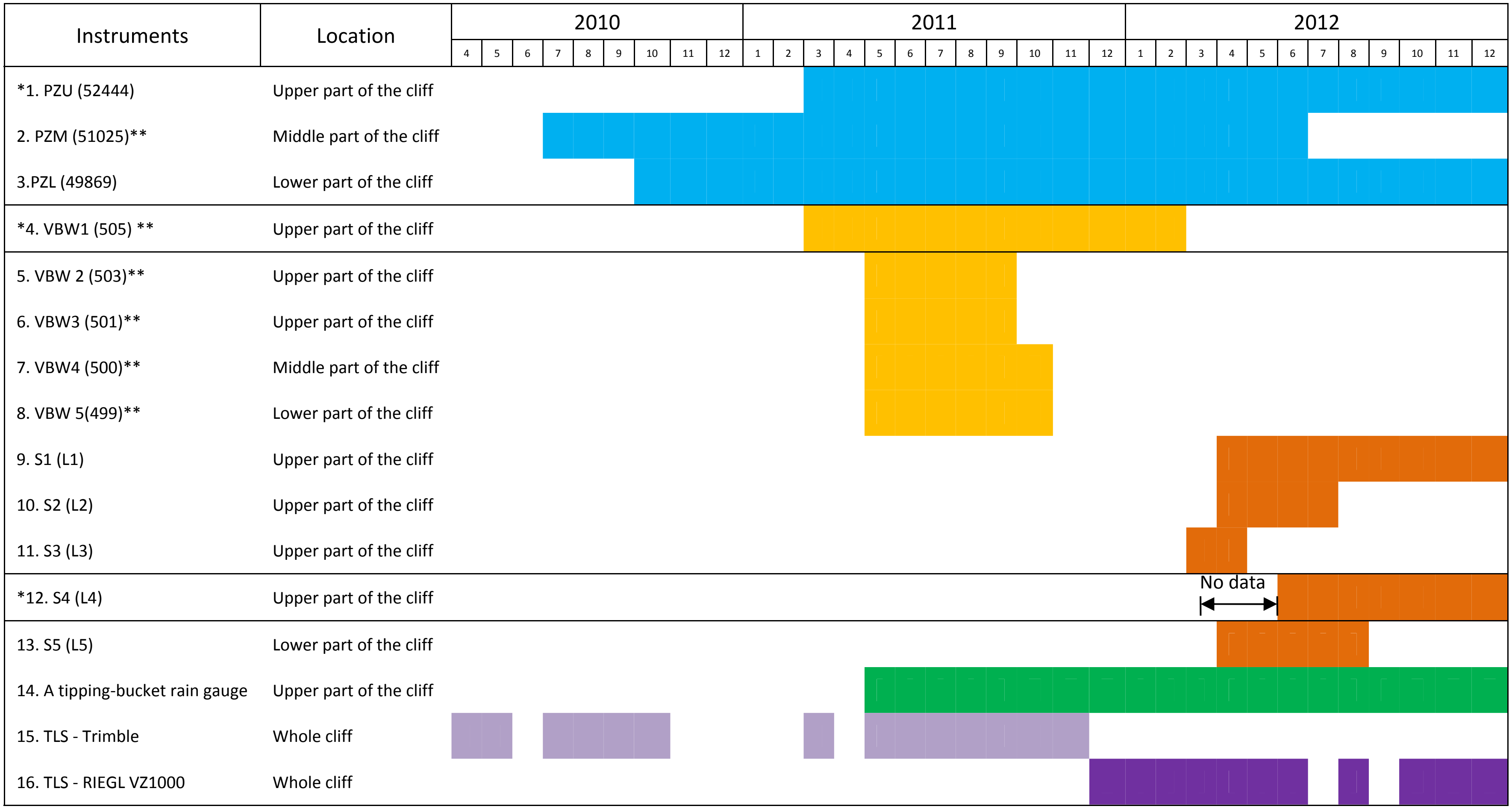

Instruments	Location	2010									2011												2012											
		4	5	6	7	8	9	10	11	12	1	2	3	4	5	6	7	8	9	10	11	12	1	2	3	4	5	6	7	8	9	10	11	12
*1. PZU (52444)	Upper part of the cliff												🟦	🟦	🟦	🟦	🟦	🟦	🟦	🟦	🟦	🟦	🟦	🟦	🟦	🟦	🟦	🟦	🟦	🟦	🟦	🟦	🟦	🟦
2. PZM (51025)**	Middle part of the cliff				🟦	🟦	🟦	🟦	🟦	🟦	🟦	🟦	🟦	🟦	🟦	🟦	🟦	🟦	🟦	🟦	🟦	🟦	🟦	🟦	🟦	🟦	🟦	🟦						
3.PZL (49869)	Lower part of the cliff							🟦	🟦	🟦	🟦	🟦	🟦	🟦	🟦	🟦	🟦	🟦	🟦	🟦	🟦	🟦	🟦	🟦	🟦	🟦	🟦	🟦	🟦	🟦	🟦	🟦	🟦	🟦
*4. VBW1 (505) **	Upper part of the cliff												🟨	🟨	🟨	🟨	🟨	🟨	🟨	🟨	🟨	🟨	🟨	🟨										
5. VBW 2 (503)**	Upper part of the cliff														🟨	🟨	🟨	🟨	🟨															
6. VBW3 (501)**	Upper part of the cliff														🟨	🟨	🟨	🟨	🟨															
7. VBW4 (500)**	Middle part of the cliff														🟨	🟨	🟨	🟨	🟨	🟨														
8. VBW 5(499)**	Lower part of the cliff														🟨	🟨	🟨	🟨	🟨	🟨														
9. S1 (L1)	Upper part of the cliff																									🟧	🟧	🟧	🟧	🟧	🟧	🟧	🟧	🟧
10. S2 (L2)	Upper part of the cliff																									🟧	🟧	🟧	🟧					
11. S3 (L3)	Upper part of the cliff																								🟧	🟧								
*12. S4 (L4)	Upper part of the cliff																									No data		🟧	🟧	🟧	🟧	🟧	🟧	🟧
13. S5 (L5)	Lower part of the cliff																									🟧	🟧	🟧	🟧	🟧				
14. A tipping-bucket rain gauge	Upper part of the cliff														🟩	🟩	🟩	🟩	🟩	🟩	🟩	🟩	🟩	🟩	🟩	🟩	🟩	🟩	🟩	🟩	🟩	🟩	🟩	🟩
15. TLS - Trimble	Whole cliff	🟪	🟪		🟪	🟪	🟪	🟪					🟪		🟪	🟪	🟪	🟪	🟪	🟪	🟪													
16. TLS - RIEGL VZ1000	Whole cliff																					🟪	🟪	🟪	🟪	🟪	🟪	🟪		🟪		🟪	🟪	🟪

3.2.1 TLS

3.2.1.1 Choice of technique

Sequentially measuring slope morphology is necessary to in order to gain a quantitative record of change in the cliff face to develop an understanding of coastal erosion and the quantification of whole-slope movements. A literature review suggested that a number of methods have been used previously for monitoring coastal change including both aerial/satellite and terrestrial techniques (e.g. digital photogrammetry, dGPS, aerial photographs, InSAR, and LiDAR). However, aerial data usually has lower resolution, are more expensive, are intended for use over large areas and are less effective on steep slopes due to line-of-sight occlusion. Therefore terrestrial data capture is considered more appropriate for a study of this nature. Many studies have illustrated the ability of TLS to monitor coastal erosion (e.g. Lim et al., 2005; Rosser et al., 2005; 2007) and soft-rock cliff recession (e.g. Hobbs et al., 2002; 2008; Quinn et al., 2008; and, Quinn, 2009). However, TLS has shown to produce both temporal and spatial resolutions that are useful for examining landslide processes. dGPS provides accurate results in point data format, but as a point-by-point survey technique, this approach has difficulty assessing the overall landslide geometry or the wider evolution of landslide of the whole cliff face. Conversely, the TLS is able to produce high-resolution 3D surfaces across the area of interest.

3.2.1.2 Theoretical background of TLS

The primary TLS system used here was a RIEGL VZ-1000 which provides high speed, non-contact data capture for ranges up to 1,400 m using an infrared laser and a fast scanning mechanism. High-accuracy laser ranging is based upon echo digitization. The line scanning mechanism is based upon a fast rotating multi-facet polygonal mirror, which provides fully linear, unidirectional and parallel scan lines.

TLS data processing can be separated into four steps namely: (1) panorama scan (i.e. panorama of a full 360° view around the scanner); (2) reflector search and scan of control targets used to coregister scans; (3) image acquisition; and (4) detailed scan. Point clouds are recorded in a coordinate system relative to the scanner, termed SOCS. Alignment of multiple scans of the same date into relative coordinates transforms the data in the project coordinate system (PRCS). Multiple scans were aligned using firstly ’coarse registration’ – based upon manual identification of common features in adjacent scans, and then multistation adjustment (MSA) to improve accuracy based on a modified iterative closest point algorithm which typically achieved < 0.02 m separation of neighbouring and sequential scans. A global coordinate system (GLCS) was not utilised in this study because there was only one study site and its scale was small and transformation into OSGB coordinates greatly increases the data volume purely due to the numerical size of the coordinates.

3.2.1.3 Usage in this study

The TLS survey was performed almost every month to monitor landslide activity on the cliff face, enabling a monthly 3D surface of the cliff to be produced. Data capture using the Trimble was limited due to the rising tides (e.g. a station on the beach was needed for 45 minutes in order to complete one scan). The more efficient RIEGL VZ1000 scanner was deployed each month since December 2011 (Figure 3.5 b). For this research, Trimble data was used to provide a guide for instrument installation. Only the data form RIEGL VZ1000 was used to calculate the erosion rates and the volume of change across the cliff face. Table 3.3 shows the comparison between the Trimble GS200 and the RIEGL VZ 1000.

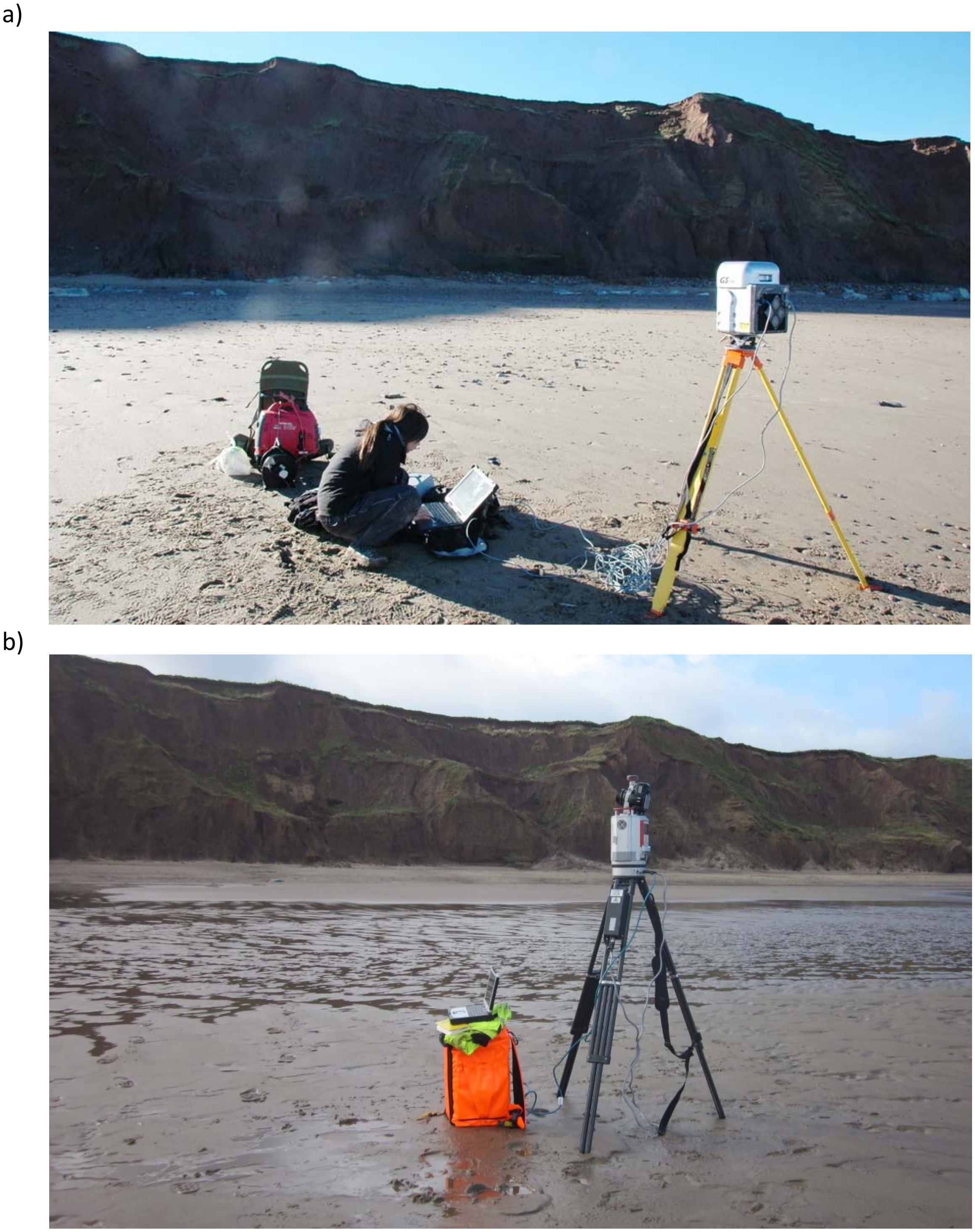

Figure 3.5 Photographs of two devices: a) Trimble GS200 device includes a tripod, a laser scanner, a generator and a computer; b) RIEGL VZ 1000 consists of a tripod, a laser scanner and a computer

Table 3.3 Comparison of terrestrial laser scanner specifications

Range performance	Trimble GS200	RIEGL VZ1000
Range (m)	200	up to 1400 m
Speed (points/ sec)	Up to 5000/ sec	up to 122,000/sec
Distance accuracy (mm)	7-8 mm at 100 m	5 mm
Angular accuracy (°)	0.001	0.008
Beam diameter (mm)	3 mm at 50 m	30 mm
Laser wavelength (nm)	532	1550 (near infrared)

The TLS data was collected monthly by scanning from three stations on the beach. Each station was approximately 100 m from the toe of the cliff and 80 m apart from each other along the coast (with overlapping scan areas to facilitate joining of the scans during data analysis). Four control targets were installed on the top of the cliff to be used as references for the alignment of successive scans. The width of the cliff that was scanned was about 250 m and its height was 30 m, producing a scan area in elevation view of *c.* 7,500 m². The average point spacing across the area was 0.05 m.

The post-processing was undertaken using a combination of different software packages (RiSCAN PRP, ArcMap, MATLAB and Stata). Figure 3.6 describes the workflow of TLS data processing. RiSCANPro is initially used for reducing the scan data size (decimation), removing any spurious points resulting from vegetation, registering to the project coordinate system and surface comparison (Step 1).

In detail, firstly, the point clouds collected in each month were manipulated by using a point filter. A single step point filter randomly decimates the point cloud to half of its original size. In this study, 5 point filter steps were used. Vegetation in each point cloud data was removed by using an amplitude gate or reflection intensity threshold, whereby vegetation was identified to consistently return higher reflections relative to the bear glacial till. The amplitude range was used between the minimum amplitude of 8 dB and the maximum of 50 dB.

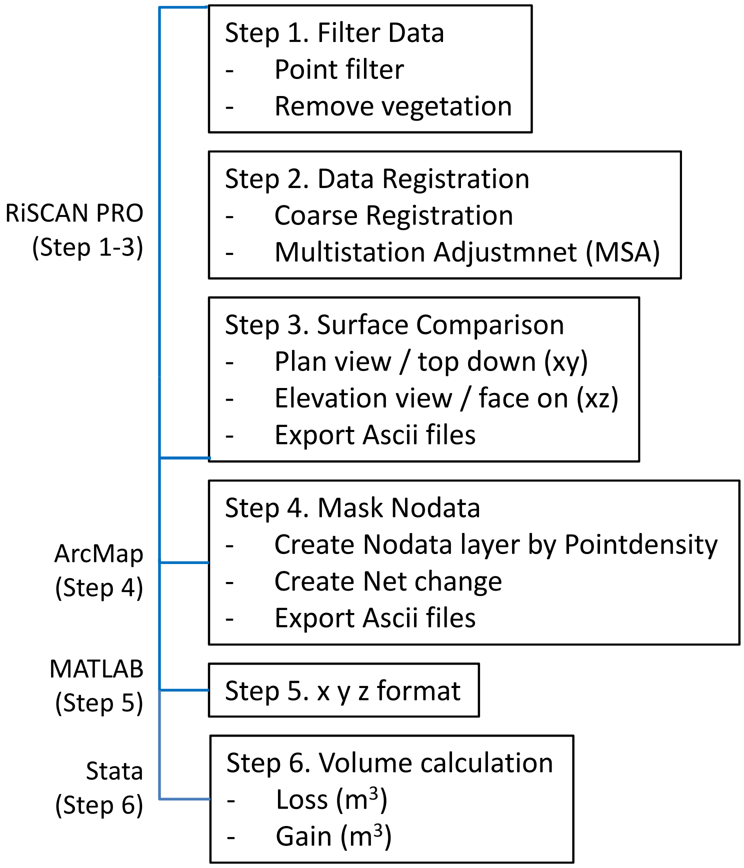

Figure 3.6 Workflow of TLS data processing

The cleaned files were then registered initially using manual coarse registration (Step 2). The coarse registration was mainly based upon retroreflective targets (i.e. at least 4 control points in contiguous scans) and the resulting alignment was improved by using MSA, which generally achieved a maximum plane error of 0.02 m. Surface patches were automatically detected within the point cloud, and reduced to a single point and a polar vector. These points and poles Are then used as the basis for the alignment using a modified ICP algorithm (iterative closest point algorithm). In the final step, all data sets (11 months) were aligned to the first scan captured at the site (December 2011). As a result, the successive scans each aligned with an RMS separation of < 0.04 m. Areas with no data, such as sections of the cliff which were occluded, were excluded from the analysis.

An example of a point cloud of the cliff face can be seen in Figure 3.7. Once aligned, the data is projected in two views to enable surface comparison: plan/top down view (xy), and elevation/face-on view (xz) (Figure 3.8). Surface comparison was used to extract values of change between each sequential laser scan epoch. For each data point in scan *n* the distance (difference) is calculated normal to a base plane (e.g. xy) to the nearest point on the next scan (*n* + 1)The surface comparison for each survey epoch was based on both monthly and cumulative changes. For monthly change, data was compared with the preceding month. For cumulative change, each was compared to the initial first scan or reference month (December 2011). Following completion of the surface comparison for each month, the minimum, mean and maximum differences were recorded and statistics were calculated. All the surface comparisons were exported into Ascii files for analysis in ArcGIS and Matlab (Step 4 and 5). Finally, the volumes of monthly and cumulative changes were calculated by using Stata (Step 6), by multiplying the change values by the area of the pixels in the change images.

3.2.1.4 TLS accuracy

A number of factors during data collection and processing determine the accuracy of the surfaces generated. The reflectance of the TLS signal return is determined by surface characteristics, which include surface colour, wetness, roughness, and mineral composition, in addition to the atmospheric influence on ambient light conditions (Lim, 2006; Sturzenegger et al., 2007; Hodge et al., 2009). Errors can be caused when processing the TLS data during alignment of the successive scan surfaces and generation of the DEMs (Buckley et al., 2008; Hodge et al., 2009). The TLS data exhibits RMS positional errors of 0.04 m, however movement occurs across very small (< 0.04 m) to relatively large (>1 m) scales.

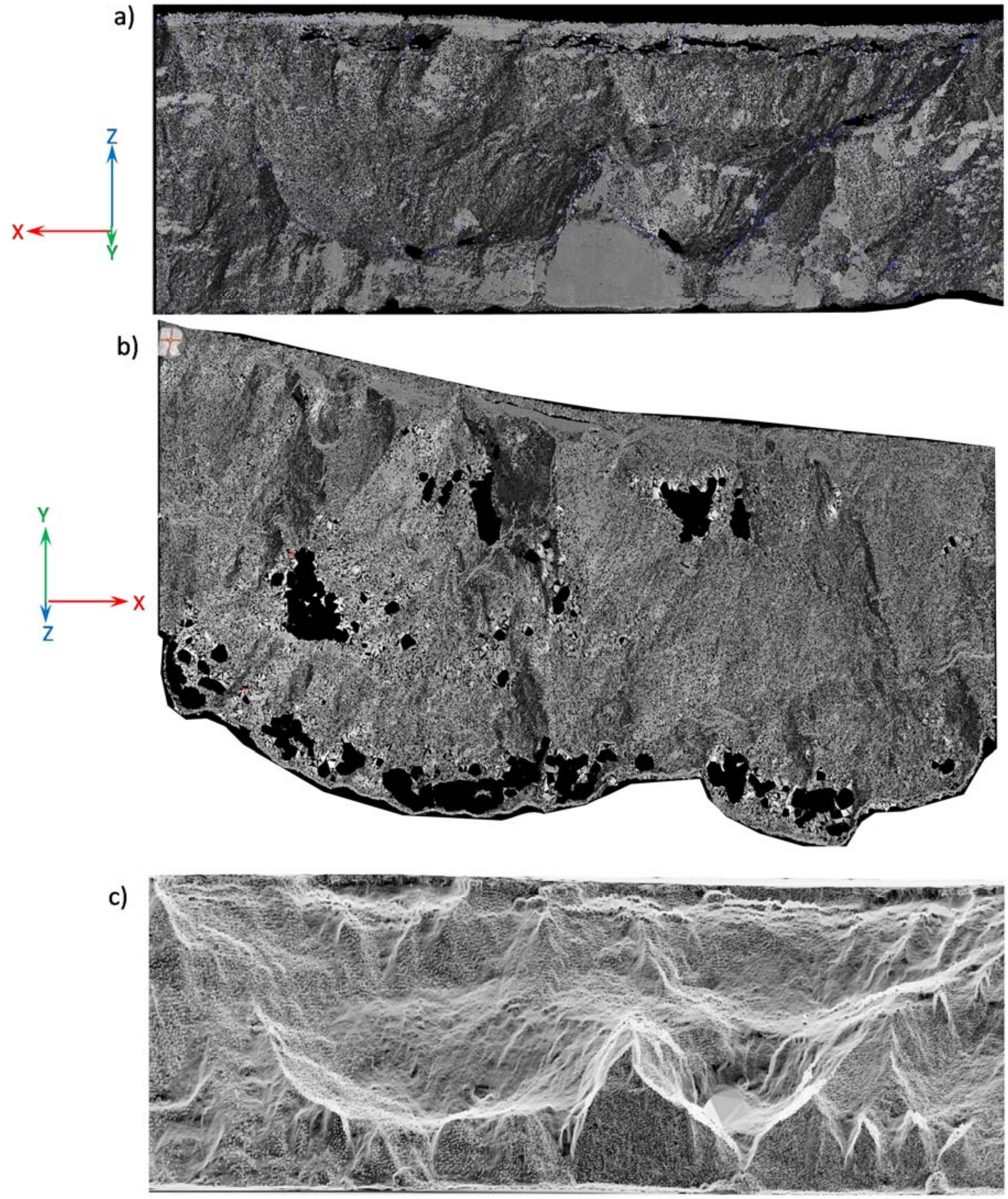

Figure 3.7 Example of point cloud of the cliff face produced by the laser scanner: a) and b) show the point cloud data from elevation/face-on (xz) and plan/top down (xy) views, respectively. Note that black areas are those sections of the cliff which are occluded from the scanner. c) Example of 2D image of the cliff face, generated from the point clouds projected in the xz view, and shaded with slope angle (light areas are oblique to the view direction).

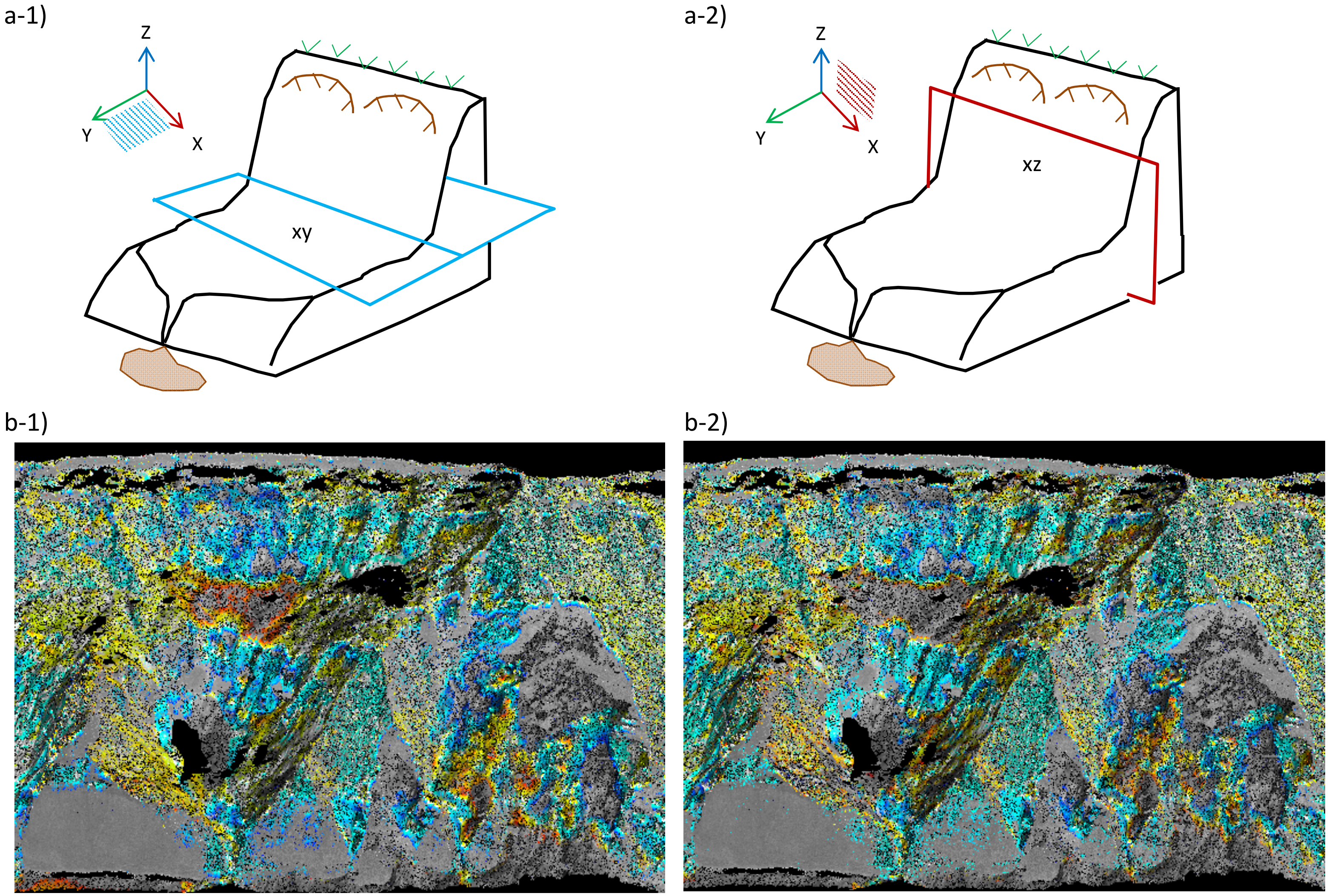

Figure 3.8 An example of surfaces comparison between 23rd April and 24th May 2012: a-1 is plan/top-down view (xy) and a-2 is elevation/face-on view (xz) used to extract values of change between these two months. The resultant, b-1 is the change detected from the xy view and b-2 is the change detected from the xz view. However, both b-1 and b-2 are presented in an elevation view facing out to the North Sea.

3.2.2 In-situ monitoring

The Upgang landslide had been monitored using in-situ instruments located across the cliff. Three separate zones were considered namely the upper, middle and lower sections. The monitoring equipment was designed primarily based on the temporal resolution that could be achieved, so that periods of landslide movement could be linked to triggering factors. The monitoring network system comprised equipment to monitor landslide movement, rainfall, groundwater and barometric pressure (Figures 3.9). Initially, three boreholes were installed at the upper, middle and lower sections of the cliff. Shallow piezometers were installed in these boreholes, named PZU, PZM and PZL. Five vibrating-wire extensometers were installed along the cliff, named VBW1, VBW2, VBW3, VBW4 and VBW5. However, the vibrating-wire extensometers were replaced one year into the monitoring period due to the limited displacement range of the equipment (< 0.05 m). The compact string poteniometer extensometers (SP2-50) were installed instead (i.e. S1, S2, S3, S4 and S5). These extensometers consisted of a wire that was anchored on the main scarp of the landslide and extended up to and past the ground surface (Figure 3.10). A summary of the monitoring instruments and their locations/depths as can be seen in Table 3.4.

The two dataset indicates that the upper part of the cliff experienced the most landsliding. The analysis therefore focussed on one extensometer and its corresponding area as it was the only equipment that recorded movement continuously throughout the monitoring period. The recently reactivated landslide, which was located at the East side of the upper section of the cliff was considered (i.e East side of the study site at VBW1 and S4). The landslide displacement, rainfall and groundwater were recorded at hourly intervals by individual data loggers.

Figure 3.9 Map of the Upgang monitoring instruments including ten extensometers (VBW1, VBW2, VBW3, VBW4, VBW5, S1, S2, S3, S4, and S5); three piezometers (PZU, PZM and PZL) and a rain gauge. Note: VBW – vibrating-wire extensometer; S – compact string pot extensometer.

Table 3. 4 Summary of monitoring instrumentation used in this study

Instruments	Elevation (m AMSL)	Depth of piezometer tip (m)	Length of extensometer	Measurement precision	Data logger
PZU (52444)	34	6.5	-	±0.0325 m	
PZM (51025)	23	4.5	-	±0.0325 m	
PZL (49869)	13.2	4.5	-	±0.0325 m	
VBW1 (505)	30		4	0.001 mm/record	Single channel VW –DT1973
VBW2 (503)	33	-	4	0.001 mm/record	Single channel VW –DT1973
VBW3 (501)	33	-	4	0.001 mm/record	Single channel VW –DT1973
VBW4 (500)	24	-	4	0.001 mm/record	Single channel VW –DT1973
VBW5 (499)	17.1	-	4	0.001 mm/record	Single channel VW –DT1973
S1 (L1)	33	-	4	0.3 mm/record	HOBO U12-4 external channel
S2 (L2)	33	-	4	0.3 mm/record	HOBO U12-4 external channel
S3 (L3)	30	-	4	0.3 mm/record	HOBO U12-4 external channel
S4 (L4)	30	-	4	0.3 mm/record	HOBO U12-4 external channel
S5 (L5)	17.1	-	3	0.3 mm/record	HOBO U12-4 external channel

Figure 3.10 Vibrating-wire and string pot extensometer installations, which is parallel to the shear surface.

3.2.2.1 Landslide movement data and filtering techniques

The landslide displacement was monitored by the self-logging vibrating-wire extensometer 'VBW1' from March 2011 to March 2012. This extensometer was replaced with the compact string poteniometer extensometer 'S4' later in May 2012 and data was collected up until December 2012. The extensometers provided continuous displacement data of the landslide at 15-minute intervals. Two and a half months of data were missing as time was needed to build, calibrate and install the string extensometer S4 after the wire extensometer VBW1 was broken after an movement event which exceeded the instrument range.

The data were filtered to remove 'noise' caused by environmental disturbances such as diurnal temperature variations and wind load on the extension cables, using time series filters. For the vibrating-wire extensometer, the resolution was approximately 0.001 mm/record, raw data were smoothed using a 1-day moving average, a period including 96 measurement intervals. For the string extensometer 'S4', the resolution is more coarse (0.3 mm/record). Thus, the raw data of string extensometer were smoothened using a moving average with 10 intervals (Figure 3.11), to derive an hourly cumulative displacement.

It should be noted that choice of equipment is of significant importance in investigating landslide movements. The vibrating wire extensometer is very useful for detecting small (< mm) very slow movements. However, it has a limitation as the wire can only extend by around 5 cm prior to reset, and the measurements are highly sensitive to 'noise' On the other hand, the string extensometer is suitable for recording larger magnitudes of movement, but the resolution is more coarse and 'noise' in some periods of monitoring obscured very small movements.

a)

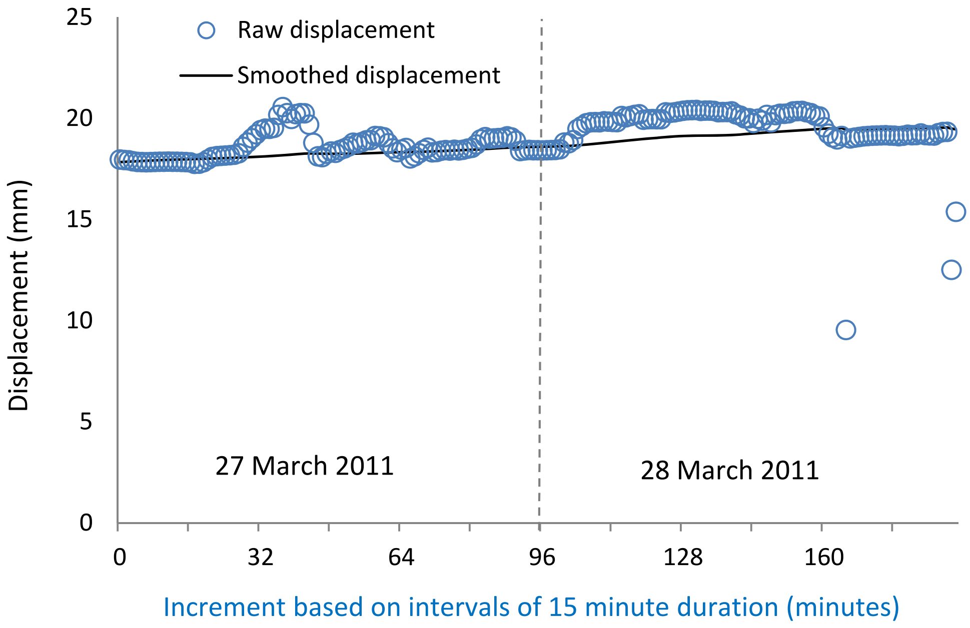

b)

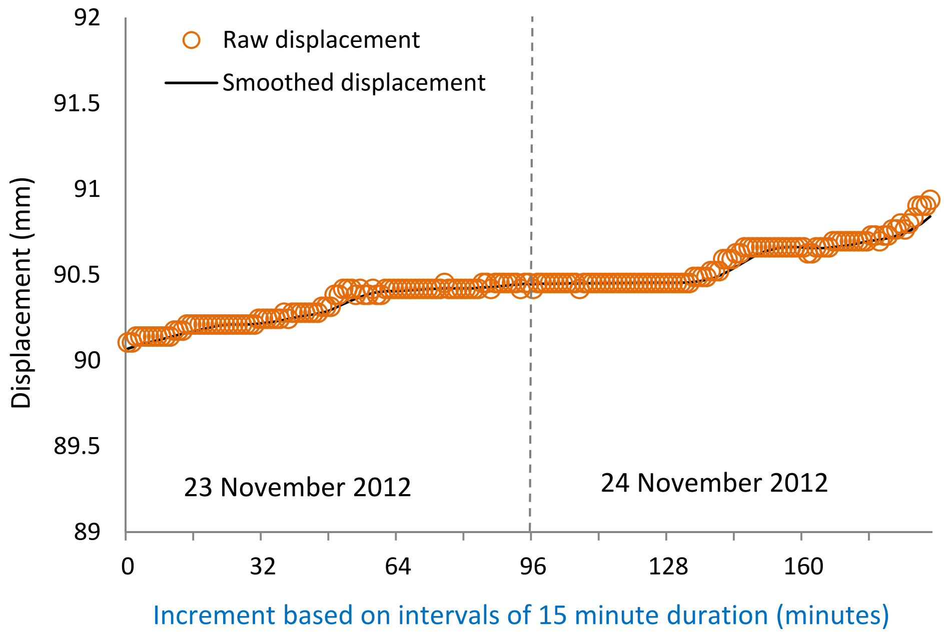

Figure 3.11 Raw (circle) and smoothed (line) displacements during 188 increments or 2 days: a) vibrating-wire extensometer 'VBW1' displacement data using a 1-day moving average and b) String extensometer 'S1'displacement data using a moving average with 10 intervals.

3.2.2.2 Groundwater measurement

Initially, three boreholes were installed at the upper, middle and lower sections of the cliff as shown in Table 3.4. Shallow Casagrande piezometers were installed in these boreholes (PZU, PZM and PZL). Each piezometer measures the groundwater level within a screened response zone shielded with a geotextile wrap, with the depth and length of each response zone selected on the basis of logging of materials from the boreholes (Figure 3.12 - 3.13). Each response zone was sealed using bentonite clay. Typically these response zones corresponded to the assumed landslide slip surface estimated from the surface geometry of the landslide, and zones where materials appeared to be particularly disturbed within the landslide mass. The VBW transducers measured the groundwater head within the Casagrande (standpipe) piezometer at 15-minute intervals and stored in data loggers (Divers). The groundwater monitoring data was averaged over each hour, and then corrected for barometric effects by substracting the hourly mean change in barometric, using data from the barometric-pressure sensor at Loftus station 30 km away.

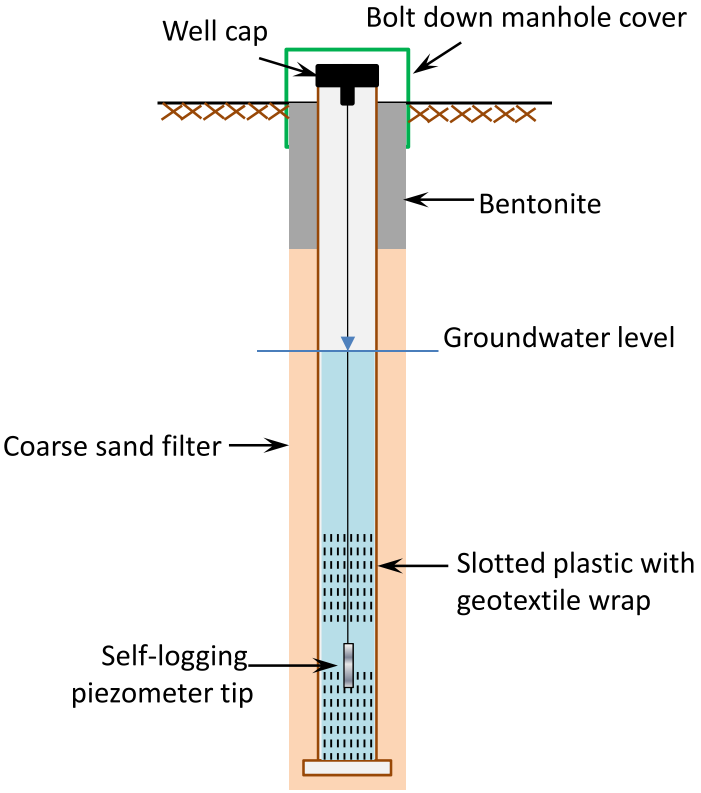

Figure 3.12 Schematic diagram of a piezometer well

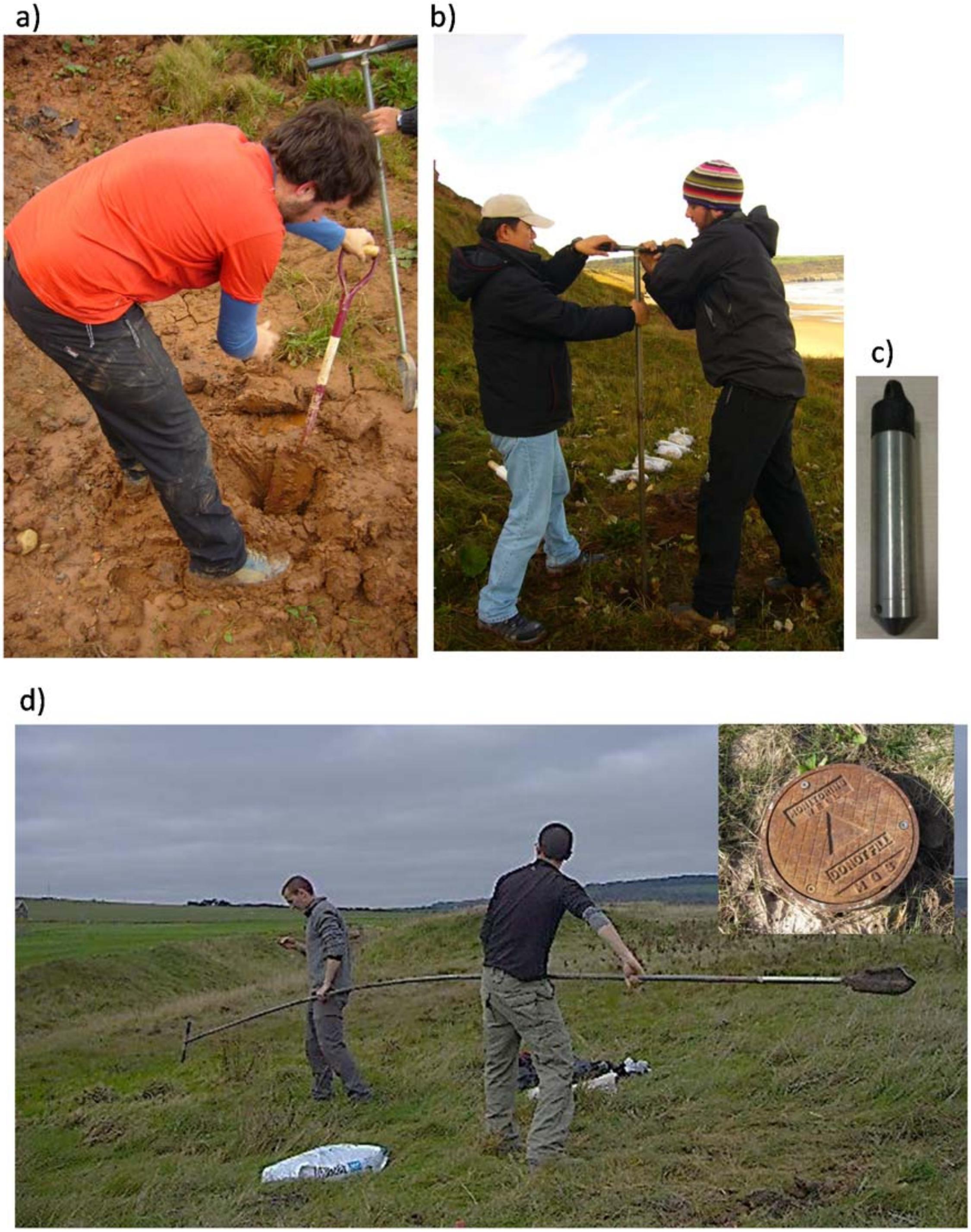

Figure 3.13 Piezometer installation by hand auger: a) preparing the borehole for Casagrande piezometer; b) Using the hand auger to drill a borehole of about 4 inch in diameter; c) Standpipe piezometer tip; d) The long extendable steel rods of hand auger is about 6 m.

3.2.2.3 Precipitation measurement

Precipitation was monitored at the top of the Upgang cliff using a tipping-bucket rain gauge. Tips of the metal bucket occurred with every 0.2 mm of precipitation collected. A reed switch detects these events and produces a momentary contact closure signal for logging in rainfall data Logger (Figure 3.14). The base of the rain gauge was a flat cement surface to help keep the rain gauge level. Precipitation and temperature data were logged every 15 minutes. Hourly rainfall was calculated and was combined with groundwater and ground movement records.

Figure 3.14 A tipping bucket rain gauge and its data logger on top of the cliff

3.2.2.4 Field sampling

Sediment sampling was undertaken at the upper section of the cliff at the head of the main landslide scarp at a depth from the surface of about 3 m (Figure 3.9 and 3.15). Undisturbed samples from both the East (E) and West (W) sides of the site were collected in order to determine whether there are differences in terms of physical properties and shear strength parameters (see Chapter 6). These samples were collected on two occasions: in May 2011 and August 2011. This location was chosen as the materials resembled that of the Withernsea till. The sediment at the main scarp was freshly exposed and unaffected by landslide movement. Each sample measured 15 x 15 x 15 cm (Figures 3.15 c). The undisturbed samples were immediately trimmed and stored in rigid boxes,and wrapped with cling film to preserve the moisture content. A total of 14 samples were stored in the fridge at a constant temperature and humidity until required for laboratory testing.

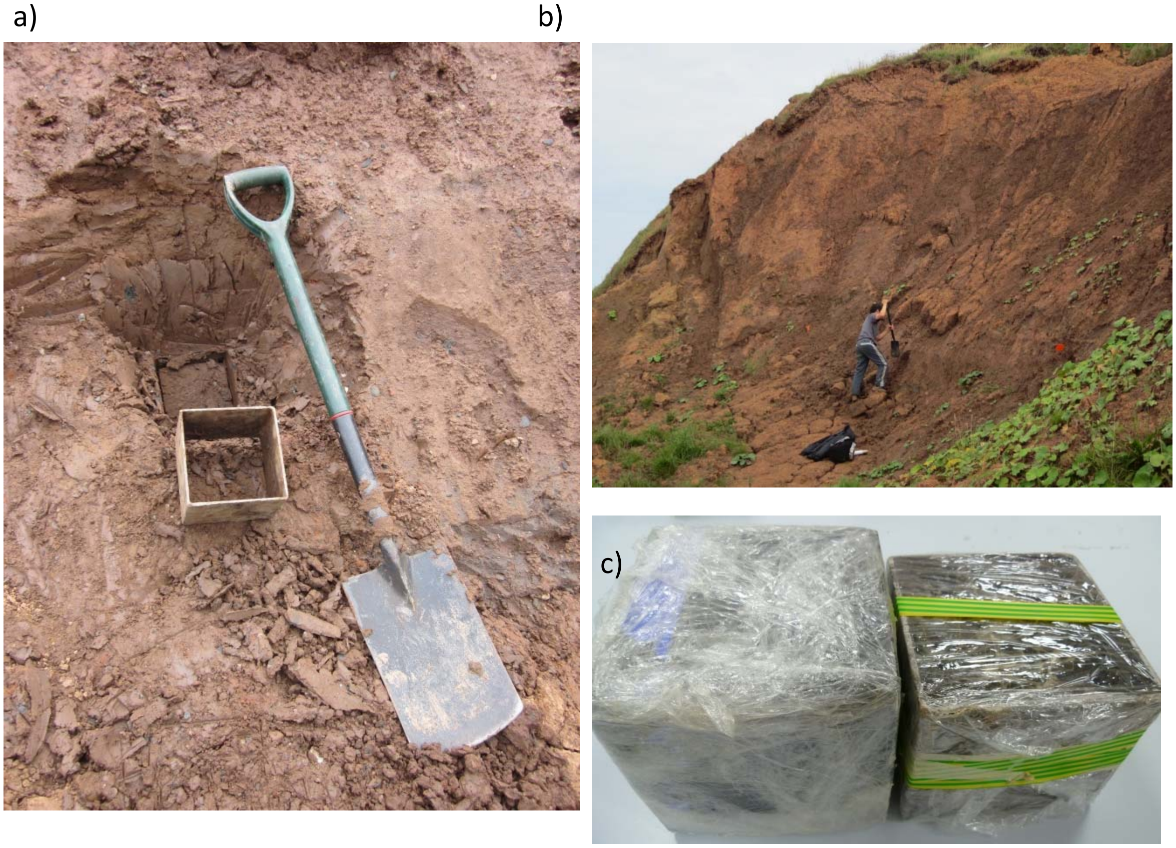

Figure 3.15 Collection of undisturbed glacial till samples at the Upper section of the cliff: a) Sampling equipment: b) Sampling location and c) Examples of undisturbed samples with cling film wrap

3.2.3 Laboratory methods

A series of detailed laboratory tests were undertaken to determine the standard physical and geotechnical characteristics of the glacial till at the upper section of the cliff, and to explore the relationship between groundwater and movement patterns. Simulations of pore water pressure conditions as derived from the field monitoring data were used to examine the accelerated behaviour of landslide. The experimental programme consisted of three stages: 1) Physical properties testing of the landslide materials; 2) Strain-controlled compression tests using direct shear box tests or strain-controlled to determine the failure envelopes of the material; and 3) Specialist direct shear tests with a pore pressure reinflation stage at constant stress using the back pressured shear box (BPS) to simulate landslide failure under elevated pore pressures at constant deviator stress in direct shear.

3.2.3.1 Physical property testing

Standard geotechnical tests were used to determine the physical properties of glacial till. These tests comprised particle size analysis, specific gravity, loss on ignition and Atterberg limits. Further physical properties were established during conventional shear box testing. These included moisture content, bulk density, dry density and void ratio (Table 3.5)using methods outlined in (BSI, 1990; Head, 1980).

Table 3.5 Summary of physical properties tests undertaken

Physical property	Measurements/Definition	Test method
Particle size analysis	Measurement of the diameter and distribution of particles within sample	Coulter Laser Granulometer method
Specific gravity	The ratio of the mass of dry solids to the mass of distilled water displaced by the dry soil	Density bottle method: BSI, 1990b: 8.3
Loss on ignition	Indicator of organic matter content	BSI, 1990c: 4.3
Moisture content	The amount of water present in a moist sample	Oven-drying method (105°C): BSI, 1990b: 3.2
Atterberg limits	A primary form of classification for cohesive soils. Fine-grained soil is tested to determine the liquid and plastic limits, which are moisture contents that define boundaries between material consistency states.	Cone penetrometer method (Liquid limit): BSI, 1990b: 4.3 and Plastic limit: BSI 1990b:5
Void ratio	The ratio of volume of voids to volume of solids	Height of solids method. Head (1980)
Bulk density	The ratio of total mass of soil to total volume	Linear measurement method: BSI, 1990b: 7.2
Dry density	Mass of the solid particles divided by the total volume	BBSI, 1990b: 7.2.5

3.2.3.2 Back-pressured shear box apparatus

Shear strength of the soil material and pore pressure reinflation testing (PPR) were carried out using a GDS back-pressured shear box apparatus (BPS) (Figure 3.16). The BPS is used for direct shear testing on soil specimens with control of sample pore pressure, following the methods outlined by Carey (2011). The apparatus can function as both a conventional direct shear and back-pressured shear machine. The standard BPS apparatus uses a standard sample 100 mm x 100 mm and 20 mm depth. The sample was moved into the pressure vessel and connected to the shear actuator and the shear loadcell. In order for the back pressure to be applied, the top of the pressure vessel was closed. Subsequently, the water back pressure was applied using a pressure controller through a high air entry porous stone in the base of the shear box. Pore water volume change was also recorded by this controller. Consolidation was performed using the feedback controlled actuator. The shearing stage began as soon as the specimen was consolidated and the required degree of saturation attained. The entire system and tests were controlled by GDSLAB software. Computer controlled parameters of the software were: 1) Shear force and displacement; 2) Effective stress; 3) total stress; 4) Pore air and pore water pressures and 5) Axial (normal) force and displacement (with optional axial actuator).

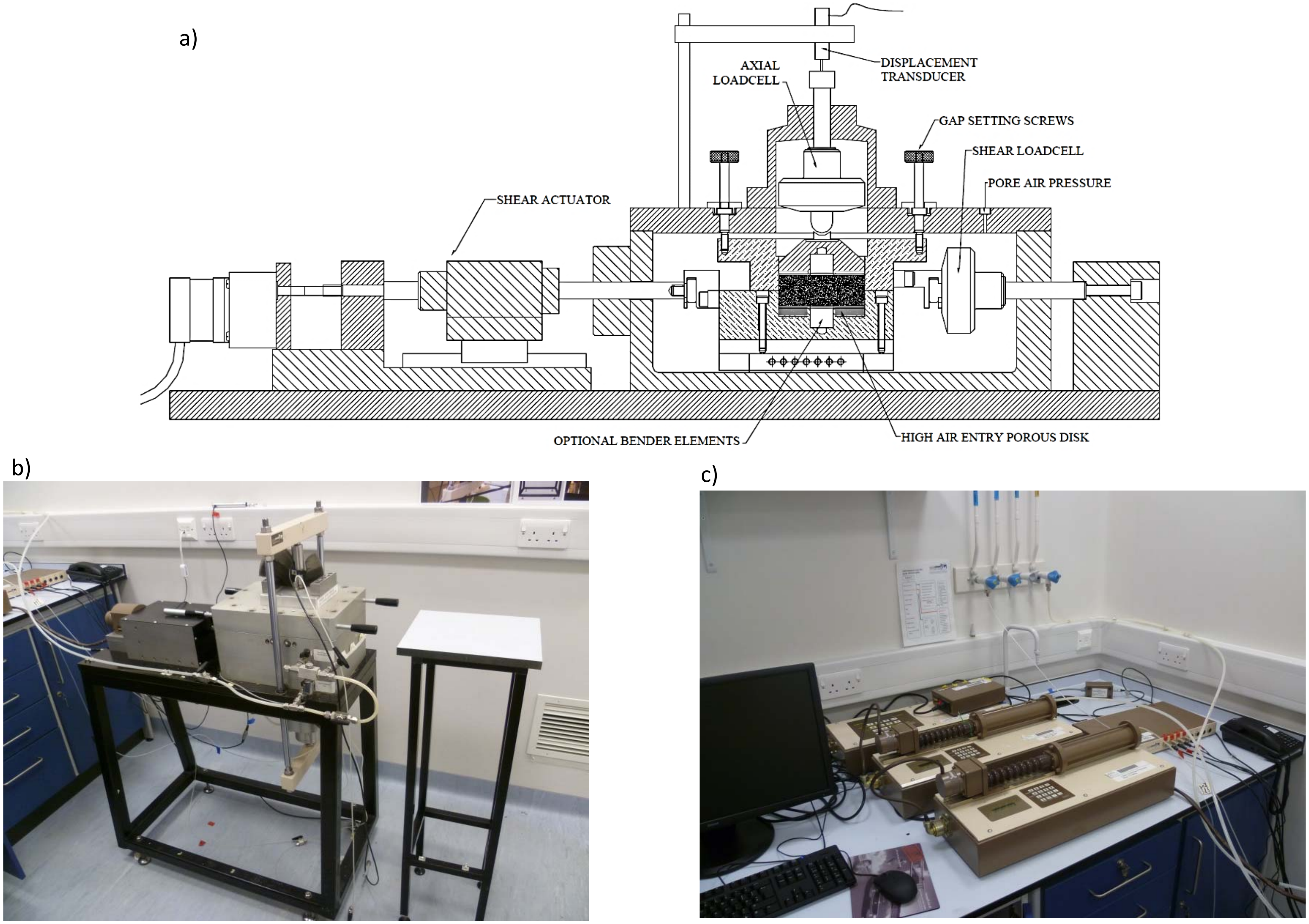

Figure 3.16 Schematic diagram of the GDS Back-pressured shear box (a). Photograph of the GDS back-pressured shear box (b) and the hydraulic pressure controllers (c)

3.2.3.3 Stage 1 preparation of soil samples

To prepare for both a conventional direct shear and PPR tests, the undisturbed soil samples were trimmed to 100 mm in plan and 20 mm in height using a straight-edged knife, wire saw and scalpel. The diameter and the height of the trimmed samples were measured using digital calliper. The left over materials from the trimming process were used to determine sample moisture content and physical properties such as specific gravity, loss on ignition and Atterberg limits.

3.2.3.4 Stage 2 sample saturation

The saturation stage was performed to simulate saturated soil conditions during heavy rainfall at the site. Firstly, the sample was flushed at a very slow rate with carbon dioxide to remove air from the sample. Thereafter, de-aired water was flushed into the sample to replace the carbon dioxide. Following this process, a simultaneous increase in the back pressure and cell pressure was undertaken to dissolve the carbon dioxide into solution in the sample. During this stage the cell pressure was kept at 10 kPa above the back pressure to maintain a positive effective stress and to prevent sample swelling during the saturation process.

3.2.3.5 Stage 3 sample consolidation

The consolidation stage was performed to simulate the field stress state associated with the weight of the overlying and surrounding soil material at original sample depth. In this research consolidated samples were tested at effective stresses ranging from 50 kPa to 175 kPa. The normal load was applied through a feedback controlled actuator that again permitted the control of stress and sample displacement. The average consolidation time for each sample was 12 hours.

3.2.3.6 Stage 4 drained compression (shearing)

After consolidation, the sample was subjected to drained shear compression at a constant strain rate (strain-controlled compression). For drained testing, the sample was sheared at a very slow strain rate of 0.01% of the initial sample length per minute as drainage was permitted (BSI, 1990d). This means the calculated strain rate of drained shear for samples of 100 mm in height was approximately 0.01 mm/min. These tests were performed to define the sample failure envelopes under drained conditions, as a reference for the design of the pore pressure reinflation (PPR) tests.

3.2.3.7 Pore water reinflation (stress-controlled reinflation)

The PPR test or stress controlled reinflation test was designed to simulate the behaviour of the reactivated landslide in the field by keeping the total normal stress and the shear stress constant while increasing the pore water pressure. These stress-controlled tests were designed to examine the strain development of the soil samples in response to changes of pore water pressure alone. The rates were chosen with reference to the field groundwater monitoring data during accelerated movement periods (i.e. non-linear deformation). For the PPR test, saturation and consolidation stages were the same as the strain-controlled compression tests (section 3.2.3.4 and 3.2.3.5). Subsequently, the drained initial shear (DIS) stage was performed only after reaching 80% of the maximum sample strength (Petley, 2002). The chosen effective stress after the DIS stage and shear stress were 75 kPa and 40 kPa respectively. These values represent a soil depth of approximately 3 m. The pore water pressure was increased at the designed rates under constant shear stress until failure occurred.

3.3 Chapter summary

This chapter has introduced the study site and the approach developed to investigate the mechanisms and processes of landsliding at glacial till based upon both fieldwork and laboratory testing. The research includes a number of techniques including the use of the TLS and other in situ instrumentation. This reflects the multifaceted nature of this study and the significance of this field of study in understanding the nature, mechanisms and causes of landslide behaviour. As an overview:

1. The Upgang landslide is complex and evidence of reactivated movement is apparent. This movement is typically triggered by precipitation and marine activity.
2. In particular, this research is focused on the upper part of the landslide complex, which is influenced by changes in groundwater conditions and affects the wide slope stability. Also, the weathered glacial till layer, which has the highest level of activity of rainfall-induced landslides has been considered.
3. The monitoring period was conducted between July 2010 and December 2012, with detailed monitoring at 15 minute intervals (i.e. displacement, groundwater, rainfall measurements) between March 2011 and December 2012. Two types of extensometer were used: the vibrating-wire extensometer (March 2011-February 2012) and the compact string extensometer (April-December 2012). The Casagrande piezometers (PZ) were installed at the upper (PZU), middle (PZM) and lower (PZL) sections of the cliff. Rainfall was monitored using a tipping-bucket rain gauge.
4. TLS survey (Trimble GS200 and RIEGL VZ1000) was performed monthly to monitor landslide activity on the cliff face. Only RIEGL VZ1000 was used for change detection, to retain consistency in the data collected.
5. 14 undisturbed samples were collected from the upper section of the cliff (both east and west sides) as the material that resembled the Withernsea till.
6. Three experimental programmes were undertaken: 1) physical properties testing; 2) strain-controlled compression tests and 3) specialist direct shear tests with a pore pressure reinflation stage at constant stress using the back pressured shear box.

Chapter 4 Monitoring coastal landslides

4.1 Introduction

The aim of this chapter is to characterise changes across the cliff face during the monitoring period in 3 dimensions at high resolution. The Upgang cliff was monitored using a RIEGL VZ-1000 terrestrial laser scanner, with data collected approximately every month from December 2011 to December 2012. This produced 11 epochs of cliff change data, captured at an average 0.05 m point spacing on the ground, to assist in explaining the temporal and spatial variation in deformation across the landslide complex. The landslide characteristics include failures, volumetric changes and resultant directions of movement. These were analysed both incrementally (monthly) and on a cumulative basis. Additionally, the evolution of landslide movement has been investigated using 2D topographic profiles in order to understand the temporal landslide dynamics downslope.

4.2 TLS data acquisition

According to field observations, Upgang cliff has a wide variety of failures, which include forms indicative of mudslides, mud flows and block falls. These failures were associated with different failure mechanisms, forming the landslide complex, which is also observed by studies in comparable environments (e.g. Quinn et al., 2008). In order to better understand the change of cliff face, a combination of qualitative fieldwork observations and quantitative laser scanning has allowed for the patterns of deformation to be identified. In this study, an 11-month TLS dataset was used to examine the characteristics of the cliff face using the 3D surface comparison technique described (Table 4.1). To better understand and visualise the effect of TLS data acquisition, two distinct views - plan/top down view (xy) and elevation/face on view (xz) - were used to perform the resultant surface comparison of monthly and cumulative change across the cliff face (Figure 4.1). Negative changes (warm colours in Figure 4.1) correspond to a loss of material or a reduction of surface elevation, whereas positive values (cool colours in Figure 4.1) indicate deformation where material gain results from accretion commonly associated with deposition of landslide material from above.

Table 4. 1 TLS data acquisition between December 2011 and December 2012; 11-month TLS data acquisitions at an approximately monthly interval using a RIEGL VZ-1000 terrestrial laser scanner.

No.	Scan Date	Number of point cloud	Standard deviation (m)	Percentage of vegetation (%)	Monthly change	Cumulative change
1	11-Dec-11	2,816,105	0.046	1.54	-	-
2	13-Jan-12	8,435,469	0.040	0.46	Dec 2011- Jan 2012	Dec 2011- Jan 2012
3	23-Feb-12	3,243,443	0.053	0.62	Jan 2012 - Feb 2012	Dec 2011 - Feb 2012
4	29-Mar-12	4,178,828	0.051	0.44	Feb 2012 -Mar 2012	Dec 2011 -Mar 2012
5	23-Apr-12	4,691,068	0.055	0.79	Mar 2012 -Apr 2012	Dec 2011 -Apr 2012
6	24-May-12	3,470,302	0.020	0.45	Apr 2012 - May 2012	Dec 2011 - May 2012
7	15-Jun-12	3,428,059	0.044	0.63	May 2012 - Jun 2012	Dec 2011 - Jun 2012
8	21-Aug-12	3,514,178	0.040	1.37	Jun 2012- Aug 2012	Dec 2011- Aug 2012
9	19-Oct-12	5,019,454	0.022	1.38	Aug 2012 - Oct 2012	Dec 2011 - Oct 2012
10	16-Nov-12	4,114,718	0.049	1.31	Oct 2012 - Nov 2012	Dec 2011 - Nov 2012
11	17-Dec-12	4,948,714	0.042	1.24	Nov 2012 -Dec 2012	Dec 2011 -Dec 2012

Note: Standard deviation shows the quality of the registration

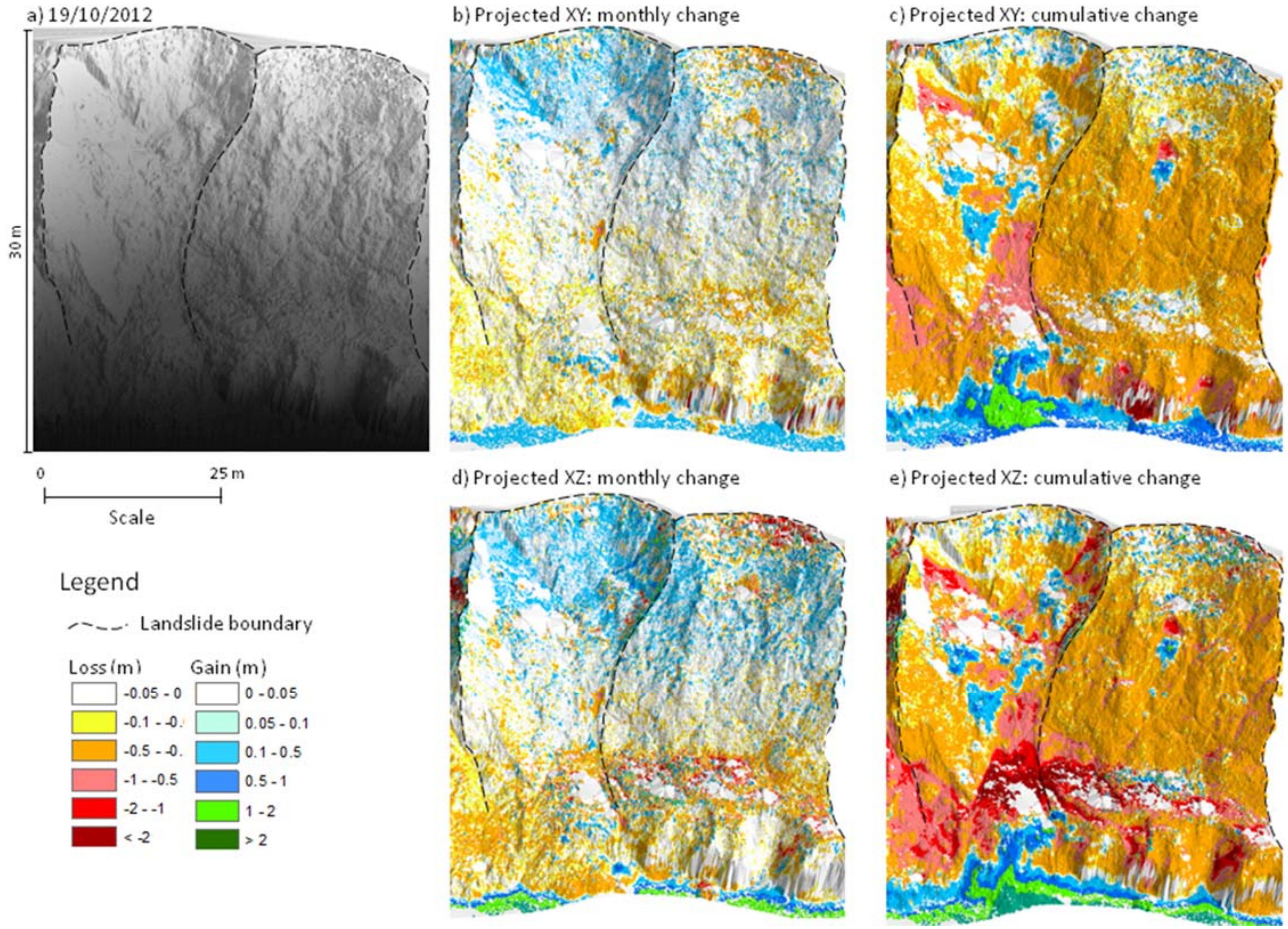

Figure 4.1 Surface change data extracted from two different views, namely, plan/top down view (xy) and elevation/face on view (xz). Note that for clarity, all diagrams are presented in an elevation view viewed as if looking from the North Sea: a) is the digital elevation model on 19th October 2012 derived from TLS data; b) and c) are the resultant surface comparison of monthly and cumulative change between 21st August and 19th October from the xy view; d) and e) are the resultant surface comparison of monthly and cumulative change between 21st August and 19th October from the xz view.

4.3 TLS monitoring

The rasterised images of change have been annotated with fieldwork observations to delimit change associated with landslides. For the purpose of discussion, the study site has been mapped and then divided into seven main units, denoted B1 to B7 on the 3D topographic terrain image (Figures 4.2 - 4.5). In order to better understand the characteristics of landslide failures, each landslide body has been further divided into four typological zones, namely:

- Zone A ‘Slide source’;
- Zone B ‘Transportation zone’;
- Zone C ‘Erosion zone’;
- Zone D ‘Toe erosion/accretion zone’.

From the TLS monitoring which describes the time series of change, there are clear patterns where landslides occur in the different zones of the cliff (Zones A-D). It is apparent that failure clusters at the various zones appear to follow the lithostratigraphic boundaries. The size of failure appears to be controlled by the underlying cliff geology, with failure dimensions often matching the bed depth. There is evidence of linkages between contiguous failures, whereby landslides on the upper part of the cliff move downslope. This can be observed in Zones A and B, termed ‘slide source and transportation zone’, which reside about 16 m from the top of the cliff. As can be seen from both the plan and elevation views (Figures 4.2 - 4.5), these two zones exhibit a patchy pattern of deformation revealed by a mixture of cool and warm deformation colours (i.e. landslide B2, B3 and B5). More specifically, the pattern of deformation changed month by month, moving down the slope (Figure 4.2 - 4.5). For example, landslide B3 illustrates mass movements that occurred between 29th March and 24th May 2012. Such movements explain the loss and gain of material changes along the same flow path from Zone B to Zone D. This pattern of downslope loss and gain of material can be interpreted as representing the movement of material in a mudslide/flow. The failed material rests on the stepped slope profile before being re-mobilised to the cliff toe and thereafter washed away by the sea. It is also interesting to note that no change was recorded along the main scarp across which the landslide flowed. Subsequently, Landslide B5 and B6 also exhibited the same behaviour. Mudslide and mudflows continue to move between 23rd April and 24th May 2012. However, small changes (*c*. 0.05 - 0.1 m) were observed across the upper part of the cliff, especially at Landslide B7, which appears to experience a slower rate of erosion. Note for example, the characteristics of surface change here show mostly a pattern of loss of material over the first six months (January-May 2012). However, the pattern of downslope loss and gain of material was detected from August to December 2012. Images of surface change from the cliff top were different from those at the bottom, as the mudflows gradually moved from the upper part of the cliff to the toe.

There is evidence of block falls at a variety of scales on the cliff face during the monitoring period. The position and shape of changes to the morphology captured in detail by the laser scanning can be used to examine the nature of the failure process. For example, Figure 4.2: Landslide B3 illustrates a large loss of material (red patch) that occurred between the data collection on 23rd April and 24th May 2012. This can be interpreted as a large scale block fall that is up to 10 m in width. Another example, Figure 4.2: Landslide B2 illustrates a smaller block fall (up to 7 m in width) that occurred between 21st August and 19th October 2012. As examples, there appears to be a concentration of block falls in Zone C, which is in a layer of sand and gravel, suggesting a particularly unstable layer unit within the cliff. However, small changes were observed after only six months, and later a large scale block fall did occur here (i.e. Landside B4, zone C in December 2012). It is interesting to note that the location of small changes appears to occur in locations where later larger changes occur. This can be seen in the data collection on 21st August, which shows gain of material (oval shape) and later loss of material with similar shape on 19th October 2012.

There is considerable evidence of toe erosion by wave action, with the lower part of the cliff, ‘Zone D’, showing increased loss of material. Gullies were observed and appeared to have experienced large changes of loss and gain of material as represented by strong red and green colours, representing toe erosion and accretion. However, accumulated material was lodged in this zone temporarily before being washed away by the rising tide. The phenomenon appeared in the lower glacial till (i.e. Skipsea till).

As seen from the rasterised images, the TLS has proven to be useful in capturing failures across the cliff face from both the plan and elevation views. In many cases, landslide events are not caused by marine basal erosion. Rather, as the landsliding dynamics at the various zones have indicated, different types of failures occurred at different lithostratigraphic boundaries as a result of variations in strength or permeability, and were mostly triggered by rainfall events. Therefore, it is evident that the cliff is subjected to both marine and groundwater variations, with some parts more influenced by one than the other. In this case, landslide failures in Zones A-C were triggered by fluctuations in groundwater, while those in Zone D were influenced by both marine activities and rainfall and groundwater. Moreover it is obvious that many of these failures and the deformation recorded is closely linked to the reworking of failed materials from earlier events.

Another way in which landslide patterns can be studied is through volume and magnitude changes across time. The next section provides a more detailed discussion in terms of the temporal patterns of change.

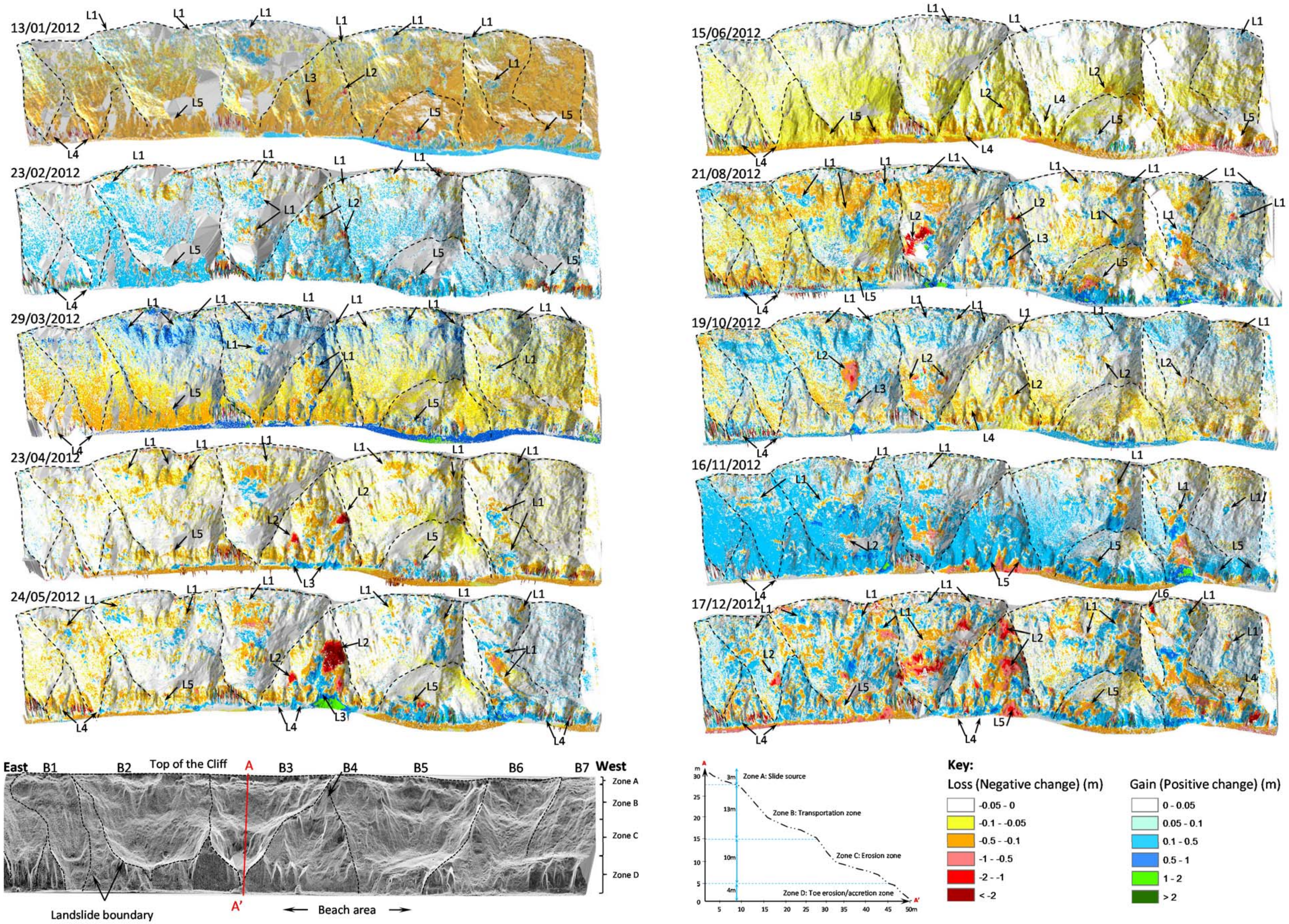

Figure 4.2 Rasterised images of monthly changes generated by the plan view (xy), presented in 3D. The cliff is divided into seven main landslides (B1-B7). L1 to L5 represent examples of failure at the Upgang cliff: L1 refers to 'Mudslide/flow'; L2 refers to 'Block fall'; L3 refers to 'Superficial earthflows'; L4 refers to 'Gullies'; L5 refers to 'Toe erosion/deposition': L6 refers to 'Translation block'. The cliff face terrain presents an elevation view facing out to the North Sea (captured in December 2011). Profile A-A': Zone A refers to shallow landslides (3 m); Zone B refers to mudslides/flows (13 m); Zone C refers to erosion zone(10 m); and Zone D refers to 'Toe erosion/accretion zone' (4 m).

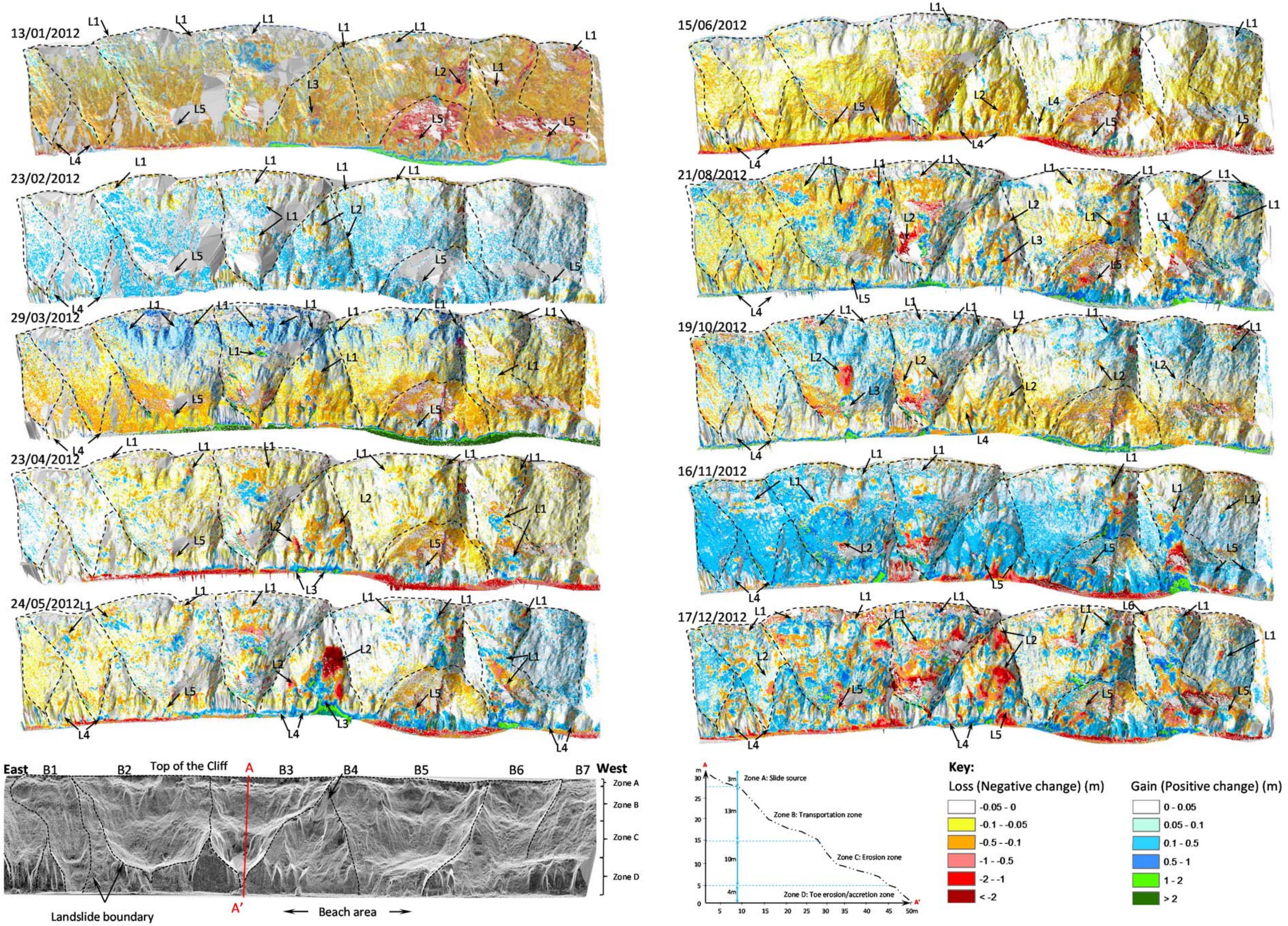

Figure 4.3 Rasterised images of monthly changes generated by the elevation view (xz), presented in 3D. The cliff is divided into seven main landslides (B1-B7). L1 to L5 represent examples of failure at the Upgang cliff: L1 refers to 'Mudslide/flow'; L2 refers to 'Block fall'; L3 refers to 'Superficial earthflows'; L4 refers to 'Gullies'; L5 refers to 'Toe erosion/deposition': L6 refers to 'Translation block'. The cliff face terrain presents an elevation view facing out to the North Sea (captured in December 2011). Profile A-A': Zone A refers to shallow landslides (3 m); Zone B refers to mudslides/flows (13 m); Zone C refers to erosion zone(10 m); and Zone D refers to 'Toe erosion/accretion zone' (4 m).

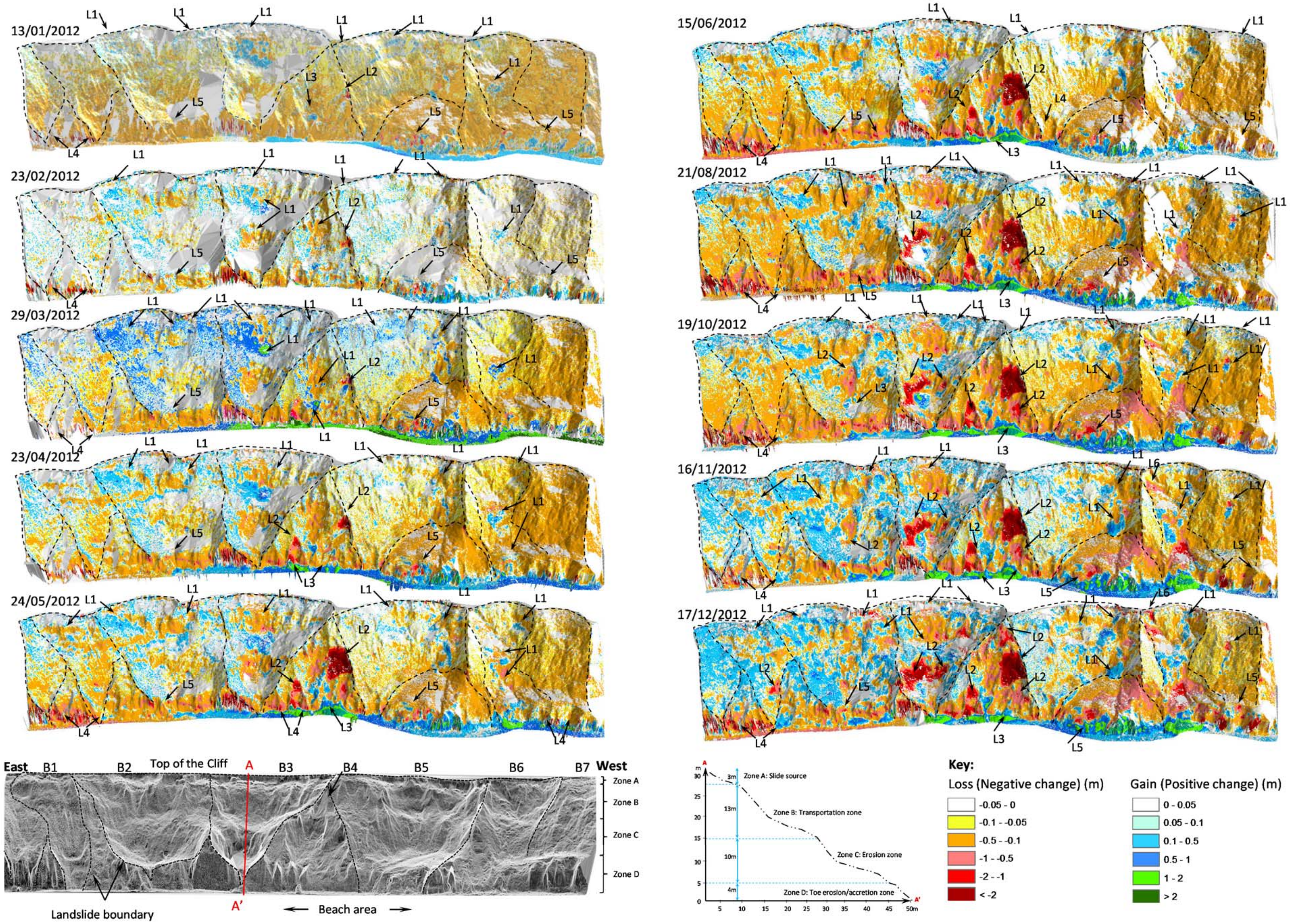

Figure 4.4 Rasterised images of cumulative changes generated by the plan view (cxy), presented in 3D. The cliff is divided into seven main landslides (B1-B7). L1 to L5 represent examples of failure at the Upgang cliff: L1 refers to 'Mudslide/flow'; L2 refers to 'Block fall'; L3 refers to 'Superficial earthflows'; L4 refers to 'Gullies'; L5 refers to 'Toe erosion/deposition': L6 refers to 'Translation block'. The cliff face terrain presents an elevation view facing out to the North Sea (captured in December 2011). Profile A-A': Zone A refers to shallow landslides (3 m); Zone B refers to mudslides/flows (13 m); Zone C refers to erosion zone(10 m); and Zone D refers to 'Toe erosion/accretion zone' (4 m).

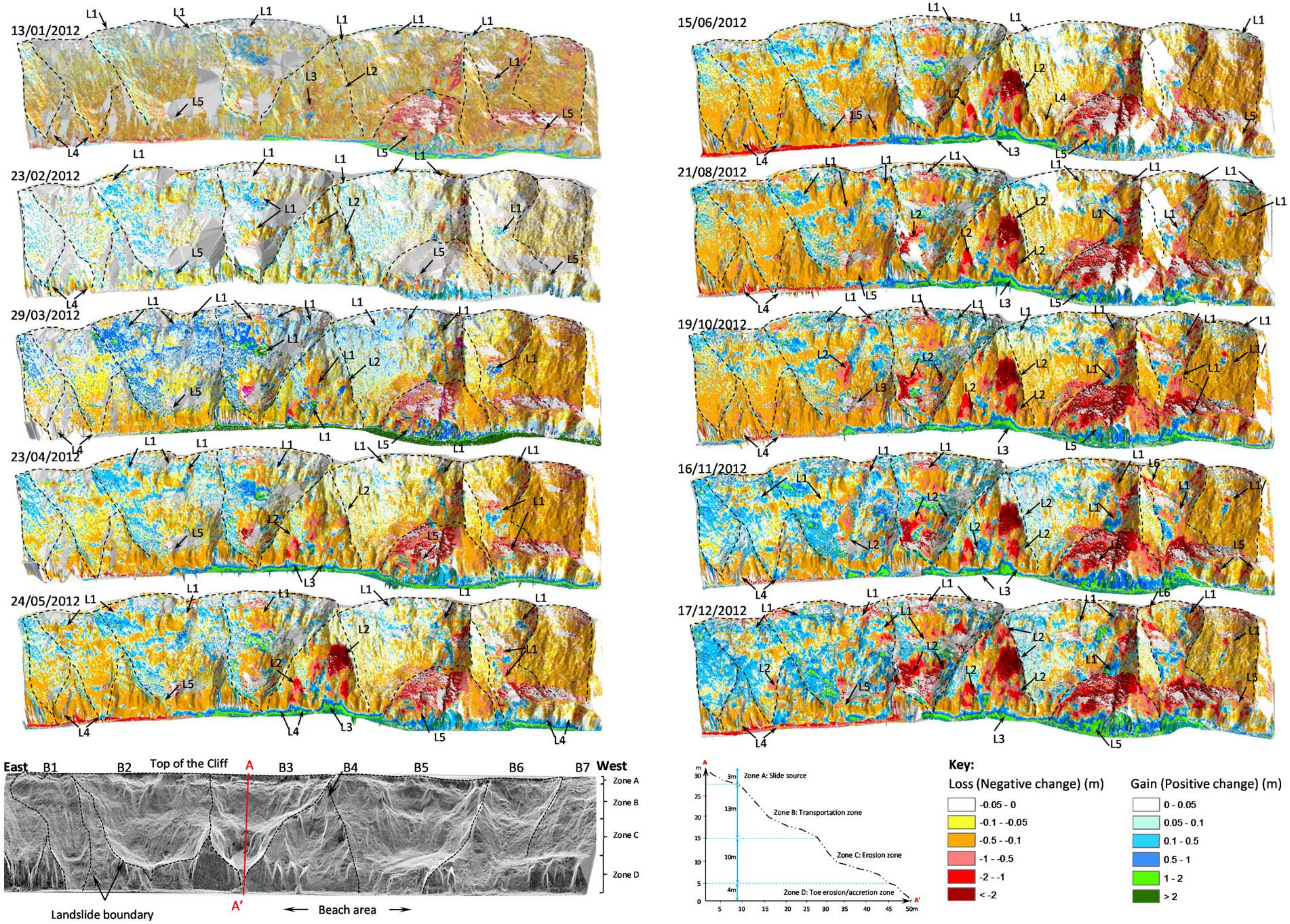

Figure 4.5 Rasterised images of cumulative changes generated by the elevation view (cxz), presented in 3D. The cliff is divided into seven main landslides (B1-B7). L1 to L5 represent examples of failure at the Upgang cliff: L1 refers to 'Mudslide/flow'; L2 refers to 'Block fall'; L3 refers to 'Superficial earthflows'; L4 refers to 'Gullies'; L5 refers to 'Toe erosion/deposition': L6 refers to 'Translation block'. The cliff face terrain presents an elevation view facing out to the North Sea (captured in December 2011). Profile A-A': Zone A refers to 'Slide source zone' (3 m); Zone B refers to 'Transportation zone' (13 m); Zone C refers to 'Erosion zone' (10 m); and Zone D refers to 'Toe erosion/accretion zone' (4 m).

4.4 Temporal patterns of change

In this section temporal patterns of change are examined through the evolution of the cliff face through time, and the temporal linkages between failure events. The total plan view surface area of the monitoring site was 12,500 m^2 (approximately 250 m in width x 50 m in depth). The section presents the temporal pattern in two views, namely plan/top down view (xy) and elevation/face-on view (xz).

4.4.1 Volume-magnitude distribution of surface change across the cliff

The aim of this section is to characterise the temporal pattern of surface change during the monitoring period including the volumetric retreat of the cliff. The temporal patterns of surface change are demonstrated most clearly when analysing distribution of loss and gain across the cliff face throughout the monitoring period. Monthly and cumulative changes can be used to explain surface change including both total volume changes across the monitored area and the magnitude of the distribution of change across the area as can be seen in Table 4.2. This volume, based on the equal sized pixels of the rasterised images generated from the TLS data, and was calculated using Equation 4.1.

The total volume of change in cubic m is calculated by:

$$dV = 1/((Pixel)^3\ ) * (\sum Vol\ ) \qquad \text{Equation 4.1}$$

Where *d*V represents volume change, pixel size of rasterised image is 0.05 m, and $\sum Vol$ represents total gain or loss for the month.

A cumulative loss and gain was also collated in order to determine the erosion rate (Equation 4.2). The erosion rate over a given epoch is calculated by:

$$Erosion\ rate = (\sum \Delta Vol)/Area \qquad \text{Equation 4.2}$$

Table 4.2 Monthly and cumulative distribution of surface change volume from the plan view and elevation view. Loss values represent monthly volume loss; Gain values represent monthly volume gain; NC represents net change values between gain and loss (i.e. gain + loss). Note: Yellow represents the maximum values of loss and gain of material; Blue represents significant positive-net change values; Orange represents significant negative-net change values; Green represents the cumulative distribution of surface change volume across the cliff.

Month	Monthly (m^3)						Cumulative (m^3)					
	Plan view (xy)			Elevation view (xz)			Plan view (cxy)			Elevation view (cxz)		
	Loss	Gain	NC	Loss	Gain	NC	Loss	Gain	NC	Loss	Gain	NC
Jan-12	-44.55	10.41	-34.13	-91.91	29.48	-62.43	-44.55	10.42	-34.13	-91.91	29.48	-62.43
Feb-12	-6.12	20.39	14.27	-4.93	26.06	21.13	-16.25	10.71	-5.54	-16.86	14.49	-2.37
Mar-12	-19.68	14.76	-4.92	-41.92	43.82	1.9	-30.61	29.2	-1.41	-63.09	66.18	3.1
Apr-12	-26.04	6.65	-19.4	-59.39	17.43	-41.97	-44.73	27.9	-16.83	-89.16	60.6	-28.57
May-12	-27.08	19.2	-7.88	-48.34	38.68	-9.66	-59.1	33.93	-25.16	-97.83	65.14	-32.69
Jun-12	-25.12	3.41	-21.71	-61.4	10.1	-51.3	-69.19	22.47	-46.71	-117.8	41.84	-75.96
Aug-12	-37.17	24.23	-12.94	-49.11	52.24	3.14	-94.61	32.75	-61.85	-140.14	62.98	-77.16
Oct-12	-21.89	21.43	-0.46	-44.34	50.24	5.9	-97.56	39.71	-57.86	-172.55	76.6	-95.95
Nov-12	-15.66	46.02	30.35	-44.37	86.95	42.58	-74.33	49.46	-24.87	-138.62	97.89	-40.73
Dec-12	-47.36	29.01	-18.34	-91.29	55.57	-35.72	-93.4	51.36	-42.04	-167.62	93.56	-74.06

When comparing the two views (plan and elevation), it is interesting to note the significant difference in volume changes registered. Taking the month of December for example, the loss in volume recorded from the elevation view was almost t twice that registered from the plan view. This suggests that in monitoring landslide failures, care is needed in the interpretation of data and the manner in which change is extracted. The difference may be due to the fact that the TLS failed to capture shallow areas of change accurately, due to occlusion differences from the two viewpoints, as seen in Figure 4.6. As a result, the distribution of volume gain and loss within a month was not well-balanced.

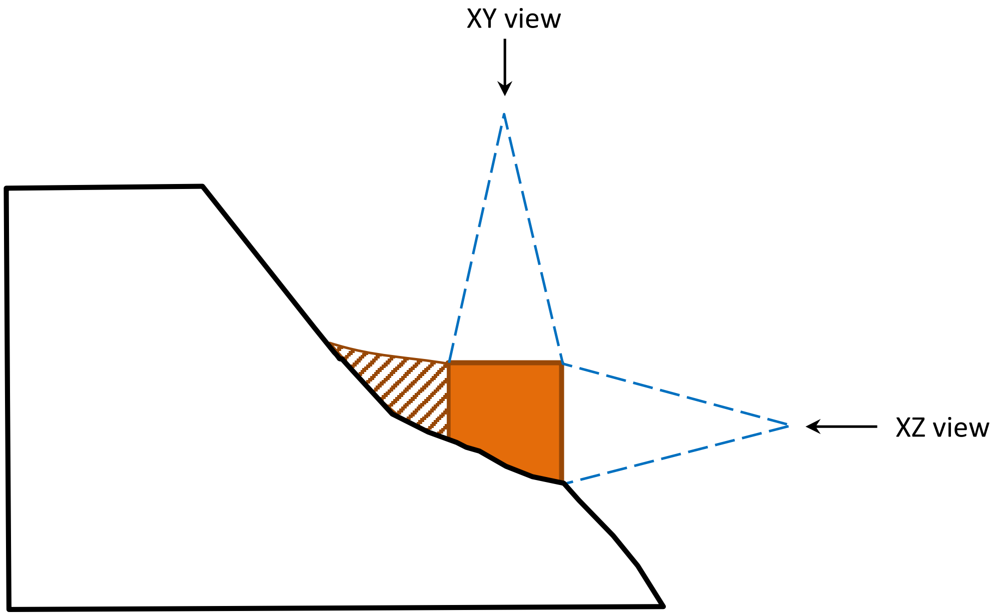

Figure 4.6 A diagram of two perspective views (xy and xz) of change (orange area) of the material on a landslide slope, with the hatched area representing the difference in change volume due to view occlusion.

In certain months, there was more loss than gain, while in others there was more gain than loss. The net change (i.e. gain-loss) in terms of volume loss was dominant in January, April, June and December 2012, whereas surface change in terms of volume gained was significant in two months which are February and November 2012. It should be noted that three months which are March, August and October represent approximately same activity of surface changes in term of volume loss and gain.

From the monitoring data, there is a clear pattern in the nature of deformation of the slope surface. The cumulative distribution of surface change volume across the cliff was 42.04 and 74.05 m^3 in the plan view and the elevation view, respectively. This is equivalent to an erosion rate across the cliff face of 3.3 mm/year or 5.9 mm/year in the plan view and the elevation view, respectively. The difference in erosion rates is due to the different views from which deformation data was projected (i.e. the incidence angle and view angles onto the surface) (Figure 4.6). It is important then to acknowledge that the results of landslide analysis might defer due to the different views adopted, and that considerations need to be taken about the suitability of each view with regards to the types of failure being studied. For instance, failures such as mudslides or superficial earthflows that move downslope can be seen clearly in the plan view, whereas lateral changes such as block falls can be captured better by using the elevation view (xz).

Surface change in terms of volume loss was dominant in January, April, June and December 2012, whereas surface change in terms of volume gained was significant in two months: February and November 2012. It should be noted that approximately similar surface changes in terms of volume loss and gain were observed for the months March, August and October (Figure 4.6 - 4.7).

An overall negative surface change (volume loss), was observed where volume from June reduced to November, before increasing again in December. This trend appears to be consistent with the trend of precipitation (430 mm between April to December 2012). Data from both the plan and elevation views confirm that the most significant loss in volume occurred during the winter months including January (44.55 m^3 – plan; 91.91 m^3 – elevation) and December (47.36 m^3 – plan; 91.29 m^3 – elevation). This observation is confirmed by looking at the mean distance of change, which is the mean pixel to pixel change in each monitoring month (see Table 4.3). Both the plan and elevation views also recorded larger magnitude changes during the winter months of January (0.14 m – plan; 0.30 m – elevation), November (0.15 m – plan; 0.40 m – elevation) and December (0.27 m – plan; 0.43 m – elevation).

Conversely, surface change in terms of volume gain was significant during autumn (August to November), when there was a relatively high amount of precipitation. In the month of November, the gain (46.02 m^3 – plan; 86.95 m^3 – elevation) was significantly more than the loss of material (15.66 m^3 – plan; 44.37 m^3 – elevation). This may be due to the occurrence of mudslides / mudflows during this period of time, and the bulking of failed material with additional water. This corresponds also with the rasterised images, which reveal a high occurrence of mudslides / mudflows from August to November. The characteristically low movement velocities of such landslides (e.g. < 0.1 / year) means that material was not lost immediately, as compared to for example, an instantaneous block fall. This may explain why the gain in volume is significantly more than the loss over this period.

a)

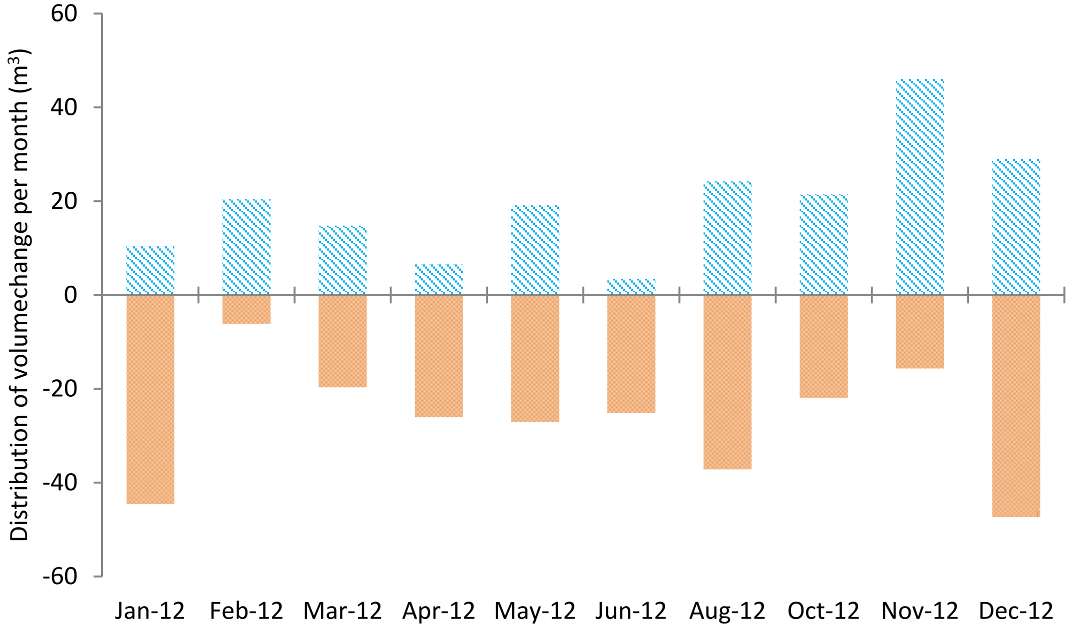

b)

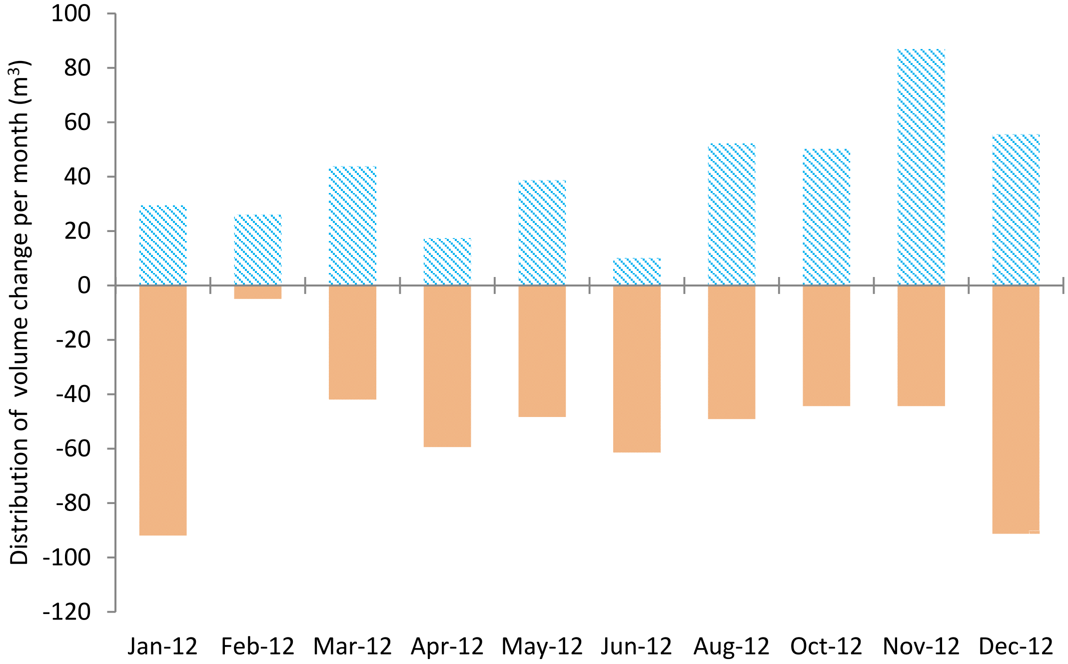

Figure 4.7 Distribution of volume change for each month from the plan view (a) and the elevation view (b). Surface change in term of volume loss is represented by negative values (orange) with the highest volumes changes being recorded in January and December 2012. Whereas the change in term of volume gained is represented by positive values (blue) with the highest volume change being recorded in November 2012.

a)

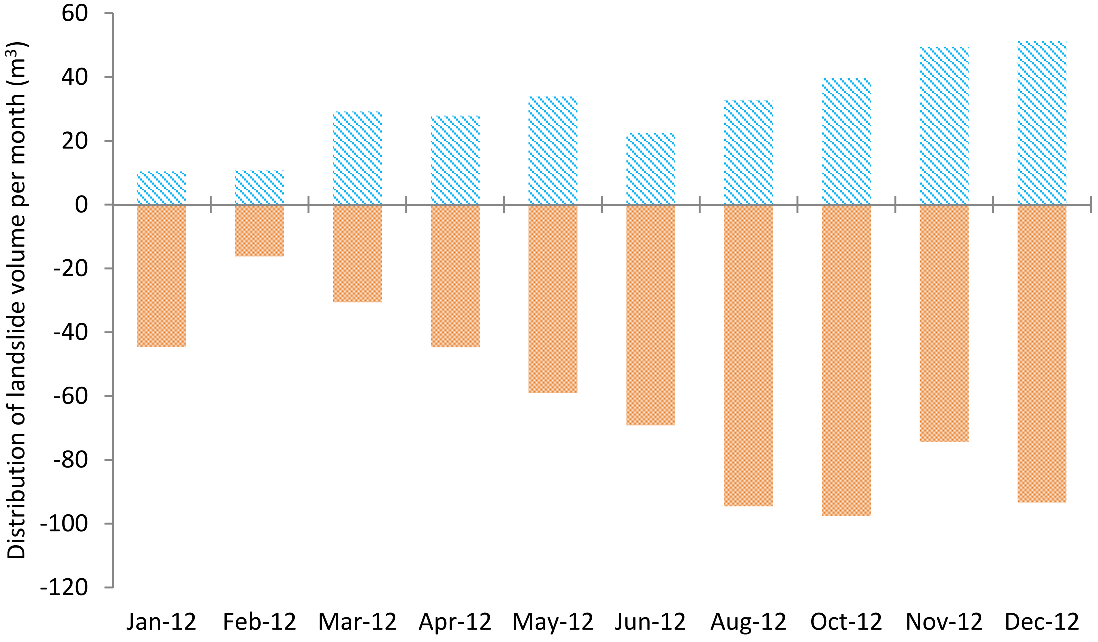

b)

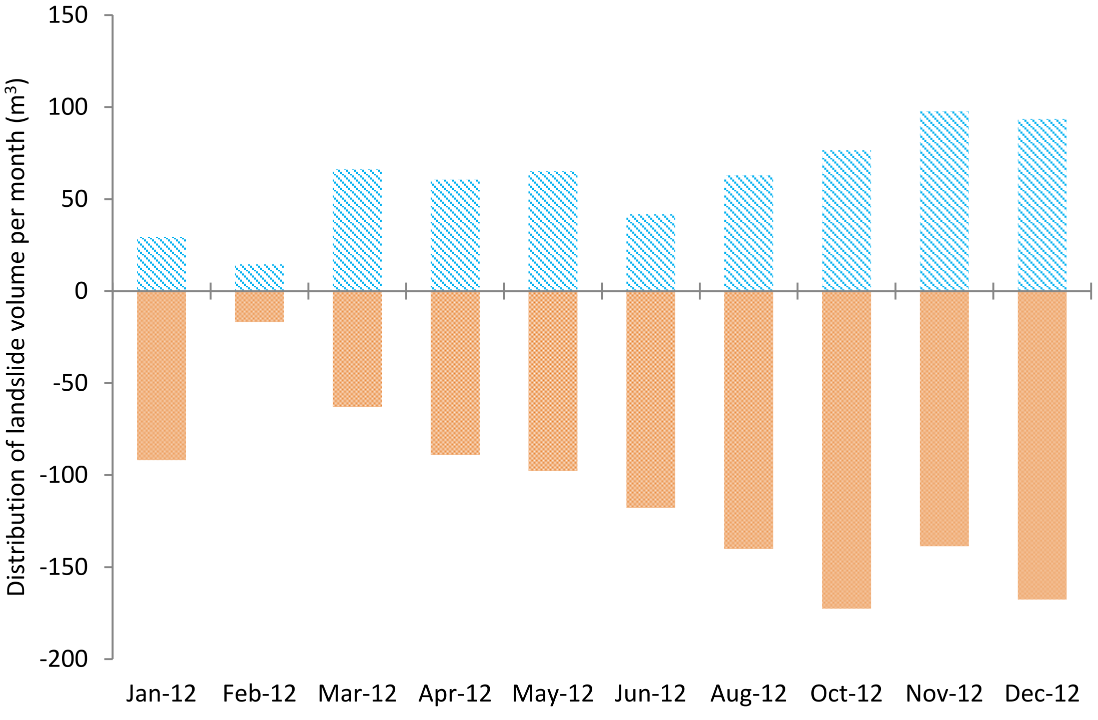

Figure 4.8 Cumulative distribution of landslide volume for each monitoring month from the plan view with 42.04 m^3 of the total net change (a) and the elevation view with 74.06 m^3 of the total net change (b). Surface change in term of volume loss is represented by negative values (orange) and the change in term of volume gained is represented by positive values (blue).

Table 4.3 Monthly distance changes in loss and gain based on rasterised images from the plan view and the elevation view. Note: Yellow represents significant values of mean distance lost; Blue represents significant values of mean distance gained. Note that significance is calculated based on the maximum and minimum mean values.

Month	Plan view (xy)								Elevation view(xz)							
	Loss (m)				Gain (m)				Loss (m)				Gain (m)			
	Mean	Std.Dev.	Min	Max	Mean	Std.Dev.	Min	Max	Mean	Std.Dev.	Min	Max	Mean	Std.Dev.	Min	Max
Jan-12	-0.14	0.15	-9.66	0.00	0.15	0.21	0.00	5.37	-0.30	0.49	-12.07	0.00	0.40	0.64	0.00	10.95
Feb-12	-0.15	1.02	-9.50	0.00	0.12	0.18	0.00	9.56	-0.17	0.61	-11.01	0.00	0.16	0.24	0.00	11.72
Mar-12	-0.08	0.09	-7.82	0.00	0.11	0.17	0.00	9.85	-0.16	0.34	-11.48	0.00	0.31	0.63	0.00	21.80
Apr-12	-0.08	0.27	-16.12	0.00	0.06	0.15	0.00	8.55	-0.18	0.41	-11.34	0.00	0.16	0.39	0.00	11.15
May-12	-0.12	0.36	-10.13	0.00	0.10	0.22	0.00	8.94	-0.21	0.51	-12.04	0.00	0.19	0.41	0.00	11.22
Jun-12	-0.08	0.12	-9.24	0.00	0.07	0.20	0.00	13.79	-0.18	0.38	-11.72	0.00	0.18	0.47	0.00	25.96
Aug-12	-0.13	0.28	-9.45	0.00	0.14	0.23	0.00	8.39	-0.21	0.44	-12.20	0.00	0.31	0.52	0.00	11.96
Oct-12	-0.09	0.15	-8.92	0.00	0.09	0.15	0.00	10.66	-0.20	0.41	-10.71	0.00	0.21	0.44	0.00	12.11
Nov-12	-0.15	0.24	-9.07	0.00	0.14	0.15	0.00	8.51	-0.40	0.69	-11.64	0.00	0.26	0.42	0.00	11.50
Dec-12	-0.27	0.37	-9.01	0.00	0.12	0.16	0.00	16.59	-0.43	0.68	-12.11	0.00	0.24	0.42	0.00	25.77

4.4.2 Magnitude-frequency distribution of surface change across the cliff

The aim of this section is to present the surface comparison of monthly change in terms of magnitude and frequency. The resultant pixels of change were depicted by kernel density, which can be read as equivalent to a histogram, as shown in Figure 4.9. Plots show a series of kernel density estimates from both plan (a) and elevation (b) views.

Overall, these two sets of graphs exhibit a similar pattern. However a slightly different frequency distribution of surface change can be observed. Small-scale changes occurred more often than larger changes, represented by a narrow distribution focussed around small values, as observed in April and June. Furthermore, as can be seen from the skewed distribution of the individual month data, there is an overall negative shift in the distribution of change over the monitoring period. This relates to a net loss of material across the cliff surface. However, large-scale positive changes were dominant during the winter months, as represented by a broader distribution of values in November and December, but these had only a low frequency of occurrence.

During the months of April, May and June, high frequencies of small scale change (between kdensity values of: 7-9), as depicted by the narrow curves (i.e. low range of value change), were observed. This could be due to the onset of low intensity rainfall during this period of the year, resulting in small scale deformation across the whole cliff slope. However, if the low range is close to zero, no change is indicated. Conversely, the winter months of January, February, November and December experienced lower frequencies of large positive changes (kdensity values of 3-4), as depicted by the broader curves (i.e. wide range of value change). It can be implied that the landslide mass moved downslope. These comparatively larger changes could be caused by the continuous intensive rainfall from the preceding months contributing to the already high groundwater level. While the change in January amounts to an overall loss of material, that in February, November and December registered a net gain. While it is not possible to explain why this is so, this observation is telling of the complexity of landslide mechanisms at a coastal glacial till.

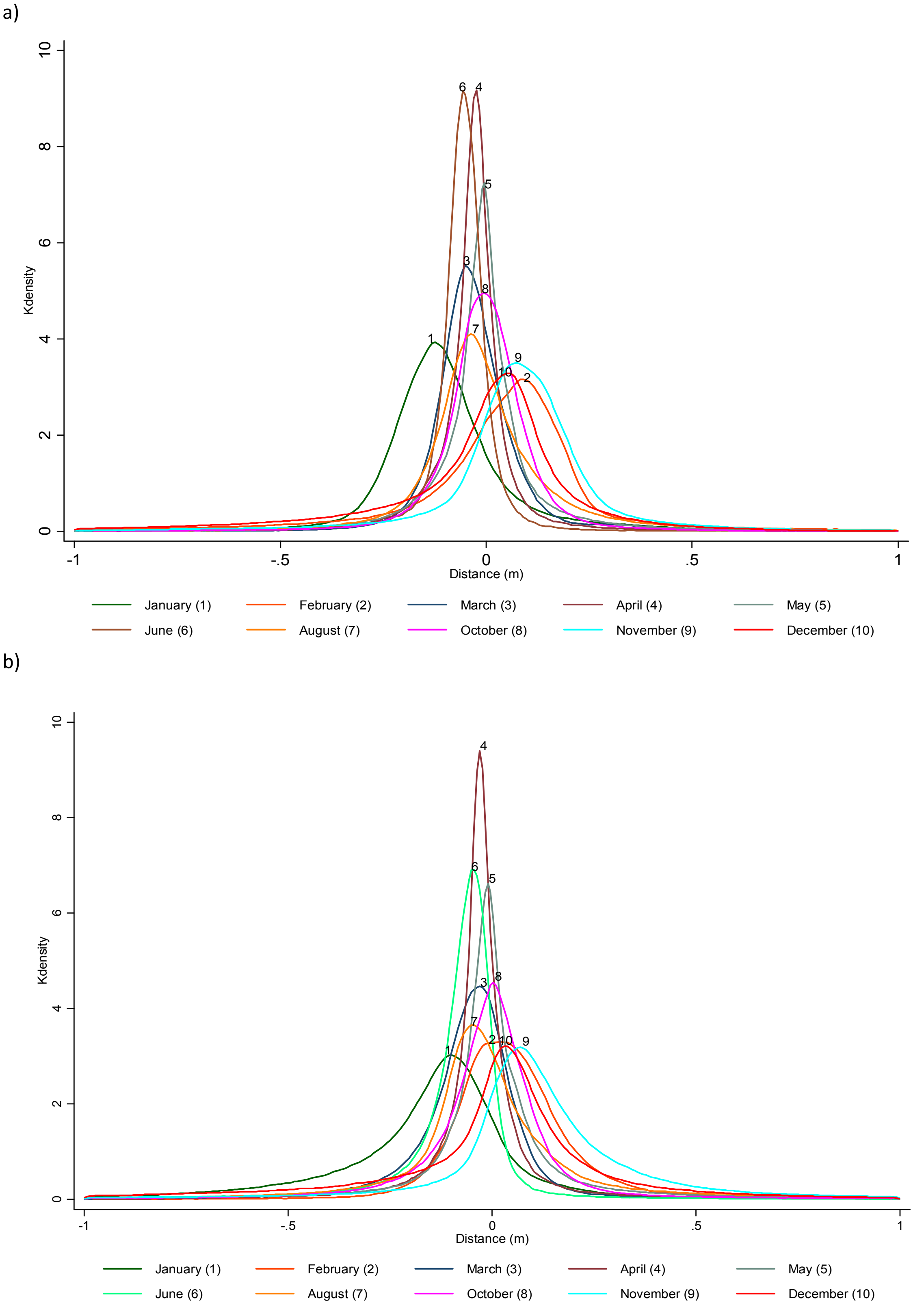

Figure 4.9 Kernel density estimate of the monthly distribution of gain and loss from the plan view (a) and the elevation view (b)

4.4.3 Evolution of change through time

The seasonal pattern of erosion and accretion month by month is clearly shown by the TLS data, with a distinct variation in failure types identified through the year. Figures 4.10 and 4.11 show the evolution through time of two landslide complexes – Landslide B3 (A-A’) and B4 (B-B’). Both complexes show numerous landslide features and failures, with the reworking of failed material and the continued removal of fresh material from the cliff. More specifically, profile A-A’ (Figure 4.10) presents a series of shallow apparently rotational landslides, mudslides/flows, and other small failures that were recorded during the monitoring period. This resulted in a distribution of loss and gain of landslide materials down the cliff slope, leading to a less noticeable change in the cliff profile at this particular cross-section over the one-year period. Profile B-B’ (Figure 4.11), however, shows a larger change in the cliff face over time. This is due largely to a block fall event recorded in May 2012. Although mudslides were the predominant failures observed within the upper glacial till, the large failure in the erosion zone and the reworking of failed materials may be triggering subsequent episodes of deformation in the later months. This hints at the temporal linkages between failure events along the cliff face. However, a fresh mudslide event was observed in Zone B in December 2012, which might not be related to the block fall event in the same month. As is evident, there is a strong lithological control on failure morphology. The varied landsliding processes and resultant cross-sectional profiles as observed at these two landslide complexes show the importance of analysing small scale localised landslide failures, and prove that landslide mechanisms do not operate uniformly across the entire cliff face.

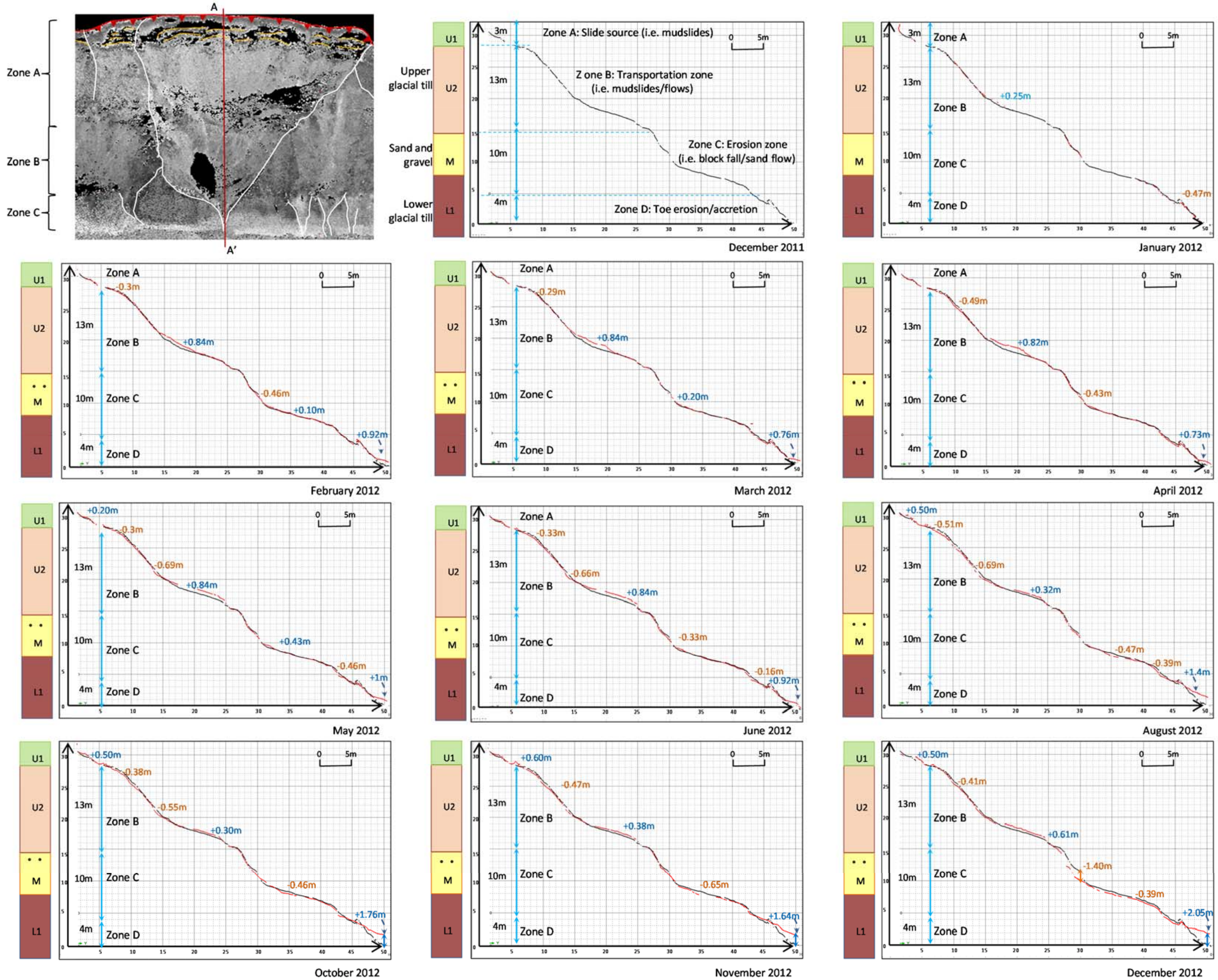

Figure 4.10 The landslide evolution of Landslide B3 is presented by profile A-A'. Four zones of landslide failures and a lithology section are provided. Negative values correspond to loss or subsidence of the material (orange), whereas positive values indicate a movement where loss material is combined with the advancing landslide. Zone A shows very small to small changes (0.05 - 0.5 m) with positive values as can be referred to shallow landslides movement along the top bench. Zone B 'Transportation zone' records a loss of material (0.3-0.7 m) underlay by U2. However, a gain of material is observed at the lower part of this zone (0.25- 0.84 m). Zone C is the erosion zone and has a significant loss of material during the Autumn-Winter months (August, October, November and December). Zone D has significant changes both in terms of loss and gain throughout the monitoring period. Note: the blue (gain) and orange (loss) numbers represent measurement of elevation change.

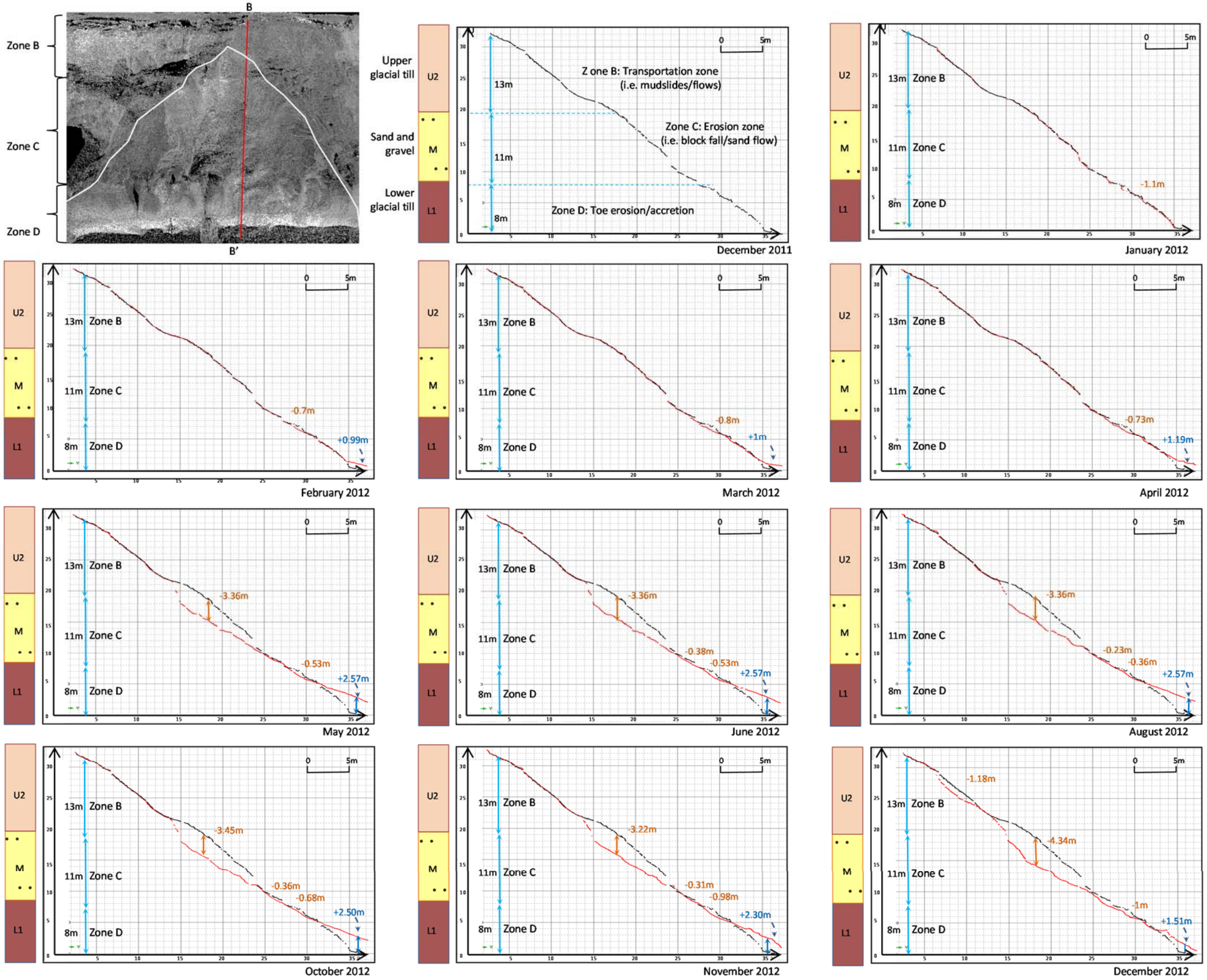

Figure 4.11 The landslide evolution of Landslide B4 is presented by profile B-B'. Three zones of landslide failures and a lithology section are provided. During the Spring months, Zone B and Zone C recorded did not record significant changes. However, Zone D has significant changes both in terms of loss and gain throughout the monitoring period. The significant block fall that was recorded in May (approximately 3.4 m) was largely a result of intensive rainfall during that period. The reworking of failed materials from the block fall can be observed in the subsequent months through the occurrence of sand flows. However, fresh mudslides were also observed in December 2012. Note: the blue (gain) and orange (loss) numbers represent measurement of elevation change.

4.5 Chapter summary

The data presented here describe the nature of cliff erosion processes. This combination of qualitative fieldwork observations and quantitative laser scanning has allowed the processes occurring during cliff retreat at the study sites to be identified. The resulting landslide complex displays seasonal movements, associated with rotational failures, sliding and deterioration of the failed mass into complex mudslides. It is evident from the data presented above that this approach has high potential for assessing landslide characteristic from the cliff face. The level of spatial detail gained also allows the pattern of individual layer within the glacial till to be examined and the influence of different factors such as precipitation and marine activity. Key findings are as follows:

1. Surface comparison using both the plan (xy) and elevation (xz) views is crucial in capturing the true nature of failures across the cliff face, especially if the cliff is non-vertical/inclined as in the case of Upgang.
2. Deformation where material is lost represents a reduction of surface elevation (negative changes), whereas deformation where material is gained (positive changes) is a result of accretion commonly associated with deposition of landslide material from above.
3. There are clear patterns where landslides occur in the different Zones A-D. The failures appear to follow the lithostratigraphic boundaries. The size of the failure appears to be controlled by the underlying cliff geology, with failure dimensions often matching bed depth.
4. Winter months (January, February, November and December) dominate the temporal patterns of surface change in terms of both loss and gain of material.

The TLS has provided a high resolution data that can be used to understand temporal and spatial patterns of landslide failures, which has been discussed in this chapter. However, the understanding of the controls on landslide dynamics is still unclear. The next chapter focuses on a more specific site of the glacial till in order to carry out intensive monitoring so as to gain a better understanding of controls on landslide initiation and cessation.

Chapter 5 Landslide movement dynamics

5.1 Introduction

The spatial patterns depicted by the terrestrial laser scanner in Chapter 4 have provided a means through which to detect and map landslide movements on a monthly temporal scale. This analysis has revealed patterns in the nature of landslide deformation. However, this type of data does not provide clarity as to exactly when and how the triggering factors dictate movement. Therefore, this chapter presents data recorded by the monitoring equipment installed at the upper section of the Upgang cliff to capture the temporal evolution of landslide movement dynamics.

Section 5.1 provides a complete record of displacement data and justification of the data recorded by VBW1 and S4 in order to explore landslide movements. In addition, groundwater monitoring data are also provided. This is followed by section 5.2, which provides an overview of the characteristics of recorded monitoring results. In order to understand the mechanical behaviour of the landslide, the following section (5.3) discusses two landslide deformation patterns: accelerated and slow movements, and examines the characteristics of each type of movement. In particular, the relationship between triggering controls and landslide deformation are explored, which includes the influence of rainfall in both accelerated and slow movements. Furthermore, periods of no movement are also identified. There are clearly periods when the slope doesn’t move, which need to be identified and separated from the periods of slow movement. Also, due to antecedent rainfall conditions, two patterns of increasing groundwater that induced accelerated movements are analysed (section 5.4). Finally, the relationship between groundwater and antecedent rainfall conditions is discussed.

5.1.1 Recorded landslide displacements

Landslide displacements were monitored in different places including upper, middle and lower parts of the cliff from March 2011 to December 2012. Displacements were recorded by vibrating-wire extensometers VBW1, VBW2 and VBW3 in 2011 at the upper part of the cliff before these extensometers were replaced by string extensometers S4, S1 and S2 in 2012. The middle and lower parts of the cliff were monitored by VBW4 and VBW5, respectively. The VBW5 extensometer was subsequently replaced with a string extensometer S5. All recorded displacement data were plotted in cumulative displacement against time as can be seen in Figure 5.1. The monitoring data suggest that the upper part of the cliff underwent the most landsliding over the monitoring period, and this area provided the dominant input of material into the head of the landslide complex. Importantly, only one location which was monitored by VBW1 (from March 2011 to March 2012) and later S4 (May 2012 to December 2012), showed very clear patterns of displacement throughout the monitoring period, and was least affected by instrument failure. Therefore, the location was chosen to further explore landslide movement patterns. In order to record landslide displacements, extensometers were used. The extensometers consisted of a cable that was anchored on the static main scarp of the landslide and extended across the ground surface. The movement data collection provided 22 months of continuous data. The data indicate that the landslide is a dynamic landslide consisting of a reactivated shallow rotational landslide that had moved through sliding with a steep, fresh scarp on the upper section of the cliff, beginning in February 2011. The estimated dimensions of the reactivated landslide was 10 x 6 m (width x length) and it had a depth of approximately 2 m (Figure 5.2).

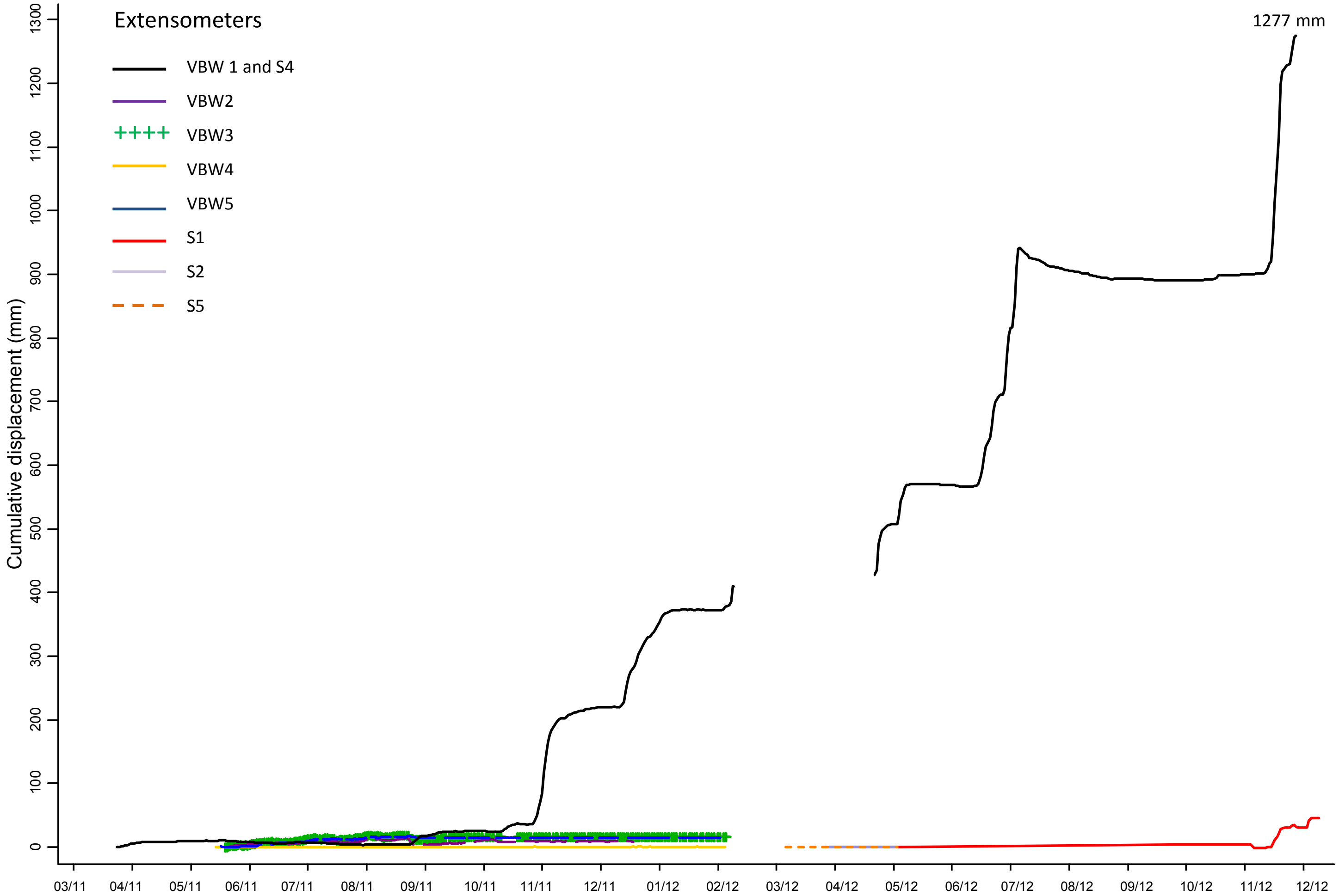

Figure 5.1 All recorded landslide displacement in different parts of the cliff; upper (VBW1, VBW2, VBW3, S1, S2 and S4); middle (VBW4) and lower (VBW5 and S5). The displacement data of the upper part of the cliff, especially VBW1 and S4 showed the most movement over the period of monitoring (cumulative displacement =1277 mm).

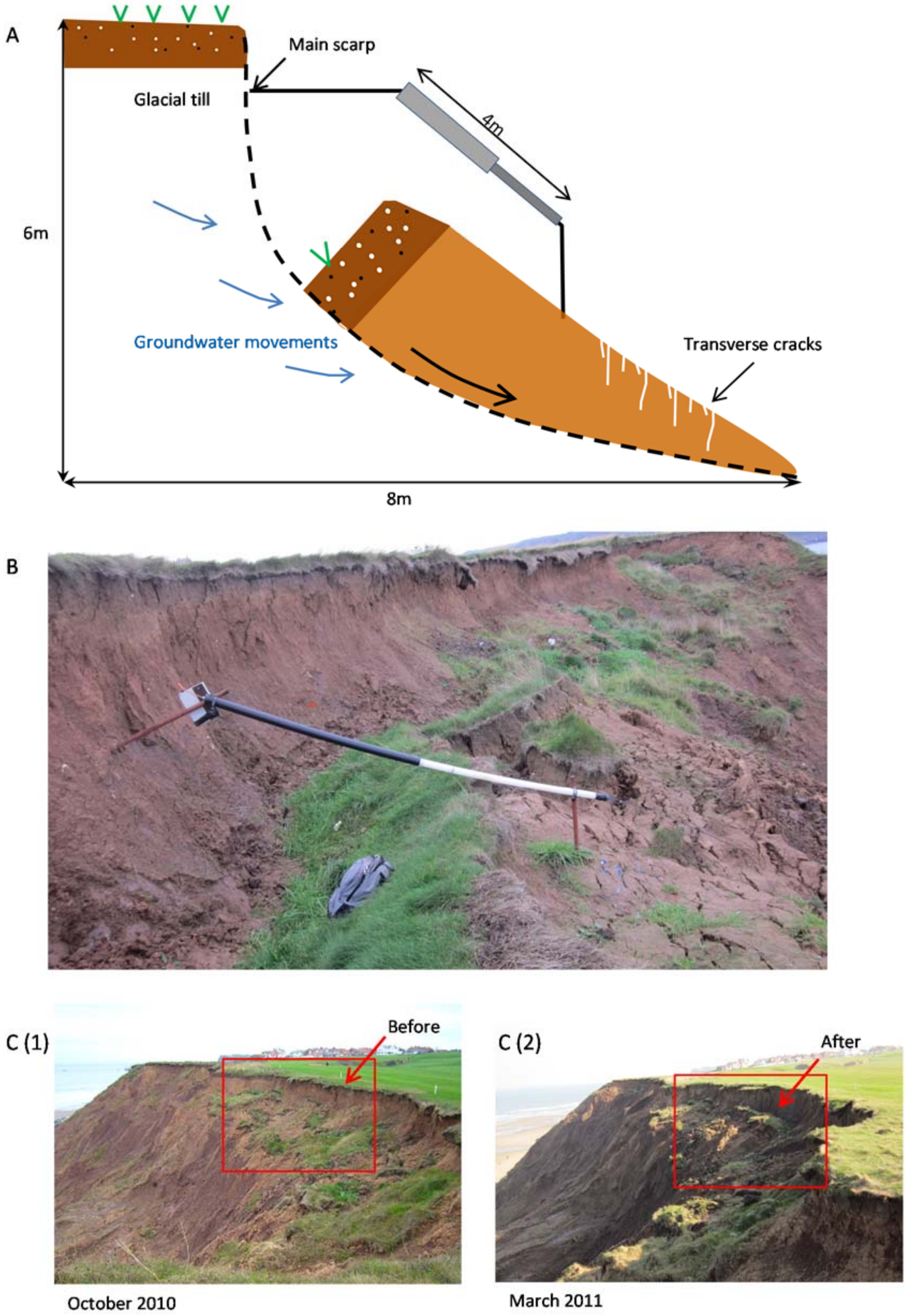

Figure 5.2 A diagram of the reactivated landslide at the upper section of the Upgang cliff at which instruments were installed (A). The extensometer consisted of a cable that was anchored on the main scarp of the landslide and extended up to and past the ground surface recording landslide displacement (B; i.e. VBW1 and S4). The photos show the upper part of the cliff before failure in 2010 (C1) and after failure in 2011 (C2).

5.1.2 Recorded groundwater

The installed vibrating-wire piezometer (PZU, 6.5 m in depth) recorded groundwater level in a Casagrande standpipe piezometer tube that was situated at the top of the cliff below the vibrating-wire extensometer (VBW1). The groundwater monitoring data were recorded at 15-minute intervals, such that groundwater level could be averaged over each hour to obtain an hourly averaged groundwater. Readings were then corrected for barometric effects (following the method detailed in Chapter 3) using data from the barometric-pressure sensor at Loftus station, located 30 km away (Table 5.1). The data suggest that the water level was barely affected by changes in barometric pressure due to the unconfined aquifer response. Overall, the corrected hourly groundwater level varied throughout the entire monitoring period. Groundwater head level was measured based on the base of borehole (Figure 5.3). The lowest recorded groundwater level was 4.0 m and the highest was 6.5 m, which is equivalent to the ground surface level (the maximum length of the piezometer pipe).

Table 5. 1 Summary of barometric changes recorded at Loftus station. Note: Max- Maximum groundwater level; Min - minimum groundwater level; Std - standard deviation of the mean groundwater

Location	Elevation (m AMSL)	Max	Min	Std. of the mean
Loftus station	158	0.37	0	0.008

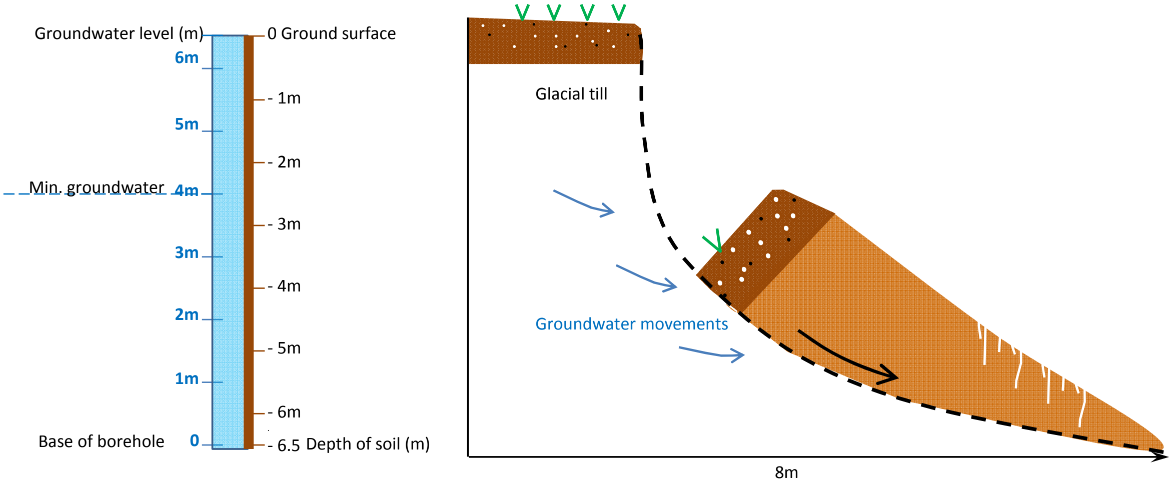

Figure 5.3 Groundwater within the landslide was measuring the standpipe in a borehole that was 6.5 m deep (PZU). The minimum groundwater level is 4 m from the base of the borehole.

5.2 Overall characteristics of recorded monitoring results

Since 2011, systematic logging of landslide displacement, groundwater and rainfall was carried out, providing hourly monitoring data. The extensometer records show that the rates of landslide movement varied between -0.079 and 1.91 mm/hr, although the rate of movement reduced significantly during dry periods. The mean hourly movement rate during the summer months was 0.2 mm/hr, whereas that for winter this rate was 2 mm/hr. The corresponding total recorded cumulative displacement during the monitoring period was 1277 mm and the total cumulative rainfall was 700.2 mm (Figure 5.4). During the early phases of periods of movement, the landslide gradually developed deformation in response to sustained intensive rainfall (Figure 5.4: a). However, during this time, groundwater declined, probably in response to the warmer, drier weather during spring-summer in 2011. On 26th August 2011, the groundwater level rapidly increased (0.11 m/hr), albeit for just six days, in response to a large rainfall event (hourly rainfall 10 mm) (Figure 5.4: b) resulting in an accelerated landslide movement (0.2 mm/hr) (Figure 5.4: c). Subsequently, the groundwater level dropped to a stable level before declining further during the dry winter period. During winter 2011 to spring 2012, the groundwater increased again resulting in a series of movements.

During summer 2012, the groundwater increased rapidly with respect to the bottom of the borehole (from a minimum of 5 m to a maximum of 6.4 m) in response to antecedent rainfall conditions. This led to sustained accelerated landslide movement for a month before it stabilised into a slow rate (mean 0.029 mm/hr) during the autumn and early winter, while the groundwater remained high (mean groundwater level about 5 m). However, the high groundwater level was particularly sensitive to intensive rainfall events, as compared to a low level. This can be observed when in November 2012 a rainfall events with an intensity of about 3 mm led to a rise in groundwater level from 5.2 m to the ground surface (6.5 m) (Figure 5.4: D), causing the displacement rate to peak at 6.27 mm/hr (Figure 5.4: E). Conversely, when the groundwater level was comparatively low in August 2011 (minimum groundwater level- = 4.3 m), a heavy rainfall event of 10 mm/hr triggered an increase of 0.6 m in groundwater level, which was associated with a displacement rate of about 0.2 mm/hr. Thus, it is apparent that a rainfall threshold controls groundwater response, above which groundwater is sensitive and responsive to rainfall events, and below which the opposite holds true (see more details section 5.4).

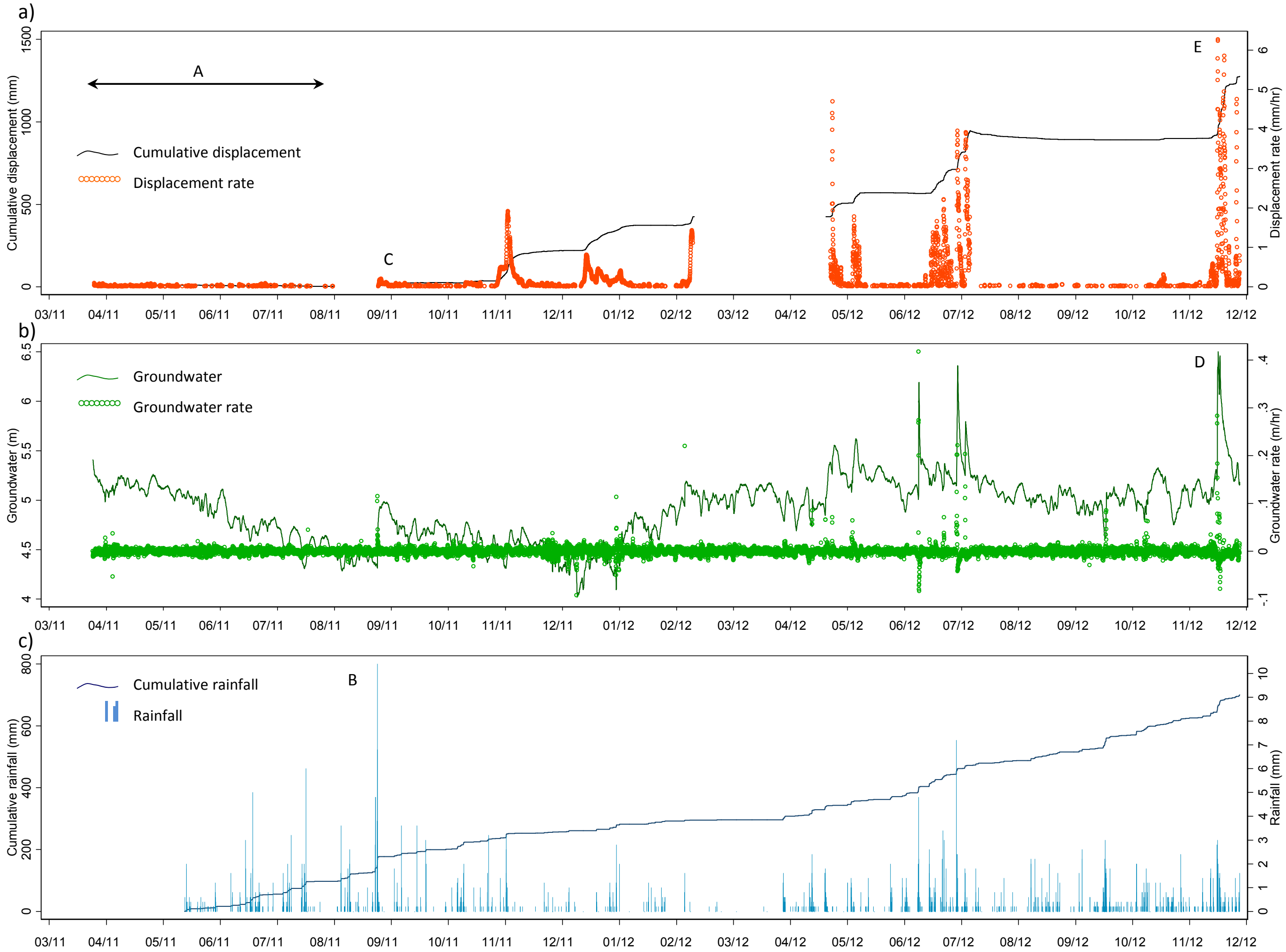

Figure 5.4 Field monitoring data between March 2011 and December 2012: a) Graph of cumulative displacement (mm) and displacement rate (mm/hr); b) Graph of groundwater (m) and groundwater rate (m/hr); c) Graph of cumulative rainfall (mm) and hourly rainfall (mm) over the entire monitoring period. Note: A- period of landslide gradually developed deformation, B- maximum hourly rainfall 10 mm, C- first time of accelerated movement, D- maximum groundwater level 6.5 m, E- maximum displacement rate 6.27 mm/hr and blank – no data available

5.3 Landslide displacement patterns

5.3.1 Threshold of landslide displacement

In order to explain the dynamics of this landslide, displacement rates have been considered. Analysis of the data required first the definition of what constitutes a landslide event or a movement period, versus stable conditions and noise. Firstly, a threshold indicating the start of movement was defined as the lowest rate at which landslide movement accelerated could be detected. To assess whether these lower displacements were statistically significant, analyses using the normalised cumulative distribution of displacement rate was undertaken using the hourly cumulative displacement of the entire monitoring data (Figure 5.5). Values that are close to 1 depict a high displacement rate, whereas values that tend towards zero represent a low to negligible displacement rate. From Figure 5.5, a range of the cumulative distribution was identified (the values between 70 and 90th percentiles). 90% of the cumulative distribution was associated with a displacement rate of < 0.4 mm/hr, whilst 70 % of the cumulative distribution was associated with a displacement rate of < 0.06 mm/hr. In this study, the threshold start has been defined as the 85th percentile of cumulative displacement rate (0.2 mm/hr) on the basis that it is the point with the steepest positive gradient of cumulative displacement. Thus, for the purposes of this analysis, accelerated movements were considered to occur when the displacement rate equalled or exceeded 0.2 mm/hr. Slow movements were considered to occur when the displacement rates between 70th- 85th percentiles of cumulative distribution represent periods of slow movement (0.06 < displacement rate < 0.2 mm/hr). Importantly, the two landslide movement patterns correspond to two of the main types of movement defined by Cruden and Varnes (1996) – very slow (16 mm/yr < displacement rate < 1.67 m/yr) to slow (1.67m/yr < displacement rate < 13 m/month). In addition, periods of 'no movement' is observed when the displacement rate is below the 70th percentile of cumulative distribution (displacement rate less than 0.06 mm/hr).

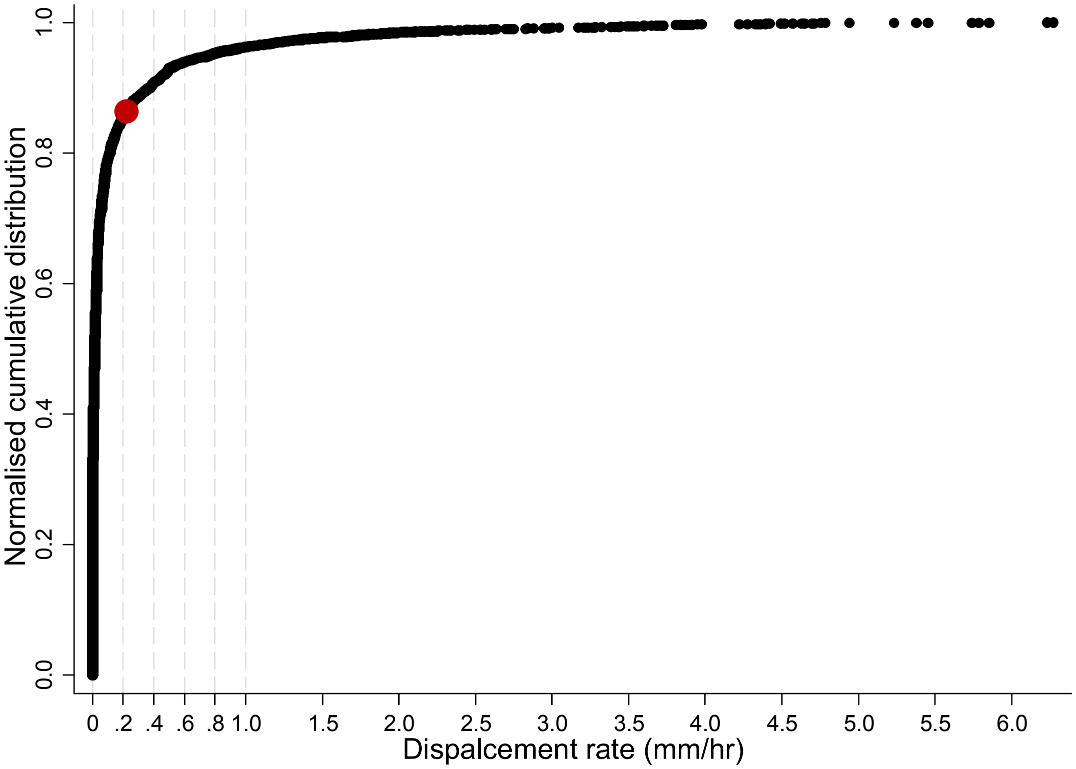

Figure 5.5 Plot of normalised cumulative distribution of displacement rate against displacement rate showing a narrow range between 0.06 and 0.4 mm/hr of displacement rate at the values between 70th and 90th percentiles of cumulative distribution. The threshold start of accelerated movement is likely in the middle of the range as 85th percentiles of cumulative distribution (≥ 0.2 mm/hr). The displacement rates between the 70th - 85th percentiles of cumulative distribution represent periods of slow movement (0.06< x< 0.2 mm/hr). In addition, ‘no movement’ is considered below the 70th percentile of cumulative distribution (< 0.06 mm/hr).

These three types of movement are distinctly different as can be seen from the cumulative displacement and displacement rate plot over time (Figures 5.6). The 12 instances of accelerated movement, which are represented by steep positive gradients, occurred over a time-period ranging from days to approximately 30 days. However, the four periods of slower movements are represented by relatively low gradients of cumulative displacement. In additional, periods of no movement show both positive and negative values slope of cumulative displacement.

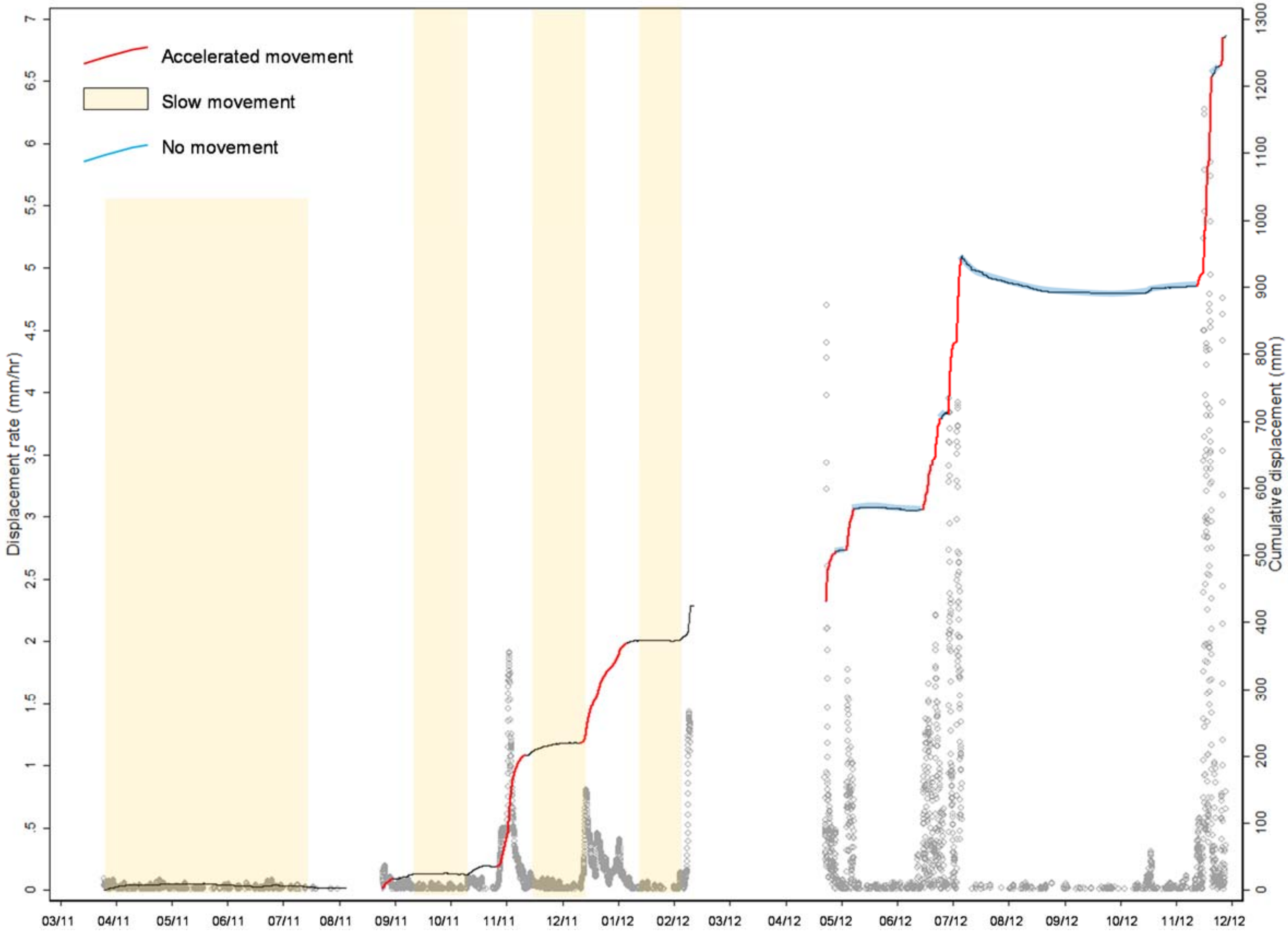

Figure 5.6 Plot of cumulative displacement and displacement rate over the entire monitoring period showing repetitive patterns of accelerated, slow and no movements. Note: Red represents periods of accelerated movement; Pale yellow represents periods of slow movement and Blue represents period of no movement.

5.3.2 Characteristics of the accelerated movements

The observed geometry of the upper landslide is that of a rotational movement. The shallow landslide consists of a small volume of material, but is characterized by rapid movements. The transverse ridges of the landslide continue to move down-slope, especially during the wet months (Chapter 4, Figure 4.2-4.5 rasterised images of surface change). This shows the pattern of downslope loss and gain of material (i.e. Landslide B3) that can be interpreted as representing the movement of material in a mudslide. The landslide was reactivated during periods of heavy rainfall with a steep positive gradient of cumulative displacement. The characteristics of accelerated movement can be seen in terms of cumulative displacement and displacement rate over time in Figure 5.7 and summary of accelerated movement can be seen in Table 5.2.

The 12 accelerated movement periods occurred over a time-period of two to 30 days, but with considerable variation in displacement rates. Patterns of the displacement rate either showed in a few cases balanced rates of rapid acceleration and deceleration (e.g. Periods 8, 11, 12 and 21), but for the most part (i.e. Periods: 2, 4, 6, 9, 14, 15, 17 and 19) patterns were complex, although acceleration was often more rapid than was deceleration. For example, Period 2 (Figure 5.7) showed rapid acceleration (0.2 mm/hr) followed by a short period of deceleration (approximately 0.15 mm/hr), and then rapid acceleration again before the rate rapidly declined. Period 6 comprised three episodes of sub-movements, which are a set of rapid acceleration and deceleration, each with a different magnitude of displacement rate. The first movement had higher rates of acceleration and deceleration (0.8 mm/hr) than the rest of the period (approximately 0.4 mm/hr). Period 11 comprised five sub-movements, which showed the highest displacement rate (approximately 2.21 mm/hr) in the first sub-movement, but lower displacement rates in subsequent sub-movements. In this case each sub-movement showed equal rates of rapid acceleration and rapid deceleration. Such a pattern could be found either individually or as part of many similar ones to constitute a movement period. This suggests that the accelerated movement periods actually consist of multiple movements with different rates of displacement. It should be noted that each period of accelerated movement has a broadly consistent form, where movement trends increase relatively rapidly (e.g. between 0.2 and 6.3 mm/hr), followed by a period of slower movement (steady state; see the next section for more details).

Table 5.2 Summary of accelerated movements

Period	Dates	Total hour	Total movement (mm)	Displacement rate (mm/hr)			
				Mean	Std.	Min.	Max.
2	26/08/2011 - 1/09/2011	154	13.399	0.100	0.044	0.012	0.200
4	14/10/2011-14/11/2011	740	176.573	0.239	0.369	0.010	1.914
6	15/12/2011-09/01/2012	608	148.944	0.245	0.163	0.041	0.808
8	29/04/2012 - 05/05/2012	133	74.464	0.609	0.894	0.014	4.697
9	10/05/2012 -15/05/2012	104	61.470	0.647	0.414	0.014	1.778
11	22/06/2012 - 28/06/2012	144	74.227	0.603	0.447	0.019	1.658
12	28/06/2012 - 04/07/2012	144	69.736	0.659	0.563	0.014	2.211
14	6/07/2012 - 10/07/2012	91	105.801	1.259	1.126	0.024	3.951
15	10/07/2012 -13/07/2012	85	124.774	1.862	1.132	0.024	3.917
17	21/11/2012 - 23/11/2012	63	16.952	0.292	0.149	0.014	0.583
19	24/11/2012-02/12/2012	185	309.669	1.721	1.678	0.029	6.272
21	03/12/2012 - 06/12/2012	65	43.768	0.675	1.203	0.005	4.755

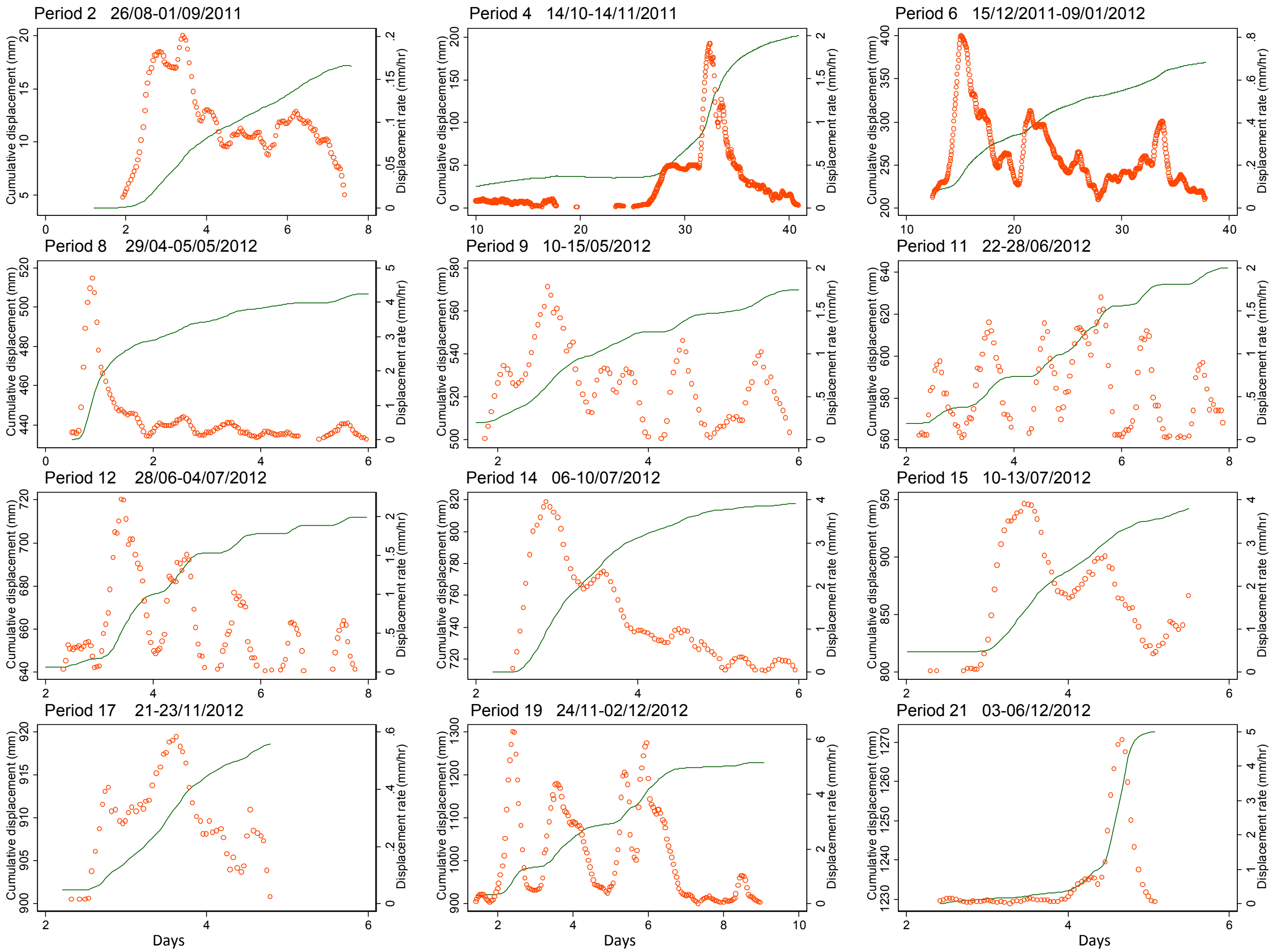

Figure 5.7 Plot of cumulative displacement and displacement rate against time (days) showing characteristics of accelerated movements. All show a positive steep gradient slope of cumulative displacement and a variety of displacement rates (0.2 – 6.27 mm/hr).

5.3.3 Characteristics of slow movement

The resolutions of the vibrating-wire extensometer (VBW1) and the string extensometer (S4) were approximately 0.001 mm/record and 0.3 mm/record, respectively, where the record is the time increment between readings. The readings made with the extensometers allow for an accuracy of 0.01 mm/hr in terms of the displacement rate. As such, it is possible to identify slow movements over and above measurement error.

Slow movement presents a positive gradient of cumulative displacement with very low velocity of about 0.06 - < 0.2 mm/hr. However, for the low rates of displacement associated with these movement periods, it is difficult to identify their precise start and end points. Estimates of when these movements occurred are shown in Table 5.3. Four periods of slow movement indicate both a negative and positive gradient in displacement, which indicates apparently upslope and downslope movement of the landslide over a time-period of approximately 31 - 73 days. Patterns of the displacement show complex periods with variable rates of rapid acceleration and deceleration (Figure 5.8). The pattern of the displacement rate of slow movement is characterised by positive rates (acceleration) and negative rates (deceleration) with very low magnitude displacement rates (e.g. Period 1, 3, 5 and 7).

Table 5.3 Summary of slow movement

Period	Dates	Total hour	Total movement (mm)	Displacement rate (mm/hr)			
				Mean	Std.	Min.	**Max.**
1	24/03/2011-05/06/2011	1,751	10.631	0.004	0.022	-0.064	**0.091**
3	01/09/2011-14/10/2011	1,013	8.556	0.008	0.027	-0.079	**0.107**
5	14/11/2011 -15/12/2011	756	19.130	0.024	0.038	-0.062	**0.142**
7	09/01/2012-06/02/2012	653	4.745	0.006	0.028	-0.054	**0.102**

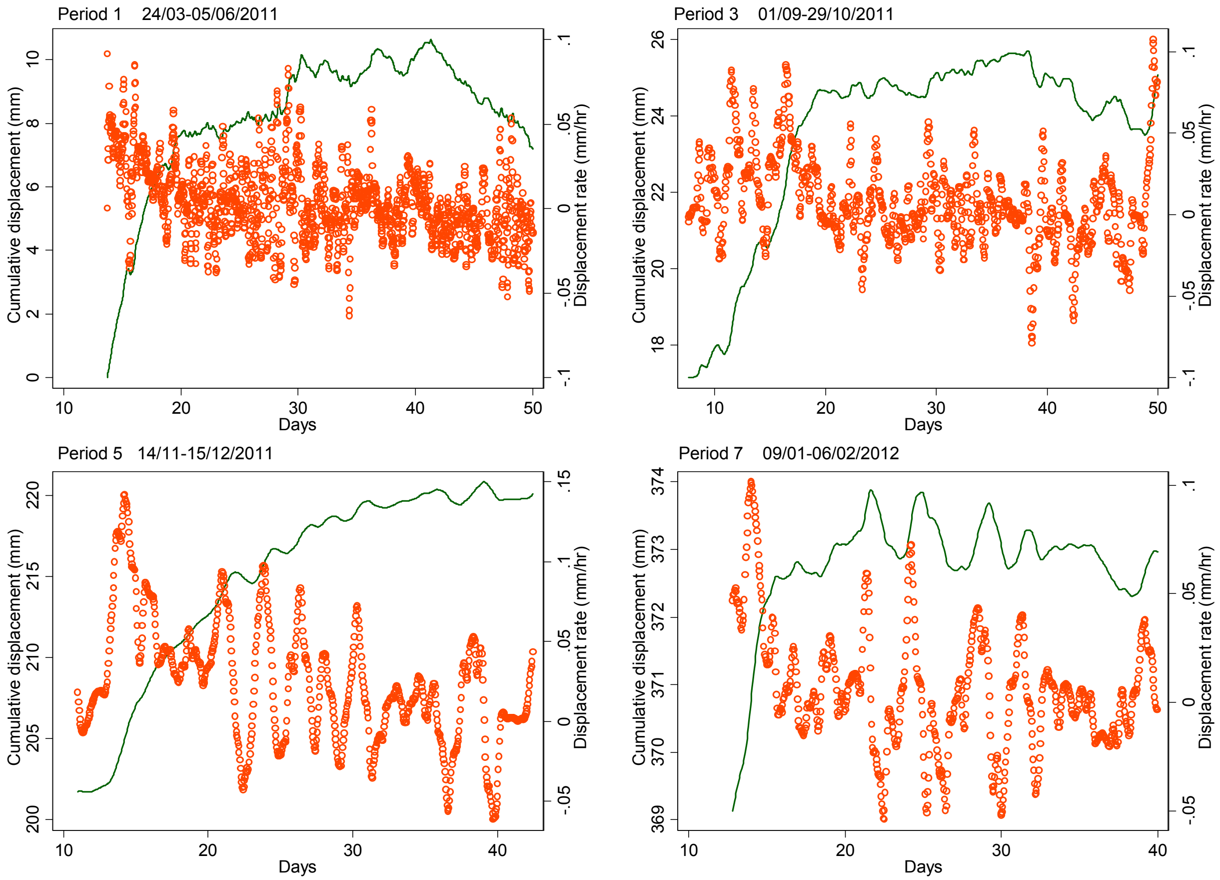

Figure 5.8 Plots of cumulative displacement and displacement rate against time (days) showing characteristics of slow movements at very low displacement rates (up to 0.15 mm/hr). The slow movement show a positive slope of cumulative displacement (downslope).

5.3.4 Characteristics of periods of no movement

No movement, relative to the errors of the instrument, is considered when the displacement rate is less than 0.06 mm/hr. The displacement data suggest that there were times when the landslide was not moving, probably during periods when the movement is comparable to the precision of the instrument. 'No movement' relates to error, which occurs in two different patterns, as can be seen in Figure 5.9: 1) short periods of downslope movements (positive values), and 2) long periods of apparently upslope movements (negative values), probably causing no net change in landslide position. For the former, it might be a case where the displacement was too small (< 0.3 mm) for the instrument to detect. For the latter, upslope movements (negative movements) may be caused by the shrinkage and swelling of clay material when it changed soil moisture, and subsequently offset any downslope movements, leading to no net change in displacement. From the data collected, three periods of no movement show a positive slope of cumulative displacement and displacement rates close to zero (i.e. Period 13, 18 and 19). Conversely, two periods of no movement show a negative slope of cumulative displacement with low negative displacement rates (i.e. Period 10 and 16).

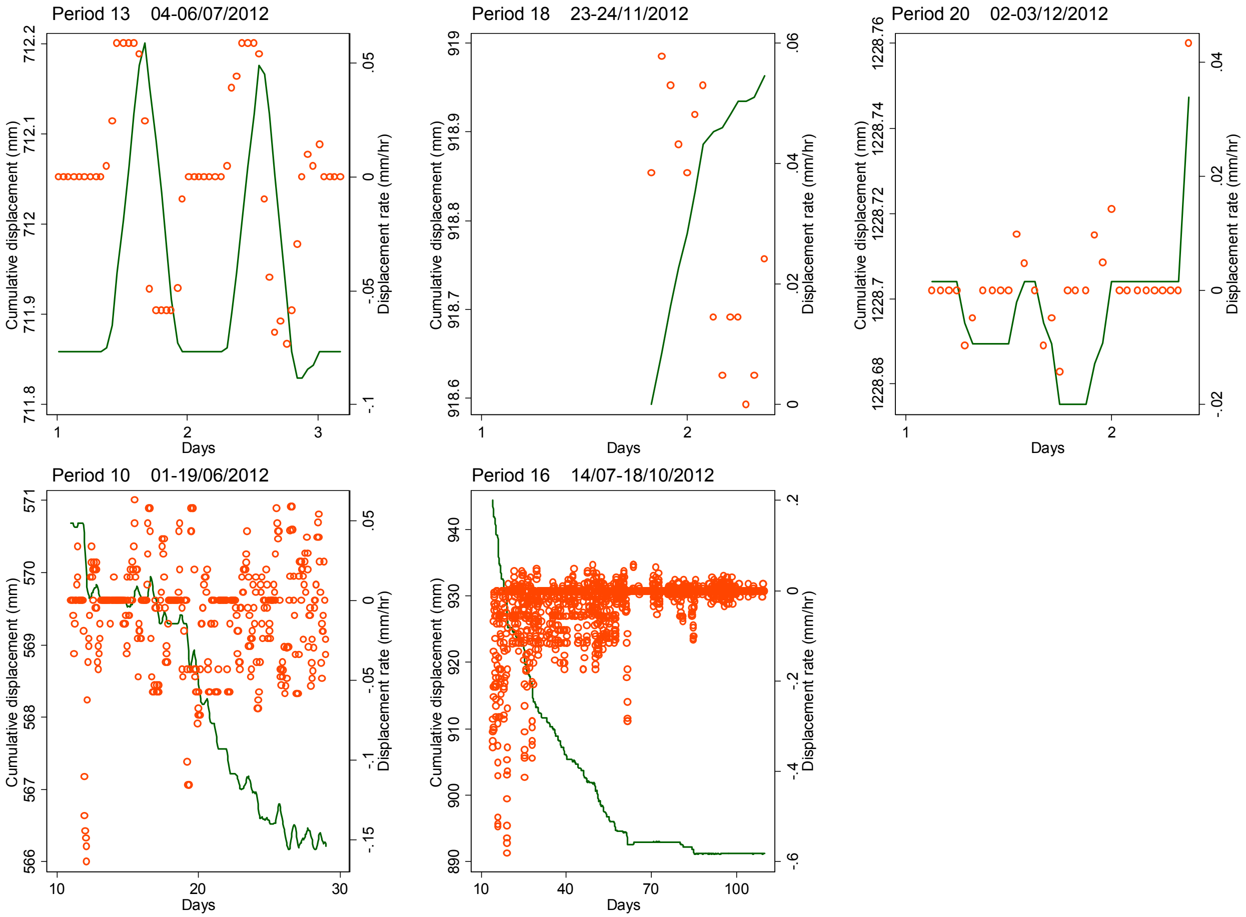

Figure 5.9 Plot of cumulative displacement and displacement rate against time (days) showing characteristics of no movements. Three periods of no movement show a positive slope of cumulative displacement and displacement rates close to zero (i.e. Period 13, 18 and 19). Two periods of no movement show a negative slope of cumulative displacement with low displacement rates (i.e. Period 10 and 16).

5.4 Factors affecting movements

The aim of this section is to identify patterns of rainfall and groundwater and their relationship with landslide movements (accelerated, slow and no movement as discussed in the previous section). Firstly, precipitation patterns that influence accelerated movements, slow movements and no movements are identified (section 5.4.1). The patterns are based on the duration and magnitude of rainfall in order to correlate between rainfall and landslide movements. As an effect of antecedent rainfall conditions, groundwater patterns that influence landslide movement are defined (section 5.4.2). Lastly, the relationship between groundwater and rainfall is examined based on the lag correlation analysis (section 5.4.3).

5.4.1 Precipitation

The rainfall data were processed at 15-minute intervals for the monitored period (13th May 2011- 7th December 2012), and then aggregated to generate an hourly precipitation. The total rainfall from May to December 2011 was 270 mm (i.e. average 33.75 mm/month). This amount increased to 430 mm (i.e. average 53.75 mm/month) during the wet period in 2012 during the eight months between April and December.

To understand the characteristics of rainfall affecting periods of accelerated, slow and no movements, the rainfall patterns were categorized based on rainfall duration and magnitude. All these attributes influenced the build-up of water pressure, based on the 21 periods of discrete movements, as summarised in Table 5.4. The cumulative hourly rainfall and hourly rainfall have been plotted with the corresponding 12 periods of accelerated movements, 4 periods of slow movements and 5 periods of no movement (Figure 5.10).

Table 5.4 Summary of landslide movements, groundwater and rainfall for the 21 movement periods observed. Note: Dates: Day/Month/Year; Max- Maximum; Mean - the average; Std - standard deviation of the mean; Gw -groundwater; Total change from maximum to minimum (i.e. maximum groundwater level – minimum groundwater level); Max. Precipitation - the maximum hourly precipitation in a period; Total precipitation: The total precipitation in a period; Precipitation Duration – the total rainfall hour. Note: Colourless represents periods of accelerated movement; Green represents periods of slow movement; Grey represents periods of no movement (upslope) and Light blue represents periods of no movement (downslope).

Period	**Dates**	**Total hour**	**Total movement (mm)**	**Displacement rate (mm/hr)**				**Groundwater, Gw (m)**				**Rate of change of groundwater (m/hr)**				**Precipitation (mm)**			**Total change from maximum to minimum (m)**
				Mean	Std.	Min.	**Max.**	Mean	Std.	Min.	Max.	Mean	Std.	Min.	Max.	Max.	Total	Duration	
1	24/03/2011- 05/06/2011	1,751	10.631	0.004	0.022	-0.064	**0.091**	5.088	0.102	4.819	5.408	0.000	0.005	-0.053	0.037	2.00	16.40	39	0.589
2	26/08/2011 - 1/09/2011	154	13.399	0.100	0.044	0.012	**0.200**	4.905	0.140	4.317	4.987	0.004	0.014	-0.007	0.115	10.40	36.60	18	0.670
3	01/09/2011- 14/10/2011	1,013	8.556	0.008	0.027	-0.079	**0.107**	4.690	0.084	4.482	4.934	0.000	0.005	-0.032	0.022	3.60	46.40	77	0.453
4	14/10/2011- 14/11/2011	740	176.573	0.239	0.369	0.010	**1.914**	4.556	0.110	4.312	4.780	0.000	0.005	-0.032	0.017	3.20	29.00	43	0.467
5	14/11/2011 - 15/12/2011	756	19.130	0.024	0.038	-0.062	**0.142**	4.435	0.154	4.021	4.701	-0.001	0.009	-0.092	0.037	1.20	8.80	21	0.680
6	15/12/2011- 09/01/2012	608	148.944	0.245	0.163	0.041	**0.808**	4.426	0.139	4.095	4.770	0.001	0.010	-0.050	0.114	2.80	20.00	32	0.675
7	09/01/2012- 06/02/2012	653	4.745	0.006	0.028	-0.054	**0.102**	4.790	0.095	4.591	4.961	0.000	0.006	-0.022	0.026	1.20	10.40	21	0.370
8	29/04/2012 - 05/05/2012	133	74.464	0.609	0.894	0.014	**4.697**	5.426	0.105	5.254	5.555	0.000	0.010	-0.011	0.071	0.20	1.20	6	0.301
9	10/05/2012 - 15/05/2012	104	61.470	0.647	0.414	0.014	**1.778**	5.445	0.122	5.175	5.622	0.001	0.011	-0.020	0.064	0.40	2.00	8	0.447
10	01/06/2012 - 19/06/2012	431	-4.115	-0.010	0.035	-0.164	**0.063**	5.161	0.199	4.880	6.191	0.000	0.031	-0.083	0.418	4.80	47.00	35	1.312
11	22/06/2012 - 28/06/2012	144	74.227	0.603	0.447	0.019	**1.658**	5.269	0.074	5.149	5.387	0.000	0.006	-0.012	0.019	1.40	13.20	32	0.238
12	28/06/2012 - 04/07/2012	144	69.736	0.659	0.563	0.014	**2.211**	5.240	0.067	5.096	5.372	0.000	0.010	-0.019	0.071	3.40	15.20	16	0.276
13	04/07/2012 - 06/07/2012	53	0.371	0.000	0.038	-0.073	**0.059**	5.168	0.007	5.148	5.190	-0.001	0.032	-0.010	0.005	0.60	1.20	4	0.042

Table 5.4 (continued) Summary of landslide movement, groundwater and rainfall for the 21 movement periods observed. Note: Dates: Day/Month/Year; Max- Maximum; Mean - the average; Std - standard deviation of the mean; Gw -groundwater; Total change from maximum to minimum (i.e. maximum groundwater level – minimum groundwater level); Max. Precipitation - the maximum hourly precipitation in a period; Total precipitation: The total precipitation in a period; Precipitation Duration – the total rainfall hour. Note: Colourless represents periods of accelerated movement; Green represents periods of slow movement; Grey represents periods of no movement (upslope) and Light blue represents periods of no movement (downslope).

Period	**Dates**	**Total hour**	**Total movement (mm)**	**Displacement rate (mm/hr)**				**Groundwater, Gw (m)**				**Rate of change of groundwater (m/hr)**				**Precipitation (mm)**			**Total change from maximum to minimum (m)**
				Mean	Std.	Min.	**Max.**	Mean	Std.	Min.	Max.	Mean	Std.	Min.	Max.	Max.	Total	Duration	
14	6/07/2012 - 10/07/2012	91	105.801	1.259	1.126	0.024	**3.951**	5.642	0.296	5.146	6.358	0.002	0.045	-0.042	0.221	7.20	11.40	16	1.212
15	10/07/2012 - 13/07/2012	66	124.774	1.918	1.102	0.058	**3.917**	5.525	0.162	5.249	5.795	0.000	0.034	-0.018	0.203	1.80	10.20	15	0.546
16	14/07/2012- 18/10/2012	2,305	-52.885	-0.022	0.063	-0.582	**0.058**	5.033	0.108	4.612	5.272	0.000	0.006	-0.029	0.085	3.00	121.20	217	0.660
17	21/11/2012 - 23/11/2012	63	16.952	0.292	0.149	0.014	**0.583**	5.105	0.065	5.005	5.238	0.004	0.009	-0.018	0.034	1.80	11.80	15	0.233
18	23/11/2012 - 24/11/2012	14	0.371	0.029	0.020	0.000	**0.058**	5.283	0.018	5.249	5.309	0.005	0.004	-0.002	0.011	0	0	0	0.060
19	24/11/2012- 02/12/2012	185	309.669	1.721	1.678	0.029	**6.272**	5.773	0.342	5.198	6.501	0.001	0.041	-0.079	0.283	3.00	45.00	60	1.303
20	02/12/2012 - 03/12/2012	31	0.072	0.001	0.009	-0.014	**0.043**	5.380	0.057	5.266	5.436	-0.005	0.005	-0.016	0.002	0.60	2.00	5	0.170
21	03/12/2012 - 06/12/2012	65	43.768	0.675	1.203	0.005	**4.755**	5.250	0.058	5.205	5.382	0.002	0.007	-0.011	0.022	1.40	4.40	12	0.177

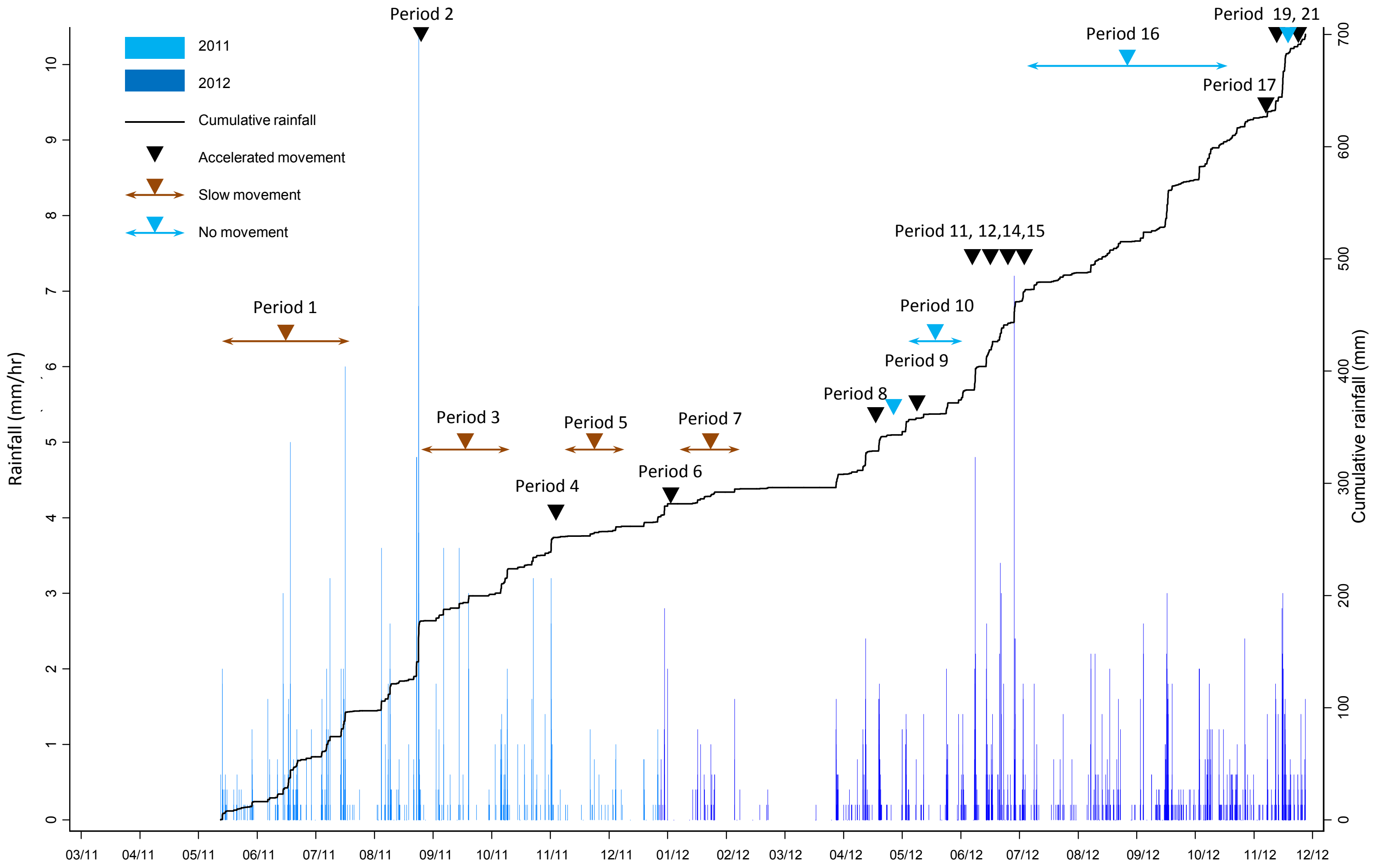

Figure 5.10 Plot of cumulative rainfall and hourly rainfall over time with three patterns of accelerated, slow and no movements between 2011 and 2012.

The cumulative hourly rainfall and hourly rainfall have been plotted with the corresponding 12 periods of accelerated movements (Figure 5.10). Interestingly, the movements occurred in periods of varying rainfall in terms of both duration and magnitude, most probably in response to the associated increases in groundwater level. The three characteristics of the precipitation affecting periods of accelerated movement based on rainfall duration and magnitude (the maximum hourly rainfall) conditions were as follows:

1) *Short duration of rainfall (5 - 10 hrs) with a low magnitude (< 2 mm)*

Short rainfall duration between 5 and 10 hours and low rainfall magnitude (< 2 mm) can generate accelerated movements when groundwater levels are already high. This pattern was observed in 16% of accelerated movement events. A relatively high velocity of displacement (peak rate = 1.7 - 4.7 mm/hr) was observed in Periods 8 and 9 (Table 5.4 and Figure 5.10) with a minimum groundwater level of > 5.2 m. This may suggest that the groundwater has exceeded a certain threshold level (approximately > 5.2 m) above which the soil is responsive to short periods of rainfall.

2) *Medium duration of rainfall (10 - 20 hrs) with a medium - high magnitude (2 -10 mm)*

Medium duration rainfall, typically occurring over 10 to 20 hours, with a high magnitude (between 2 and 10 mm) are the most frequent controls on accelerated movement events (50 %). These were associated with groundwater levels in the range 4.3 to 6.4 m, and typically with a rate of change of groundwater level of approximately 0.2 m/hr, leading to displacement rates in the range 0.2 to 4.7 mm/hr. The data indicates that high magnitude rainfall can induce landslide movement due to a rapid increase in groundwater, even though the initial groundwater level might be low (i.e. Period 2). Conversely, the higher measured displacement rates show that rainfall infiltration was sufficient to cause landslides during high groundwater levels (i.e. Periods 12, 14, 15, 17 and 21; Table 5.4 and Figure 5.10).

3) *Long duration of rainfall (> 20 hrs) with a medium magnitude (2 - 4 mm)*

Rainfall duration of more than 20 hours and rainfall magnitudes between 2 mm and 4 mm represent 34% of accelerated movement occurrences. The resultant greater total displacements (74.2 – 309.7 mm) and the variation of displacement rates (0.8 - 6.3 mm/hr) were a response to the prolonged period of rainfall. A phase in which groundwater level approached the ground surface was observed in Period 19, and caused the most movement distance (approximately 309 mm) with a maximum displacement rate of 6.3 mm/hr. As for the other periods (i.e. Period 4, 6, 11), the displacement rates varied between approximately 1 and 2 mm/hr, probably because of the lower groundwater levels (< 5 m) and the small variations of rate of change of groundwater level (0.01 - 0.1 m/hr).

Conversely, the slow movements (Table 5.4) also occurred in periods of varying rainfall duration and magnitude. Long duration rainfall (> 20 hours) with a low- to medium magnitude (1-4 mm) was identified. Long rainfall duration (i.e. more than 20 hours) caused displacements up to 20 mm at low displacement rates (approximately 0.1 mm/hr). However, low groundwater levels were observed, varying between 4.02 m and 5.43 m, with very low rates of change of groundwater level (approximately 0.02 m/hr).

Additionally, no movement occurring under two key attributes were observed below:

1) *Short duration of rainfall (≤ 5 hours) with a low magnitude (< 1 mm)*

No movement was associated with short rainfall durations with low magnitude, or even in periods with no rainfall but with high levels of groundwater (> 5.0 m). There was little change between maximum and minimum groundwater levels during the movement periods, although the minimum groundwater level is high (approximately 5.1 m). The change of groundwater varies between 0.04 and 0.1 m. This pattern was observed in Periods 13, 18 and 20 (Table 5.4 and Figure 5.10).

2) *Long duration of rainfall* (> 20 hrs) with a medium magnitude (3 - 4 mm)

No movement was also associated with rainfall duration of more than 20 hours and rainfall magnitudes between 3 mm and 4 mm. The resultant total displacements (-4.12 – -52.885 mm (apparently upslope)) and a very low displacement rate (approximately 0.06 mm/hr) was observed, probably in response to groundwater decline (i.e. Periods 10 and 16).

5.4.2 Influence of groundwater

Most slopes with shallow soils (< 5 m depth) require saturated conditions or a positive change in pore water pressure (excess pore pressure) to induce slope failure (Sidle and Ochiai, 2006). Periods of accelerated movement typically correspond to times when groundwater levels correspond to or exceed a key threshold. Therefore, the influence of groundwater is considered in terms of effective stress changes. To understand the characteristics of groundwater affecting periods of accelerated movements, the groundwater patterns were categorized based on the 12 periods of discrete movement, as summarised in Table 5.4.

The cumulative displacement and hourly groundwater level for each of these periods have been plotted with the corresponding movement data (Figure 5.11). The groundwater data suggest that two types of groundwater level change (based on the bottom of borehole) were associated with movement events: 1) Increasing groundwater nearly or reach ground surface (low effective stress on the shear surface). 2) Increasing groundwater in the shear zone without full saturation of the soil column (change of effective stress on the shear surface). These two increasing groundwater regimes are relative to borehole depth. Interestingly, both types of groundwater increment exhibit either no lag time or only a one hour lag time, and cause the landslide displacement to respond almost immediately (for more detail, see section 5.4.3).

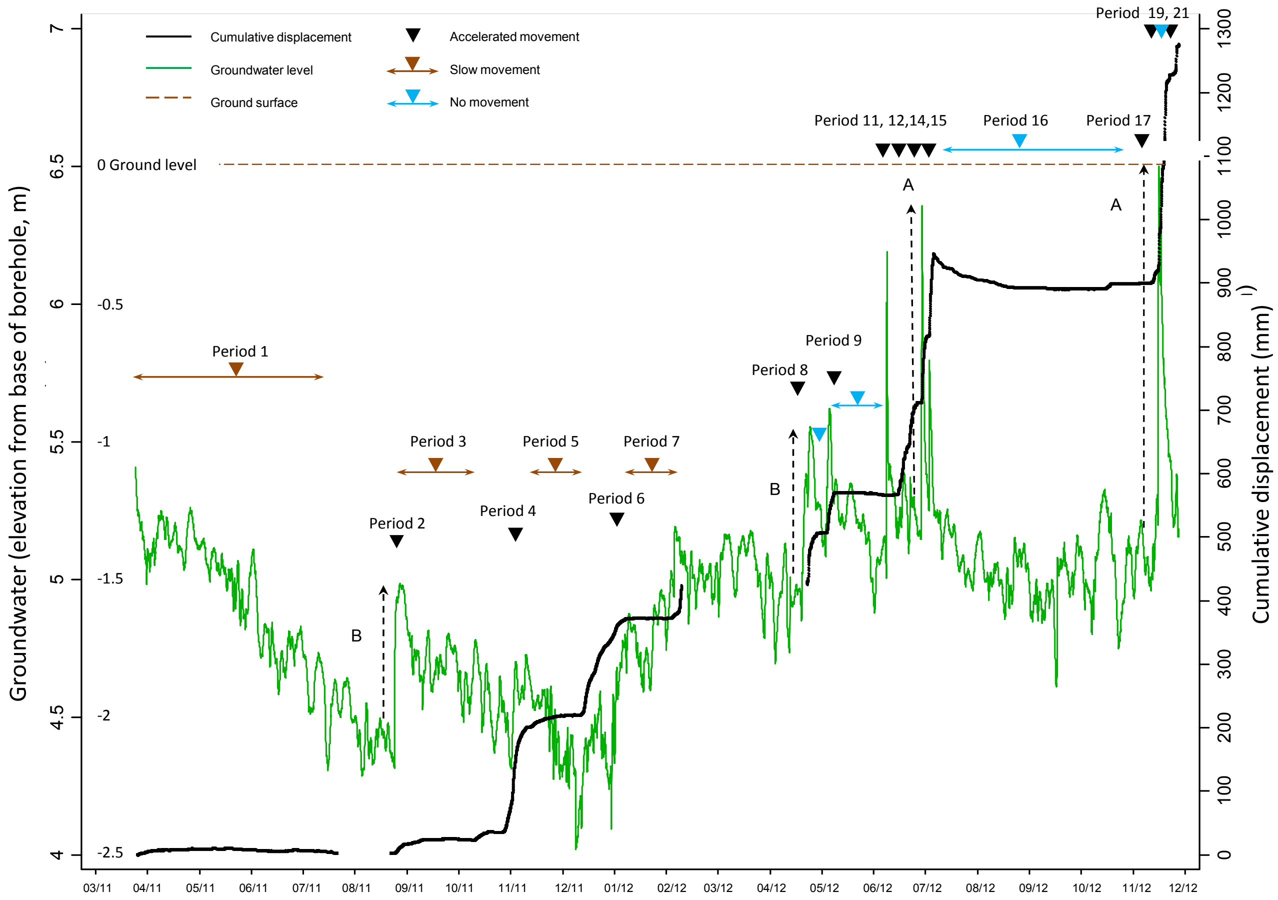

Figure 5.11 Plot of groundwater level and cumulative displacement over time showing three patterns of accelerated, slow and no movements between 2011 and 2012. Patterns of increasing groundwater of accelerated movement based on bottom of borehole (A and B patterns). A is a regime of increasing groundwater that is nearly reaching or has reached ground surface (low effective stress on the shear surface (i.e. Period 14 and 19). B is a regime of increasing groundwater in the shear zone without full saturation of the soil column (change of effective stress on the shear surface) (i.e. Period 2, 4, 6, 8, 9, 11, 12, 17 and 20). Slow movements occur during drier periods and low groundwater levels (mean groundwater 4.83 m). No movements are observed during groundwater decline with a variety of groundwater levels between 4.611 m and 6.191 m (i.e. Period 10, 13, 16, 18 and 20).

1) Increasing groundwater at or above the ground surface (low effective stress on the shear surface).

The groundwater table at the slope surface occurred in two scenarios, namely the groundwater level increasing to close to the ground surface, and groundwater level being at the ground surface. In period 14 (Figure 5.11), a high magnitude of rainfall (maximum hourly rainfall = 7.2 mm) led to a rise of groundwater almost to the ground surface (6.4 m). The landslide responded by travelling 105.8 mm. In Period 19 (Figure 5.11), continuous, intense rainfall with a very high total (45 mm) caused the groundwater level to reach the ground surface (6.5 m). This led to a phase of continuous accelerated movement with a complex response pattern.

2) Increasing groundwater in the shear zone without full saturation of the soil column above (change of effective stress on the shear surface).

The regime of increasing groundwater levels without full saturation was the most common pattern of groundwater increase associated with periods of accelerated movements. Increasing groundwater level was always below ground surface, and did not exceed 6 m. In Period 2, for example, groundwater rose rapidly in response to intense hourly rainfall (10 mm) resulting in accelerated landslide movements (Table 5.4 and Figure 5.11). However, the displacement rate was low (0.2 mm/hr) and displacement distance was short (approximately 13 mm) due to the initially low groundwater level (4.3 m). Period 9 (Figure 5.11) represents another case of change of the effective stress at the shear surface. In this period, the initial groundwater was higher (5.2 m), resulting in a higher displacement rate (1.7 mm/hr) and longer displacement distance (61 mm) as compared to Period 2. As such, increasing groundwater levels leads to a short duration of landslide movement with high displacement rates and long displacement distances. Conversely, a smaller change in effective stress can cause landslide movements with longer durations at a variety of displacement rates, although groundwater level was lower than under lower effective stresses.

Overall, based on the 21 periods of discrete movement, as summarised in Table 5.4, a wide variety of increases in groundwater led to accelerated movements (Std.Dev: 0.496).

However, slow movements responded to smaller fluctuations of groundwater (Std.Dev: 0.270) and the majority of slow movements occur during period of low groundwater. Periods of no movement responded to a very narrow fluctuation of groundwater level (Std.Dev: 0.139). However such periods were observed under a variety of groundwater levels between 4.61 m and 6.19 m, as can be seen in Figure 5.12.

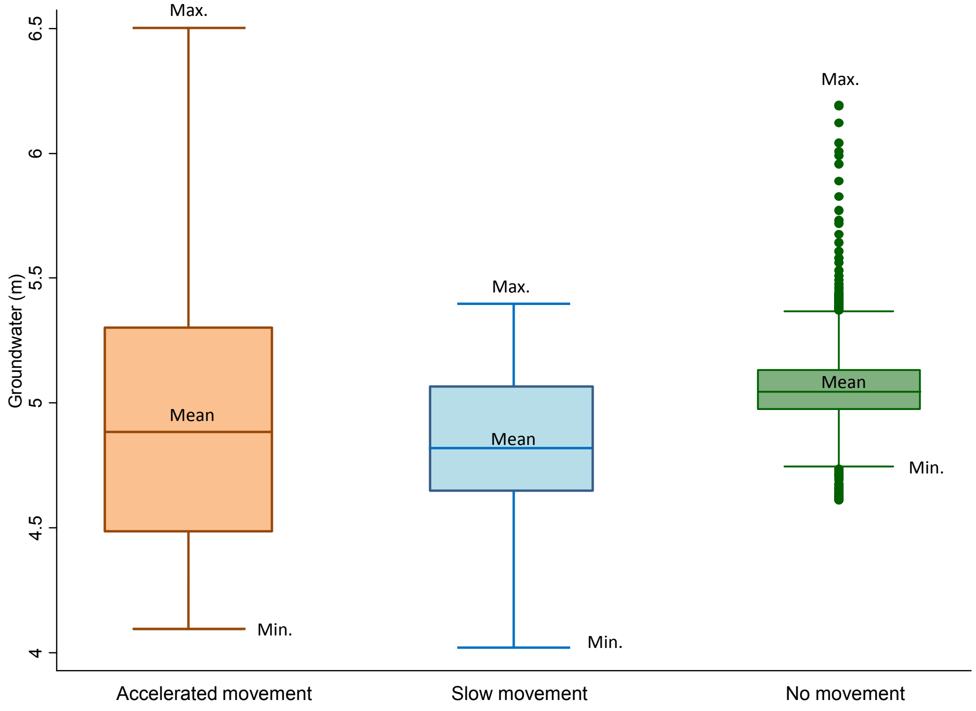

Type of movement	Groundwater			
	Mean	Std.Dev	Min	Max
1. Accelerated movement	4.897	0.496	4.100	6.501
2. Slow movement	4.827	0.270	4.020	5.408
3. No movement	5.057	0.139	4.611	6.191

Figure 5.12 Changing groundwater level over accelerated movement (left) and slow movement (right). Statistics denoted by the box plots are presented maximum, mean, standard deviation of the mean and minimum of groundwater level.

5.4.3 Rainfall and groundwater control on displacement

Although the monitoring data show that groundwater level responded almost immediately to rainfall, a correlation analysis was undertaken to explore the relationship between groundwater and rainfall in order to establish the time frame over which rainfall influences this response. Thus, the lag time between rainfall events and groundwater rise can be quantified (e.g. Lee and Lee, 2000; Chae et al., 2010; Mair and Fares, 2011). The groundwater at a given time and the accumulated antecedent rainfall has been assessed incrementally, e.g. $G_t \rightarrow R_{t-1-2}$; $G_t \rightarrow R_{t-1-2-3}$; $G_t \rightarrow R_{t-1-2-3}$, where G_t is groundwater at a given time and R_t is the antecedent rainfall, based on hourly data. The correlation analysis assumes a linear relationship between groundwater and rainfall.

The correlation is obtained by dividing the covariance of the two variables by the product of their standard deviations. The results show that the correlation is highest (0.35) (Figure 5.13) for rainfall accumulated over a 1 to 2 hour period, indicating that groundwater responded almost immediately. As such, displacements can be observed in response to increasing ground water level alone, independent of absolute groundwater level. The correlation analysis between groundwater and displacement rate is illustrated in Figure 5.14. The results show that the correlation is highest (0.54) at zero lag time, indicating landslide movement initiates immediately when the groundwater increases. This is as expected for a small, shallow landslide in comparatively permeable materials.

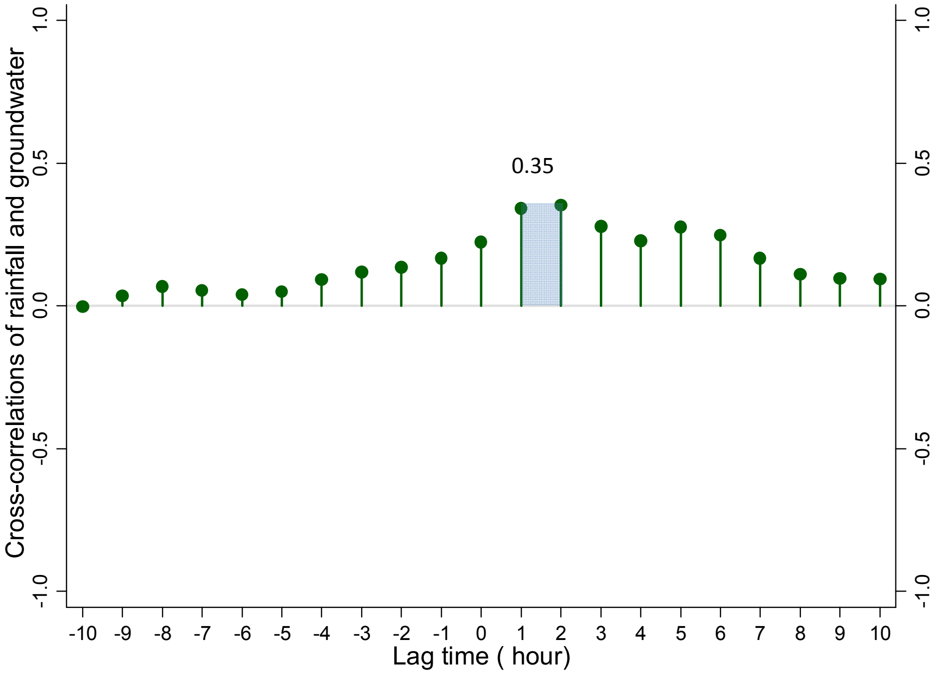

Figure 5.13 A plot of the cross-correlation functions for rainfall and rate of groundwater level change for 24 hours showing the correlation is considered statistically significant at a level of 0.35 for a 1-2 hour lag time.

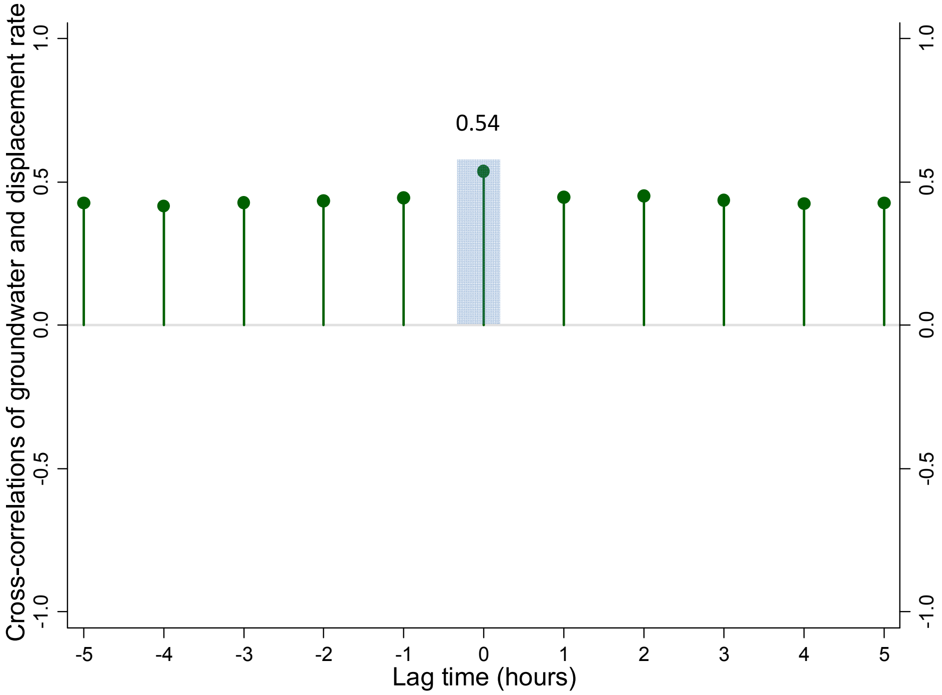

Figure 5.14 A plot of the cross-correlation functions for groundwater level and displacement rate change for 10 hours showing the correlation is considered statistically significant at a level of 0.54 for no lag time.

5.5 Chapter summary

The mechanisms of landslide movements induced by rainfall and the associated changes groundwater have been examined based on 21 discrete periods of movement at the Upgang landslide. The conclusions are as follows:

1. The Upgang landslide is characterised by shallow landslides at the upper section of the cliff. A reactivated landslide has been monitored using instruments (i.e. vibrating-wire extensometer ‘VBW1’, string extensometer ‘S4’ piezometer ‘PZU’ and a rain gauge) in order to understand the mechanisms of and controls upon landslide deformation.

2. Three patterns of landslide deformation are identified, namely accelerated movement, slow movement and no movement based on a threshold of ≥ 0.2 mm/hr, 0.06 mm/hr < x < 0.2 mm/hr and less than 0.06 mm/hr respectively. Accelerated movements occurred during periods of heavy rainfall with varying velocities (0.2 - 6.27 mm/hr), whereas slow movements occurred with very low velocity (0.01 - 0.2 mm/hr).

3. Rainfall magnitude duration records are useful in estimating periods of likely landslide activity as the accelerated movements almost exclusively occurred simultaneously with increases in groundwater level. The influence on landslide deformation can be associated with three attributes of monitored rainfall. Accelerated movements typically occurred during wet periods, which followed the three patterns of rainfall:

    1) Short duration rainfall (5 - 10 hrs), with a low magnitude (< 2 mm)
    2) Medium duration of rainfall (10 - 20 hrs) with a medium-high magnitude (2 -10 mm)
    3) Long duration of rainfall (> 20 hrs) with a medium magnitude (2 - 4 mm)

Conversely, slow movements occurred during drier conditions (hourly rainfall up to 4 mm) in long (> 20 hrs) rainfall events. No movement occured in tandem with small changes of groundwater level, caused by two key scenarios of rainfall: 1) Short duration of rainfall (≤ 5 hours) with low magnitude (< 1 mm) and 2) Long duration of rainfall (> 20 hrs) with medium magnitude (3 - 4 mm).

4. Groundwater level varies throughout the entire monitoring period (ranging from 4.0 to 6.5 m) in response to rainfall events, showing only a short lag time (1 - 2 hrs). The sudden and temporary increasing groundwater exhibits two patterns of increasing groundwater level leading to accelerated movements. A wide variety of increases in groundwater led to accelerated movements. Two types of groundwater level change caused accelerated movements:

1) Increasing groundwater that is nearly reaching or has reached the ground surface (low effective stress on the shear surface).
2) Increasing groundwater in the shear zone without full saturation of the soil column (change of effective stress on the shear surface).

The first pattern of increasing groundwater caused high displacement rates. However, the latter pattern is commonly found during accelerated movements. Slow movement is complex, as it responds to only a narrow fluctuation of groundwater level especially during periods of absolute low groundwater levels. Conversely, periods of no movement respond to a very narrow fluctuation of groundwater.

In this research, three types of landslide movements (accelerated, slow and no movements) were affected by hydrological conditions. The landslide movements were controlled by infiltration of surface water and groundwater, which was brought about by precipitation. The resultant increase in groundwater coincides directly with the timing of landslide movement, suggesting causality. Importantly, due to the site-specific nature of this discussion, these findings should not be generalised.

Chapter 6 Control of groundwater on landslide movement

6.1 Introduction

As discussed in Chapter 5, the relationship between monitored groundwater and landslide displacement rates is more complex than might be expected. In order to better understand this relationship and the deformation mechanisms on the glacial till during the development of failure, a programme of innovative laboratory tests has been conducted. This chapter presents the laboratory testing results of physical properties tests, back-pressured shear box tests (BPS), and Pore Pressure Reinflation tests (PPR).

To understand the deformation mechanisms on the glacial till, three objectives were addressed:

1) Characterisation of the physical properties of the glacial tills at the Upper section of the Upgang landslide;
2) Determination of the shear strength parameters (ϕ' and c') using back-pressured shear box testing;
3) Examination of the relationship between displacement rate and groundwater (PPR tests).

6.2 Physical properties

The physical properties of the Upgang soil samples are summarized in Table 6.1. The samples represent glacial till derived from the North Sea Lobe of the British-Irish Ice sheet during the Devensian glacial stage of the Late Pleistocene (Hemimgway and Riddler, 1980; Bell, 2001; Roberts et al., 2012). The glacial till comprises Withernsea till, which is reddish brown with a mud matrix, sand lenses and granule-pebble sized clasts. The number of samples used depended on the amount needed (the larger the amount, the lesser the number of samples), the duration of individual tests (the longer the duration, the fewer the number) and the availability of samples.

The characteristics of soil were classified using two classification systems that use the grain-size distribution and plasticity. Firstly, based on their particle size distribution, the glacial till can be classified as ‘Fine-Silt’, with less than 10% of particles larger than 2 mm. It is largely composed of silt (71-75%), with about 21-29% clay and less than 10% sand (Figure 6.1). According to the analysis of the Atterberg limits, the soil samples can be classified as ‘Inorganic clays’ of medium-high plasticity, denoted as CI-CH. This is apparent as the plots of plasticity indexes against liquid limits lay above the A-line on the Casagrande chart (Figure 6.2). Three glacial till samples comprised high plasticity clay and only one sample fell into the medium plasticity range. The plastic limit of the till samples ranged between 25% and 28% with liquid limits ranging between 48% and 60%.

Additionally, the specific gravity values varied between 2.53 to 2.67, with an average of 2.59 as the samples were made up of a mixture of fragments ranging in size from clay to coarse silt. These samples show an inorganic nature by having a low organic content (4-7% loss on ignition). The initial void ratio and dry densities ranged between 0.69 - 0.67 (average of 0.62) and 1.43 - 1.67 mg/m^3 (average of 1.53 mg/m^3), respectively. A range of natural moisture contents (16.61 to 23.30%; average of 21.96%) were observed in the glacial till samples. This is lower than the average plastic limit value (27.12%).

Table 6.1 Physical properties of Upgang‘s glacial till.

Physical properties	Glacial till (Textural Group: Mud; Sediment Name: Fine Silt)			
	Mean	Min	Max	# Samples
Particle size analysis				
Gravel > 2mm	0.10			2
Sand Coarse (0.6-2 mm)	0.00	0.00	0.00	5
Medium (0.2-0.6 mm)	0.00	0.00	0.00	5
Fine (0.06-0.2 mm)	1.88	0.00	7.50	5
Silt Coarse (0.02-0.06 mm)	9.06	0.80	20.20	5
Medium (0.006-0.02 mm)	20.70	13.80	23.50	5
Fine (0.002-0.006 mm)	43.80	37.00	45.70	5
Clay < 0.002 mm	24.46	21.50	28.80	5
Specific gravity, G_s	2.59	2.53	2.67	5
Loss on ignition, LOI	5.63	4.305	7.081	12
Moisture content, % (at 105° C)	21.96	16.61	23.30	12
Liquid limit, LL*%*	55.85	48.14	60.34	4
Plastic limit, PL*%*	27.12	25.39	28.00	4
Plasticity Index, PI%	28.74	22.75	32.33	4
Initial void ratio, e	0.62	0.59	0.67	3
Bulk density of saturated material, ρ_{wet}, mg/m^3	1.96	1.92	2.04	3
Dry density, ρ_{dry}, mg/m^3	1.53	1.43	1.67	3

Number of undisturbed samples used

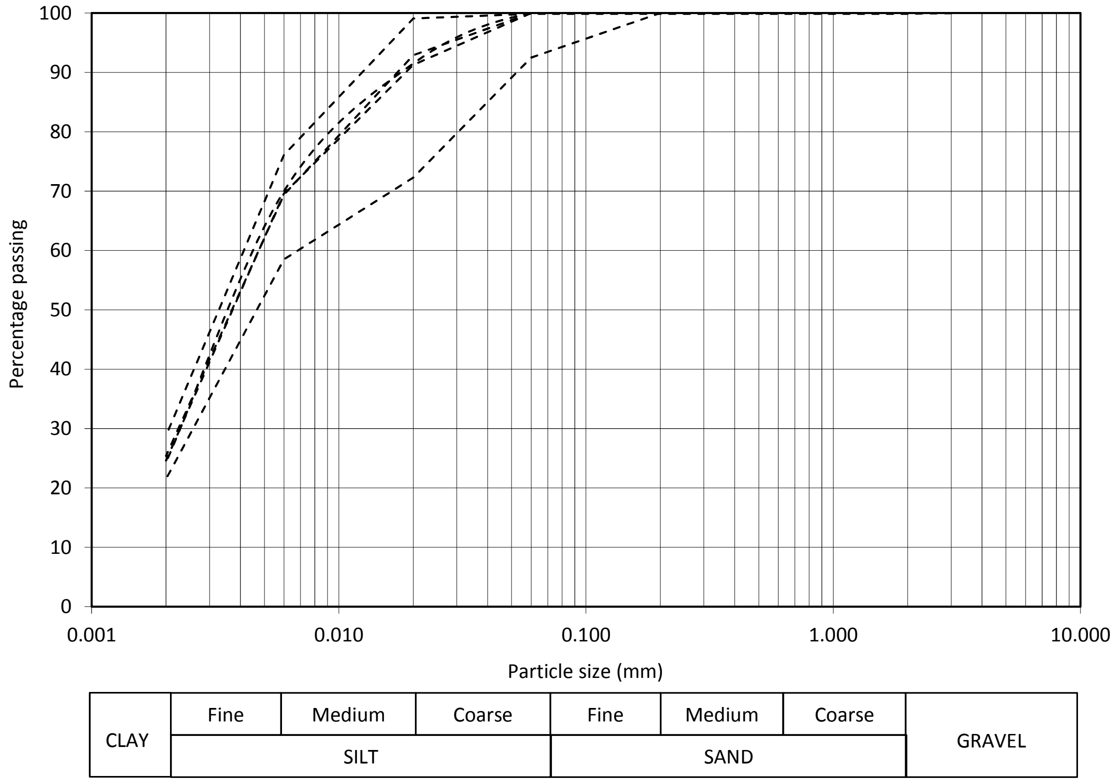

Figure 6.1 Particle size distribution chart of five glacial till samples showng gradings that are typical of glavial till gradings, i.e, they represent well graded silt. The dominant particles are Silt (71-75%) and Clay (about 21-29%), whilst Sand content is minor(less than 10%).

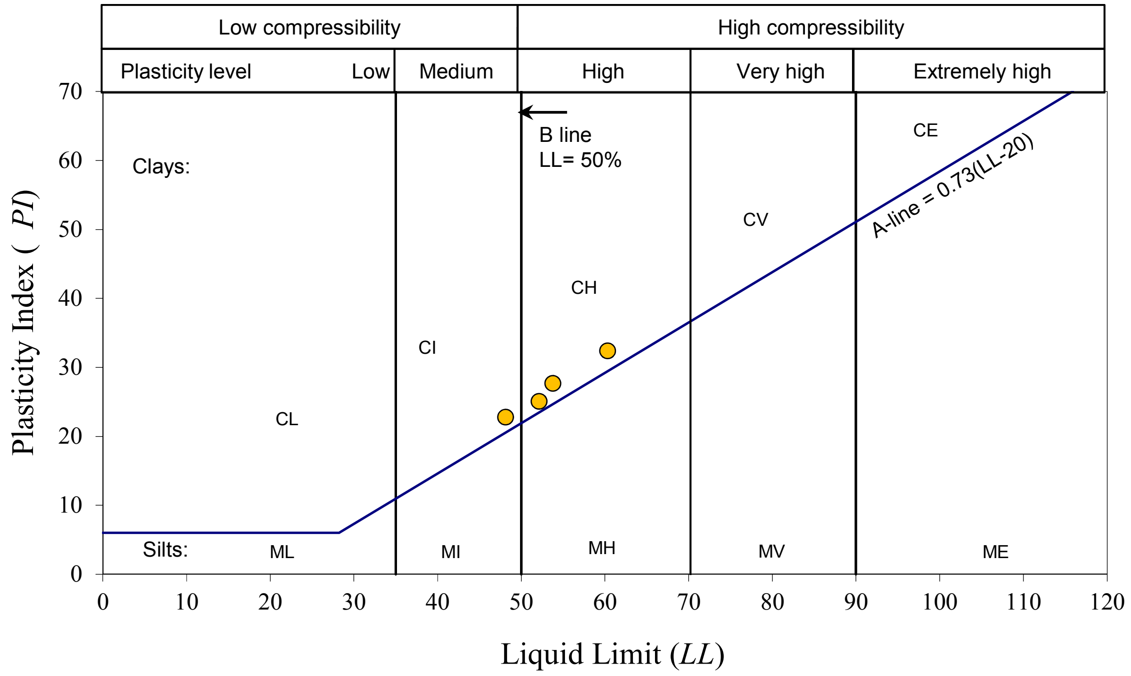

Figure 6.2 Classification of glacial tills in the plasticity chart. Three samples fell into the high plasticity level (CH) and only one sample fell into the medium plasticity level (CI). Three samples had percentage of liquid limit over the B-line (>50%) denoting high compressibility.

6.3 Compressibility

6.3.1 Pre-consolidation stress

The pre-consolidation stress (σ'_c) is an important property that in a simplistic sense refers to the maximum stress to which an over-consolidated clay has been subject (Head, 1988). This stress is an important consideration when determining the various stresses applied to the soil samples during the testing programme. In the case of tills, it can be inferred that the reason for their over-consolidation is the load applied by the overlying ice. This overburden pressure can be deduced by the determination of the pre-consolidation pressure (Gass, 1961). In this research, the back-pressured shear box apparatus was used to consolidate saturated samples of the till soils in confined conditions. The effective stress (σ') was applied to two samples (W01, E01) in a sequence of increments of 10, 20, 25, 50, 100, 200, 400, 800, and 1,600 kPa. These samples were allowed to consolidate for 12 hours in each phase before the next increment was applied. The pre-consolidation stress was estimated using logarithm equations (Figure 6.3), based on an analysis of the intersection between the two consolidation curves.

The two samples show a similar pattern of compression behaviours, with a pre-cosolidation stress at approximately 122 and 125 kPa for W01 and E01, respectively. This result indicates that the till is not heavily over-consolidated, as has been observed in other studies (e.g. Boulton and Paul, 1976; Bell, 2002). This can probably be explained by the development of high pore water pressures, and thus low effective stress states, beneath the glacial ice. Bell (2002) used this explanation to explicate why lodgement tills, which may have been deposited under considerable thicknesses of ice, are often not heavily over-consolidated. This suggests that pre-consolidation stress is not directly related to the thickness of the overlying ice (Boulton and Paul, 1976). However, the pre-consolidation stress remains important in the determination of the stresses to be applied in the direct shear testing programme.

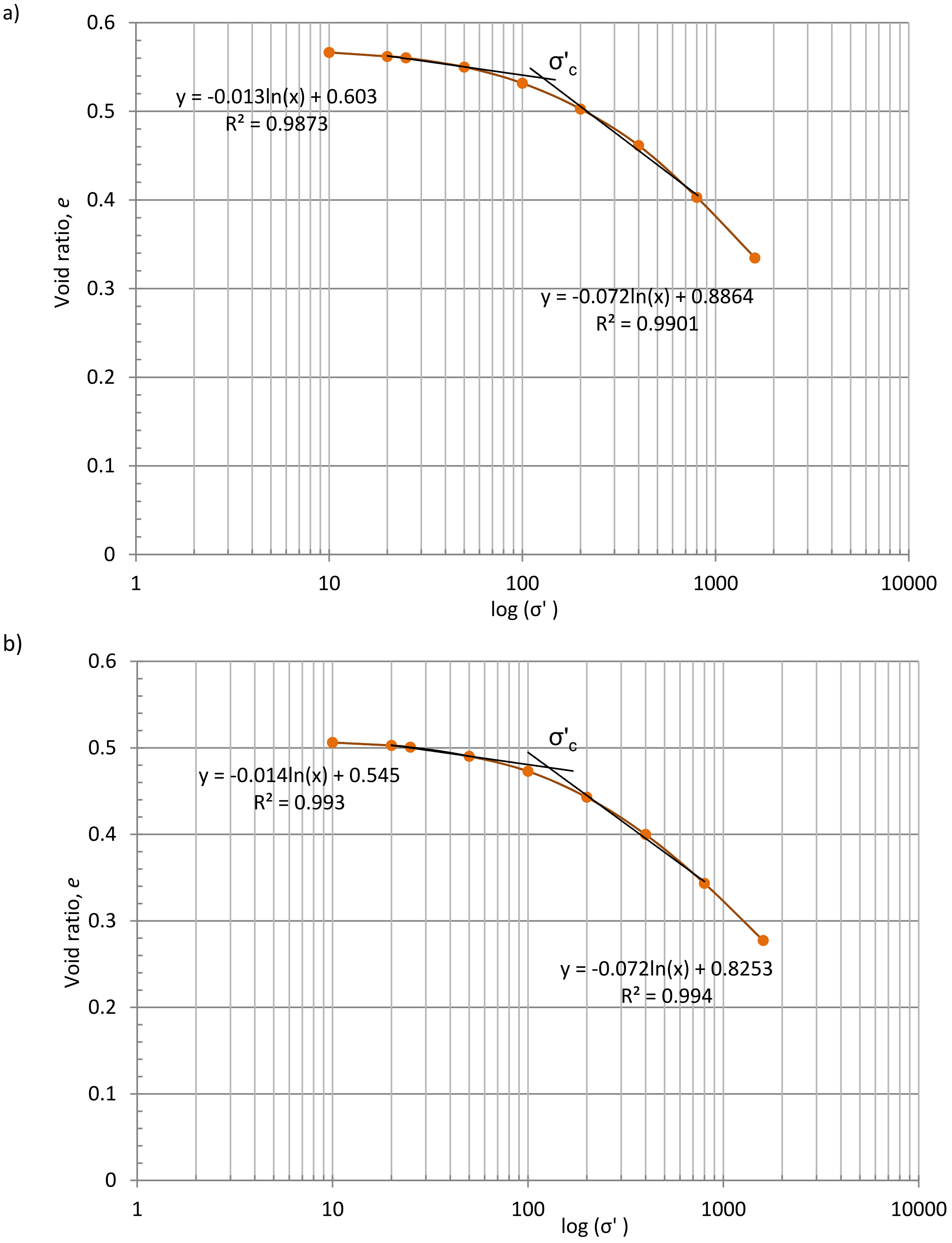

Figure 6.3 The log (σ_v) curve of axial effective stresses at 10, 20, 25, 50, 100, 200, 400, 800 and 1600 kPa against voids (*e*) for the two tests. a) The resultant pre-consolidation stress (σ'_c) is about 122 kPa on Sample W01. b) The resultant pre-consolidation stress (σ'_c) is about 125 kPa on Sample W02.

6.3.2 Consolidation

Consolidation is an initial phase of the BPS tests, required before a shear force is applied in order to establish the requisite stress state. Consolidation properties are presented in Table 6.2. As expected, an increase in vertical displacement has led to a corresponding increase in effective stress, generating an associated decrease in void ratio (Figure 6.4).

The consolidation curves show an increase of axial displacement in the initial stages of the application of increased vertical load. This is followed by larger axial displacements as PWP decreased (Figure 6.4a). The consolidation curves confirm that the axial displacement is positively related to the applied stress i.e. that samples subjected to higher effective stress resulted in a larger amount of axial displacement. Unexpectedly, the axial displacement of W04 (σ' = 125kPa) was found to be higher than the axial displacement of W05 (σ' = 175 kPa) after consolidation, and the latter‘s void ratio appeared to be associated with a higher initial void ratio. However, complexities in the consolidation behaviour were also observed, which could not simply be explained by the effective stress level or the initial void ratio. This was illustrated by the observed variability in axial displacement and void ratio under the same effective stress (Figures 6.4b and c), resulting from the heterogeneous nature of the glacial till.

Table 6.2 Axial displacement and initial void ratio after the consolidation stage. The axial displacement after the consolidation stage ranged from 0.65 to 1.79 mm (75 kPa: 0.80-0.87 mm; 125 kPa: 1.17-1.73 mm; 175 kPa: 1.71-1.76 mm). The void ratio after consolidation was between 0.48 and 0.58 (75 kPa: 0.53-0.56; 125kPa: 0.49-0.53; 175 kPa: -0.480.51).

Testing	Sample No.	Effective stress (kPa)	after consolidation stage		after shear stage	
			Axial displacement (mm)	Void ratio, e	Axial displacement (mm)	Void ratio, e
BPS	W02	50	0.65	0.58	0.84	0.56
	W03	75	0.80	0.56	1.02	0.55
	W04	125	1.73	0.49	2.13	0.46
	W05	175	1.48	0.51	1.76	0.49
BPS	E02	75	0.87	0.53	1.01	0.52
	E03	125	0.76	0.54	1.00	0.52
	E04	175	1.50	0.51	1.80	0.48
PPR	W06	75	0.84	0.56	1.08	0.54
	W07	125	1.17	0.53	1.32	0.52
	W08	175	1.71	0.49	1.92	0.47

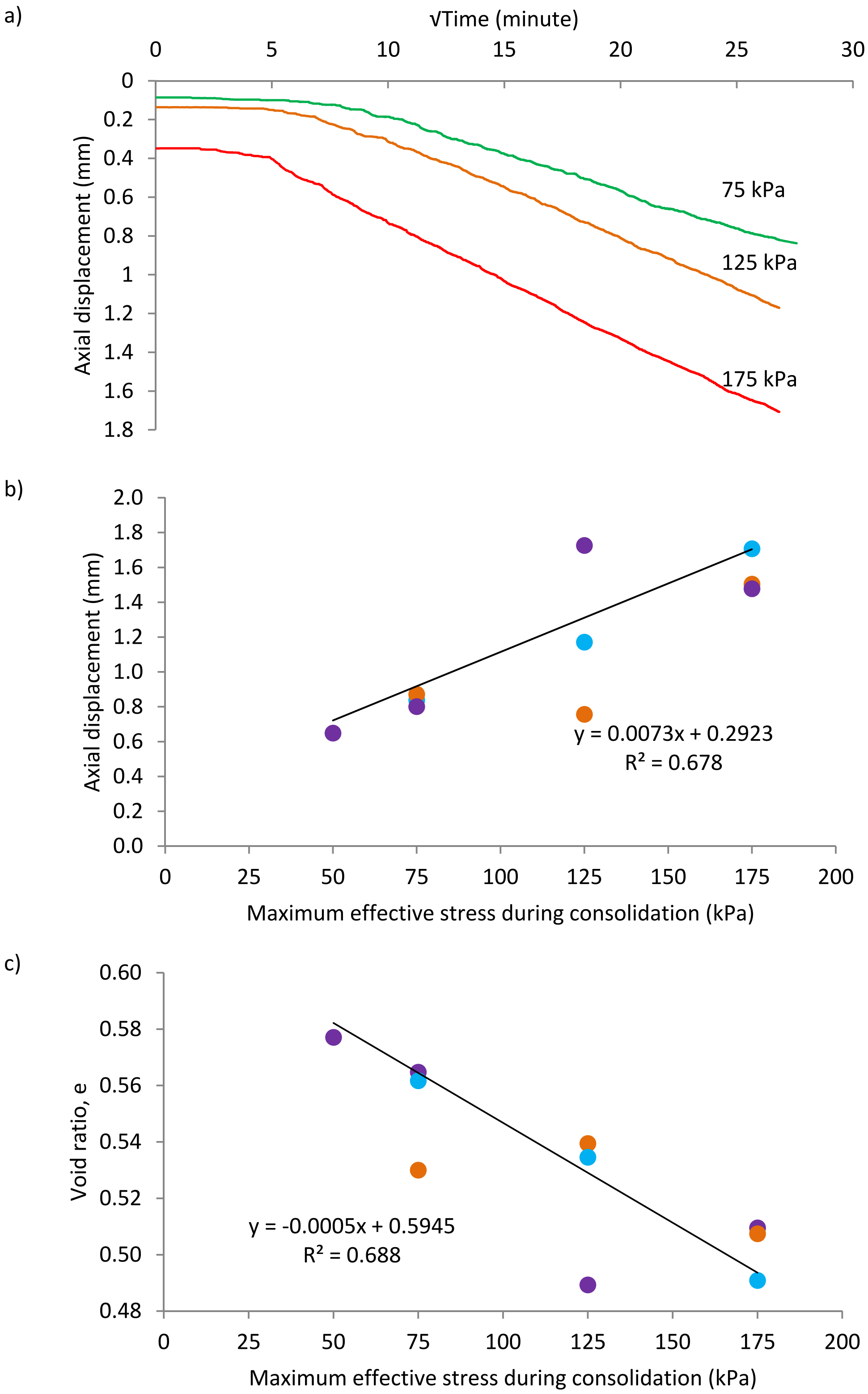

Figure 6.4 Plots of strain development during consolidation. A higher consolidation pressure resulted in a larger axial displacement with a lower void ratio, and a lower consolidation pressure was subjected to a higher void ratio: a) consolidation curves at effective stresses 75, 125 and 175 kPa: b) plots of maximum effective stress against axial displacement: c) Plots of maximum effective stress against void ratio. (Dots: Purple represents data from direct shear tests: W02, W03, W04, W05; Orange represents direct shear tests: E02, E03, E04; Blue represents data from PPR tests: W06, W07, W08).

6.4 The strain-controlled compression tests (BPS tests)

The aim of the direct shear tests was to assist in the design of the PPR tests. To undertake this study a series of laboratory tests was conducted using the back-pressured shear box apparatus (Table 6.3). This test allows the determination of the consolidated drained shear strength of the till in direct shear. The test is performed by deforming a specimen at a controlled strain rate on a single shear plane. Two sets of samples, (West, samples W02, W03, W04, W05; and East, samples E02, E03, E04) were sheared under effective stresses of 50, 75, 125 and 175 kPa. The rate of shearing (strain rate) was applied slowly (0.01 mm/minute) to allow drainage of the samples to prevent pore water pressure build-up.

Table 6.3 The conventional shear strength testing programme applied in this study

Sample No.	Test type	Mean effective stress (kPa)	Strain rate, mm/minute
W02	Direct shear failure envelope	50	0.01
W03		75	0.01
W04		125	0.01
W05		175	0.01
E02	Direct shear failure envelope	75	0.01
E03		125	0.01
E04		175	0.01

6.4.1 Stress-strain soil behaviour

The nature of deformation processes of the glacial till has been revealed by plotting the shear stress and shear displacement curves. All samples show a generally ductile style of behaviour (Figure 6.5). At the higher stress levels (i.e. σ' =75, 125 and 175 kPa), the samples showed minor strain-weakening at high strain levels, although this may be a consequence of the small cross-sectional area of the shear box at high strains.

Axial displacement increases resulted in a decrease in void ratio, which became relatively stable at higher shear displacements (Figures 6.6 and 6.7). Consequently, plastic behaviour was observed, which involved contractive behaviour during the shear stage. At the initial shear stage, effective stresses of 50, 75, 125 and 175 kPa led to a corresponding axial displacements of 0.84, 1.02, 2.13, and 1.76 mm, respectively, leading to a decreasing void ratio proportionate to applied stresses (*e* = 0.46-0.56). Also, the changes in axial displacement after the shear stages confirmed that void ratio decreased from the consolidation stage and was positively related to the amount of stress applied (Table 6.2).

a)

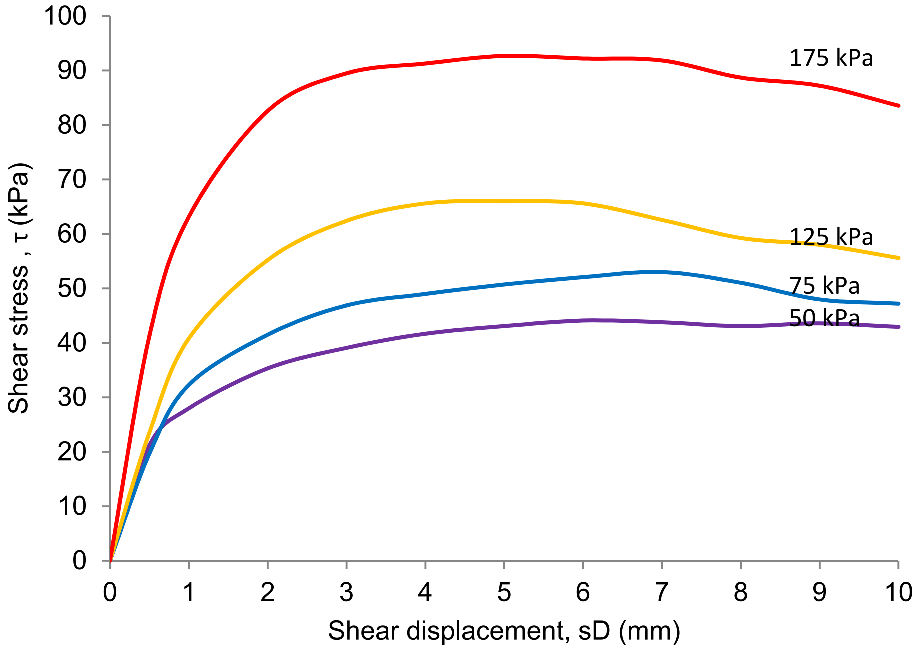

b)

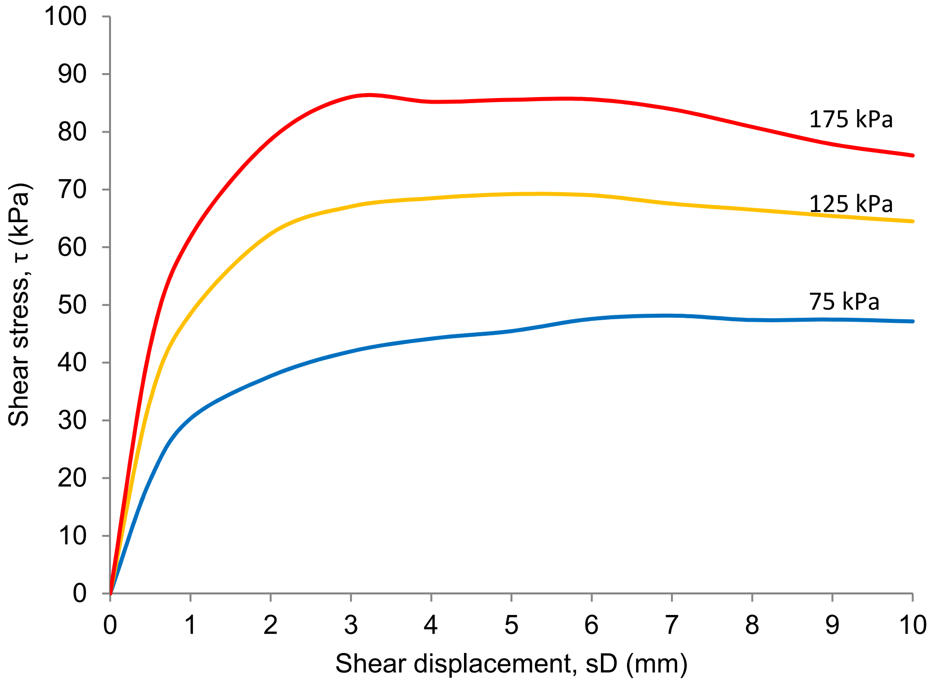

Figure 6.5 Shear stress against Shear displacement curves illustrating the characteristics of ductile deformation during the direct shear tests at effective stresses 50, 75, 125 and 175 kPa: a) West samples (W02, W03, 04, W05); b) East samples (E02, E03, E04).

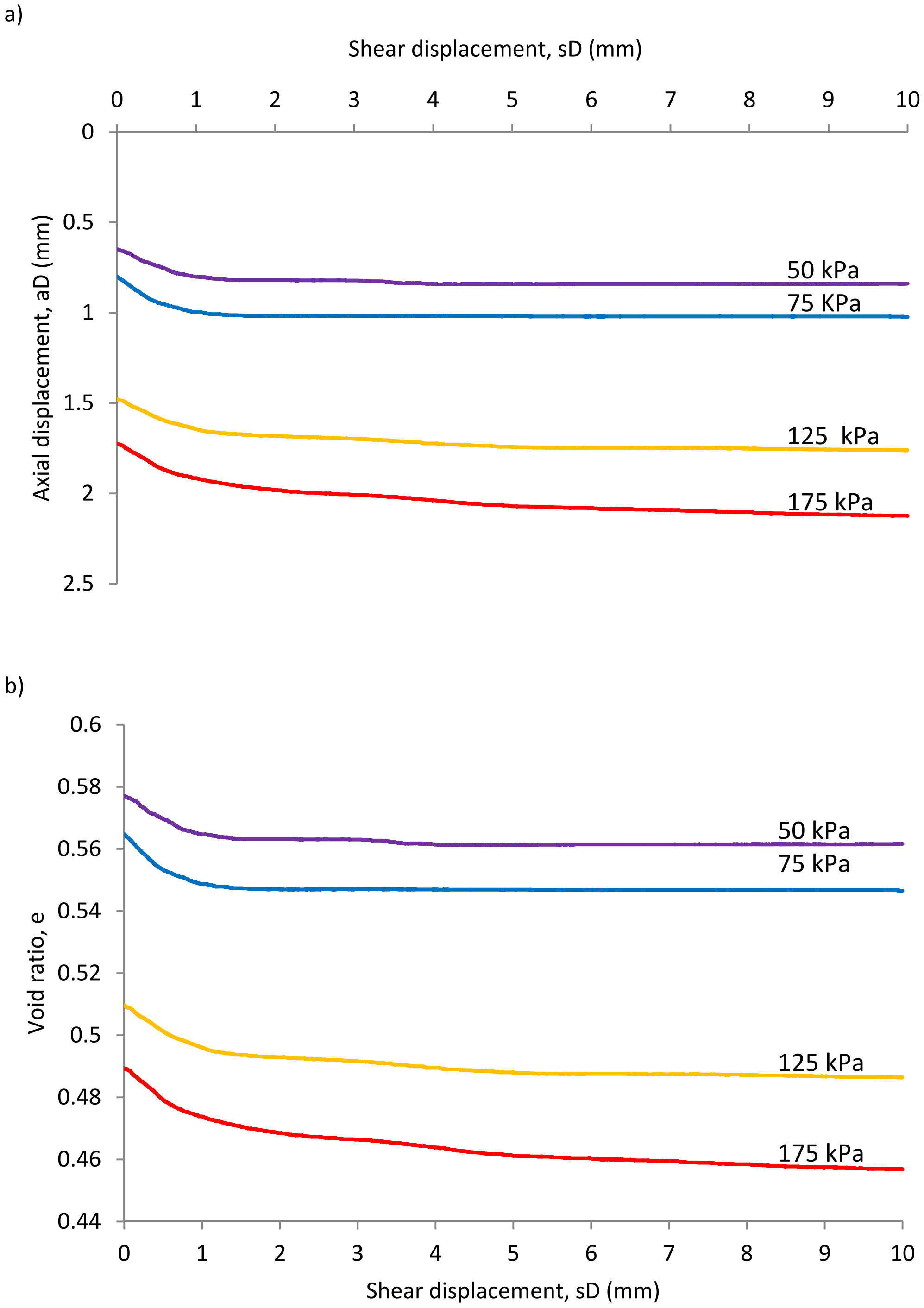

Figure 6.6 Contractive behaviour of West samples (W02, W03, 04, W05) showing decreasing void ratios that are positively related to the amount of stress applied during the shear stage: (a) Plots of axial against shear displacements and (b) Void ratio against Shear displacement at effective stresses 50, 75, 125 and 175 kPa.

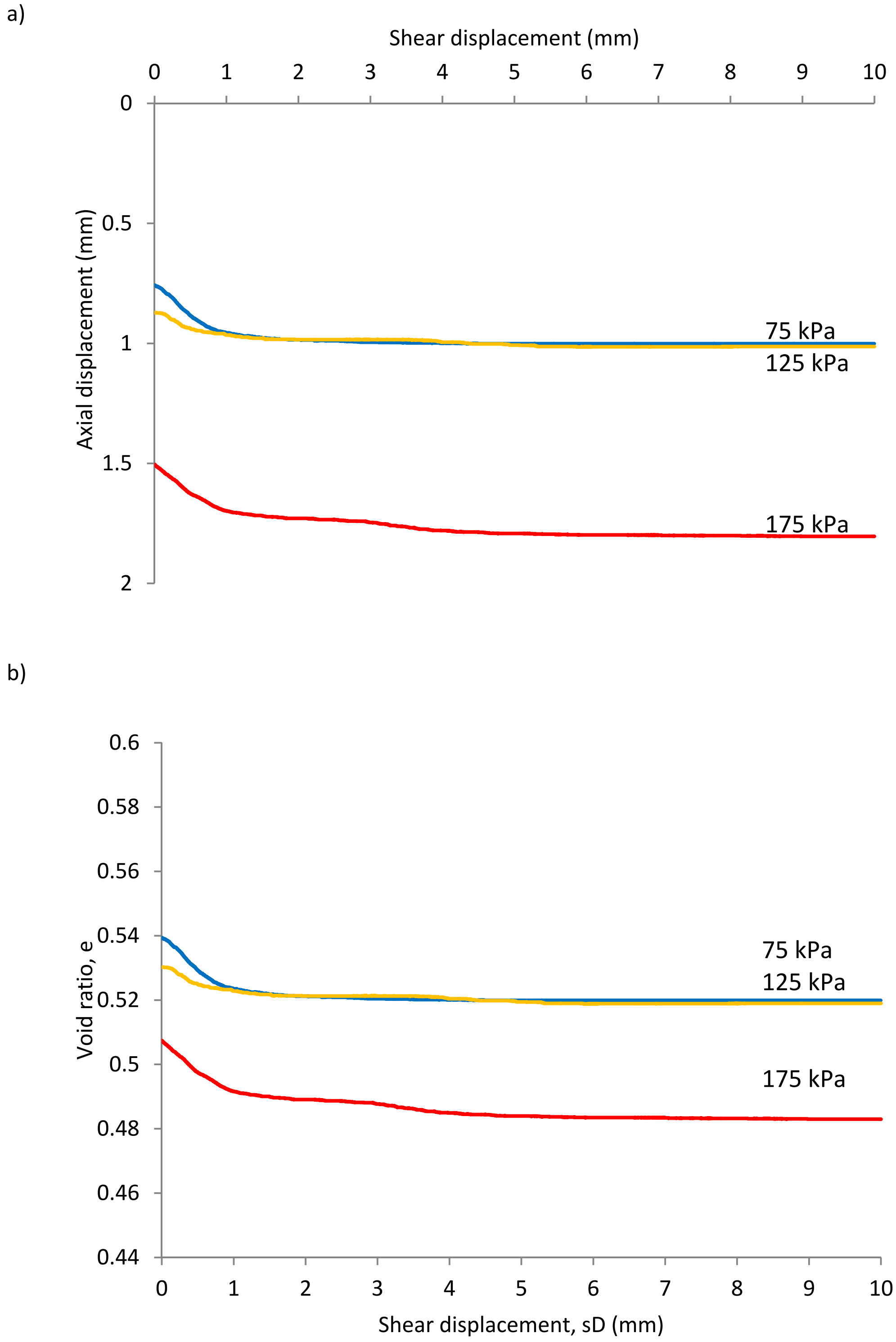

Figure 6.7 Contractive behaviour of East samples (E02, E03, E04) showing decreasing void ratio during the shear stage similar to West samples: (a) Plots of axial vs. shear displacements and (b) Void ratio vs. Shear displacement at effective stresses 75, 125 and 175 kPa.

6.4.2 Strain development prior to failure

The effective cohesion and angle of internal friction during the BPS test can be used to represent the strain development process of the till (Table 6.4, 6.5). This process shows both samples registering changes in frictional strength and effective cohesion at small shear displacements (≤ 4mm). For the samples from the West (W02, W03, W05), the frictional angle increased from 9.2° to 22.5° during an increase of shear displacement from 0.5 mm to 4 mm, followed by a decrease of frictional angle at higher shear displacements. Similarly, for the samples from the East (E02, E03, E04), the frictional angle increased from 9.1° to 21.6° during an increase of shear displacement from 0.5 mm to 3 mm, after which a decrease of frictional angle was found at a higher shear displacement. However the cohesion continued to increase before becoming relatively stabilised (Figure 6.8). It should be noted that due to the sample's behaviour as clay, the effective cohesion does not become zero under increasing pore water pressure.

A similar observation can also be made when plotting shear stress against effective stress (Figure 6.9). The steepness of the resulting envelopes increases rapidly at small shear displacements (≤ 4 mm). The derived effective cohesion is similar at larger shear displacements, however frictional strength decreases. This was indicated by the largely constant slope of $\tau_{max} – \sigma'$ at 3-7 mm shear displacements (Figure 6.9).

Table 6.4 Strain development in terms of failure parameters (c’ and ϕ') on West samples (W02, W03, 04, W05). The maximum shear stress is denoted by $\tau_{Max.}$

Shear displacement (mm)	Shear stress (kPa)				Effective stress (kPa)				c' (kPa)	ϕ' (°)	R²
	50	75	125	175	50	75	125	175			
τ_{Max}	44.10	53.00	66.00	92.67	50.20	74.16	117.30	170.76	23.10	21.62	0.99
0.5	21.21	19.68	23.53	41.26	47.74	72.77	122.00	170.47	9.70	9.20	0.77
1	27.98	32.28	40.80	63.14	48.89	72.64	120.30	170.83	11.96	15.75	0.95
2	35.31	41.49	55.20	82.58	49.28	72.98	119.90	170.46	13.84	21.10	0.97
3	39.08	46.87	62.40	89.47	49.58	72.91	118.20	170.80	16.97	22.44	0.99
4	41.68	48.98	65.60	91.28	50.41	74.09	117.70	170.72	19.13	22.50	0.99
5	43.07	50.72	66.00	92.67	49.78	73.21	117.30	170.76	21.12	22.23	0.99
6	44.10	52.06	65.60	92.20	50.20	73.88	115.80	170.18	22.63	21.73	0.99
7	43.79	53.00	62.58	91.84	49.88	74.16	113.60	170.70	22.98	21.31	0.98
8	43.08	51.03	59.25	88.69	49.66	72.80	112.30	171.43	23.16	20.19	0.97
9	43.59	47.97	58.00	87.21	49.92	73.36	111.10	170.76	22.16	20.08	0.96
10	42.93	47.21	55.60	83.54	49.23	74.29	109.60	171.55	23.18	18.65	0.96

Table 6.5 Strain development in terms of failure parameters (c’ and ϕ') on East samples (E02, E03, E04). The maximum shear stress is denoted by $\tau_{Max.}$

Shear displacement (mm)	Shear stress(kPa)			Effective stress (kPa)			c' (kPa)	ϕ' (°)	R²
	75	125	175	75	125	175			
τ_{Max}	48.15	69.20	86.02	71.93	122.11	171.90	21.82	20.75	1.00
0.5	19.73	33.54	42.94	71.16	122.42	171.47	9.48	9.06	0.78
1	30.30	48.46	61.77	71.24	121.04	170.33	11.97	15.31	0.94
2	37.68	62.32	78.65	71.59	121.88	170.87	14.13	20.41	0.96
3	41.96	67.06	86.02	72.22	121.21	171.90	17.30	21.64	0.98
4	44.17	68.48	85.20	72.21	120.95	172.87	20.05	21.49	0.98
5	45.47	69.20	85.55	71.41	122.11	172.17	21.61	21.34	0.98
6	47.59	69.01	85.63	72.60	120.73	172.38	23.60	20.58	0.97
7	48.15	67.54	83.91	71.93	120.93	173.17	23.99	20.07	0.95
8	47.39	66.50	80.85	71.25	121.48	172.98	23.74	19.09	0.93
9	47.47	65.42	77.84	71.39	122.84	172.91	23.10	18.76	0.92
10	47.17	64.49	75.90	71.87	121.92	171.52	23.95	17.44	0.91

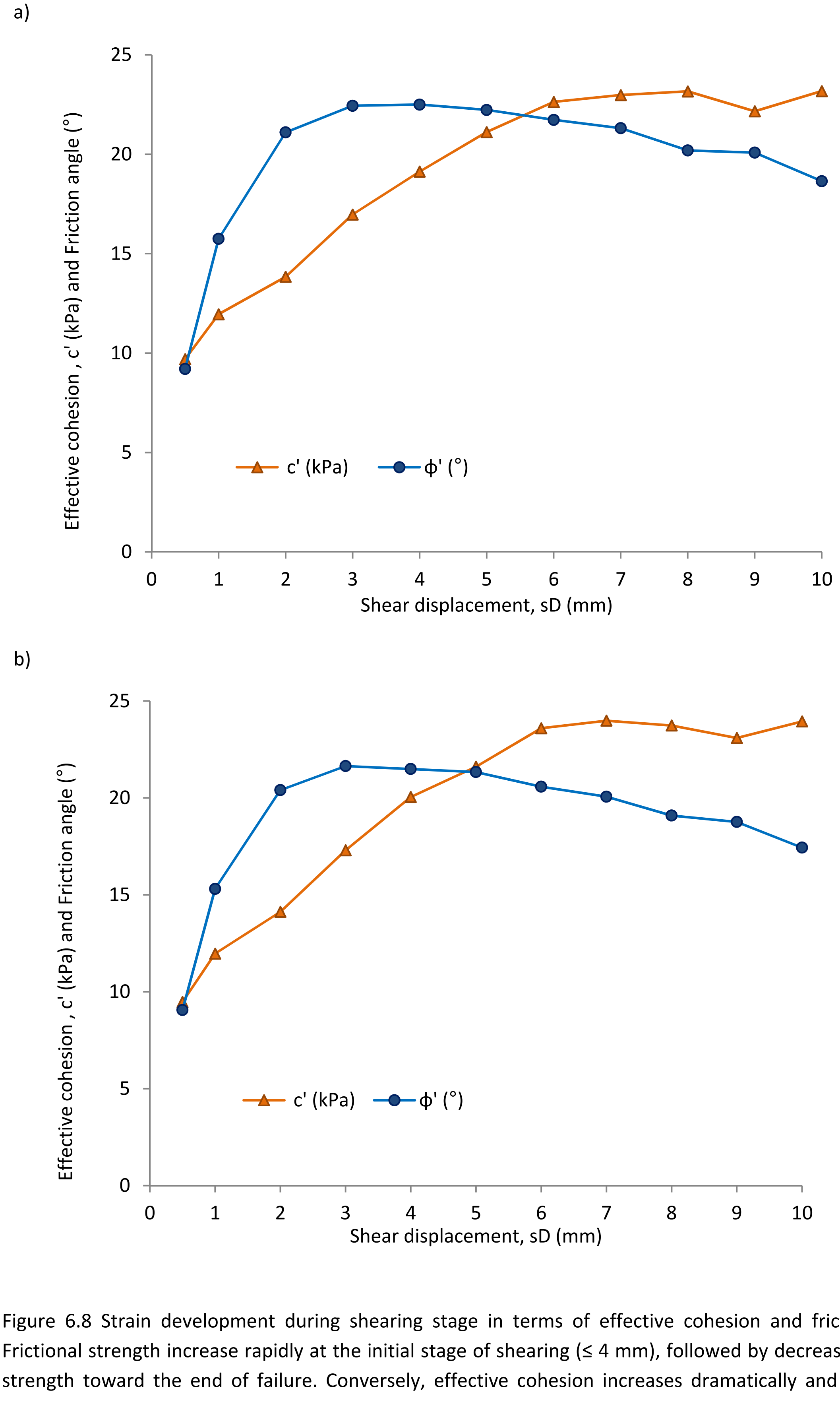

Figure 6.8 Strain development during shearing stage in terms of effective cohesion and frictional angle. Frictional strength increase rapidly at the initial stage of shearing (≤ 4 mm), followed by decreasing frictional strength toward the end of failure. Conversely, effective cohesion increases dramatically and followed by stabilisation: a) West samples (W02, W03, 04, W05); b) East samples (E02, E03, E04).

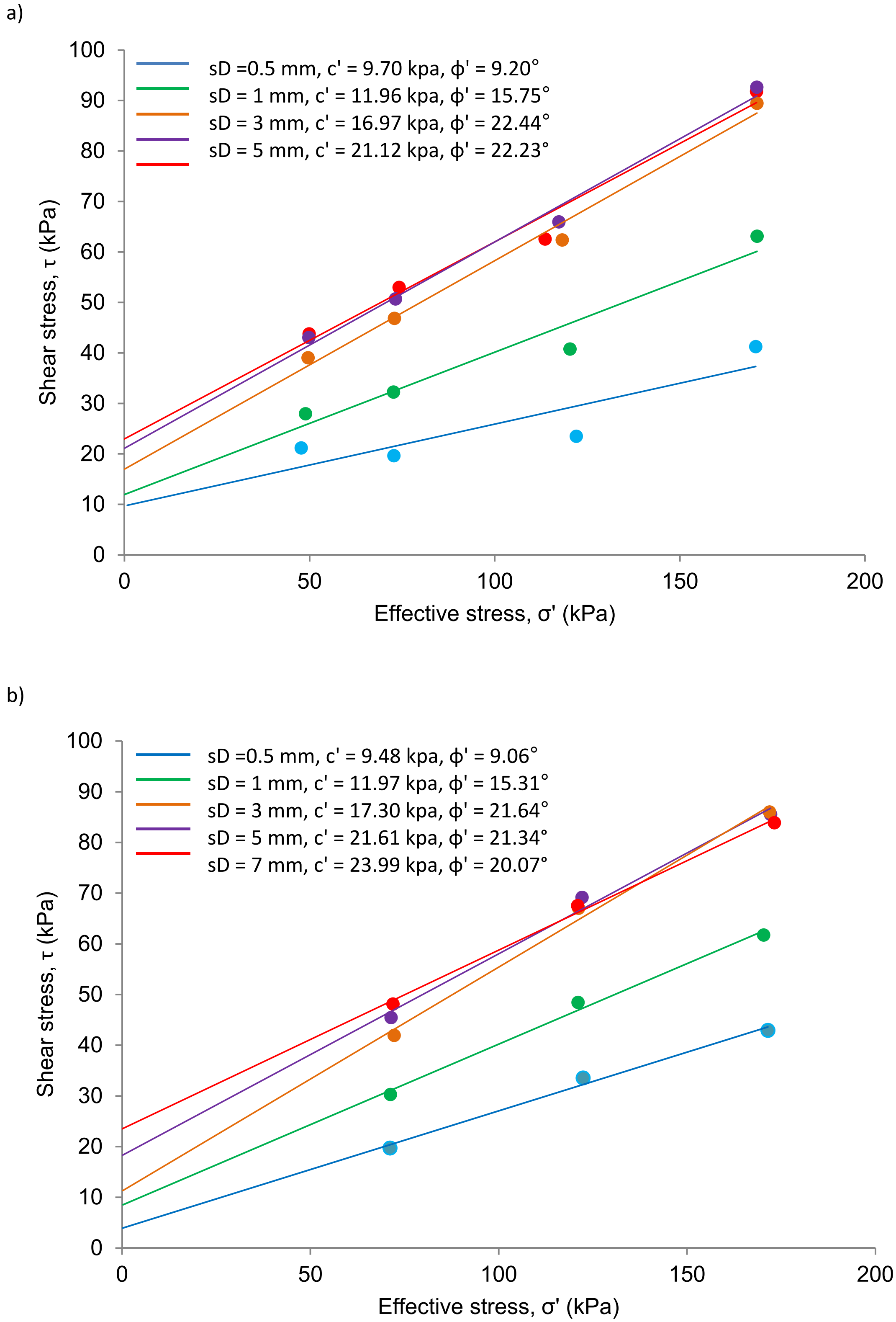

Figure 6.9 Strain development during shearing stage revealed by failure envelopes at equal strains. West sample (a) and East sample illustrated the largely similar constant slopes of T_{max}– σ’ at 3-7 mm shear displacements.

6.4.3 The direct shear failure envelope

The peak strength failure envelope is typically defined by the maximum shear stress (τ_{Max}) observed during monotonic shear. In this research, three values of of τ_{Max} were chosen at the effective stresses of 75, 125 and 175 kPa applied to the two sets of samples (West and East samples), allowing the failure envelopes to be determined. They are characterised by a near-perfect linear correlation ($R^2 \geq 0.99$) with similar derived effective frictional angles (ϕ') and effective cohesions (c') (Figure 6.10). The highest effective frictional angle for the sample was mobilised between 4 mm shear displacement (for West samples) and 3 mm shear displacement (for East samples) (Table 6.4, 6.5). Therefore, the effective frictional strength (ϕ') observed in the glacial till samples ranged from 20.75° to 21.64°, and the effective cohesion (c') ranged from 21.59 to 23.03 kPa. These shear strength parameters are at the low end of that of previously tested samples from the Hessle and Withernsea till in Dimlington formation, in which the friction angle ranged from 20° to 30° and the effective cohesion ranged from 21 to 38 kPa (Bell, 2002).

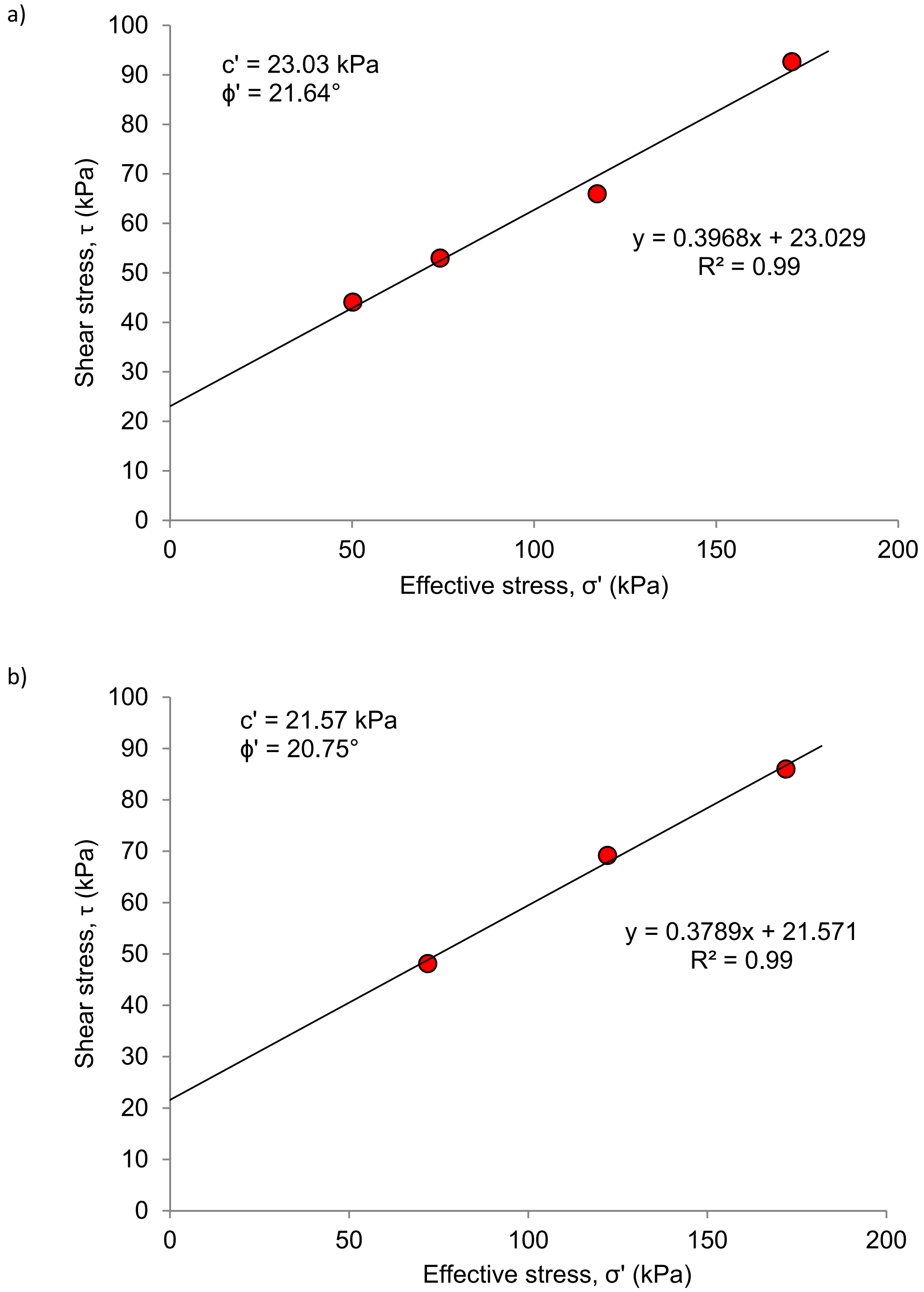

Figure 6.10 Failure envelopes defined by the stress conditions at maximum shear stress, derived from effective stresses at 50, 75, 125 and 175 kPa: a) West samples (W02, W03, 04, W05); b) East samples (E02, E03, E04).

6.5 The stress-controlled pore pressure reinflation tests (PPR tests)

The PPR tests were undertaken to replicate the field stress conditions of shallow landslides during high-intensity rainfall events in order to investigate the soil deformation processes (Table 6.6). To achieve this, the back-pressured shear box (BPS) was used to perform direct shear testing on undisturbed samples under consolidated, constant shear stress-path tests. A shear stress representing 80% of peak strength (in line with the methodology of Petley, 2002) was applied at normal stresses of 75, 125 and 175 kPa (corresponding to shear stresses of 40, 55 and 70 kPa, respectively) using undisturbed samples. The PWP increase rate used was linear at 10 kPa/hr. This replicates the approach of Ng (2007). As such, the reinflation failure envelope can be defined (1) and the till behaviour under the reinflation stress-strain path could be explored (2).

Importantly, cyclic reinflation tests, which represent non-linear pore water pressure reinflation were used. It should be noted that the non-linear reinflation test used an average reinflation rate based on the sinusoidal wave form (Figure 6.11). The sinusoidal wave form is similar to rising groundwater patterns during reactivation (Appendix A: e.g. Period 2, 4, 8, 9). These tests used a normal effective stress of 75 kPa, with a constant shear stress of 40 kPa (80% of peak strength), as the Upgang landslide occurs on a relatively shallow slip surface. Three different reinflation rates were used as average rates of 0.5, 1 and 2 kPa/hr to build a cyclic test program, based upon the field monitoring data (Chapter 5, Table 5.4) in order to cover the low (0.5 kPa/hr), mean (1 kPa/hr) and higher (2 kPa/hr) groundwater rates measured during periods of accelerated movements. However, the highest rates observed during the accelerated movement (> 2 kPa/hr) could not be simulated due to limitations imposed by the travel distance of the BPS apparatus (which has a maximum of 20 mm of shear displacement). As such, the hysteresis relationship between groundwater or PWP and displacement rate was explored and compared at different reinflation rates (3).

Table 6.6 Pore pressure reinflation testing programme used in this study

Sample No.	Test type	PPR rate, kPa/hr	80% Peak strength kPa	Amplitude kPa
W06	Reinflation failure envelope	10	40	-
W07	Reinflation failure envelope	10	55	-
W08	Reinflation failure envelope	10	70	-
W09	Point failure-reinflation at 40 kPa	0.5	40	30
W10	Point failure-reinflation at 40 kPa	1	40	30
W11	Point failure- reinflation at 40 kPa	2	40	30

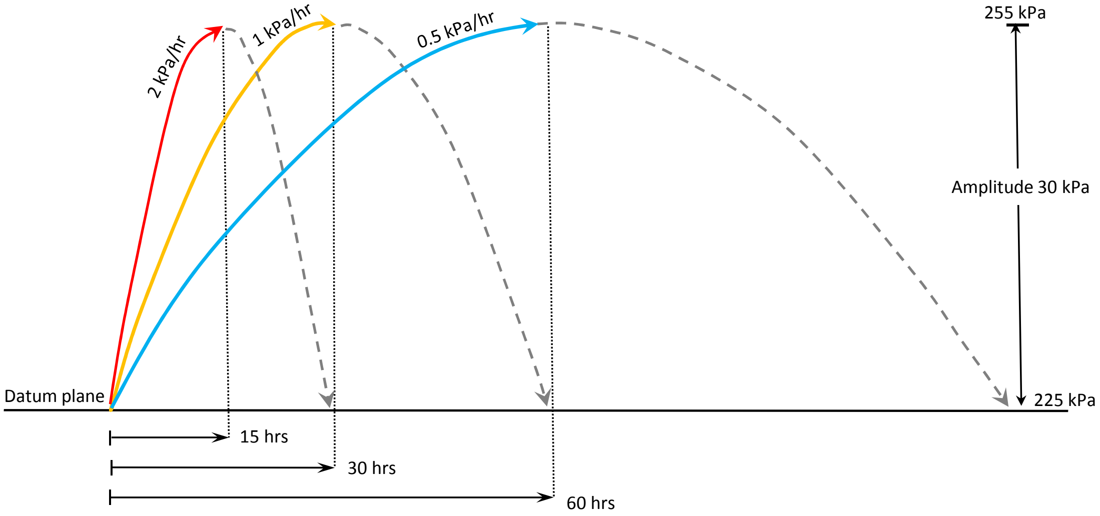

Figure 6.11 The cyclic test diagram showing three different sets of non-linear reinflation tests using the sinusoidal wave form. The average reinflation rates are 0.5 (blue), 1 (gold) and 2(red) kPa/hr. PWP increases very fast at the initial stage and gradually slows down when groundwater is nearly at the peak of the amplitude (30 kPa). The increasing PWP rates of 0.5, 1 and 2 kPa/hr take 60, 30 and 15 hours to reach the peaks, respectively. Thereafter, PWP decreases (dashed lines) back to the same datum (225 kPa)

6.5.1 Drained initial shear (DIS)

The drained initial shear (DIS) stage imposes the appropriate stress state in the samples. As such it does not represent any element of the landslide process. In the PPR tests the samples were brought to a pre-failure stress state below their maximum strength (as determined from the mean failure envelope derived from direct shear tests) (Figure 6.12), consistent with the methodology of Ng (2007).

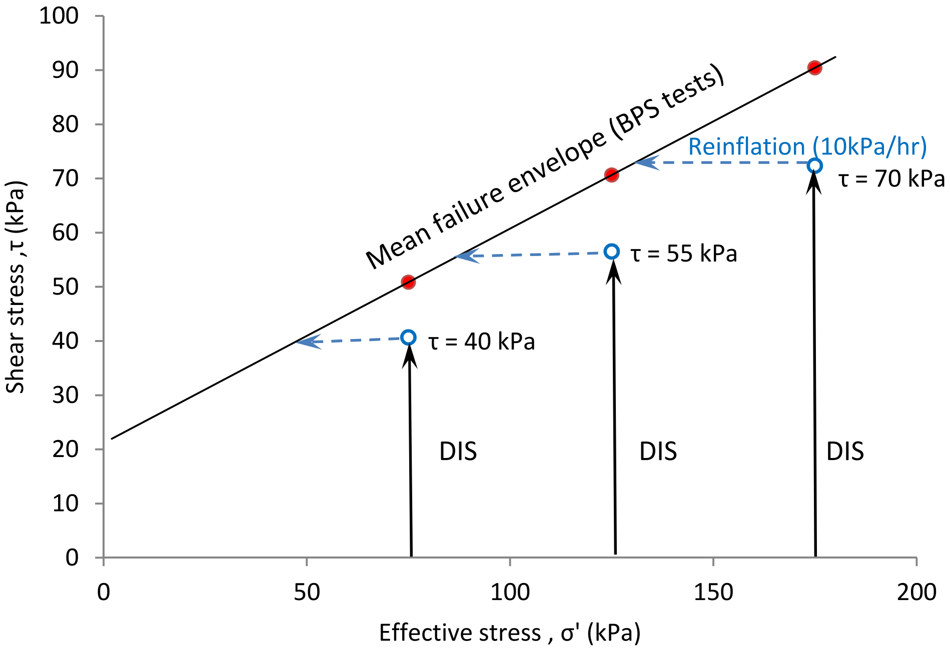

Figure 6.12 Stress paths followed in the PPR test programme, Samples were brought to 80% peak strength at three effective stresses during drained initial shear (DIS), before being sheared by increasing pore pressure. The mean failure envelope was derived from mean of T_{max} (red dots) based on two set of BPS tests (West and East samples)

During the DIS stage, the void ratio decreased as axial displacement increased, similar to the behaviour of the shear stage of direct shear test (Table 6.7). This is probably due to contractive behaviour during the shear stage (Figure 6.13). The axial displacement after the DIS stage increased positively with applied shear stresses to values of 1.08 mm at 75 kPa, 1.32 mm at 125 kPa and 1.92 mm at 175 kPa. Corresponding void ratios were 0.54, 0.52 and 0.47 respectively. The recorded shear displacements varied between 1.37 and 2.85 mm (W06, W09, W10, W11), indicating considerable heterogeneity in the material.

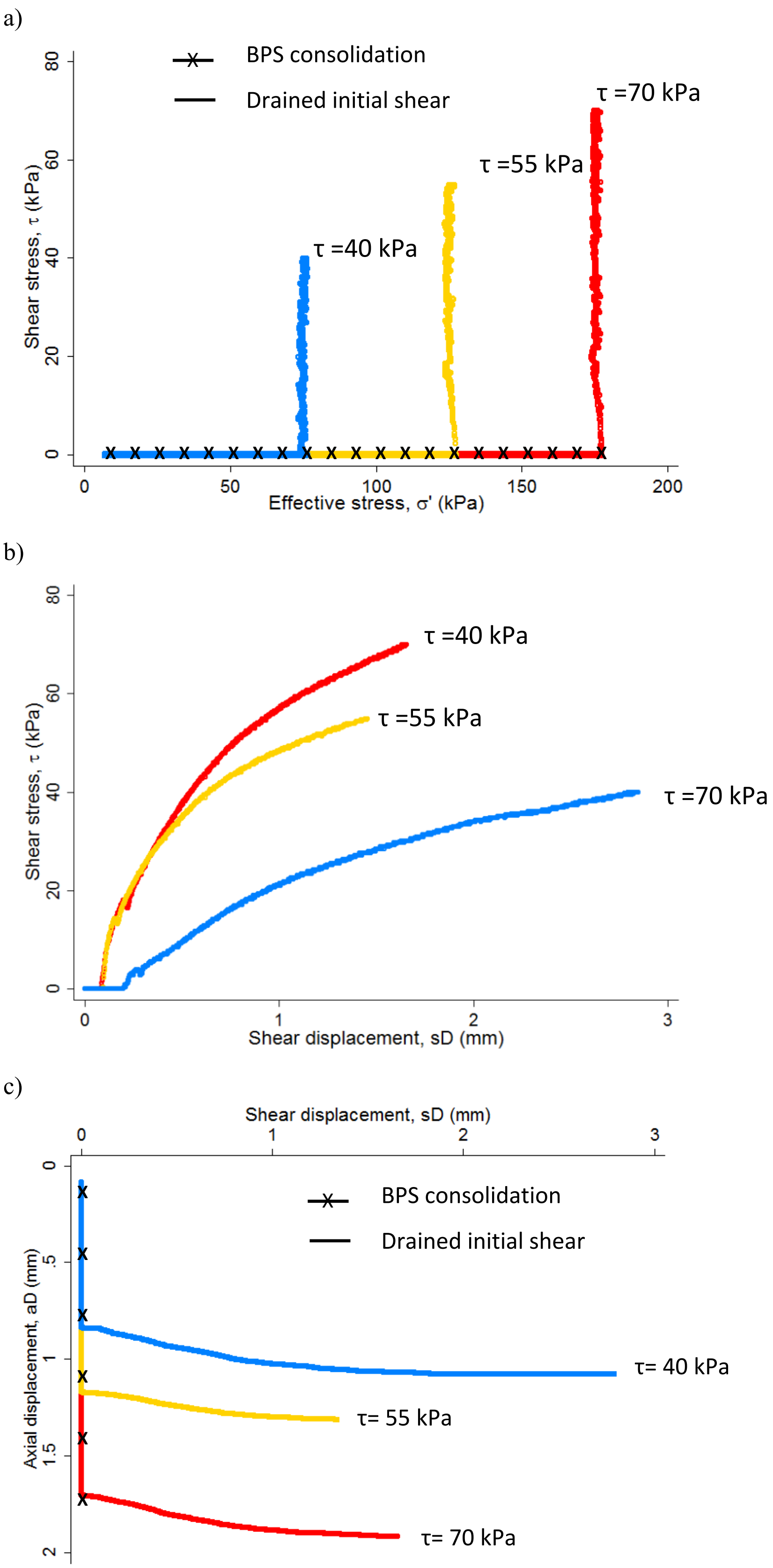

Figure 6.13 Soil behaviour during BPS consolidation and drained initial shear for the PPR tests (PPR rate = 10 mm/hr) at effective stresses 50, 75, 125 and 175 kPa: a) Stress path; b) Plastic stress-strain relationship; c) Axial against shear displacements showing increasing axial displacement when shear stress levels increase.

Table 6.7 Axial displacement, shear displacement and voids ratio after the drained initial shear stage in the PPR tests. The axial displacement increased positively with applied shear stresses corresponding void ratios decrease

PPR rates (kPa/hr)	Sample No.	Drained initial shear pressure (kPa)	After drained initial shear		
			Shear displacement (mm)	Axial displacement (mm)	Void ratio, e
10	W06	40	2.85	1.08	0.54
10	W07	55	1.46	1.32	0.52
10	W08	70	1.66	1.92	0.47
0.5	W09	40	1.92	1.08	0.54
1	W10	40	1.40	1.11	0.54
2	W11	40	1.37	1.03	0.55

6.5.2 Reinflation stress-strain behaviour

The stress-strain soil behaviour during the PPR tests is shown in Figure 6.14. Samples (W06, W07, W08) showed a stiff stress-strain behaviour at small shear displacement (sD ≤ 3 mm) during the initial drained shear, similar to the BPS tests. However, during the subsequent reinflation, the shear stress remained constant under control of the actuators. Late in the test the samples showed a phase of weakening. This is an artefact of the testing methodology in which the machine, which was optimised for precision rather than high displacement rates, could not generate sufficiently high movement rates to maintain the shear stress as the sample drastically weakened.

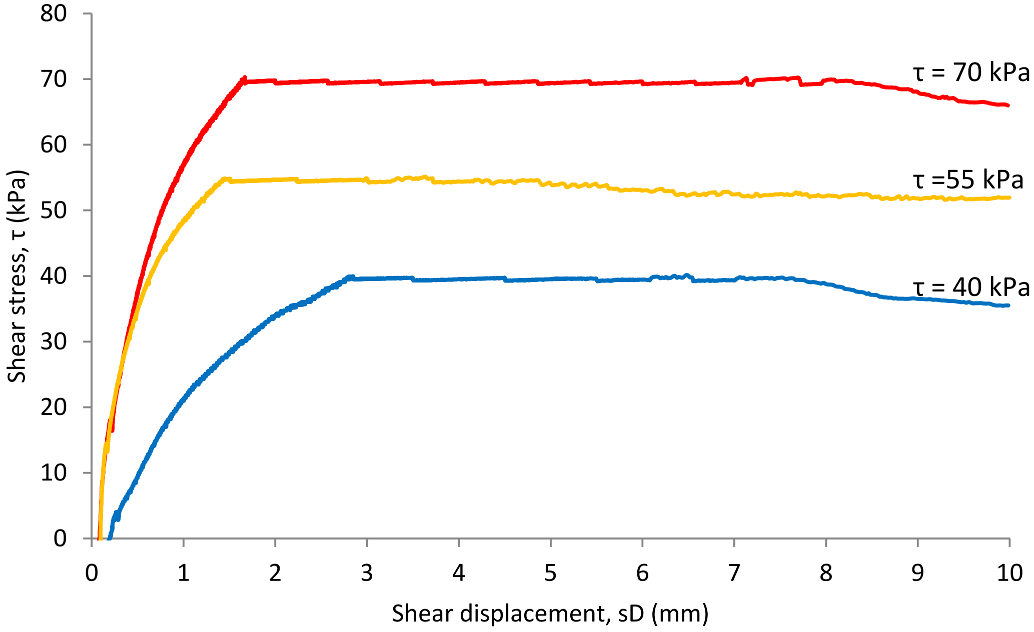

Figure 6.14 Shear stress against shear displacement showing soil behaviour during the 10 kPa/hr PPR tests at effective stresses of 75, 125 and 175 kPa and shear stresses of 40 (W06), 55 (W07) and 70 (W08) kPa respectively.

During the DIS stage, samples displayed contractive behaviour. Conversely, dilation of the samples was noted during the reinflation processes, as indicated by the decreasing axial displacement (Figure 6.15). This dilation is inevitable as the test is being conducted by driving water into the sample, pushing the grains apart. During the initial stages of reinflation, the dilation was significant, and was associated with a gradual development of increase shear displacement. The largest decrease of axial displacement was generated at the lowest shear stress level (i.e τ= 40 kPa), which may relate to the higher void ratio after the lower DIS phase (Table 6.7), which facilitated greater deformation by the subsequent reinflation.

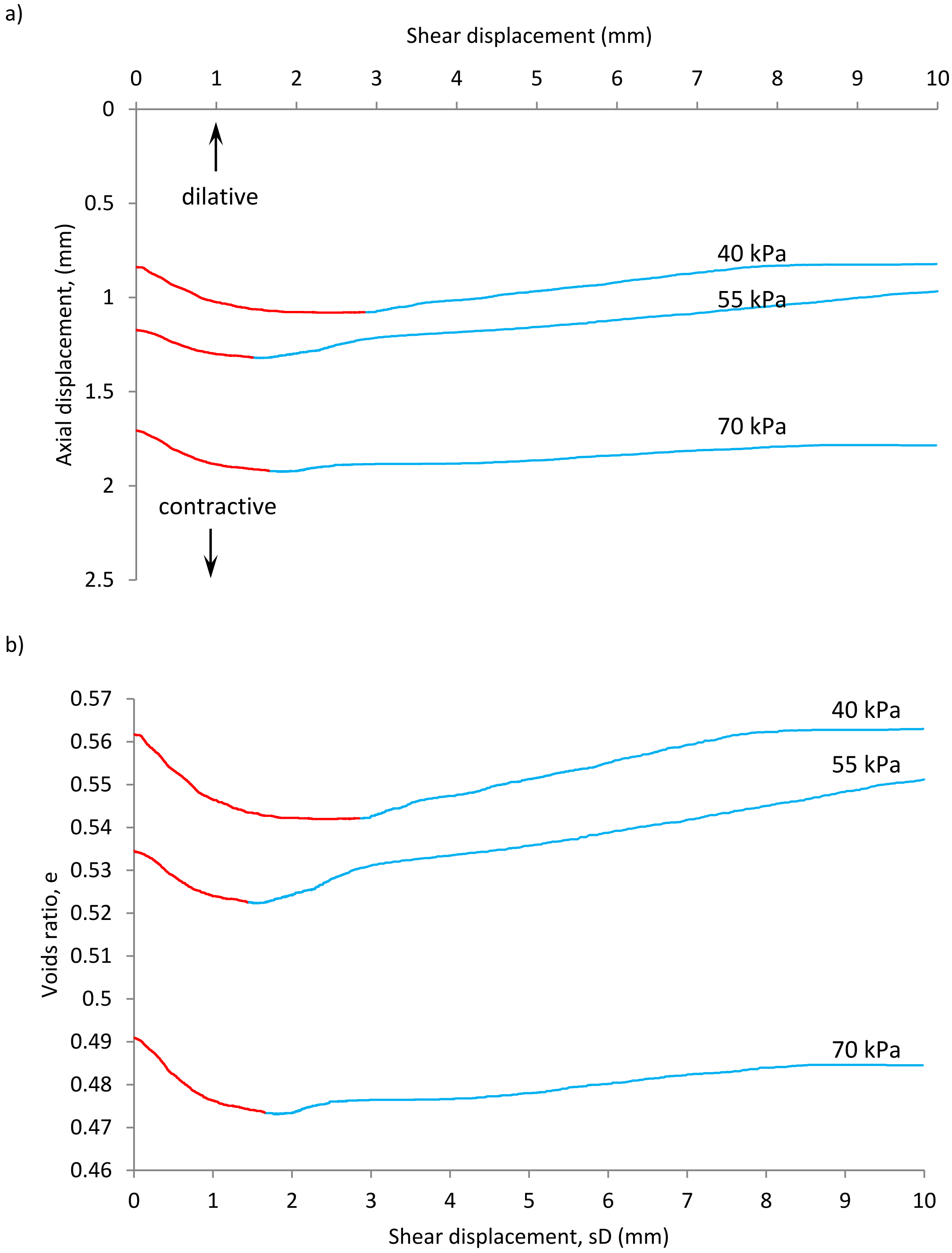

Figure 6.15 Contractive and dilative behaviour during the DIS and reinflation stages at the constant shear stresses of 40, 55 and 70 kPa: a) axial displacement against shear displacement: b) Voids ratio against shear displacements. The red lines represent the DIS stage and blue lines represent the reinflation stage. Voids ratio increase from 0.54 to 0.56 at a constant shear stress of 40 kPa; from 0.52 to 0.55 at a constant shear stress of 55 kPa and from 0.47 to 0.48 at a constant shear stress of 70 kPa.

6.5.3 Strain development prior to failure

As discussed in section 6.5.2, samples behaved from contractive to dilative at failure due to increasing pore water pressure. This can be explained by the strain development during the reinflation process in terms of effective cohesion and effective frictional angle. These strength parameters are derived from the strain rate contours (Table 6.8). Strain rates of 0.1, 0.2, 0.3, 0.4, 0.5, 0.6, 0.7 and 0.8 microstrains per hour (µs/hr) were recorded and the respective strain rate contours were determined (Figure 6.16). The contours were spread until strain rate reached 0.8 µs/hr. The closely-spaced contour was observed at the lower shear stresses. This implied that, given the sample depth (σ'), slopes with a lower angle (lower shear stress) would sustain a high pore water pressure. Moreover, the acceleration towards final failure would be more sudden (Figure 6.16).

During the initial reinflation phase, the axial strains increased with a decrease in the void ratio (Figure 6.15). In other words, the cohesion gradually increased with small horizontal displacements as contractive behaviour. However, it dropped sharply at shear strain rate of 0.2 µs/hr to relatively constant values at the larger strains (c' drop from 18.26 to 15.48 kPa) due to the higher void ratio. At the same time, the development of frictional strength initially increased rapidly but then dropped markedly, as the soil particles were resisting against the shear force condition. The maximum frictional angel is 28.72° at a strain rate of 0.5 µs/hr. This can be seen clearly in Figure 6.17.

Table 6. 8 Strain development in terms of failure parameters (c' and ϕ') on West samples (W02, W03, 04, W05).

Strain rate (µm/hr)	Shear stress,T			Effective stress,σ'			Effective cohesion,c' (kPa)	Effective friction angle,ϕ'	Correlation coefficient, R²
	75kpa	125kpa	175kpa	75kpa	125kpa	175kpa			
0.1	39.15	54.62	69.43	51.80	76.60	116.08	16.74	24.81	0.97
0.2	39.45	54.53	69.46	48.57	74.54	112.93	18.26	24.72	0.99
0.3	39.32	54.36	69.42	44.94	72.39	106.29	17.03	26.05	1.00
0.4	39.72	54.38	69.38	45.96	71.66	102.54	16.12	27.60	1.00
0.5	39.02	54.85	69.84	44.12	74.49	102.18	15.52	28.72	0.99
0.6	36.69	53.03	68.85	41.45	67.84	99.94	14.64	28.61	0.99
0.7	36.55	52.84	68.43	41.80	67.35	99.91	14.60	28.04	0.99
0.8	35.99	51.78	66.45	41.02	63.96	97.43	15.48	28.54	0.99

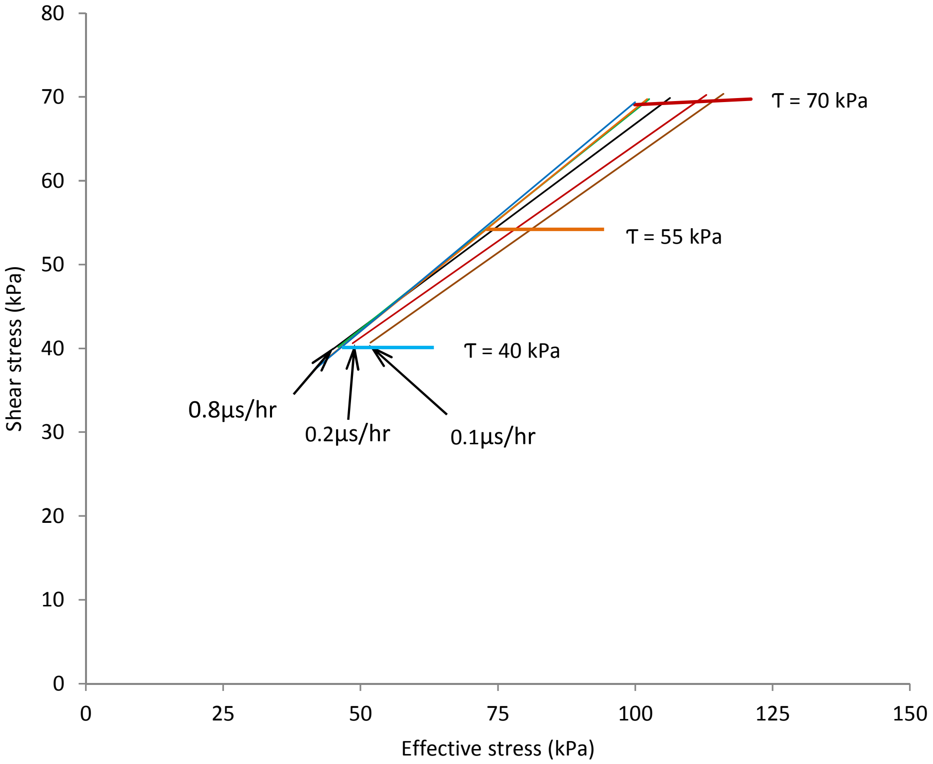

Figure 6.16 Strain development expressed in strain rate contour following the 10 kPa/hr average PPR tests at 40, 55 and 75 kPa. The acceleration appeared the most abrupt at lower shear stress levels, as shown by the closely-spaced contours at strain rates of 0.3-0.8 μs/hr.

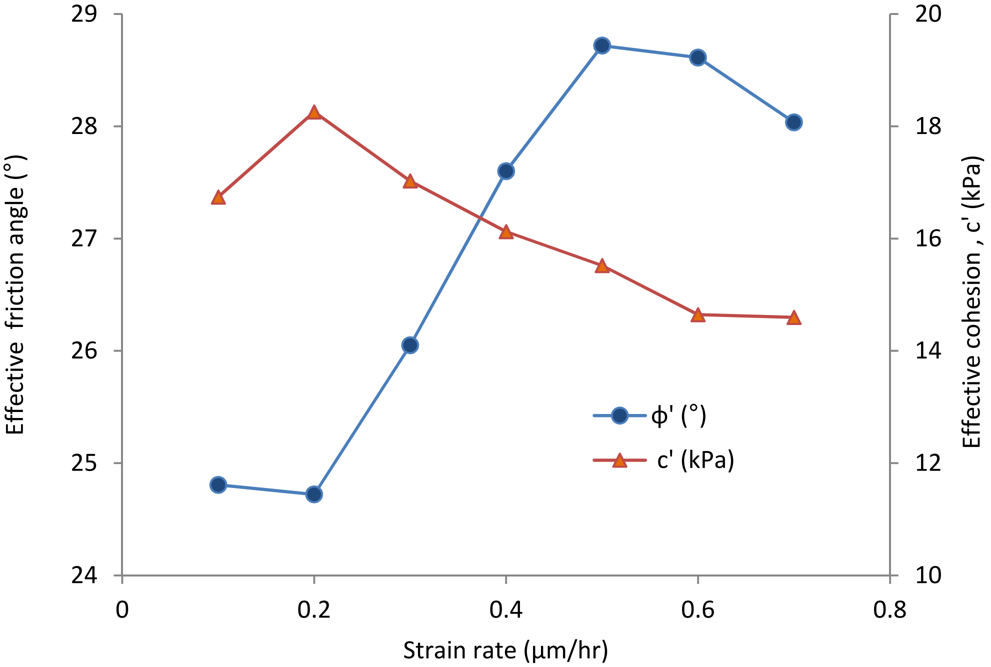

Figure 6.17 Strain development during PPR tests in terms of effective cohesion and frictional angle. The effective cohesion dropped sharply at a shear strain rate of 0.2 μs/hr (approximately c’= 18.26) to relatively constant values at the larger strains (c’ = 15.48 kPa). Meanwhile, the frictional angle increased dramatically with a maximum of ø’ = 28.72 and then dropped towards the end of failure.

6.5.4 The PPR failure envelope

The failure envelope is typically derived from the maximum shear stress value. However, this approach does not apply to the stress-controlled reinflation tests, as shear stress is constant. Ng (2007) suggested that an appropriate failure criterion for PPR tests should be based upon a critical strain rate (Table 6.8 and Figure 6.16). In this research, the failure envelope appeared to be more approximately defined during the strain rate at 0.5 µs/hr where the peak effective frictional angle has been reached (ϕ' = 28.72°) while the effective cohesion is dropping (c' = 15.52 kPa) (Figure 6.18). It should be noted that the frictional angle is higher than those determined from the BPS tests, which are 20.8° (East samples) and 21.6° (West sample). Moreover, due to the increasing PWP that causes greater separation of clay particles, the effective cohesion is lower than those determined from the BPS tests (21.57 and 23.09 kPa). The implications of these results will be discussed in Chapter 7.

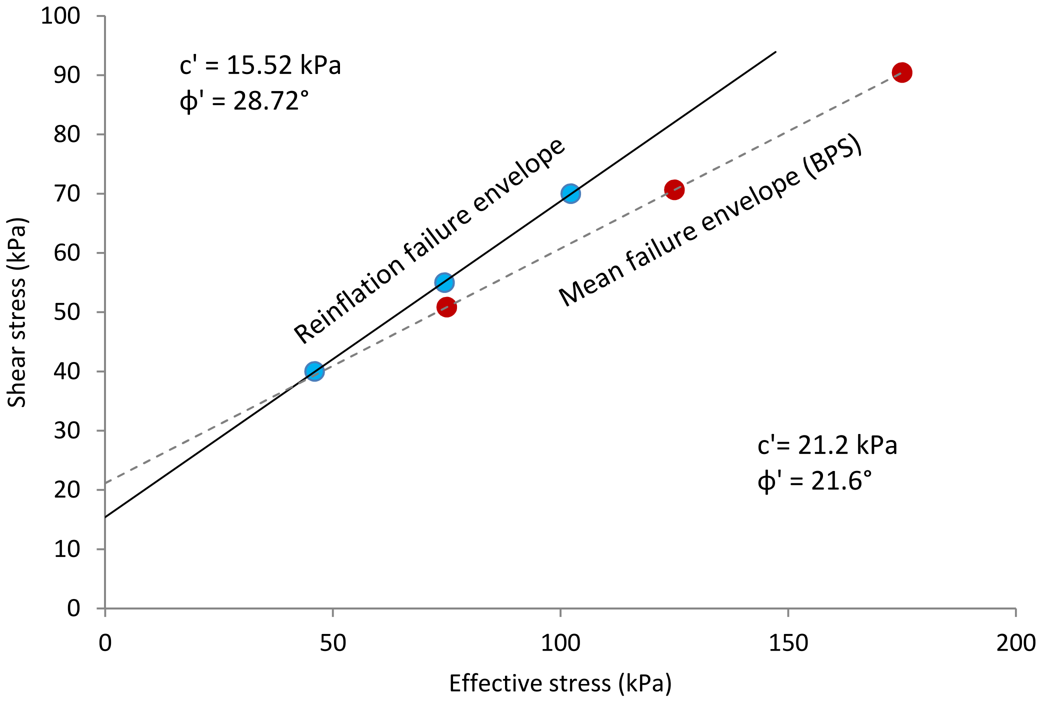

Figure 6.18 Reinflation failure envelopes defined by the stress conditions at the strain rate of 0.4 µs/hr derived from three PPR tests at shear stresses of 40, 55 and 70 kPa (blue dots). The corresponding strength paramenters are ϕ' = 28.72° and c' = 15.52 kPa. For comparison the mean failure envelope (BPS) derived from mean of T_{max} (red dots) based on two set of BPS tests is shown. The frictional angle is higher than the BPS frictional angle (21.6°), whilst the cohesion is lower (21.2 kPa)

6.5.6 A linear rate of pore water pressure increase (10 kPa/hr)

This section examines soil behaviour under the linear PPR tests. Plots of displacement rate against time revealed a behaviour separated into three phases – transient (primary), steady-state (secondary) and accelerating (tertiary) movement (Figure 6.19). Initially, displacements increased at a decreasing displacement rate after the target stresses were reached after approximately 1000 (τ = 40 kPa), 4,000 (τ = 55 kPa) and 12,000 (τ = 70 kPa) seconds (i.e. primary movement). The transition from primary movement to secondary movement appeared to occur thereafter during short periods - between 1,000 - 2,000 (τ = 40 kPa); 4,000 - 10,000 (τ = 55 kPa); 12,000 – 16,000 (τ = 70 kPa) seconds, when the displacement rate began to increase at a relatively constant rate. However, displacement rates vary significantly, probably indicating changes in the local structure of the sample. It should be noted that Varnes (1982) suggested that secondary creep results from concurrent processes of primary and tertiary creep. Finally, during the tertiary stage, the displacement rates accelerate with time, and lead to failure. For samples at a higher normal effective stress, higher acceleration rates were noted and the failure occurred at a later point.

The acceleration to failure has been explored by plotting the inverse displacement rate (Δ) against normal effective stress and against time – a so-called Saito analysis. These plots show non-linear trends in landslide movement (Figure 6.20). At the initial reinflation process, deceleration was found with a slight decrease of effective stress. This can clearly be seen at the lower shear stress 40 kPa, at which effective stress decreased from 75 kPa to about 50 kPa. However, the acceleration trend thereafter was observed to tend towards a steady state. Plastic deformation occurs, as indicated by the asymptotic trends in the Saito analysis (Petley et al., 2002).

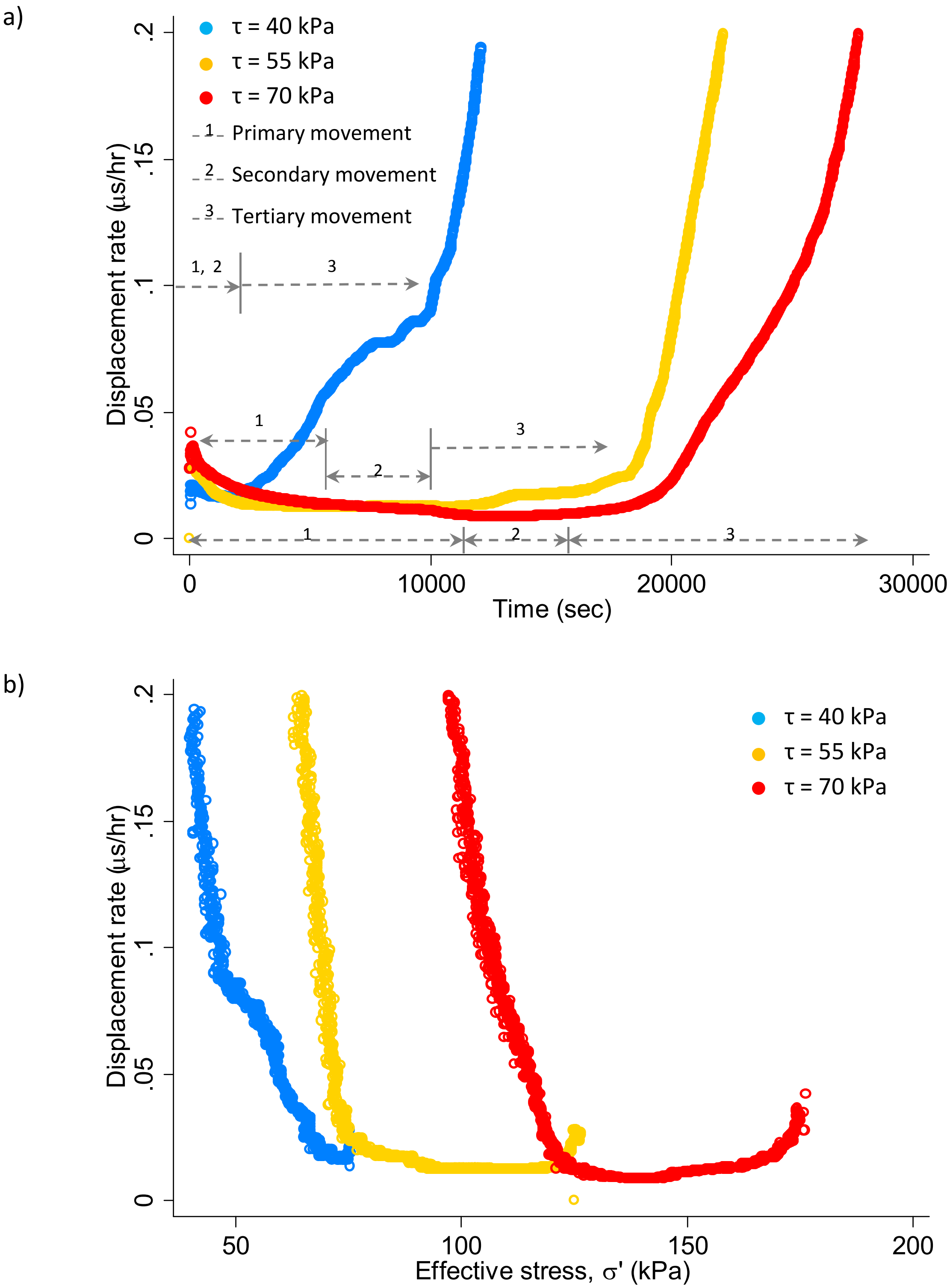

Figure 6.19 Plots of displacement rate against time (a) and plots of displacement rate against effective stress (b) at the reinflation rate of 10 kPa/hr with constant shear stresses of 40, 55 and 70 kPa. The plastic deformation illustrated the asymptotic trend, indicating three phases of movement, namely transient (1), steady-state (2) and accelerating (3) movement phases. Note: the dashed lines represent movement phases.

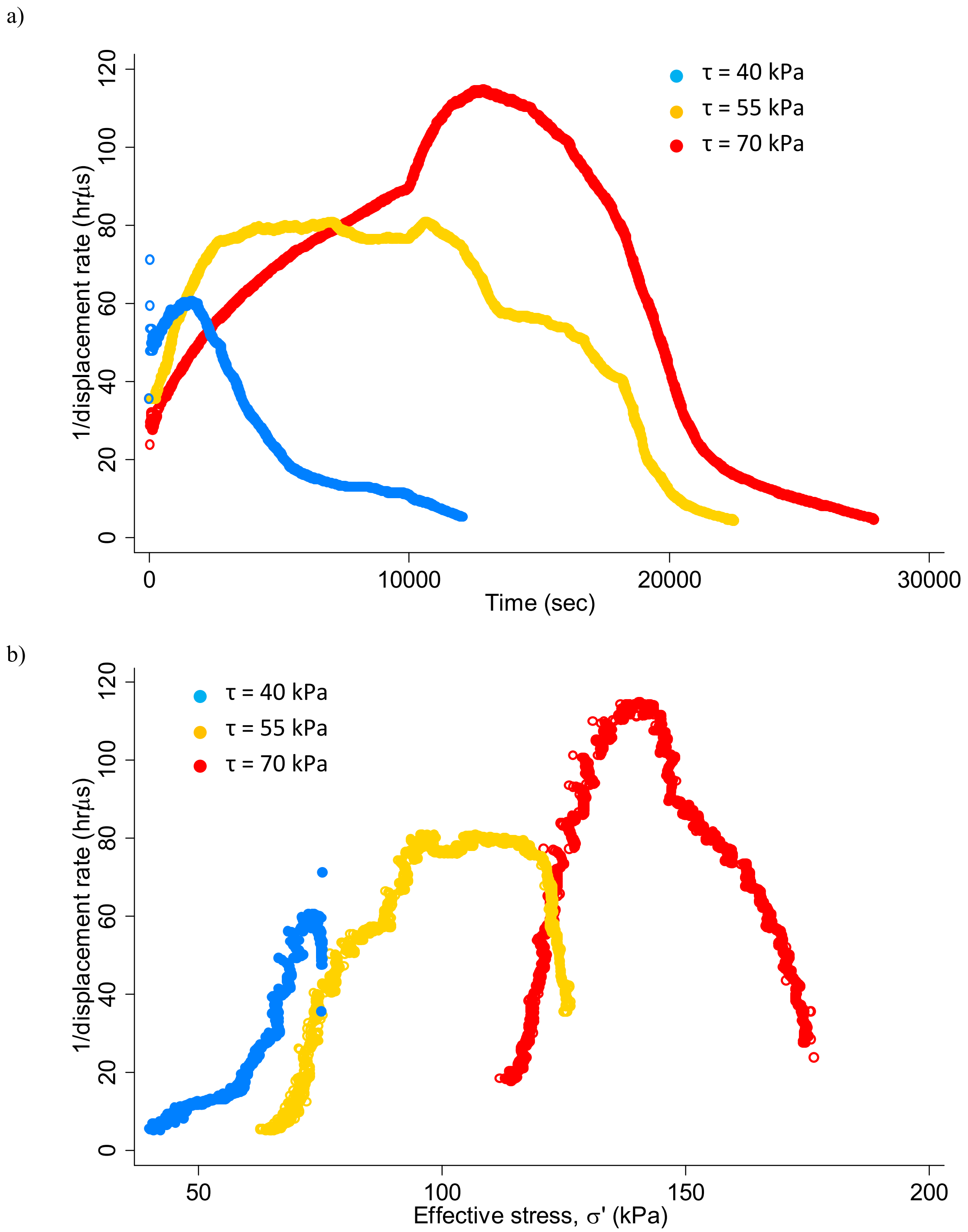

Figure 6.20 Plastic deformation behaviour at the linear reinflation rate of 10 kPa/hr with constant shear stress of 40, 55 and 70 kPa: a) plots of Δ-*t* and b) Δ-σ’ are illustrated by the asymptotic trend.

6.5.7 Non-linearity of pore water pressure increase

This section compares soil behaviour during PPR tests at different PPR rates (Figures 6.21 - 6.24). In each case, at the start of the PPR phase the observed displacement rate decreased, followed by increasing displacement rate. At the initial phase of reinflation, the displacement rate decreased due to the increase of pore fluid getting to the sample rather than shear deformation. This happened in a short period when effective stress decreased from 75 kPa to about 65 kPa, irrespective of the different reinflation rates applied. As effective stress decreases in all three samples, the rate of displacement peaked and then declined, although at a different point in each case (48 kPa for the 0.5 kPa/hr sample; 52 kPa for the 1kPa/hr sample; and 51 kPa for the 2 kPa/hr sample).

Plastic deformation of glacial till samples at different reinflation rates was explored by plotting the inverse displacement rates (Δ) against normal effective stresses or against time (*t*) (Figures 6.23 and 6.24). These plots show similar trends of deceleration and acceleration movements, which are responding to the increase of PWP. The accelerating behaviour of the samples showed asymptotic trends, indicating plastic deformation (Petley et al., 2005a). Overall it is clear that there is a complex relationship between pore water pressure and displacement rate. The decrease of displacement rate can be explained by two components, which is a rate dependent on the stress state plus a rate dependent on the rate of change of normal effective stress. The latter component is declining due to the decreasing rate of the PPR (Figure 6.11), thus giving an overall reducing rate of displacement.

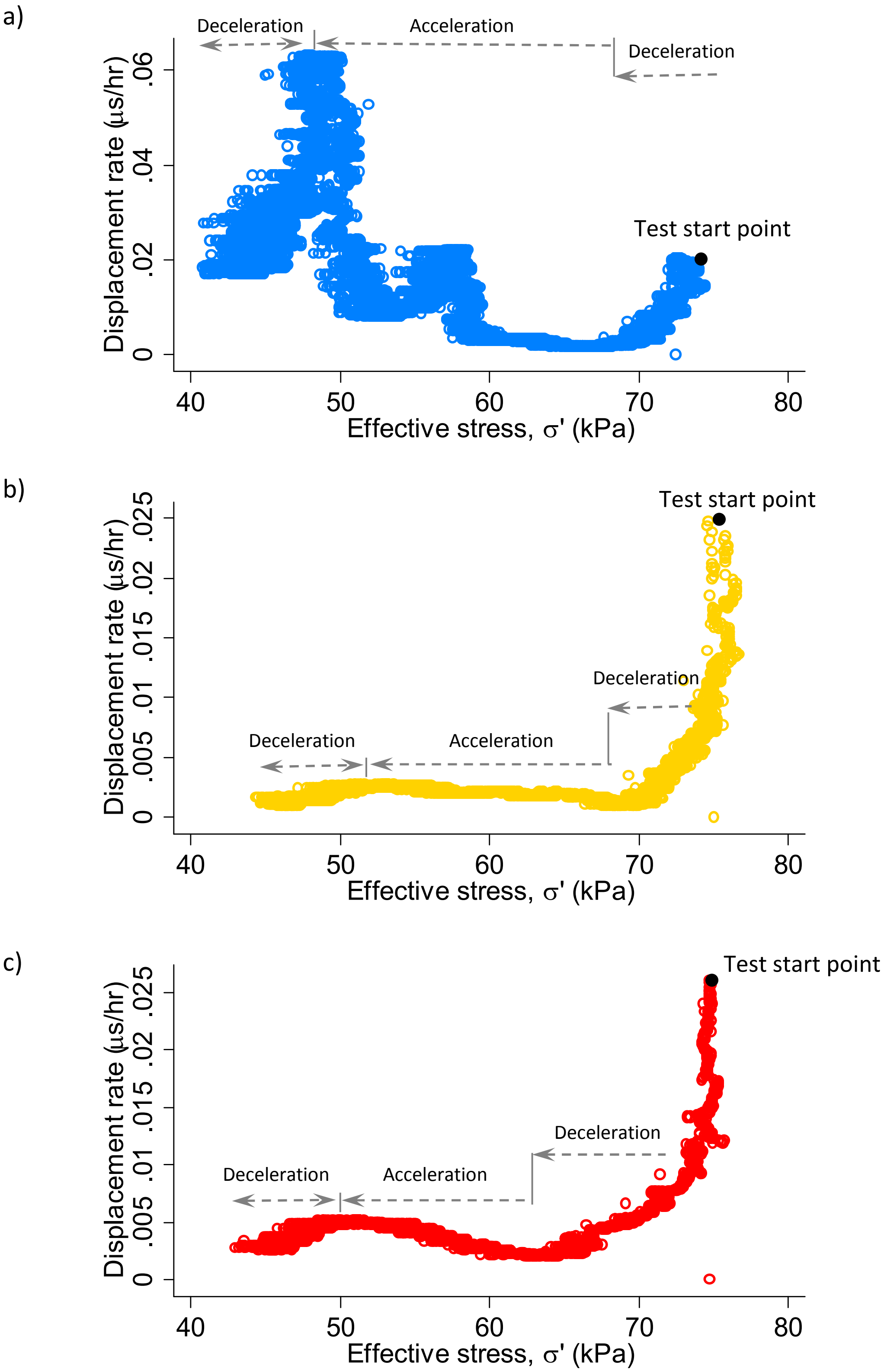

Figure 6.21 Plots of displacement rate against effective stress under a pore water pressure increment of 0.5 (a), 1(b), and 2(c) kPa/hr. Decelerations are found at the initial stage of increasing PWP, followed by accelerations. However, the movements show deceleration towards the end of the reinflation stage even though PWP is still increasing. Thereafter, a phase of acceleration was found at effective stresses of less than 60 kPa at the reinflation rate of 0.5 kPa; at effective stresses of less than 68 kPa at the reinflation rate of 1 kPa and at effective stresses of less than 65 kPa at the reinflation rate of 2 kPa.

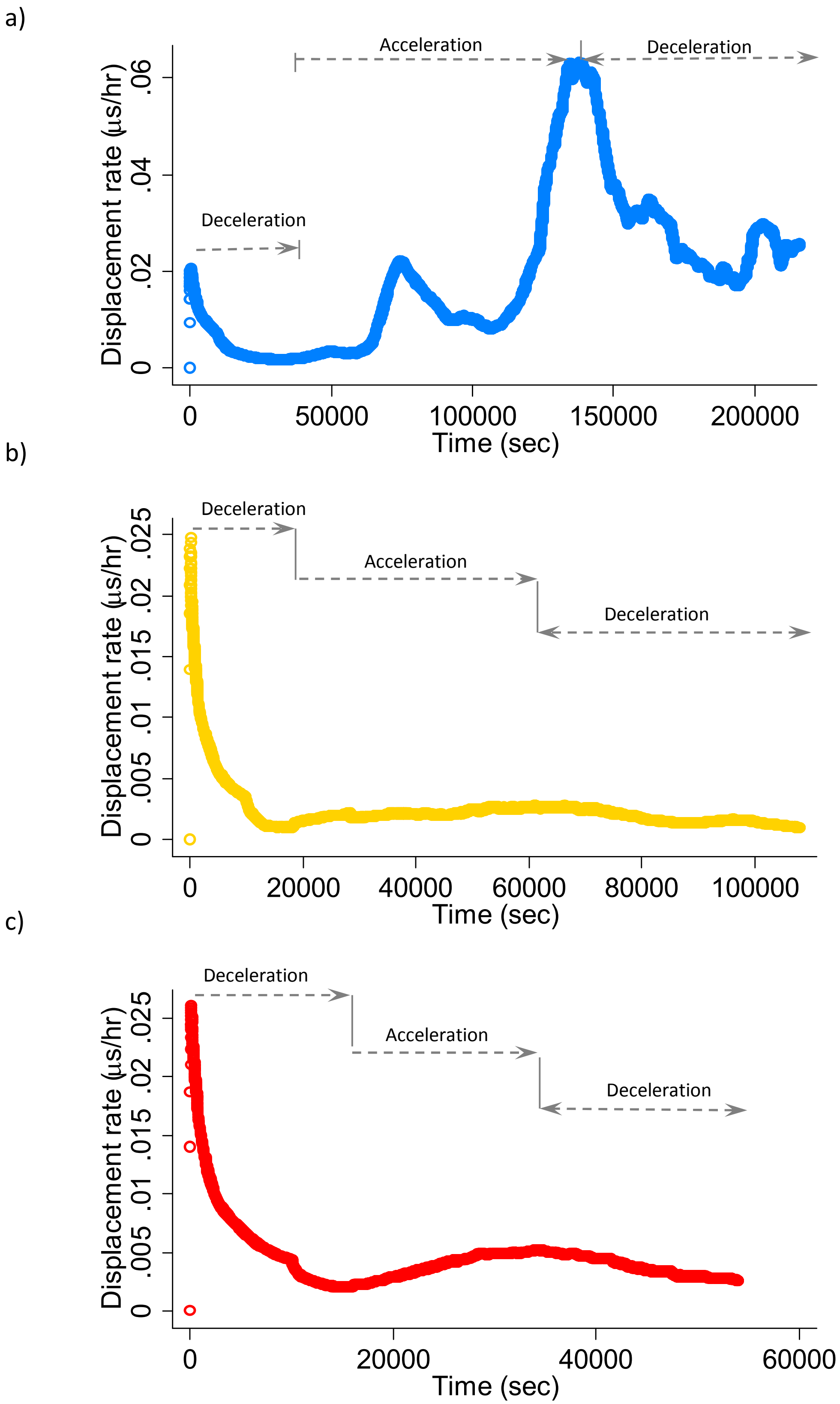

Figure 6.22 Plots of displacement rate over time under reinflation rates of 0.5 (a), 1(b), and 2(c) kPa / hr. Decelerations are found at the initial stage of increasing PWP, followed by accelerations. However, the movements show deceleration toward the end of the reinflation stage.

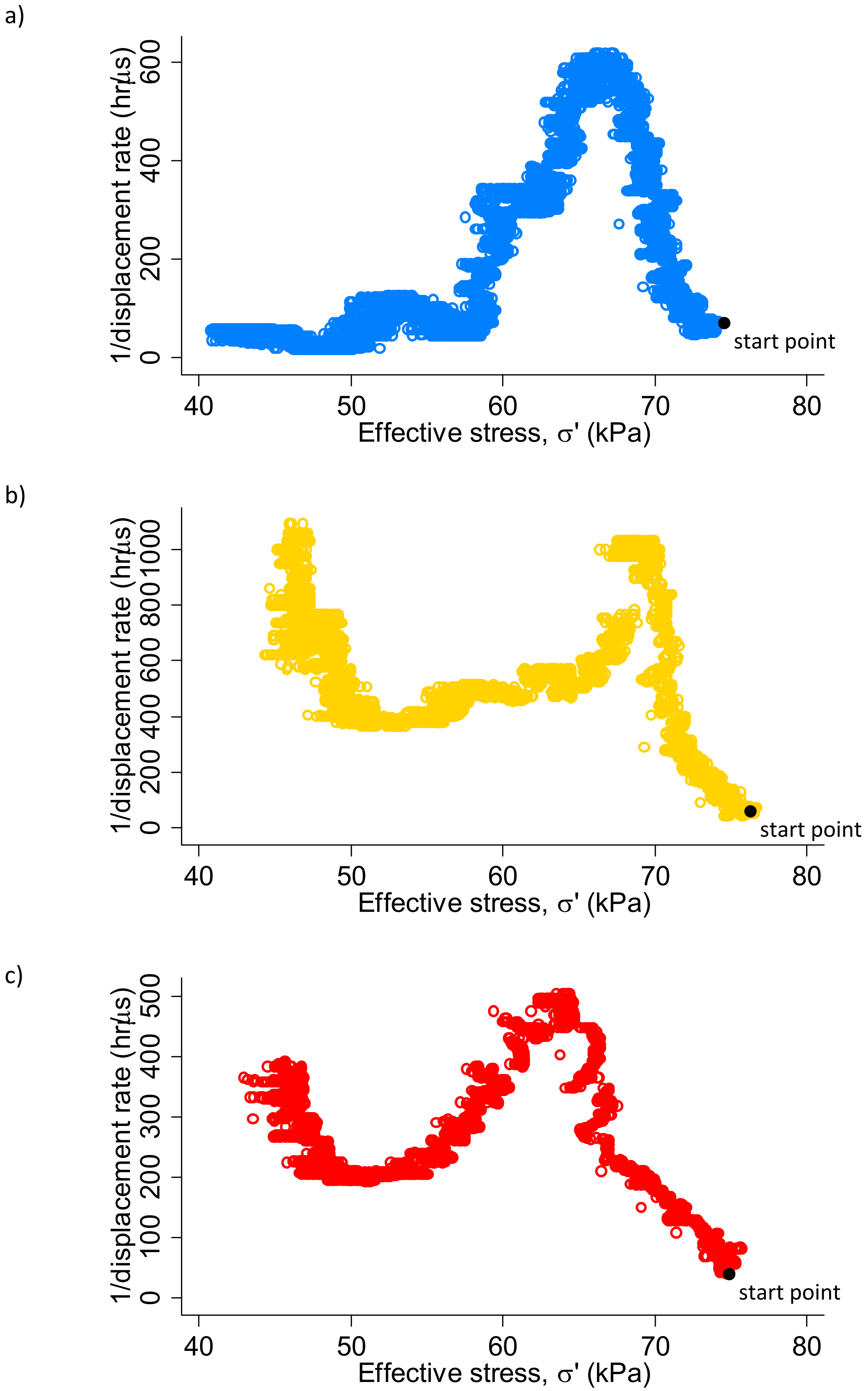

Figure 6.23 Plots of Δ-σ' under PPR rates of 0.5 (a), 1(b) and 2(c) kPa/hr showing the complex behaviour of deceleration and acceleration movements during increasing PWP. Higher reinflation rates are related to highly rapid accelerations.

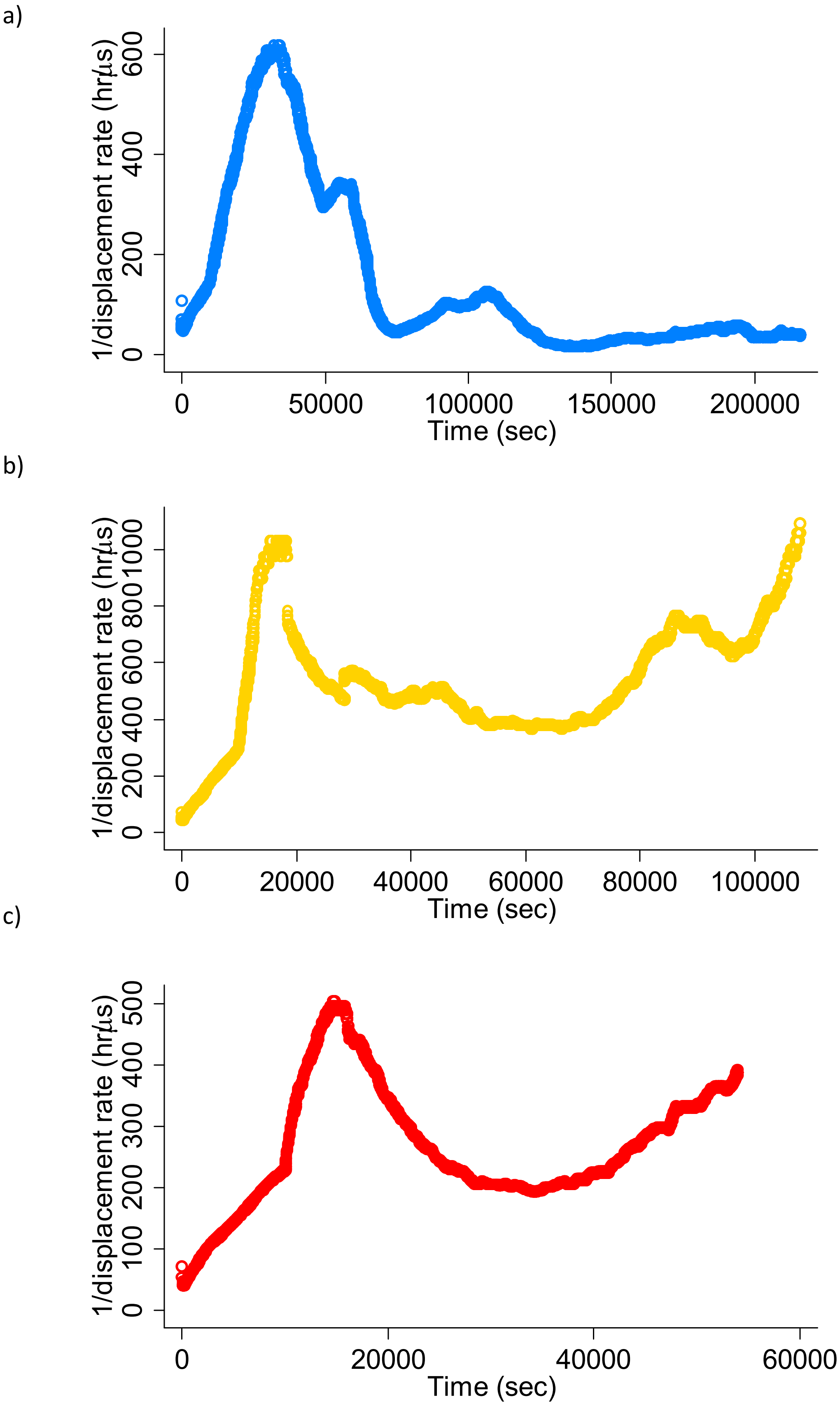

Figure 6.24 Plots of Δ-*t* under pore water pressure increment of 0.5 (a), 1(b) and 2(c) kPa/hr showing deceleration at the initial stage, followed by acceleration toward the failure before deceleration.

6.6 Chapter summary

The material properties of two sets of samples collected from the study site can be characterised as ‘Fine-Silt’, with less than 10% of particles larger than 2 mm. They are largely composed of silt (typically 71-75%), with about 21-29% clay and less than 10% sand. According to the Atterberg limits, the soil samples can be classified as ‘Inorganic clays’ of medium-high plasticity (CI-CH). The plastic limit of the till samples ranged between 25% and 28% with liquid limits ranging between 48% and 60%. These samples show an inorganic nature by having a low organic content (4-7% loss on ignition).

The soil strength parameters mobilised during the BPS and PPR tests, in terms of the effective frictional angle ('ϕ) and cohesion (c’) were determined by the Mohr circles constructed at different shearing displacements (0-10 mm). As strains developed towards failure, the sample showed a rapid mobilisation of friction followed by a gradual decrease. However, a key difference between the strain-controlled compression (BPS) and the stress-controlled reinflation (PPR) tests was found in the development of cohesion. The BPS process generated an increase in cohesion under compression, followed by stabilisation, whereas in the PPR tests, cohesion increased initially and decreased throughout the test.

- **For the strain-controlled BPS tests**, the failure envelope was defined for the plastic samples where the highest effective frictional angle and cohesion were mobilised with reference to the strain development. The mobilised effective frictional angle ('ϕ) and cohesion (c’) were 21.6°, 23.1 kPa (For the West samples) and 20.8°, 21.6 kPa (for the East samples)

- **For the stress-controlled PPR tests**, the criterion of maximum shear stress could not apply. The maximum effective frictional angle and cohesion were found at a strain rate of 0.5 µs/hr. The mobilised effective frictional angle 'ϕ and cohesion were 28.72°, 15.52 kPa, respectively.

Chapter 7 Discussion

7.1 Introduction

This chapter combines the results of the field monitoring and the laboratory tests. The results are used to evaluate the behaviour of the landslide complex, and in particular to consider the mechanisms of movement currently operating. In so doing, the patterns of landslide movement and the nature of the relationship between the displacement rate and groundwater are examined. The TLS data has revealed the overall pattern of movement across the slope, to reveal the deformation effects brought about by rainfall, changing groundwater levels and marine action. Furthermore, the TLS helped to locate and identify areas for more detailed field monitoring, which has in turn allowed analyses of slow (i.e. post-failure creep) and accelerated movements (i.e. reactivation). Whilst the 'where' and 'how' of these landslides have been addressed by the TLS and field monitoring, the 'why' has been investigated through laboratory testing. In particular, results from the laboratory tests reveal why the glacial till reacts to seasonal changes in groundwater levels in terms of the dilative and shear strength properties of the material.

7.2 Landslide morphology arising from cliff face erosion

In this study, landslide activity has been observed to be distributed across the cliff face, and to occur as a result of a triggering factor (i.e. rainfall) and toe erosion caused by marine activity. This study has been extremely fortunate in that the unusually wet period in 2011/2012 led to a large number of landslide movement events. The morphology of the landslide includes rotational/translational slides (zone A), mudslides/mudflows (zone B), blockfalls (zone C), topples and gullies (zone D) (Figure 7.1). The observed distribution and complexity of change across the whole cliff face suggests that environmental conditions, marine erosion, rainfall and material properties dictate the nature of landsliding.

The cliffs at Upgang have a very complex morphology that has developed as a result of mass wasting processes. This complex topography is likely to result in a highly complex groundwater system. Therefore, the role of groundwater in controlling the mass movements will differ greatly, for example showing considerable variation between the upper or lower sections of the cliff. Importantly, the type of materials from which the slope is composed has a significant impact on the variation in failure mechanism. For instance, the upper section of the cliff, which is made up of the Hessle till (weathered till), has been shown to be especially susceptible to shallow landslides. The section of weathered till in zone A (see Figure 4.2-4.5: Landslide B3) shows shallow rotational landslides, which are less than 3 m in depth. These landslides were triggered by rainfall and were very sensitive to seasonal changes. The mudslides were often reactivated due to high groundwater levels developed along pre-existing shear surfaces.

Similar variations in failure type are evident throughout cliff sections composed of Withernsea till (middle part of the cliff). Here, in Zone B, mudslides/flows occurred predominantly and moved downslope to the toe of the cliff. Such movements explain the loss and gain of materials along the same flow path as can be seen from the negative (loss) and positive (gain) changes in the rasterised TLS images.

The sand and gravel bed at Zone C is a result of block falls and superficial earthflows (sand or mud flows), which were triggered by rainfall. This zone shows a great loss of material at the middle part of the cliff as a result of block fall. Block falls, ranging from small (0.1 m) to large (> 2 m) sizes, generally occur in the sand and gravel rich layers.

Lastly, the Skipsea till, the lower glacial till is at the base of the cliff. Rain-induced earthflows from zones above were observed to be contributing to the accretion. However the material was lodged in this position temporarily before being washed away by the rising tide. Gullies were also observed along the cliff toe as a result of erosion by groundwater. This suggests that erosion at the toe could be attributed to marine processes, which led to failures such as fall, and topple. Therefore, material dynamics at this zone are controlled by both rainfall and marine activities.

a) Pattern of surface change and landslide failures

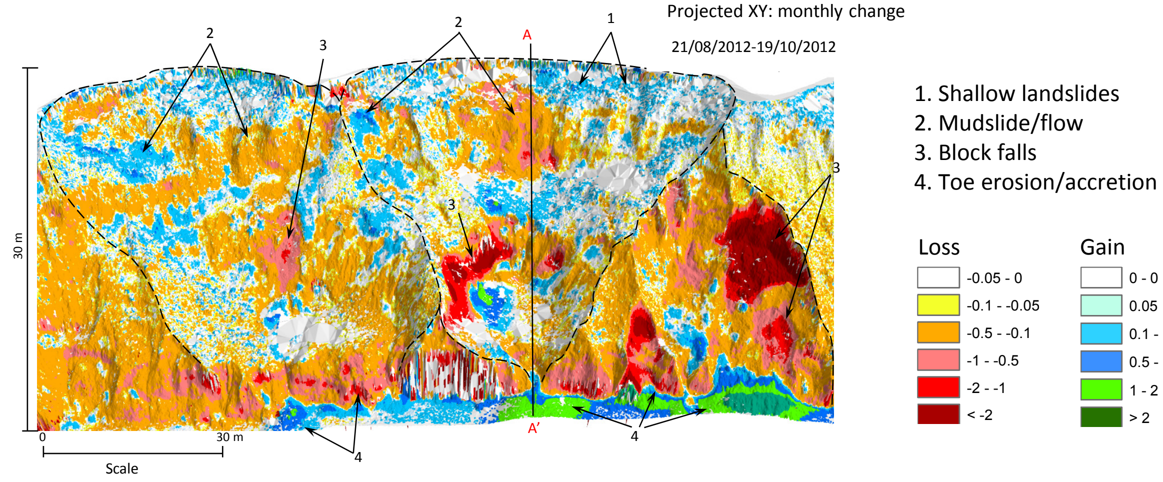

b) Cross section A-A’

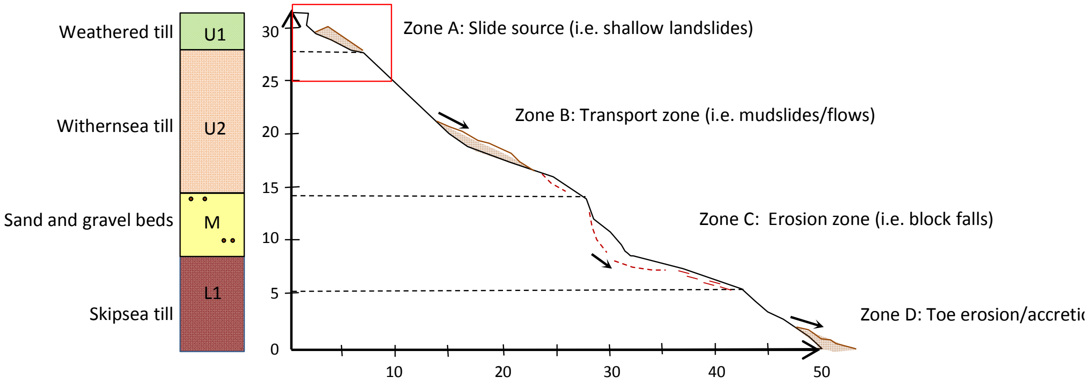

c) Reactivation zone

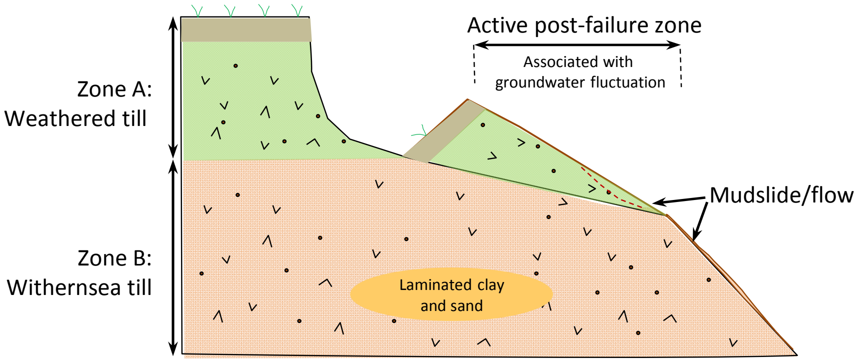

Figure 7.1 Cross section of A-A’ of landslide B3 based on terrestrial laser scanner data presents landslide morphology arising from coastal erosion. a) Pattern of landslide geometries and failure mechanism is here presented by the monthly changes between 21st August and 19th October 2012. b) Cross section A-A’ showing high activities of landslide movement from upper to lower parts of the cliff with a variety of landslide types such as mud slides, mud flows, block fall and toe erosion. (c) Reactivation zone is associated with high groundwater fluctuations leading to reactivate shallow landslides at the Upper section of the cliff.

The observed behavior of these coastal landslides are similar to those observed in a study of landslides in till on the Holderness coast, Yorkshire (Quinn, 2009), where the cliff is entirely composed of glacial clays deposited during the Devensian Glaciation (i.e. Hessle, Withernsea, Skipsea and Basement). Quinn (2009) suggested that the slides, which occur along lithostratigraphic boundaries as a result of variations in strength or permeability, are made possible by the removal of previously failed material by rain, waves or tides, but which are triggered by rainfall events. In this study, different failure mechanisms occurred in a variety of lithologies. Also, a significant level of landslide failures occurred as a result of the reworking of failed material and the continued removal of fresh material from the cliff. Therefore, there are temporal linkages between failure events along the cliff face (Table 7.1).

Table 7. 1 Summary of landslide processes based on the rasterised image

Site section	Landslide zone	Underlying material	Landslide processes
Upper	Zone A	Weathered till (U1)	Slide source: basal erosion and episodic failures in wet periods bring the slope to a threshold state for mudslide/mudflow
	Zone B	Withernsea till (U2)	Slide source and transportation zone- continuing mudslide/flow on stepped slopes can generate a fresh slide and also transport the landslide material downslope
Middle	Zone C	Sand and gravel beds (M)	Erosion zone - steep slope failures when undercutting and climate permit, a variety of block falls (up to 10 m diameter)
Lower	Zone D	Skipsea till (L1)	Toe erosion/accretion zone caused by both rising sea level and rainfall. The zone is covered by layers of mobilised landslide material through the cliff toe during wet periods and is subsequently washed away by wave action

Two key limitations of the use of TLS in this study are:

- The TLS data is restricted to changes >0.05 m
- The analysis is based on a low sampling frequency (approximately monthly surveys of the cliff face)

In common with Hobbs et al. (2010), this study struggled to detect and characterize shallow movements in the stepped topography due to variable view angles onto the surface. Moreover, integration of the TLS data with the extensometer data does not prove conclusive in this thesis due to the time limitations, but future research could examine the changes proximal to the area occupied by the extensometer for validation.

7.3 Statistical analysis of landslide displacements

The characteristics of surface change across the cliff demonstrate that the landslide morphology is controlled by a main triggering factor – rainfall. However, a detailed understanding of the controls on landslide dynamics is still unclear. Therefore, this section focuses upon the in-situ monitoring data, which was collected from the upper section of the cliff, in order to evaluate the hydrological factors that control the movements of the landslide. To achieve this, a detailed statistical analysis has been undertaken to consider the influence of, and relationships amongst, various parameters. 12 discrete accelerated movement events defined by a minimum movement threshold of ≥ 0.2 mm/hr in response to hydrological factors form the focus (Table 7.2), for which correlation and multiple regression analyses have been applied. All variables including a dependent (i.e. the maximum displacement rate) and independent variables (e.g. groundwater and rainfall) were transformed to a normally distributed variable to allow a multiple regression model to be run with confidence. Potential transformations include taking log, the square root or raising the variable to a power were tested using the *ladder* command (STATA) which examines a range of standard transformation and reports the results of a chi-square test for each, whereby the smallest result tends towards a more normal distribution, and hence is most suitable for regression.

The resulting multi-regression equation is as follows:

$$Y = \alpha + \beta_1 X_1 + \beta_2 X_{2+\ldots+} \beta_n X_n \qquad \text{Equation 7. 1}$$

Where Y is the dependent variable, β_i (where i = 1, 2,.., n) is the coefficient of the dependent variable Y on the independent variable X_i (i = 1, 2,…, n), and α is a constant.

Table 7.2 Summary of landslide movement, groundwater and rainfall for the 12 accelerated movement events. Note: Dates: Day/Month/Year; Max- Maximum; Mean - the average; Std - standard deviation of the mean; Gw -groundwater; Total change from maximum to minimum (i.e. maximum groundwater level – minimum groundwater level); Max. Precipitation - the maximum hourly precipitation in a period; Total precipitation: The total precipitation in a period; Precipitation Duration – the total rainfall hour.

Period	Dates	Total hour	Total movement (mm)	Displacement rate (mm/hr)				Groundwater, Gw (m)				Rate of change of groundwater (m/hr)				Precipitation (mm)			Total change from maximum to minimum (m)
				Mean	Std.	Min.	**Max.**	Mean	Std.	Min.	Max.	Mean	Std.	Min.	Max.	Max.	Total	Duration	
2	26/08/2011 - 1/09/2011	154	13.399	0.100	0.044	0.012	**0.200**	4.905	0.140	4.317	4.987	0.004	0.014	-0.007	0.115	10.40	36.60	18	0.670
4	14/10/2011-14/11/2011	740	176.573	0.239	0.369	0.010	**1.914**	4.556	0.110	4.312	4.780	0.000	0.005	-0.032	0.017	3.20	29.00	43	0.467
6	15/12/2011-09/01/2012	608	148.944	0.245	0.163	0.041	**0.808**	4.426	0.139	4.095	4.770	0.001	0.010	-0.050	0.114	2.80	20.00	32	0.675
8	29/04/2012-05/05/2012	133	74.464	0.609	0.894	0.014	**4.697**	5.426	0.105	5.254	5.555	0.000	0.010	-0.011	0.071	0.20	1.20	6	0.301
9	10/05/2012 - 15/05/2012	104	61.470	0.647	0.414	0.014	**1.778**	5.445	0.122	5.175	5.622	0.001	0.011	-0.020	0.064	0.40	2.00	8	0.447
11	22/06/2012-28/06/2012	144	74.227	0.603	0.447	0.019	**1.658**	5.269	0.074	5.149	5.387	0.000	0.006	-0.012	0.019	1.40	13.20	32	0.238
12	28/06/2012-04/07/2012	144	69.736	0.659	0.563	0.014	**2.211**	5.240	0.067	5.096	5.372	0.000	0.010	-0.019	0.071	3.40	15.20	16	0.276
14	6/07/2012 - 10/07/2012	91	105.801	1.259	1.126	0.024	**3.951**	5.642	0.296	5.146	6.358	0.002	0.045	-0.042	0.221	7.20	11.40	16	1.212
15	10/07/2012 - 13/07/2012	66	124.774	1.918	1.102	0.058	**3.917**	5.525	0.162	5.249	5.795	0.000	0.034	-0.018	0.203	1.80	10.20	15	0.546
17	21/11/2012-23/11/2012	63	16.952	0.292	0.149	0.014	**0.583**	5.105	0.065	5.005	5.238	0.004	0.009	-0.018	0.034	1.80	11.80	15	0.233
19	24/11/2012-02/12/2012	185	309.669	1.721	1.678	0.029	**6.272**	5.773	0.342	5.198	6.501	0.001	0.041	-0.079	0.283	3.00	45.00	60	1.303
21	03/12/2012-06/12/2012	65	43.768	0.675	1.203	0.005	**4.755**	5.250	0.058	5.205	5.382	0.002	0.007	-0.011	0.022	1.40	4.40	12	0.177

In this analysis, the relationship between the maximum displacement rate (i.e. the dependent variable) and the hydrologic parameters, such as groundwater level and precipitation (i.e. the independent variables), is considered. Various derivatives of the datasets have been used to represent the range of independent variables responding to the maximum landslide displacement rate. The mean values of the groundwater variables provide a measure of average conditions. The maximum values indicate extreme conditions of high groundwater fluctuation in response to heavy rainfall (NB in this study period the precipitation totals and magnitudes were unusually high for this location). The standard deviation values of groundwater variables were included to reflect the variability of the groundwater. Total, maximum and rainfall duration represent the cumulative rainfall, the maximum hourly rainfall in a period and the total rainfall hour, respectively. These parameters have been transformed to normally distributed variables in terms of mean, standard deviation of the mean (Std) and the maximum (Max) in each parameter (Table 7.3). The majority of the regression model results showed a statistically insignificant relationship between the maximum displacement rate and independent variables. Only the statistically significant relationships are focussed upon below.

Table 7.3 Data fields used in regression modelling

Dependent variables	ID code	Units	Transformation	chi2	P(chi2)
Maximum displacement rate	R	mm/hr	square root	0.79	0.673
Independent variables					
1.Maximum groundwater	Max.Gw	m	1/square	0.04	0.978
2.Mean groundwater	Mean.Gw	m	cubic	0.66	0.718
3. Std.Dev. groundwater	Std.Gw	m	1/square root	0.61	0.738
4. Maximum groundwater rate	Max.GwR	m/hr	square root	1.36	0.507
5. Mean groundwater rate	Mean.GwR	m/hr	Identity	3.53	0.171
6. Std.Dev groundwater rate	Stdv.GwR	m/hr	inverse	0.23	0.891
7.Change of groundwater	C.Gw	m	log	0.82	0.664
8.Maximum rainfall	Max.Rain	mm	square root	2.38	0.305
9.Total rainfall	T.Rain	mm	square root	0.19	0.910
10.Rainfall duration	D.Rain	hour	log	0.10	0.953

Note: The transformed values have been chosen based on the minimum chi-squared value (chi2) or P(Chi2) value that is tending towards 1 (more normally distributed).

7.3.1 The relative significance of the independent variables

The nature of the relationship between the landslide displacement rate and the independent variables has been summarised in terms of the correlation coefficient (r-value), and plotted in Figure 7.2, by order of correlation significance, irrespective of sign. The correlation values represent the strength of the relationship between the maximum displacement rate and the independent variables.

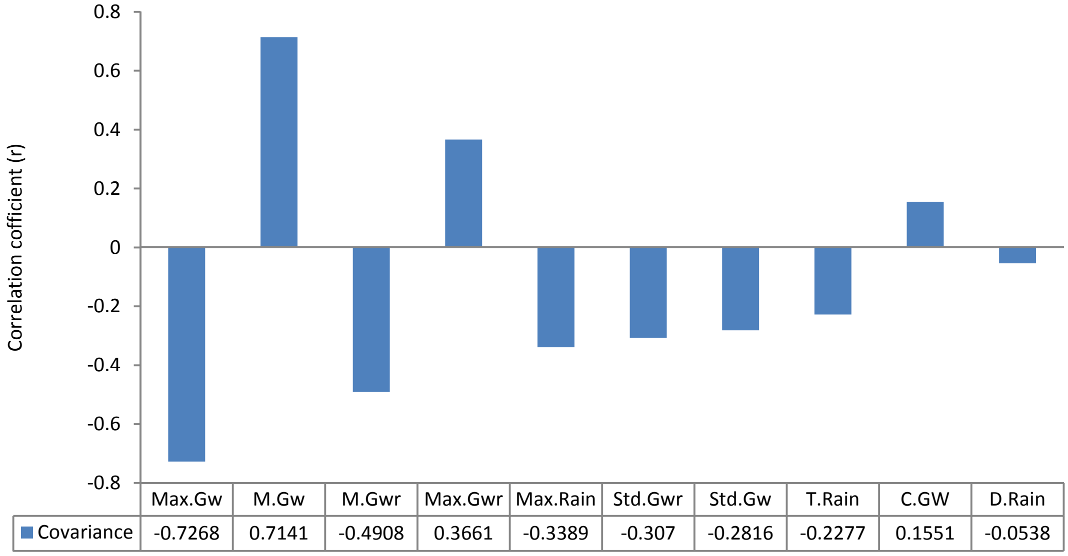

Figure 7.2 Ordered covariance values for landslide movement and independent variables. In general, most of the independent variables have a negative relationship with the landslide displacement rate (R) especially the Max.Gw. However, M.Gw, Max.Gwr and C.GW are positively related.

In general, most of the independent variables have a negative relationship with the maximum landslide displacement rate (R), most notably the maximum groundwater level (Max.Gw). An increase in groundwater level leads to an increase in displacement rate. However the maximum displacement rate is observed and then decline when groundwater level remains high. This is probably associated with a change in the rate of change of groundwater. This shows a negative relationship between the maximum displacement rate and the maximum groundwater level. This is consistent with field observations for periods of accelerated movements (e.g. Periods 2 and 4), in which the rate of displacement increases and reaches a peak during the stage of increasing groundwater level. However, as the rate of change of groundwater declines, landslide displacement rate decreases, although groundwater level itself remains relatively high. Hence movement rate relates not only to absolute groundwater level but also the rate of change in groundwater.

The landslide displacement rate is also negatively related to the maximum rainfall (Max.Rain) and other rainfall factors such as the total magnitude of rainfall (T.Rain). This is probably due to the lag time between rainfall and groundwater response. Conversely, three variables (i.e. mean groundwater (M.Gw), maximum rate of change of groundwater (Max.Gwr) and total change from minimum to maximum groundwater level (C.GW)) recorded a positive relationship with the maximum displacement rate. In terms of groundwater, the Max.Gw had a higher correlation (e.g. -0.727) as compared to M.Gw or Max.Gwr, which have smaller correlation coefficients (i.e. 0.714 and 0.366, respectively).

In order to gauge the strength of the correlation and degree of explained variability produced by the regression model, Pseudo-r^2 values generated in a simple regression are conventionally used (Clark & Hosking, 1986; Parker, 2009), as opposed to a single r value. These measurements have been proposed as an equivalent statistic to evaluate the goodness-of-fit of regression models (Long, 1997). Thus, the Pseudo-r^2 values of each variable have been compared. The regression is calculated for each variable using a regression equation, which starts with a simple regression between the displacement rate and the Max.Gw, upon which multiple regressions are undertaken by incrementally adding more variables into the model. The Pseudo-r^2 values are shown in Figure 7.3. The key independent variables controlling the landslide displacement rate is simplified incrementally by removing less significant independent variables. As shown in Figure 7.3a, the change in the Pseudo-r^2 values brought about by including T.Rain and C.GW are relatively less significant than that resulting from inclusion of other variables. This is further confirmed by running the multi-regression model again using fixed Max.Gw and Max.Rain values (Figure 7.3b). Thus, T.Rain and C.Gw were removed. As such, the three independent variables used in the optimum landslide regression model are core to controlling the displacement rate: Max.Gw, Max.Rain and D.Rain. As the key factors including the maximum groundwater level (Max.Gw), the maximum hourly rainfall or magnitude of rainfall (Max.Rain) and rainfall duration (D.Rain), filed monitoring data suggest that groundwater increases lead to increased displacement rate, and the temporary fluctuation of groundwater is controlled by both the magnitude and duration of rainfall. Moreover, these three important factors have also been described by Massey (2010) at the Taihape landslide where the pore pressure at a given time and the accumulated antecedent rainfall have been assessed incrementally by performing a correlation analysis assuming a linear relationship between pore pressure and rainfall.

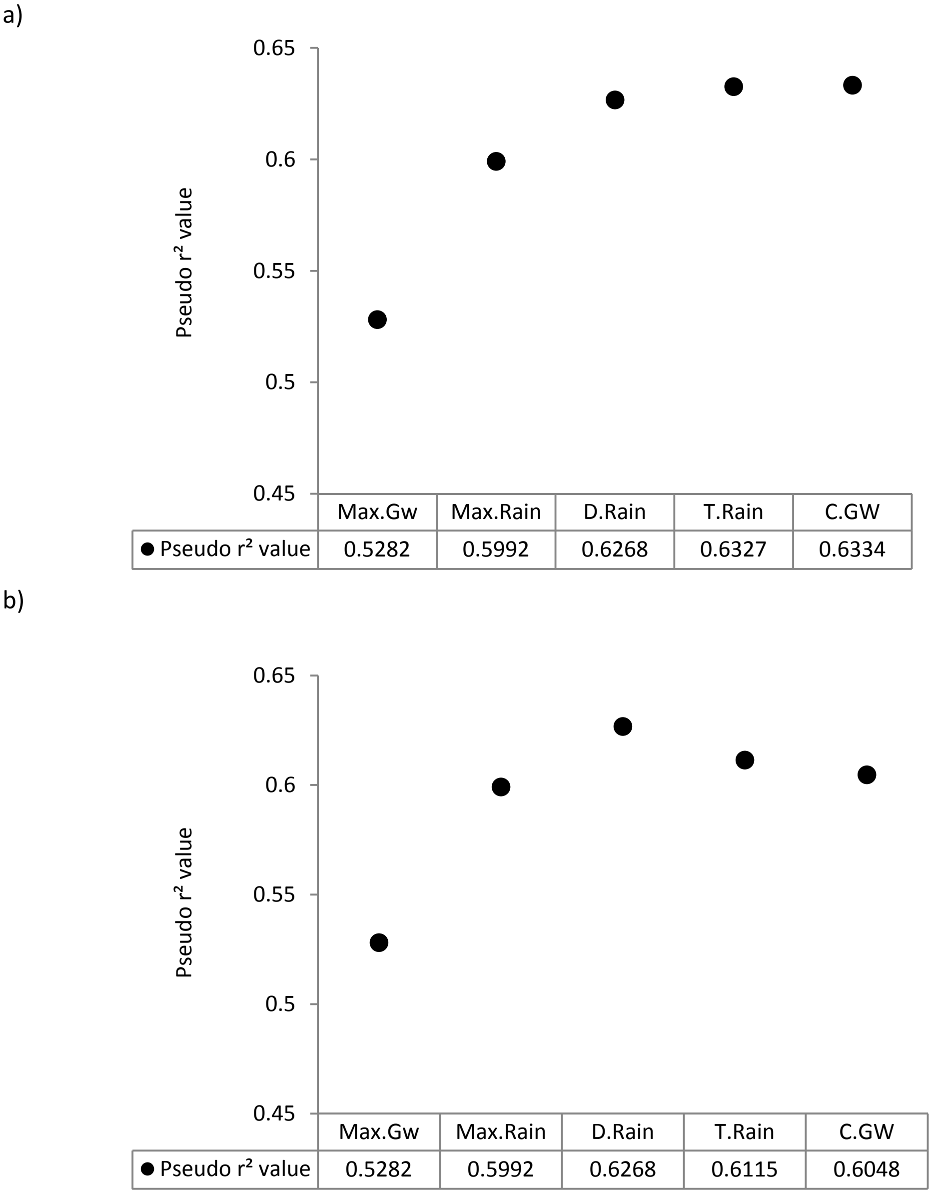

Figure 7.3 Plots of Pseudo-r² values against independent variables. a) Results of multi regression by adding each variable into the regression models. This shows that the Pseudo r² value has dramatic increment from Max.Gw, Max.Rain to D.rain and then followed by relatively constant Pseudo r² values (T.Rain, C.Gw). The insignificance of T.Rain and C.GW is consistent with the observation in b. b) The multi- regression models use two main variables (Max.Gw and Max.Rain) and record changes after adding either D.Rain, T.Rain or C.GW. The result shows that T.Rain and C.Gw are less significant as the Pseudo r² values drop.

7.3.2. Landslide movement event regression modelling

The result of multiple regression analysis between the maximum landside displacement rate (R) and Max.Gw, Max.Rain and D.Rain, for each of the movement periods, is shown in Table 7.4.

Table 7.4 Summary of the descriptive statistics and analysis results between the maximum displacement rate and independent variable (Max.GW, Max.Rain and D.Rain)

Number of observations	12
F(4,7)	15.67
Prob(F)	0.0000
R-squared (r^2)	0.6268
Root MSE	0.45655

Independent variables	Coefficient (β)	Standard error	t	P>|t|	Beta (b)	VIF
Max.Gw	-70.944	12.376	-5.73	0.0001	-0.718	1.20
Max.Rain	-0.277	0.135	-2.04	0.076	-0.338	1.19
D.Rain	0.172	0.183	0.94	0.373	0.182	1.02
_cons (α)	3.897	0.809	4.81	0.001	-	Mean VIF 1.14

Note: the Variance Inflation Factor (VIF) value is associated with collinearity, with VIF < 5 indicating the independent variables are less correlated with each other (O'Brien 2007).

According to Gujarati (1995: 244 - 250), the "F value'' and "Prob(F)'' statistics test the overall significance of the regression model. Specifically, they test the null hypothesis that all of the regression coefficients are equal to zero. This tests the full model against a model with no variables and with the estimate of the dependent variable being the mean of the values of the dependent variable. The F value is the ratio of the mean regression sum of squares divided by the mean error sum of squares. Its value will range from zero to an arbitrarily large number. The value of Prob(F) is the probability that the null hypothesis for the full model is true (i.e., that all of the regression coefficients are zero). For this analysis, F-value is 15.67 (greater than 0) and Pro(F) is zero leading one to reject the null hypothesis, indicating the model is statistically significant. Thus, the independent variables (Max.Gw, Max.Rain and D.rain) are related to the dependent variable and this regression can be used to examine the relationship between the maximum displacement rate and the hydrological parameters.

A coefficient of determination (r^2) is usually defined as the proportion of variance of the response that is predictable from (can be explained by) the independent variables. This indicates the strength of the impact of the hydrological variables on the maximum displacement rate. Table 7.4 shows $r^2 = 0.63$, indicating that 63% of the maximum displacement rate can be explained by Max.Gw, Max.Rain and D.Rain. The Max.Gw has a negative relationship ($\beta = -70.944$) and is strongly significant ($b = -0.718$). The negative relationship is also found in Max.Rain ($\beta = -0.277$), but the model strength is less than Max.Gw ($b = -0.338$). The negative relationship between displacement rate and rainfall is probably associated with time. For example, the increased rainfall has resulted in a significant increase in the number of landslides, represented by high displacement rates. However, there is a lag time (1 - 2 hours) between rainfall and groundwater, which has affected landslide movements. Conversely, when the rainfall continues, the landslide displacement rate increases proportionately with the duration of rainfall (D.Rain). In order to check the degree of correlation among several independent variables, the Variance Inflation Factor (VIF) has been calculated. The VIF values show little correlation among independent variables (Mean VIF = 1.14). This suggests that the regression model has less impact from multicollinearity (interaction effects between variables) among the independent variables.

In order to check how well the model predicts the observational data, model residuals have been derived. In a sense, the residuals represent the degree of failure of the model to predict a given data value. Therefore, the residuals provide a wealth of information on the quality of the analysis. As shown in Figure 7.4a, the residuals plotted against the predicted values show a random pattern, indicating that the model is reasonable and has no structural bias. As such, a new equation for displacement rate based on the correlation coefficients is derived:

$$R\ \text{Model} = 3.897 - 70.944(\text{Max.Gw}) - 0.277(\text{Max.Rain}) + 0.172(\text{D.Rain}) \quad \text{Equation 7. 2}$$

Where, 'R model' represents a regression model of the maximum displacement rate, Max.Rain is the maximum hourly rainfall and D.Rain is rainfall hour during accelerated movement.

a)

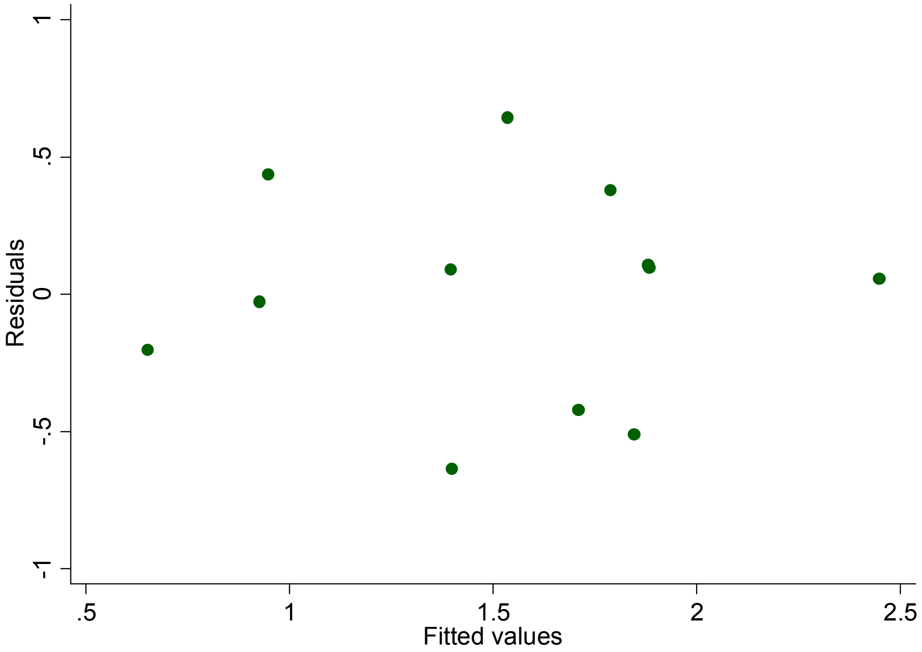

b)

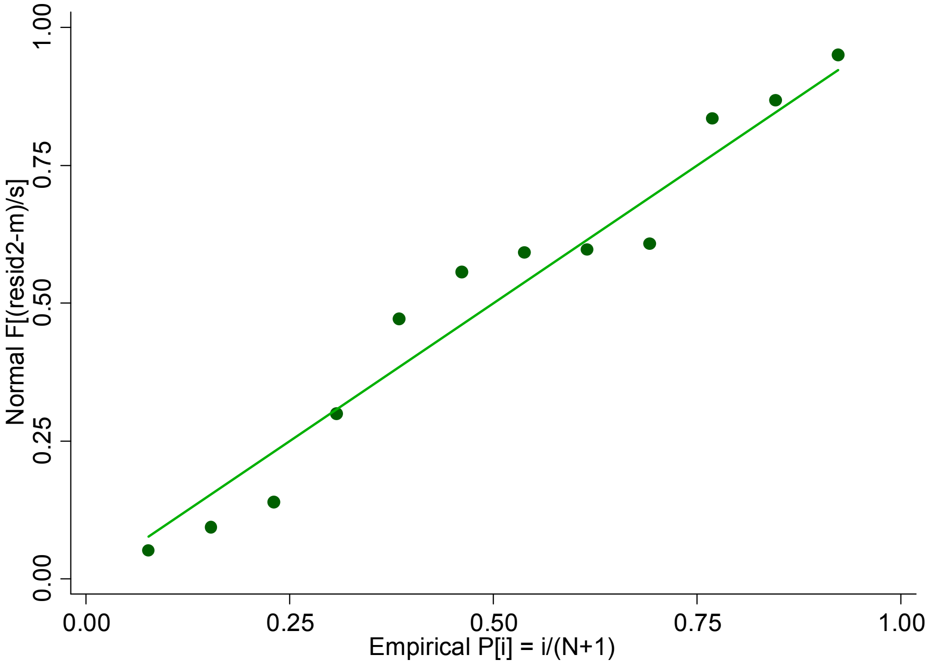

Figure 7.4 Plot of the residuals against the predicted values present a random pattern, so the model is reasonable (a). The normalized probability plot shows distribution of displacement rate nearer to the centre of the distribution (b).

Figure 7.5 shows a comparison between displacements rates obtained from field data and predicted displacement rates derived by applying the regression model. As discussed earlier, 63% ($r^2 = 0.63$) of the maximum displacement rate can be explained by Max.Gw, Max.Rain and D.Rain. Thus, the R model suggests that there are other additional factors besides the current regression parameters, which also have an impact on the observed displacement rate, in addition to an inevitable level of inherent variability in this natural system. Such additional factors may be related to the deformation of the material along the slide plane, or local heterogeneity (as discussed in section 7.2). Taking these factors into consideration may then lead to a more powerful model from which landslide behaviour forecasting could be based. Additionally, laboratory tests also show that increasing groundwater levels in the material reduces shear resistance. This will be discussed in more detail in the next section.

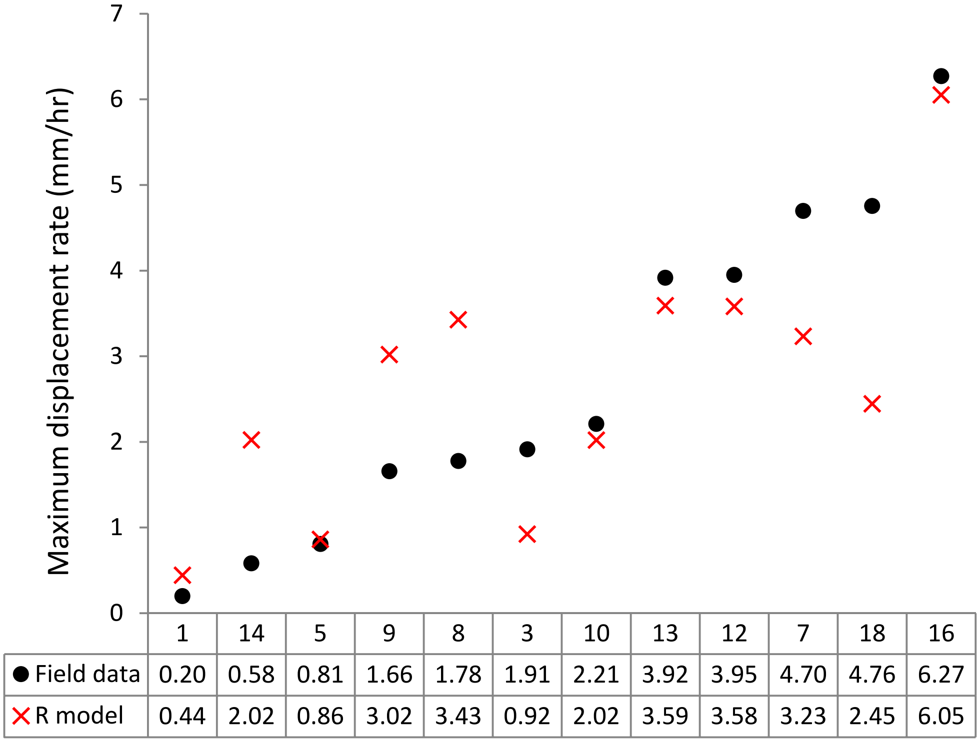

	1	14	5	9	8	3	10	13	12	7	18	16
● Field data	0.20	0.58	0.81	1.66	1.78	1.91	2.21	3.92	3.95	4.70	4.76	6.27
✕ R model	0.44	2.02	0.86	3.02	3.43	0.92	2.02	3.59	3.58	3.23	2.45	6.05

Figure 7.5 Ordered displacement rates from field data and the predicted displacement rates from running the R model (Equation 7.2)

7.4 Mechanisms of landslide deformation

Following the previous section on the statistical analysis of the controls on landslide displacement, this section examines the mechanisms and processes of landside deformation. The movement patterns of a landslide in the post-failure phase, including slow movement (post-failure creep) and accelerated movement (reactivation), observed in the field monitoring data are compared with the laboratory test results. The pore water pressure reinflation (PPR) test results are used to examine the underlying mechanisms for the accelerated movements. A focus is placed on the mechanisms of ductile deformation and the dilative behaviour in landslide deformation

7.4.1 Post- failure creep

The slow movement of the Upgang cliff can be interpreted as post-failure movement (Hutchison, 1988). Clearly in this case the initial failure events occurred prior to this study. The monitoring records show that the displacement of landslide mass after an initial slope failure is very slow (0.06 - < 2 mm/hr), as indicated by the creeping behaviour. Slow movements occurred in periods of varying rainfall durations (> 20 hrs) with a low to medium magnitude (maximum hourly rainfall of 1-4 mm) (Table 7.5) over a time period of 31-73 days, as can been seen in the two examples of slow movement in Figures 7.6 and 7.7. Under such rainfall conditions, this movement is probably associated with a lower groundwater level than that of accelerated movements (average groundwater level of slow movement - about 4.83 m v average groundwater level of accelerated movement - about 5.05 m). Moreover, slow movements occur within a narrower range of the variability of groundwater level (Std.Dev = 0.27 m) than accelerated movements (Std.Dev = 0.543 m). Accelerated movements are associated with high groundwater levels (Figure 7.6), in this case the accelerated movement occurred between 26th August and 9th September 2011. The rate of increase of groundwater was high (peak rate of 0.1 m/hr) due to the intense rainfall (10 mm/hr). This was followed by a phase of slow movement that occurred between 09th September and 14th October 2011, as the groundwater level declined. The displacement rates of Periods 2 and 3 were dependent on the duration of the groundwater change. In Period 2, a rapid increase in groundwater fluctuation occurred over a short period of time. However, after the groundwater declined, it was lower than the peak level (4.98 m), but is still considered high (approximately 4.7 m). This occurred over a prolonged period of time resulting in the landside mass undergoing creeping behaviour. Another example can be seen in Periods 5 and 6 (Figure 7.7). Groundwater declined over a prolonged period of time between 14th November 2011 and 15th December 2011 (31 days) resulting in the landside mass undergoing creeping behaviour. However, a rapid increase in groundwater from 4.1 m to 4.8 m occurred over 25 days (15th December 2011 to 09th January 2012). The resultant accelerated movement occurred as a reactivating behaviour. These two examples suggest that a period of predominantly slow movement, which was followed by a period of accelerated movement, was possibly related to plastic deformation. It should also be noted that slow movements only occurred during the initial stages of deformation, after which movements are either accelerated or do not occur at all, e.g. 'no movement'.

Table 7. 5 Summary of the types of landslide movement at Upgang landslide. Note: Max: Maximum; Mean: the average; Std.Dev: standard deviation of the mean; change of groundwater: Maximum groundwater level – minimum of groundwater level; Max. precipitation: The maximum hourly precipitation in a period; Total precipitation: The total precipitation in a period; Duration precipitation: The sum of hours that rainfall > 0.2 mm in a period

Conditions	Accelerated movement				Slow movement			
	Mean	Std.Dev.	Min	Max	Mean	Std.Dev.	Min	Max
1. Total hour of event period (hr)	208.08	222.88	63	740	1,043.250	495.524	653	1,751
2. Displacement (mm)	101.648	82.081	13.399	309.669	10.765	6.086	4.745	19.130
3. Displacement rate (mm/hr)	0.906	0.998	0.200	6.272	0.009	0.029	-0.079	0.142
4. Groundwater (m)	5.053	0.543	4.287	6.501	4.827	0.270	4.021	5.408
5. Groundwater rate (m/hr)	0.001	0.019	-0.079	0.283	0	0.006	-0.092	0.037
6.Change of groundwater (m)	0.541	0.374	0.177	1.303	0.523	0.138	0.370	0.680
7. Max. precipitation (mm)	3.08	2.94	0.20	10.400	2	1.13	1.20	3.600
8. Duration precipitation (hour)	22.750	16.001	6	60	39.500	26.40	21	77
9. Total precipitation (mm)	16.670	13.736	1.200	45	20.500	17.574	8.800	46.400

Note: Std.Dev shows how much variation exits from the mean: a low Std.Dev indicates that the data points tend to be very close to the mean; high Std.Dev indicates that the data points are spread out over a large range of values.

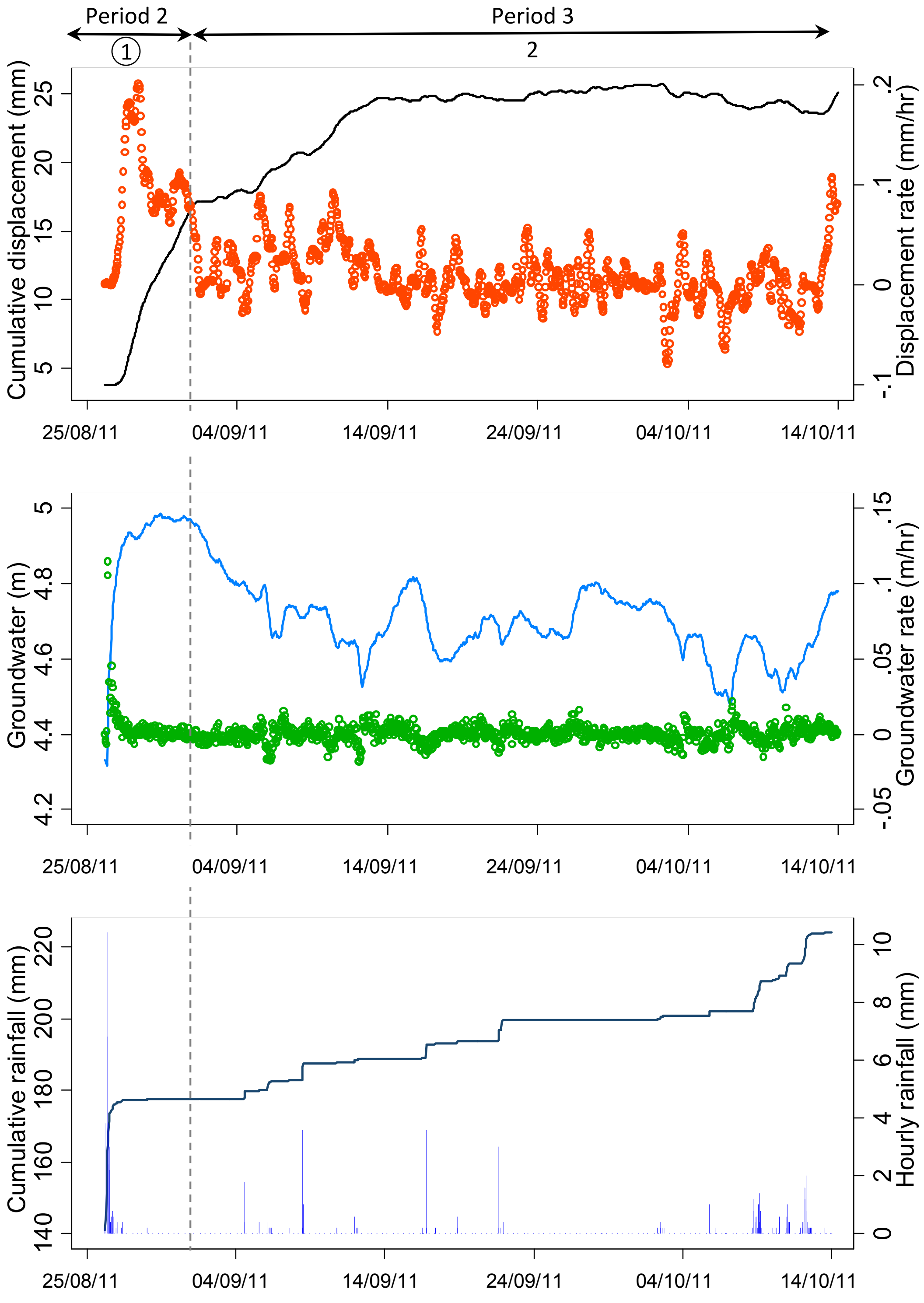

Figure 7.6 a) Plot of cumulative displacement (mm) and displacement rate (mm/hr) against time; b) Plot of groundwater (m) and groundwater rate (m/hr) against time; c) Plot of cumulative rainfall (mm) and hourly rainfall (mm) over the entire monitoring period. In Period 2, accelerated movement occurred between 26th August and 1st September 2011 with a high fluctuation groundwater (groundwater rate = 0.1 m/hr) due to heavy hourly rainfall (10 mm). This was followed by a long-duration slow movement that occurred between 01st September 2011 and 14th October 2011 when the groundwater declined. Note: Accelerated (1) and slow movement (2) in response to hydrological conditions.

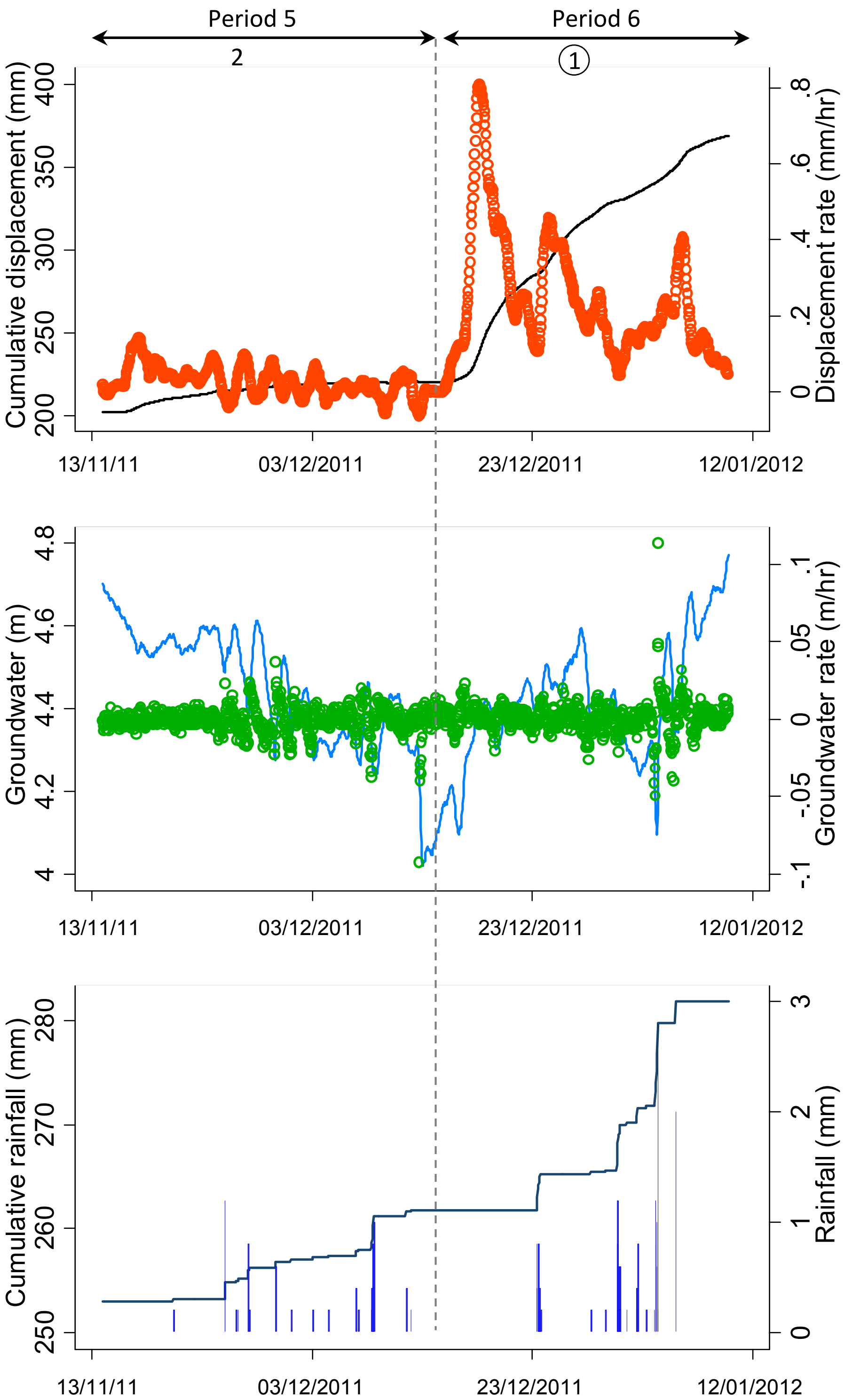

Figure 7.7 a) Plot of cumulative displacement (mm) and displacement rate (mm/hr) against time; b) Plot of groundwater (m) and groundwater rate (m/hr) against time; c) Plot of cumulative rainfall (mm) and hourly rainfall (mm) over the entire monitoring period. Period 5 - long-duration slow movement that occurred between 14th November 2011 and 15th December 2011 when the groundwater declined, and followed by Period 6 - long-duration accelerated movement that occurred between 15th December 2011 and 09th January 2012 with a high fluctuation groundwater (groundwater rate = 0.1 m/hr) during winter period. Note: Accelerated (1) and slow movement (2) in response to hydrological conditions.

7.4.2 Reactivation

The accelerated movements represent 'reactivation' of the landslide mass (Leroueil et al., 1996). This type of movement is characterised by increased displacements (here in the range of 13.39 – 309.67 mm) over a short period of time in response to increased groundwater levels (approximately 2 – 30 days). Due to a rapid and continuous increase in the void ratio in relation to high groundwater levels and high fluctuations in groundwater rate, the effective stress on the shear surface became particular low, leading to high deformation of the landslide mass. This can be seen in the four examples of accelerated movements responding to different groundwater patterns in Figure 7.8. Three phases of groundwater change were observed in the reactivation process:

1) A sudden increase in groundwater level over a short period (i.e. Period 2; groundwater rose up suddenly (from minimum groundwater 4.31 m to maximum groundwater 4.987 at a rate of 0.1 m/hr) within a few hours and remained continuously high due to heavy and intense rainfall);

2) Phases of slow but prolonged increases in groundwater level (i.e. Period 4; groundwater slowly increased (from minimum groundwater 4.31 m to maximum groundwater 4.78) at a rate of 0.01 m/hr). This pattern, which occurred over a longer period than the previous pattern, was associated with a higher displacement rate; and,

3) A series of sudden surges of groundwater (e.g. Periods 14 and 15, in which groundwater rapidly rose and was then followed by rapid decline (from up to 6.35 m to 5.15 m) at a rate of 0.2 m/hr). This pattern was associated with the highest displacement rates caused by the low effective stress on the shear surface.

This suggests that deformation within the landslide body is, as expected, affected by both hydrological and mechanical properties. The change of effective stress on the shear surface leads to high displacement rates caused by the first two patterns of increased groundwater:

1) a sudden increase in groundwater, and 2) a slow and prolonged increase in groundwater. Where the soil extends, fissures develop leading to rapid infiltration and drainage. Consolidation of the shear band may lead to strength regain, reducing the likelihood of reactivation (Angeli et al., 2004). The accelerated movement is consistent with observations at several reactivated landslides including the translational Utiku landslide (Massey et al., 2013), the Tessina landslide (Petley et al., 2005) and mudslide accelerations on the Dorset coast (Allison and Brunsden, 1990). Importantly, it is easier to infiltrate water into the soil than it is to drain from it. So groundwater responds quickly to heavy rainfall (rapid rises) and also receives water from inland (slow increases). Groundwater drains vertically, which is difficult (slow declines), and the landslide movement responds to this. Data collected here suggests that movement consists of two components – a transient component caused by strain development during rapid stress change (i.e. when groundwater increases the stress state changes, so the landslide moves), and a dynamic component caused by high groundwater levels. When groundwater is rising quickly, both components of movement can be observed (i.e. series of sudden surges of groundwater) leading to low effective stress on the shear surface. However, when groundwater is static, only the ‘dynamic’ part occurs.

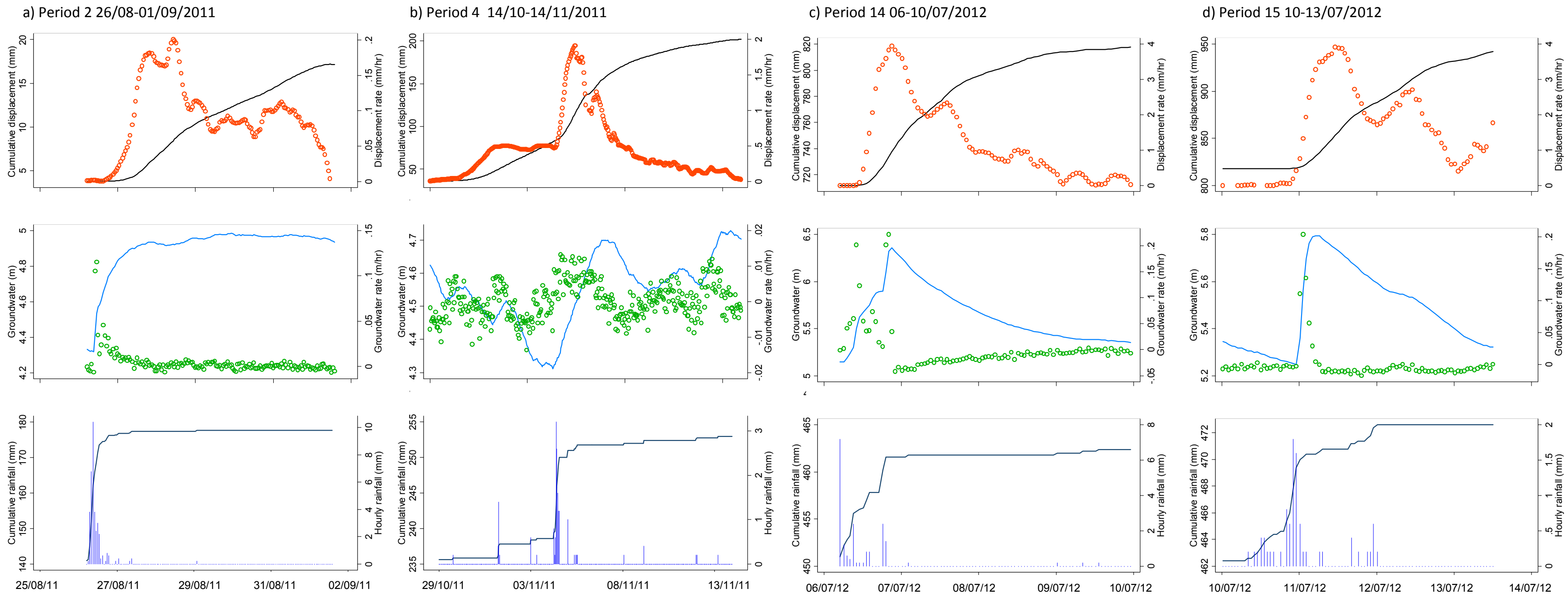
a) Period 2 26/08-01/09/2011

b) Period 4 14/10-14/11/2011

c) Period 14 06-10/07/2012

d) Period 15 10-13/07/2012

Figure 7.8 Reactivation of landslide movement corresponding to different hydrological conditions. a) A sudden surge of groundwater in a short period presented by Period 2, which occurred between 26 August and 01 September 2012 showing about 13.4 mm in total displacement with a maximum displacement rate of 0.2 mm/hr. b) Slow and prolonged increasing groundwater (groundwater slowly increased, using a few days to reach a peak (longer time than Period 2)) presented by Period 4, which occurred between 14 October and 14 November 2011 showing about 177 mm in total displacement with a maximum displacement rate of 1.9 mm/hr. c) and d) Series of sudden surges of groundwater (dramatic rise and fall of groundwater) presented by Periods 14 and 15, which occurred between 6 and13 July 2012 resulted in about 230 mm in total displacement with a maximum displacement rate of 4 mm/hr.

7.4.3 The role of plastic deformation

The monitoring data (for example for Periods 2, 4, 14 and 15) reveal an asymptotic trend in the Saito analysis (Petley et al., 2002) (Figure 7.9). This suggests that the reactivated movements of the landslide are ductile / plastic in nature, as expected. The PPR tests were designed to explore this behaviour. In this study, the PPR test results indicate that plastic yield can be determined by the initiation of movement in terms of effective stress. In the initial phase of reinflation, there was small strain development, indicating that the shear stress was less than the yield stress (Selby, 1993). Plastic deformation occurred only after the yield stress had been exceeded. Based on the PPR test results, the plastic yield stress at $\tau = 40$ kPa appeared to occur at $\sigma' = 60$ kPa (Figure 7.10). Once the yield stress had been exceeded, plastic deformation occurred, as demonstrated by the asymptotic trend in the Saito analysis. The analysis of the PPR tests confirms that the accelerated movement occurs through ductile / plastic deformation without strain localisation. This observation is similar to the behaviour of residual soil on Lantau Island, Hong Kong observed by Ng (2007) (see also Ng and Petley, 2009). The rapid increase in void ratio with decreasing effective stress led to a transition from localised sliding to generalised sliding. This is likely to be associated with the increasing volume of pore fluid that resulted in reduced contacts between soil particles. As a result of the shearing and subsequent rearrangement of the material particles, the samples became significantly restructured. During this phase of movement, displacement rates accelerated exponentially.

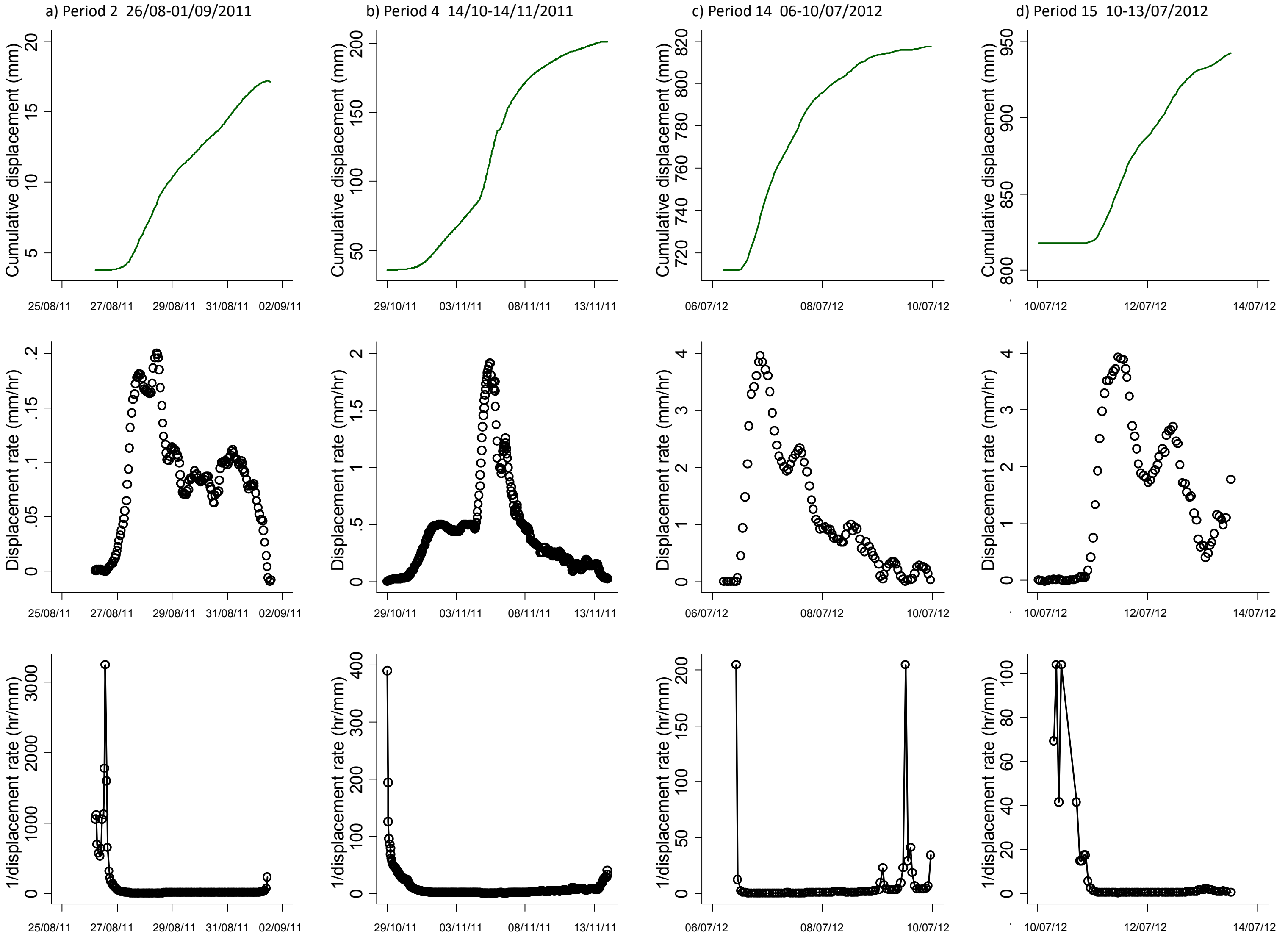

Figure 7.9 Plastic behaviour during reactivation of landslide as shown by the asymptotic trends in all accelerated movements of Period 2, 4, 14 and 15 presented by Plots of cumulative displacement against time; Plots of displacement rate against time and Plots of 1/displacement rate against time.

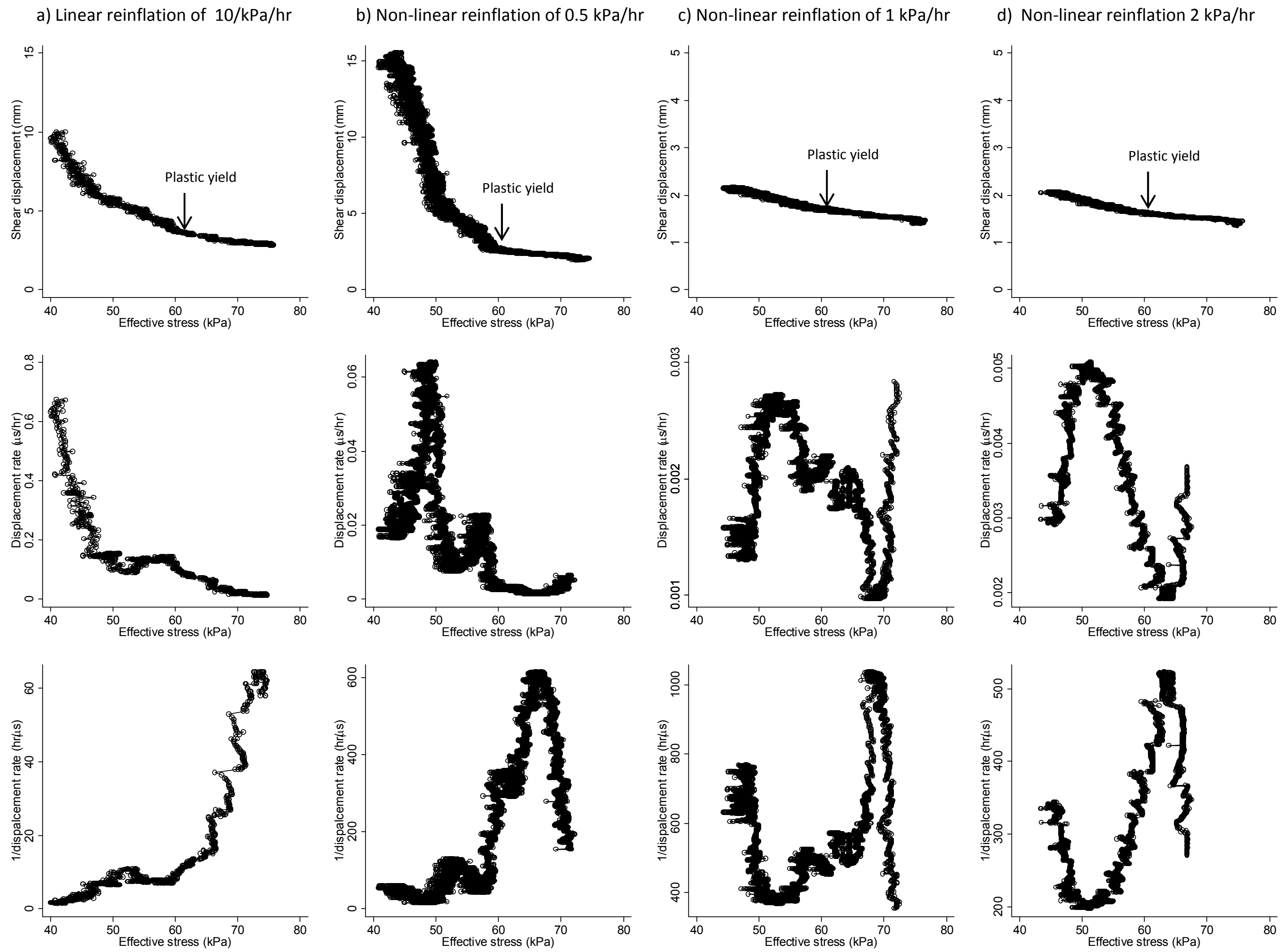

a) Linear reinflation of 10/kPa/hr

b) Non-linear reinflation of 0.5 kPa/hr

c) Non-linear reinflation of 1 kPa/hr

d) Non-linear reinflation 2 kPa/hr

Figure 7.10 Soil behaviours through the reinflation processes presented by linear (10 kPa/hr) and non-linear reinflation (0.5, 1,2 kPa/hr). a) Plots of shear displacement against effective stress showing the initiation of movement, indicating plastic yield. b) Plots of displacement rate against effective stress and c) Plots of Δ against effective stress show asymptotic trends in all reinflation tests. The asymptotic trends represent the key property of plastic behaviour that a decrease in stress (σ’) leads to a non-linear increase in displacement rate.

7.4.4 Dilative behaviour

This section aims to show the development of plastic deformation based on the analysis of the PPR tests, which indicates that the soil behaviour is affected by large void ratio increments under a non-linear pore water pressure increase. This effect is clearly seen when comparing the three different reinflation rates examined (i.e. 0.5, 1 and 2 kPa/hr) (Figure 7.11). At the initial stage of increasing pore water pressure on soil samples, as can be seen from Figure 7.11, there is no dilation. However, dilation occurred sometime later (after approximately 50,000 seconds) at higher effective stresses. This behaviour was similar to the 'push and climb' stage identified by Ng (2007), attributed to the increasing pore fluid pressure, which pushed apart the strongly interlocked soil particles and enabled them to climb over each other under shear. The dilative behaviour might be disturbed by slight contractions as some particles might fill the void space previously occupied by other particles. In other words, landslide movement is very slow, probably because the soil strength (the effective stress) remains high relative to the shear stress. The soil particles are largely interlocked and the slope is highly resistant to deformation as the groundwater is below the yield stress of the slope.

Once the yield stress was exceeded (at 60 kPa effective stress), rapid dilation was established leading to the soil samples having a large change in void ratio. The rapid dilation was attributed to 'localised sliding' where the inter-particle contacts were reduced, to the extent that some particles began sliding past each other (Ng, 2007). However, as the majority of particles remained interlocked, the slip movements were restricted. This localised sliding was observed in all three reinflation rates (0.5, 1 and 2 kPa/hr) as effective stress was decreased further. Finally, a rapid and continuous increase in the void ratio is observed in relation to low effective stresses (up to 50 kPa). 'Generalised sliding' was observed, as can be seen clearly at the reinflation rate of 0.5 kPa/hr. The large change of void ratio demonstrates a higher permeability as the soil particles were rearranged under shear, facilitated by the increasing amount of pore fluid (Ng, 2007 and Ng and Petley, 2009). However, this study does not include an analysis of permeability, which may affect the systematic changes of void ratio and effective stress.

The reinflation results can be compared with the field monitoring data in Periods 2 and 4 of accelerated movement. As discussed earlier, the maximum displacement rate in Period 2 (0.2 mm/hr) is lower than that in Period 4 (1.9 mm/hr) even though the former has a higher fluctuation of groundwater (0.1 m/hr vs 0.01 m/hr). This behaviour is associated with the longer duration of the groundwater fluctuation in Period 4, which is about three times that in Period 2. As such, Period 2 is comparable to the strain development under the reinflation rate of 1 or 2 kPa/hr, which results in 'localised sliding' with a small strain and displacement rate. On the other hand, Period 4 is synonymous with the strain development under the reinflation rate of 0.5 kPa/hr, which leads to 'generalised sliding', with a longer period of deformation and larger strain and displacement rate. Therefore, observations from the reinflation tests and the field monitoring show that the amount of shear displacement and displacement rate is more likely to be controlled by plastic deformation.

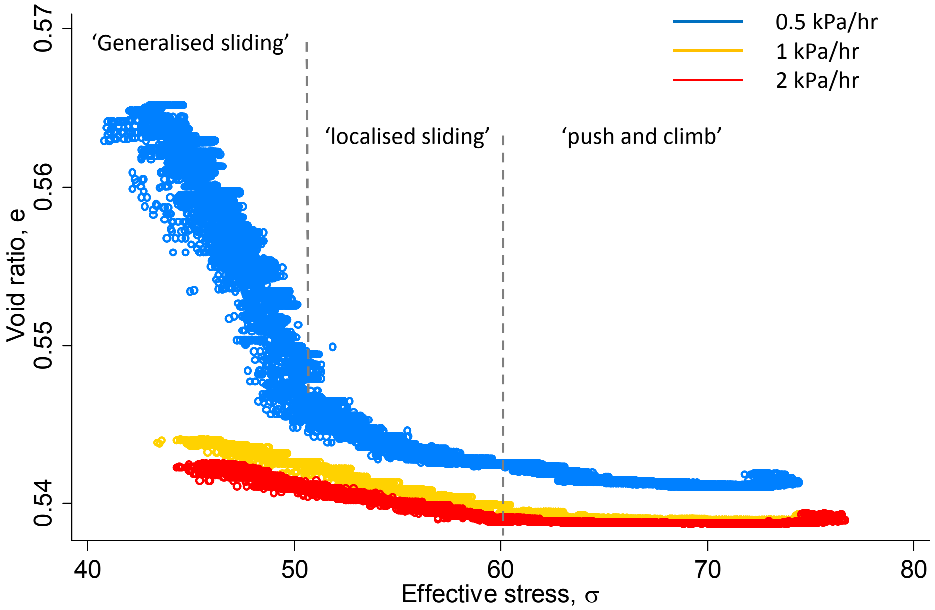

Figure 7.11 Dilative behaviour during strain development is presented by plot of void ratio against effective stress. 'Push and climb' samples developed slow dilation, indicating less permeability. Localised sliding (between 50 and 60 kPa of effective stress), rapid dilation established leading to soil samples having high permeability due to a high void ratio. Generalised slide (up to 50 kPa) can be seen clearly in the reinflation rate of 0.5 kPa/hr demonstrating a high permeability due to a large change in void ratio. This indicates that the soil samples had developed a larger void ratio in relation to low effective stresses.

7.5 Patterns of landslide movement

The purpose of this section is to discuss the short-term movement patterns recorded by ‘VBW1’ and ‘S4’ in one of the monitored reactivating landslides situated in the upper section of the glacial till. The occurrence of movement is seasonal, with velocity on average increasing during wetter periods. The landslide movement can be classified as a series of post-failure reactivated movements, or in terms of the Leroueil et al., (1996) classification, the movement patterns can be classified as Stage Three and Four (Reactivation and Active). The reactivated landslide observed in this thesis exhibited either periods of no movement, slow movements or accelerated movements in response to changing groundwater levels. The observed movements are illustrated in the conceptual graph in Figure 7.12. A typical post-failure cycle as reflected by data collected usually exhibits slow movements for a prolonged period at the outset (Phase A), before developing into a series of accelerated movements. These accelerated movements alternated with slow movements as a response to increasing groundwater (Phase B). Subsequently, occurrences of accelerated movements became higher before movement subsided, and was replaced by a period of ‘no movement’. Accelerated movements occurred again when groundwater increases returned (Phase C). The cumulative displacement is depicted as a stepped graph as the displacement rates are corresponding to a variation of groundwater. Displacement rates are especially high towards the end of the monitoring period, probably responding to high groundwater fluctuations.

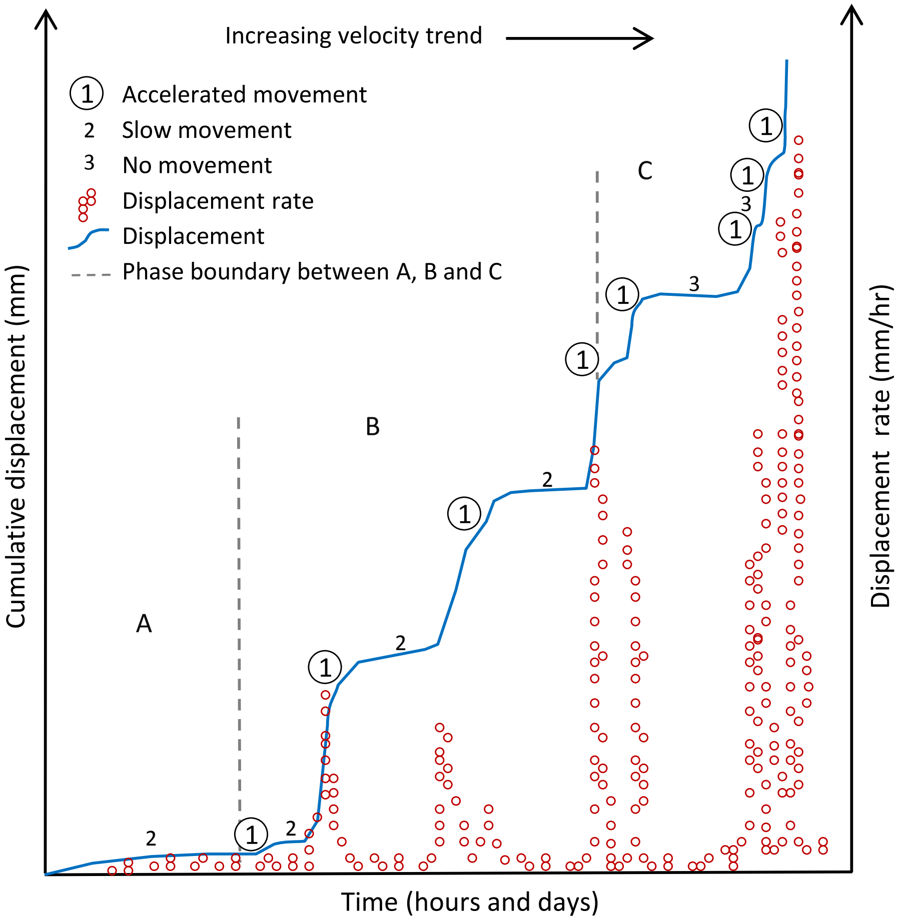

Figure 7.12 Conceptual graph plotting both cumulative displacement (mm) and displacement rate (mm/hr) against time (hours and days). The graph illustrates a movement pattern of shallow re-active landslide as represented by the Upgang landslide. Three types of landslide movements are observed, which are accelerated movements (1), slow movements (2) and no movement (3), indicating reactivation, post-failure creep and no movement behaviours. The cumulative displacement is depicted as a stepped graph as the displacement rates are corresponding to a variation of groundwater. Furthermore the displacement rate trend seems to increase towards the end of the monitoring period, probably responding to high groundwater fluctuations.

To understand the patterns of post failure, landslide movements based on field monitoring data including displacement, groundwater and rainfall were plotted as can be seen in Figure 7.13. During the initial period (Phase A), deformation is dominated by slow movements (Figure 7.13). The movement shows a positive gradient of cumulative displacement (10.6 mm) with very low displacement rates (mean hourly displacement rate of 0.04 mm/hr), probably in response to low groundwater levels (mean groundwater level of about 5 m). These slow movements are related to post-failure creep, which is associated with plastic deformation of the landslide mass, possibly indicating a progressive disaggregation of landslide blocks. Steady state creep, such as this, has been noted elsewhere (see for example Massey, 2011 for the Utiku landslide in New Zealand). The implication of the movement record is that in this case deformation is not rotational – i.e. that a different movement mechanism is occurring. In keeping with Massey (2011), it seems likely that the movement is a ductile creep type deformation of the landslide body that is effectively generating true downslope movement.

Phase B is generated by the combination of the two movement types (i.e. accelerated and slow movements). The deformation shows an increasing displacement consisting of alternate accelerated and slow movements, but with total displacement being dominated by the former. The total displacement in Phase B was approximately 372 mm and the displacement rates (0.2 – 1.9 mm/hr) were associated with periods of heavy rainfall (the maximum hourly rainfall was about 1.20 - 10.40 mm). The accelerated movements involved a slip along a part of the pre-existing basal shear surface as the reactivation of failure at residual strength. This mechanism is associated with ductile deformation as shown by the asymptotic trends in Section 7.4.2, which is related to the variation in groundwater level (maximum groundwater level of about 4.70 – 4.99 m) (Kalaugher et al., 2000; Van Asch et al., 2007; and Massey et al., 2013). This movement pattern has been observed in other landside systems as ‘graded movement’ (Allison and Brunsden, 1990), which is related to seasonal fluctuations of pore water pressure. Similarly, the accelerated movements occurred over short time periods and resulted from an increase of pore water pressure. However, there are inherent differences in terms of the landslide displacement magnitude (i.e. cm to m vs mm to cm), and triggering mechanisms due to different types of landslide (i.e. deep-seated mudslide vs shallow landslide).

Finally, in Phase C, deformation is dominated by accelerated movements, which are large displacements continuously occurring over a short period of time (3-8 days). The total displacement was approximately 881 mm, and a series of periods with larger displacement rates (approximately 0.5 – 6.27 mm/hr) associated with heavy rainfall were recorded. This mechanism is associated with ductile deformation, which is related to the variation in high groundwater level (maximum groundwater level about 5.24 – 6.50 m). The accelerated movement pattern is shown as a series of larger displacements during periods of heavy rainfall, as a continuous acceleration or ‘surge’ (Allison and Brunsden, 1990). The movement is more rapid when responding to rapid increases in groundwater associated with prolonged and intensive rainfall periods (e.g. periods 14, 15 and 19). For instance, continuous accelerated movements occurred over only a short period of time. Two such instances were recorded (between 06th and 13th July 2012 (Periods 14 and 15) and 24th November 2nd December 2012 (Period 17)). The movements showed a positive gradient of cumulative displacement with relatively high displacement rates (approximately 4 mm/hr) as a response to an increase in groundwater nearly to the ground surface (approximately 6.34 m) caused by a heavy rainfall event (maximum hourly rainfall of 7.2 mm). In particular, in Period 19, the prolonged period of accelerated movement was due to the longest prolonged continuous rainfall period (60 hours). Consequently, increasing groundwater reached the ground surface leading to low effective stress on the shear surface. This resulted in the greatest displacement (309.66 mm) recorded and a maximum displacement rate of 6.27 mm/hr. It should be noted that this happened towards the end of the monitoring period. This may mean the toe of the landslide block has transitioned to become a mudslide. This can be observed in the TLS monitoring data (Chapter 4, Figure 4.2-4.5; Landslide B3) as the pattern of deformation changed month by month, showing the pattern of downslope loss and gain of material. This suggests that the movement of material is related to the progressive landslide development of mudslide/flow. At this point, the deformation pattern shows only accelerated movement due to the rapid loss of shear strength, probably through rapid increases in groundwater level at the basal zone leading to a water content that is above the plastic limit (Petley et al., 2005).

However, some periods of no movement were observed during reactivation. The displacement data suggest that there were times when the landslide was not moving, probably periods when the movement is comparable to the precision of the instrument. This can be observed in short periods of downslope movements (positive values) with very low mean displacement rate nearly or equal zero (e.g. Period 13, 18 and 20). However, long periods of apparently upslope movements (negative values) are clearly anomalous (e.g. Period 10 and 16). As the instrument poles on the ground were not deep, seasonal changes in the location may be amplified by the tilting of these poles in response to near surface shrinkage and swelling of the ground caused by, for example, changing soil moisture. Accordingly, the soil is inorganic with clays of medium-high plasticity with a high shrink-swell potential, indicated by a liquid Limit of such soil is 48-60, and a plasticity index (PI) range of 23- 32. The soil swells during heavy rainfall events, as observed by Massey (2011) for the Taihape landslide in New Zealand. However, the geometry of underlying movement can also be creating an upslope component. Such landslides generate back tilting. However, most of the movement would be vertical and recoverable with ground drying. Moreover, very small displacement rates were observed (mean maximum displacement rate is about 0.015 mm/hr). Therefore landslide geometry is discounted. As such, the most likely explanation is that periods of no movement are comparable in magnitude to the errors of the instrument and are also related to environmental conditions.

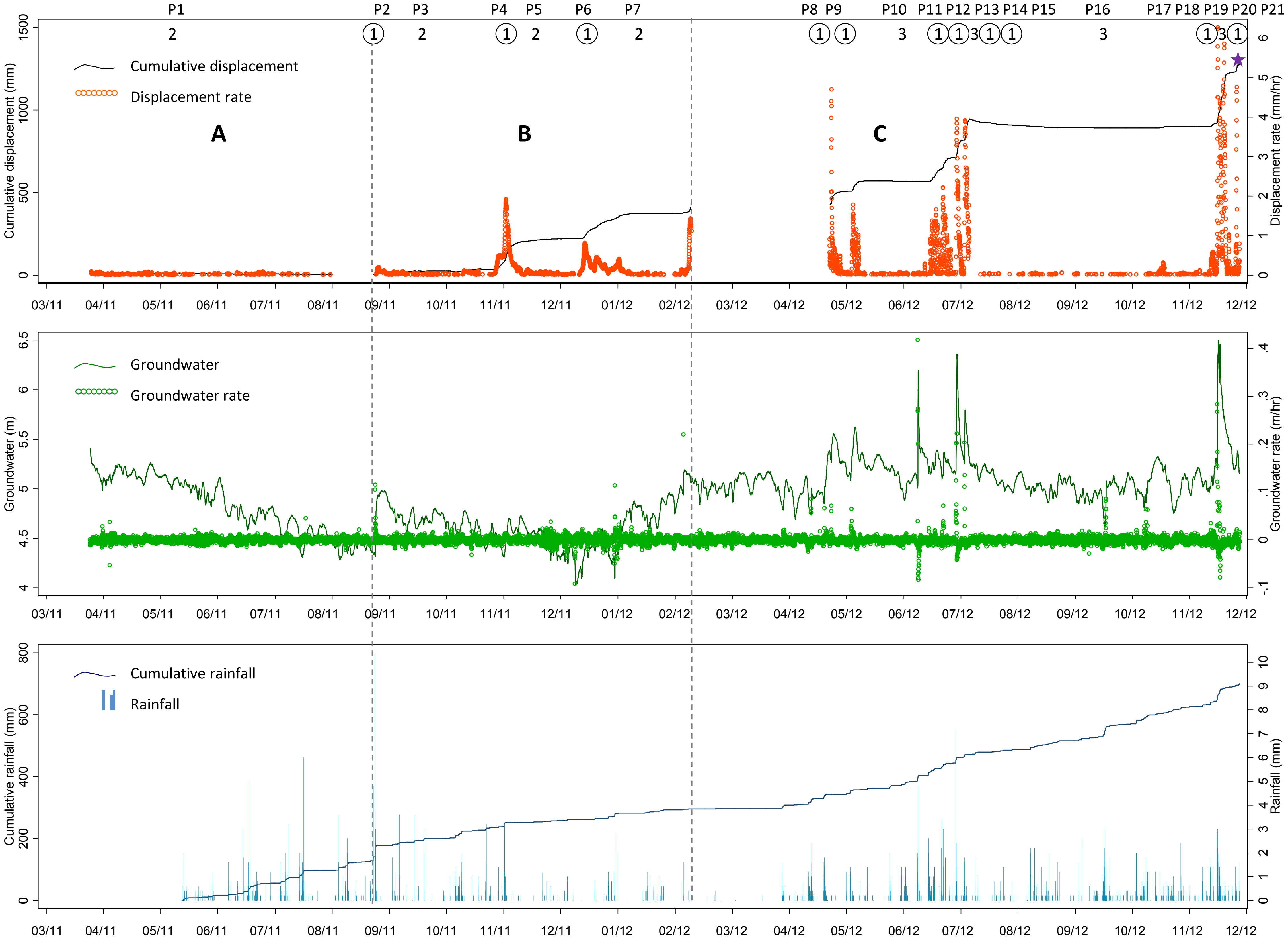

Figure 7.13 Patterns of post failure landslide movements based on field monitoring data between March 2011 and December 2012 presented in three periods (Period A, B and C). a) Graph of cumulative displacement (mm) and displacement rate (mm/hr); b) Graph of groundwater (m) and groundwater rate (m/hr); c) Graph of cumulative rainfall (mm) and hourly rainfall (mm) over the entire monitoring period. Period A is dominated by slow movement. This is due to low groundwater levels. Period B 'graded' movement is alternated by accelerated (1) and slow (2) movements, indicating reactivation and post-failure creep behaviours. Period C is dominated by accelerated movements (1) but has some periods of no movement (3). The cumulative displacement is depicted as a stepped graph as the displacement rates are corresponding to a variation of groundwater. Displacement rates are especially high towards the end of the monitoring period, probably responding to high groundwater fluctuations. Note: 1- accelerated movement; 2- slow movement; 3- no movement; P- periods of landslide movement; the asterisk – break point of the extensometer; and the dashed line – period boundary between A, B and C.

7.6 The relationship between pore water pressure and displacement rate

This section explores the relationship between displacement rate and pore water pressure in both the field and the lab datasets. Several previous studies have examined the relationship between groundwater levels or pore pressure conditions and the observed rate of movement (Table 7.6 and Figure 7.14) (e.g. Nakamura, 1984; Bertini et al., 1986; Corominas et al., 2005; Van Asch et al., 2007; Gonzalez et al., 2008; Matsuura et al., 2008; Massey et al., 2013). In each case it has been noted that there is complexity in this non-linear relationship. Generally the relationship between groundwater and displacement rate shows a marked hysteresis, with the movement rate during increasing groundwater level phases being different to that when the groundwater level is in decline. In each case the pattern of deformation can be subtly different, and in some cases the movement rate is higher for an increasing groundwater level, whereas in others, the opposite is true.

7.6.1 Observed in Field monitoring data

A similar, but more complex relationship has been found in this study, in which the onset of accelerated movements corresponded to an increase in groundwater. Two types of pattern were observed, with both clockwise and anti-clockwise hysteresis loops. The clockwise pattern (in which movement rate declines before groundwater level starts to decline) is a common pattern that is found elsewhere for similar materials (e.g. Van Asch et al., 2007; Massey et al., 2013). However, anti-clockwise patterns (in which movement rates remain high as groundwater levels decline) are only occasionally observed (e.g. Corominas et al., 2005; Gonzalez et al., 2008; Matsuura et al., 2008), generally when reactivated landslides are undergoing deformation as a response to hydrological influences (e.g. Van Asch 2007 for the La Valette landslide, France; Massey 2011 for Utiku landslides, NZ). Most of the movement periods in this study show a ‘clockwise’ pattern of hysteresis (Figure 7.14).

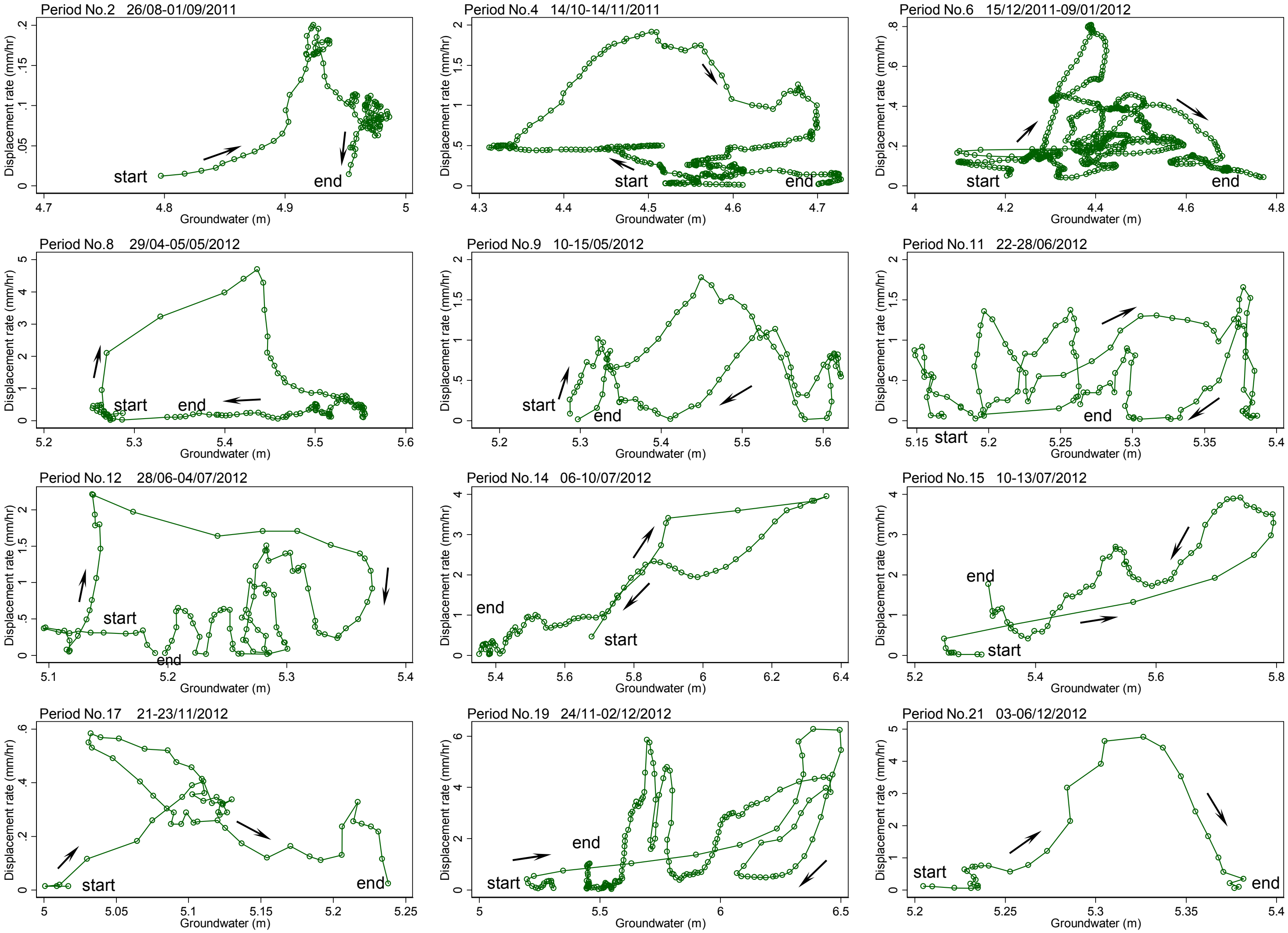

Figure 7.14 Hourly displacement rate plotted against the corresponding hourly groundwater for accelerated movement periods. Hysteresis relationship between groundwater and displacement rate mostly show a similar 'clockwise' pattern. However, occasionally the anti-clockwise pattern is found in Periods 15 and19, showing that the reactivation landslide is undergoing deformation in response to the hydrological conditions. The arrows represent the direction from the start to the end of the hysteresis relationship.

Evidence of such cohesive soil properties have been found to be similar to the observations of the translational Utiku landslide, New Zealand (Massey et al., 2013) and those of the complex landslide in the French Alps studied by Van asch et al., (2007). These two landslides are composed of a clay matrix, which resulted in a clockwise pattern of hysteresis between landslide displacement and groundwater (Table 7.6).

The hysteresis loops suggest that once movement occurs, groundwater and landslide velocity have a weaker than expected relationship in which other factors may be important. Some possible explanations suggested in previous studies include:

1) Rate-induced changes in shear strength of the slip surface (i.e. a dynamic rather than static frictional resistance), caused by a rearrangement of the clay particle bonds during shearing (Massey, 2010; 2013);
2) Consolidation of the shear band during movement leading to strength regain, and attenuation of the likelihood of reactivation (Angeli et al., 2004);
3) Progressive changes in landslide geometry (e.g. mass transfer), debuttressing of slide blocks, and shear resistance developed along the landslide flanks and between the slide blocks may also control the movement arresting processes (Morgenstern, 1995; Ferrari et al., 2011); and,
4) Viscosity functions: once movement is triggered the landslides move as visco-palstic flows rather than via rigid-plastic frictional slip (Iverson, 1985; Angeli et al., 1996; Corominas et al., 2005; Van Asch et al., 2007; Ranalli et al., 2009).

Table 7.6 Summary relationships between landslide displacement and groundwater/pore water pressure in different landslides

Hysteresis patterns	Where/Name	Landslide materials	References
Clockwise	a) The translational Utiku landslide, New Zealand	Clay layers within the Taihape mudstone	Massey et al., 2013
	b) The La Valette landslide complex in the French Alps (Middle part- a translational slide)	Strongly remoulded Terres Noires mixed with morainic deposits. The matrix is a sandy silt with a considerable clay fraction in which larger fragment (stone, gravel) are incorporated	Van Asch et al., 2007
Anti-clockwise	c) The Fosso San Martino landslide, Central Italy	A narrow stratum of weathered bedrock overlaid by a clayey silt colluvial cover in which the sliding mass moves essentially as a rigid body	Bertini et al., 1986
	d) The translational Vallcebre landslide in the Eastern Pyrenees, Spain	A set of shale, gypsum and claystone	Corominas et al., 2005; Gonzalez et al., 2008
	e) The reactive landslide for debris at the coast of Japan	The Tertiary material (i.e. soft clay, silt and rough fragments of broken stone). The general properties of these rocks make them prone to clay formation by hydration and weathering due to weak cementation.	Matsuura et al., 2008

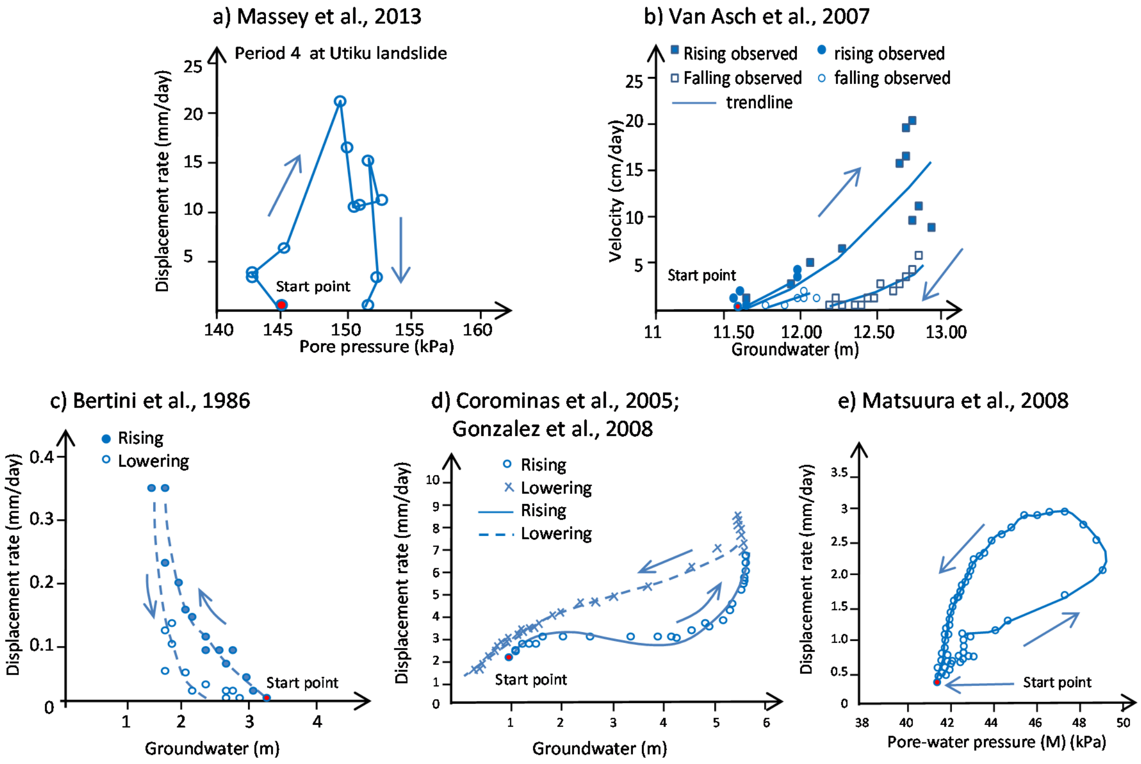

Figure 7.15 Two patterns of hysteresis between landslide displacement rate and groundwater: The clockwise pattern has been observed in cohesive materials (a and b). Conversely, the anti-clockwise pattern has been observed in weak cementing materials (c, d and e).

Conversely, due to the increasing groundwater nearly reaching (Period 15) or having reached the ground surface (Period 19), two periods of movement (Periods 15 and 19) register an ‘anti-clockwise’ pattern. The accelerated movements occurred in response to higher rates of groundwater increase and higher rainfall magnitudes. This possibly causes the soil material to be largely restructured due to particle rearrangement under shear, leading the soil to transform to a more plastic behaviour. As a consequence, the movement rates remain high as groundwater levels decline as landslide movement adopts an anti-clockwise pattern (strain softening) due to ongoing deformation of landslide mass. According to Prévost and Höeg (1975), plasticity theory can be used to explain the strain-softening behaviour in soil. Work is done when the zone of plastic yielding in a strain softening material expands during continued yielding. When the incremental external work added into the system, together with the incremental work released from the plastic, strain-softening zone equals or exceeds the work that may be absorbed by the surrounding unyielded and /or strain-hardening soil, a failure will occur.

This can be observed in the TLS data as the displacement occurred continuously in relation to the progressive landslide development of mudslide/flow (Chapter 4, Figure 4.2-4.5). Moreover, this can be confirmed with photographs, as seen in Figure 7.16. The photographs show the development of transverse cracks at the toe of the reactive landslide during wet periods (i.e. March 2011, July 2012). Usually, an ‘anti-clockwise’ behaviour can be found in brittle materials or weak rocks, such as fragments of broken rock or bedrock, as can be seen in the examples in Table 7.6 (Matsuura et al., 2008 - landslide in Japan; Gonzalez et al., 2008 - Vallcebre landslide in Spain). However, as the discussion above has shown, such behaviour can also be observed at the glacial till, despite it being primarily composed of clay.

It is interesting to note that in each of the two reactivation periods, a clockwise pattern preceded the anti-clockwise movement pattern observed. For example, in Period 14, a sharp increase in groundwater level (from about 5.1 m to 6.4 m), which almost reached the ground surface, led to accelerated movement and generated a clockwise hysteresis pattern. Later on in Period 15, as groundwater increased again (from 5.2 m to 5.8 m), a strain weakening behaviour was observed (Figure 7.7 and 7.14). Similarly in Period 19, the groundwater level reached the ground surface, leading to increasing displacement. At this stage, it presented a clockwise pattern. When the groundwater dropped the rate of displacement continued to increase, indicating that an 'anti-clockwise' pattern had developed. This demonstrates that landslide displacement may reflect a progressive change in dominance from clockwise to anti-clockwise hysteresis patterns, suggesting a progressive change from a hardening to a softening processes.

a) March 2011

b) July 2012

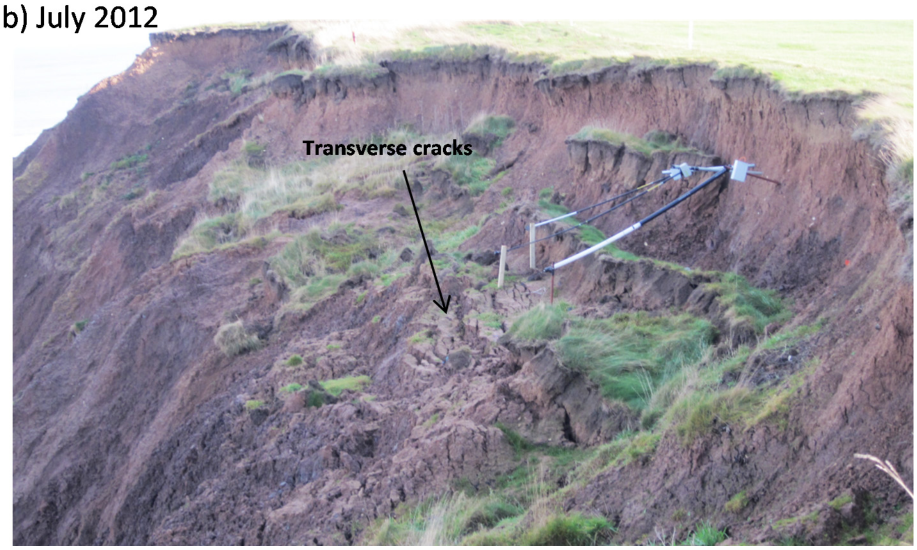

Figure 7.16 The photographs of the progressive landslide development of mudslide: a) the transverse cracks were observed clearly in March 2011 (a) and (b) some cracks have developed to become a part of mudslides during wet period (i.e. July 2012).

7.6.2 Laboratory tests observations

Three non-linear rates of increasing pore water (average PPR rate of 0.5, 1 and 2 kPa/hr) were applied in order to replicate the field stress conditions of the reactivated landslide (Figure 7.17). The developments of displacement rate respond to increasing pore water pressure in three ranges of PPR tests. All PPR tests illustrated the deceleration phase at the beginning of the tests due to the increase of pore fluid in the sample. The displacement rates accelerated in response to the increase of pore water pressure as void ratio increased significantly in relation to low effective stresses (as discussed in section 7.4.4). However, the deceleration phases were observed thereafter when pore water pressure was increasing and approaching stability leading to little changes in the pore water pressure rate (ΔP). This can suggest that the displacement rates are dependent on both the stress state and the rate of change of effective stress. As a consequence, the laboratory testing results consistently generated the clockwise hysteresis pattern (Figure 7.18), similar to field monitoring data. The clockwise pattern is a consequence of plastic or ductile deformation, particularly given that clays exhibit strain-hardening behaviour (as discussed in section 7.4.3). This suggests that the strength mobilized in reactivation is the residual strength and movements generally correspond to the sliding of rigid blocks of material along a pre-existing basal shear surface. However, residual strength is a dynamic property, with the increase or decrease in strength occurring as a result of changes in pore water pressure.

The relationship among displacement, displacement rate and pore water pressure can be explained further by a model of the development of displacement and displacement rate observed in the PPR tests (Figure 7.19). The diagram shows three stages in the development of landslide displacement. In each case, three illustrations are provided: a graph of pore water pressure against time; a graph of displacement against time; and a graph of displacement rate against time. The first situation has shown no features of increasing pore water pressure. Thus, displacement and displacement rate are zero (Figure 7.19: A). In Figure 7.19: B, pore water pressure increases above the yield point (the point when landslide starts to initiate movement), resulting in displacement and displacement rate increase as a response to increasing pore water pressure. In Figure 7.19: C, pore water pressure increases and approaches a constant. Therefore, the rate of change of pore water pressure (ΔPWP) decreases. As a result, displacement is still being observed but the displacement rate declines. The landslide rate responds to the decrease of ΔPWP even though pore water pressure remains high. This simple model, which is based on the PPR tests, explains why the displacement rate declined even though pore water pressure remained high. Thus, for a real landslide system, the key behaviour of landslide movement reacting on the pre-existing shear surface is dependent on the stress state and the rate of change of effective stress due to increasing pore water pressure and the rate of change of pore water pressure.

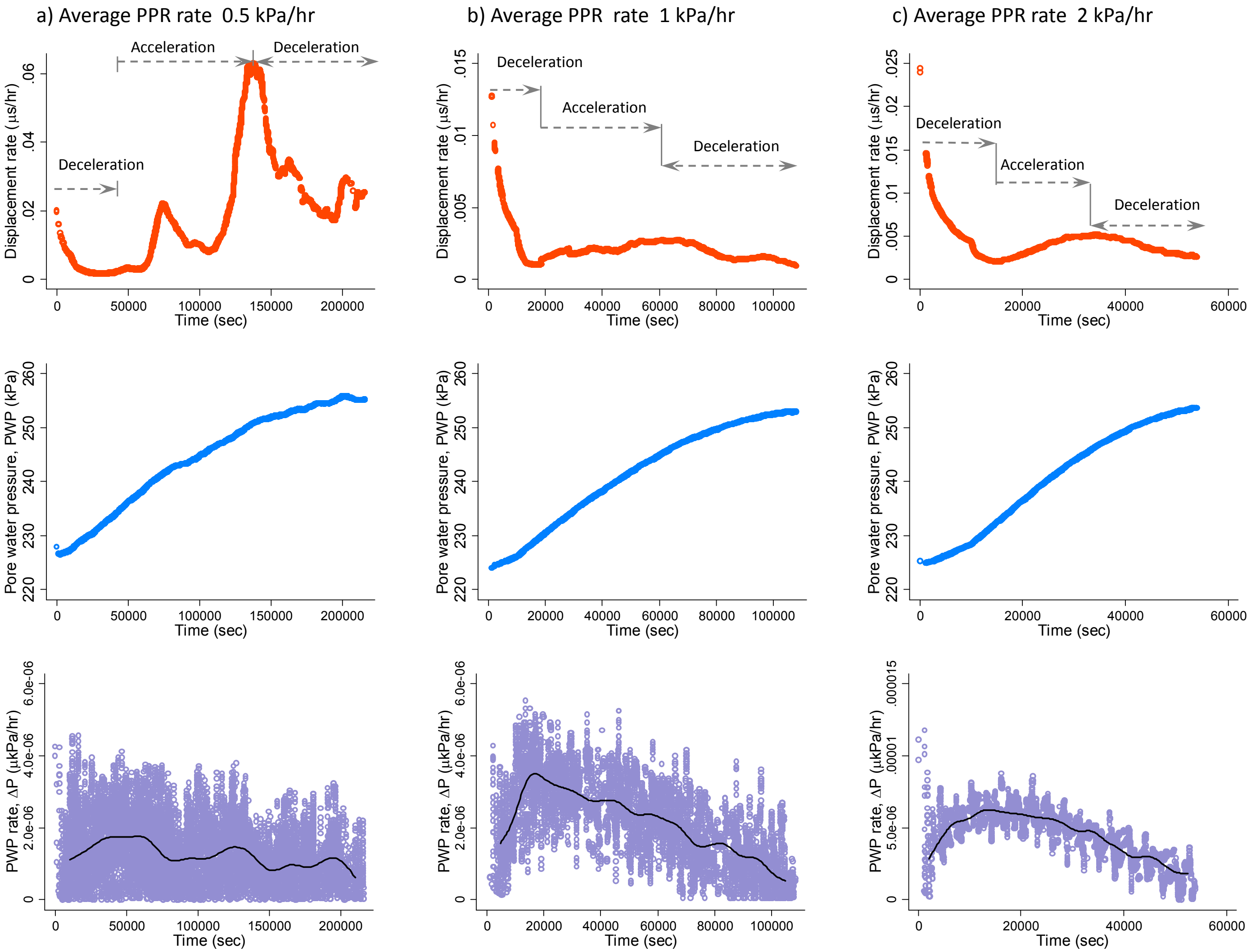

Figure 7.17 The development of displacement rate in response to increasing pore water pressure in three ranges of PPR tests (average reinflation rates of 0.5 (a), 1 (b) and 2 (c) kPa). All plots of displacement rates against time show similar patterns, which are deceleration at the initial PPR test and then acceleration stage during increasing pore water pressure before deceleration due to the pore pressure approaching constant and the change of pore water pressure declining.

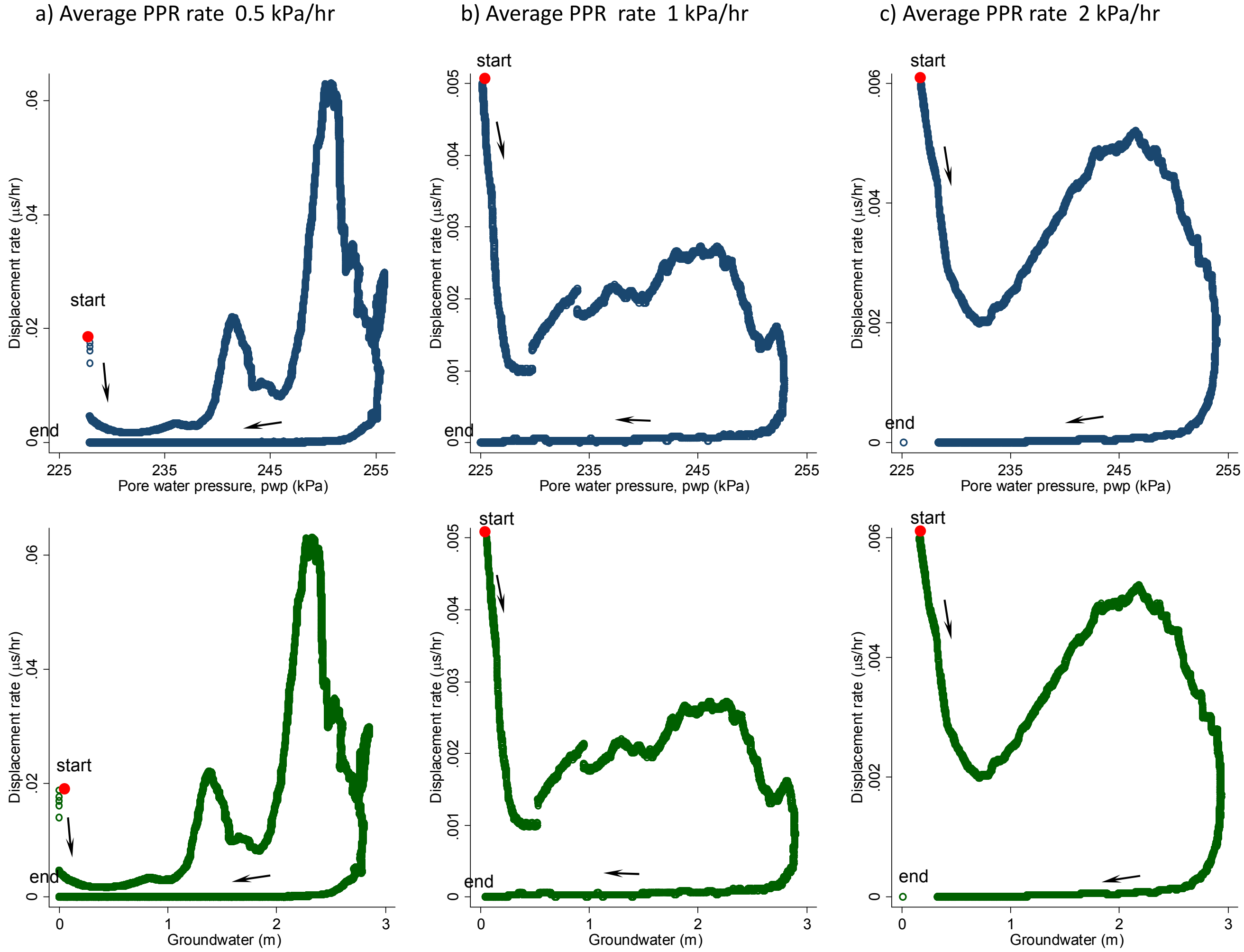

Figure 7.18 Laboratory testing results undertaken using different average PPR rates of 0.5, 1 and 2 kPa/hr presented by plots of displacement rate against pore water pressure (above) and plots of displacement rate against groundwater (below). The hysteresis relationship between landslide displacement rate and pore water pressure/groundwater of the three different reinflation rates show a similar 'clockwise' pattern. The arrows represent the direction from the start to the end of the hysteresis relationship.

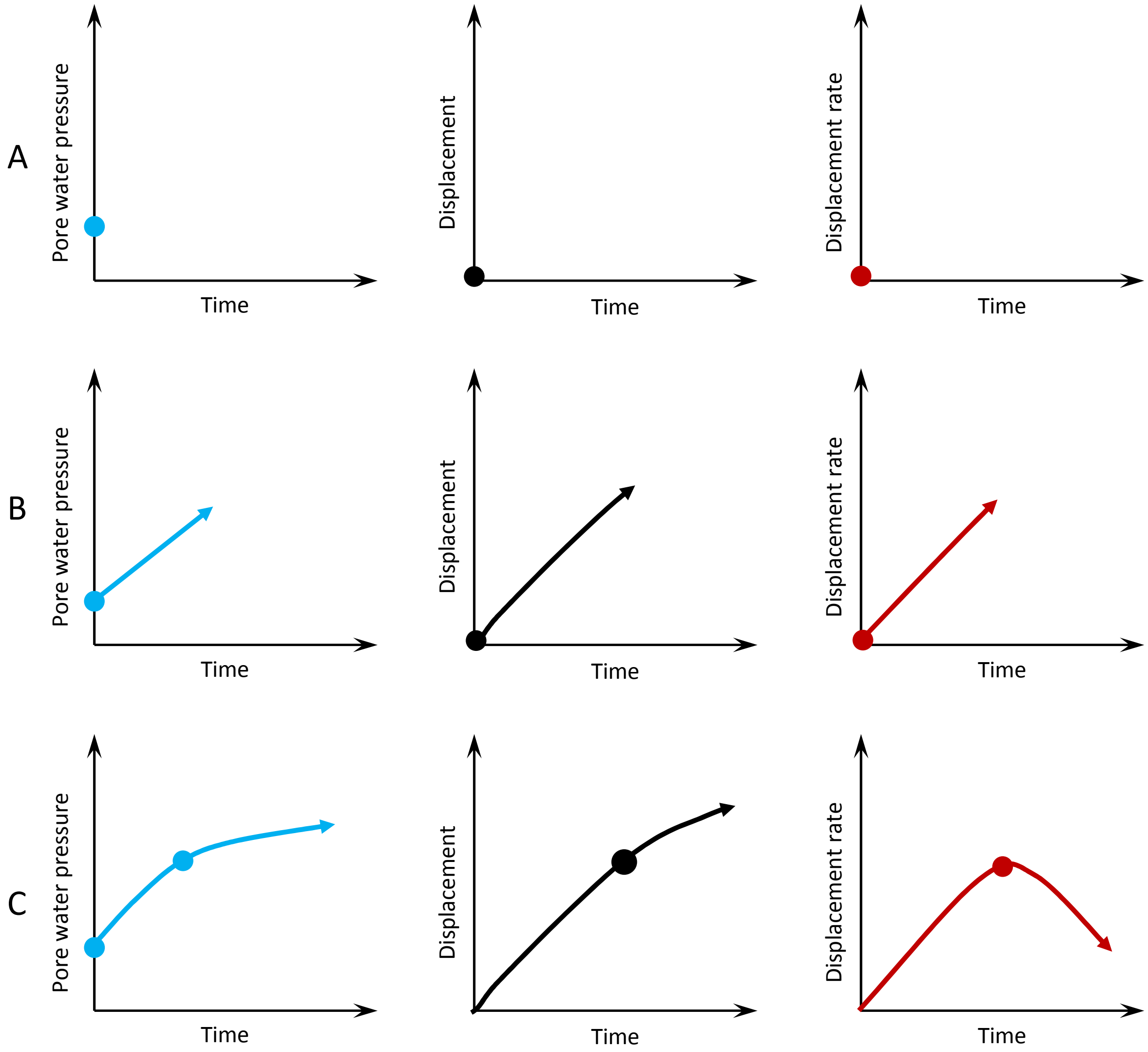

Figure 7.19 A diagram depicting the development of displacement and displacement rate observed in PPR tests showing three stages in the development of landslide displacement (A, B and C).

7.7 An event-based model of reactivated landslide movement

In the previous section the complexity of the relationship between displacement rate and groundwater level has been examined. This section seeks to further explore this relationship by deriving a model of reactivated landslide movement. This model is divided into two styles, namely: 1) A conventional model presented by an average hysteresis pattern of aggregating the 12 occurrences in which hysteresis was observed within periods of accelerated movements; and, 2) A model of hysteresis results of accelerated movement generated by gridding all observed data within reactivation periods, showing the probability of any given movement rate for any given ground water level observed.

Firstly, under the conventional model, the average displacement rates for the 12 accelerated movement periods (Figure 7.14) were calculated based on 0.1 m increments of groundwater level (between 4 and 6.5 m; see Table 7.7). Equations to model the relationship between groundwater and the average displacement rates were produced for periods of rising groundwater, and also falling groundwater levels. Finally, the average displacement rates were reproduced using the resultant equations in order to produce the average response model of the behaviour of the Upgang cliff landslide. The model was drawn across three regions that describe the maximum, mean and minimum of observed values from the monitoring data (Figure 7.20). For example, at a groundwater level of 5.5 m, the minimum displacement rate observed was 0.5 mm/hr, the mean displacement rate was 1 mm/hr, and the maximum displacement rate was 1.5 mm/hr. The model indicates that hysteresis is observed, with exponential best-fit trendlines of rising and lowering limbs separated with a clear gap. Conventionally, assuming a simple relationship between groundwater and displacement, the exponential trends in each of the three regions (i.e. maximum, mean and minimum) should show a single line. As such, the gaps as seen in Figures 7.20a and 7.20c are probably an error of the average displacement rates, which scatter and fall at different groundwater levels. The hysteresis pattern does not represent the complexity of the relationship between displacement rate and groundwater, masking the significant variability of the field monitoring data as shown in Figure 7.14. Thus, in this model, increased landslide rates as groundwater increases can be observed. So, instantaneous groundwater level alone provides a poor understanding of landslide displacement rate, as discussed above.

Table 7.7 The average displacement rates for 12 occurrences in which hysteresis was observed within period of accelerated movements falling into the rising limb (Up) and the lowering limb (Down)

Groundwater (m)	Avg. displacement rate, Up (mm/hr)			Avg. displacement rate, Down (mm/hr)		
	Max	Min	Mean	Max	Min	Mean
4.00	0.15	0.14	0.14	-	-	-
4.10	0.15	0.15	0.15	0.14	0.12	0.13
4.20	0.24	0.09	0.16	0.19	0.09	0.12
4.30	0.65	0.19	0.37	0.46	0.17	0.31
4.40	0.87	0.22	0.48	0.47	0.18	0.32
4.50	0.91	0.12	0.34	0.39	0.10	0.21
4.60	0.79	0.11	0.37	0.68	0.04	0.28
4.70	0.08	0.03	0.07	0.16	0.02	0.07
4.80	0.06	0.02	0.04	-	-	-
4.90	0.20	0.05	0.11	0.20	0.01	0.10
5.00	0.47	0.19	0.33	0.58	0.01	0.40
5.10	1.06	0.13	0.54	0.89	0.12	0.39
5.20	0.90	0.15	0.43	0.80	0.09	0.35
5.30	2.03	0.69	1.44	0.87	0.06	0.38
5.40	2.49	0.71	1.43	1.42	0.15	0.54
5.50	1.04	0.45	0.73	1.34	0.51	0.87
5.60	1.66	0.96	1.33	2.80	1.01	1.73
5.70	2.35	1.64	1.98	3.86	1.65	2.80
5.80	2.33	1.72	2.03	3.10	1.23	1.56
5.90	3.41	3.41	3.41	2.24	1.30	1.72
6.00	1.76	0.66	1.11	2.69	1.28	2.40
6.10	2.72	2.72	2.72	3.24	1.56	2.36
6.20	2.39	1.98	2.18	3.81	1.92	2.40
6.30	5.06	3.15	3.96	4.59	2.38	3.55
6.40	6.23	3.98	5.11	4.49	2.84	3.92

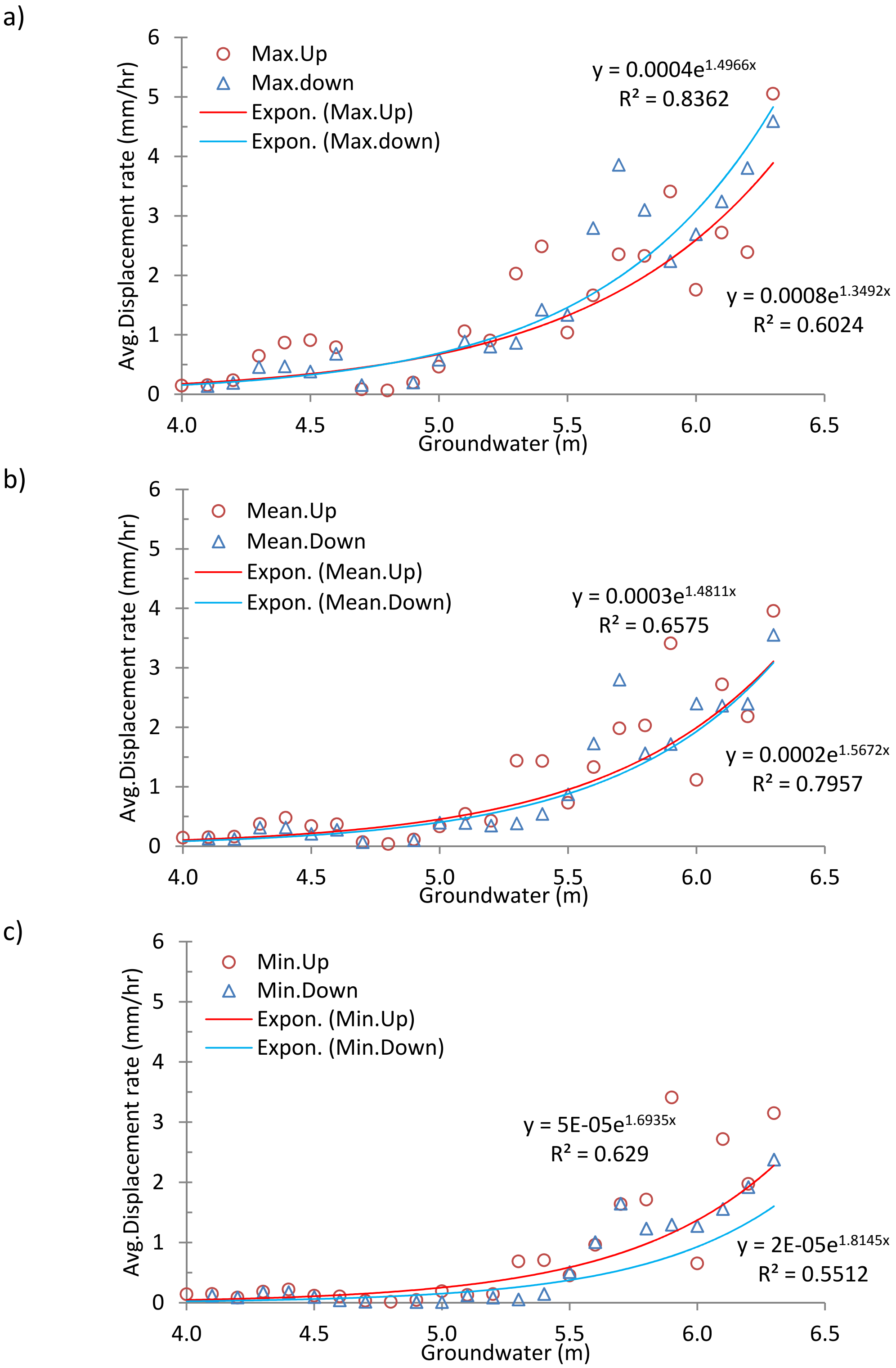

Figure 7.20 Plots of average displacement rate against groundwater level with their exponential trends showing the conventional hysteresis relationships between groundwater and displacement rates, separating the rising up (Up) and dropping (Down) of groundwater into three regions: a) Max-region (Max.Up; Max.down), b) Mean-region (Mean.Up; Mean.Down) and c) Min-region (Min.Up; Min.Down). The different landslide rates occur at the same groundwater level depending on whether groundwater is rising or dropping.

An alternative approach is to use the rasterised model to examine the landslide movement. The twelve movement periods with hysteresis results showing accelerated movement have been used to examine the groundwater conditions and displacement rates by gridding all observed data to derive a set of probabilities of movement for any given groundwater level. Here, the data is used to count the frequency of observed displacement rates relative to specific groundwater levels. As a result the probability distribution is presented in a raster format with 0.05 m resolution in ground water level and 0.05 mm/hr in displacement rate (Figure 7.21).

To illustrate the utility of this plot, the diagram shows the probability of any given displacement rate for any given groundwater value. For example, at Point x1 (Figure 7.21), the groundwater level of approximately 5.7 m, there is a 3 - 3.5% probability that the displacement rate will be approximately 1 mm/hr. At Point x2, same groundwater level (5.5 m), there is a 3 - 3.5% probability that the displacement rate will be approximately 2.5 mm/hr. However, following the x line, it is possible to find a higher rate of displacement (i.e. > 4 mm/hr) with a lower probability (≤ 2.5 % probability). It should be noted that at higher groundwater levels, the range of possible displacement rates is larger. Additionally, different displacement rates can occur at the same groundwater level. Nevertheless, the hysteresis relationship between displacement rate and groundwater is difficult to explain by looking at merely one parameter set, as suggested elsewhere (Van Asch et al., 2007).

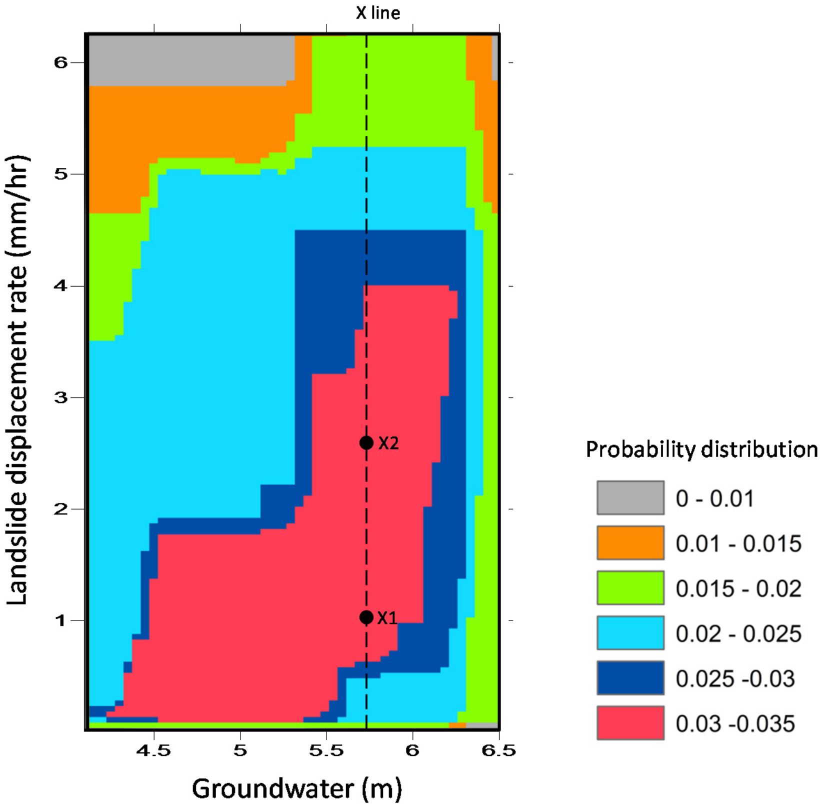

Figure 7.21 Conventional model of the relationship between average displacement rate and groundwater level presented in probability distribution. The 12 periods of accelerated movement (Periods 2, 4, 6, 8, 9, 10, 11, 13, 14, 15, 17 and 19) are used to calculate a raster hysteresis model using the data metric gridding method. The hysteresis model shows by colour rings from low to high probability (0 – 0.035). As can be seen, the landslide rates fall under a range of varied groundwater levels with a different range of probability. This suggests that the emerging hysteresis is with local and temporal variations in groundwater level. The X line represent the example at a groundwater level of 5.7 m: at x1 displacement rate falls to 1 mm/hr and at x2 displacement rate falls to 2.5 mm/hr.

7.8 Chapter summary

This chapter has discussed and evaluated the research findings under four main themes: 1) landslide morphology; 2) associated deformation mechanisms with reference to the accelerated movement; 3) hysteresis relationship between groundwater and landslide displacement rate; 4) a generalised model of reactivated landslide movement. A synthesis of these key themes has improved understanding of the episodic post-failure landside movement pattern of this landslide complex. What follows is a list of key findings:

7.8.1 Landside morphology

1. The landslide deformation can be separated into four morphodynamic zones: ‘Slide source’ (Zone A); ‘Slide source and transportation zone’ (Zone B); ‘Erosion zone’ (Zone C); ‘Toe erosion and accretion zone’ (Zone D).

2. Different landslide failures occurred at lithostratigraphic boundaries.

3. There are temporal linkages between failure events such that a significant number of landslide failures are caused by the reworking of previously failed material and the failure of fresh material from the cliff.

7.8.2 Deformation mechanism of reactivation

1. Plasticity explains the deformation behaviour of accelerated movements, as can be seen from both the field monitoring data and laboratory testing (reinflation tests), as an asymptotic trend in plots of 1/displacement rate against time (Δ-t space). The asymptotic trend reflects the key property of plastic behaviour. This suggests that reactivations of the landslide behave in accordance with either ductile or plastic deformation.

2. The dilative behaviour is affected by the systematic changes of void ratio under a non-linear pore water pressure increase. Three phases of dilative behaviour have been observed

under the reinflation process in terms of void ratio and effective stress relationship (e-σ’): a) push and climb; b) localised sliding; c) generalised sliding. As a result of the shearing and subsequent rearrangement of the material particles, the samples became significantly restructured as shown by an exponential acceleration of displacement rates.

7.8.3 Hysteresis relationship between groundwater and landslide displacement rate

1. Two patterns of hysteresis relationship between displacement rate and groundwater have been observed in this study namely, clockwise (strain hardening) and anti-clockwise (strain softening) hysteresis loops. Most of the accelerated movement periods show a ‘clockwise’ pattern, indicating that movement rate declines before groundwater levels start to decline. With regards to the anti-clockwise pattern, movement rates remain high as groundwater levels decline. The accelerated movements occurred continuously in response to the hydrological conditions (higher groundwater rate and the magnitude of rainfall). This possibly led to a significant restructuring of the soil material due to particle rearrangement under shear, causing the soil to transform to a more plastic behaviour. As a consequence landslide movement adopts an anti-clockwise pattern (strain softening) due to the ongoing deformation of landslide mass.

2. Laboratory results revealed the clockwise relationship, which is similar to that observed in the field monitoring data. This suggests that the pattern could be related to material properties. The displacement rates accelerated in response to the increase of pore water pressure as void ratio increased significantly in relation to low effective stresses. However, the deceleration phases were observed thereafter when pore water pressure was increasing and approaching stability leading to minimal changes in the pore water pressure rate (ΔP). This can suggest that the displacement rates are dependent on both the stress state and the rate of change of effective stress. The clockwise pattern is a consequence of plastic or ductile deformation, particularly given that clays exhibit strain-hardening behaviour. This suggests that the displacement mobilised in reactivation is the materials’ residual strength and movements generally correspond to the sliding of rigid blocks of material along a pre-existing basal shear surface. However, residual strength is a dynamic

property, with the increase or decrease in strength occurring as a result of changes in pore water pressure.

7.8.4 Implications for reactivated landslides based on landslide events

The complexity of the hysteresis relationship between displacement rate and groundwater level can be explored by depicting a model of reactive landslide movement into two styles – conventional and rasterised.

1. The conventional model is represented by an average hysteresis pattern of aggregating the 12 occurrences observed in the field monitoring data, indicating exponential best-fit trendlines of rising and lowering limbs. The hysteresis pattern does not represent the complexity of the relationship between displacement rate and groundwater, masking significant variability within the field monitoring data. Thus, this model predicts increased landslide movement rates as groundwater increases can be observed.

2. The model shows the probability of any given displacement rate for any given groundwater value. The rasterised model presents the probability distribution of movement under any given groundwater level, which has a raster format with 0.05 m resolution at ground water level and 0.05 mm/hr in displacement rate. This model suggests that at higher groundwater levels, the range of possible displacement rates is wider and different landslide rates can occur at the same groundwater level, questioning the ability to predict movement rate from a non-continuous measurement of groundwater.

Chapter 8 Conclusion

8.1 Key findings

This thesis has studied landslide movement patterns and mechanisms on a reactivated coastal landslide complex influenced by groundwater fluctuations. More specifically and uniquely, the spatial and temporal patterns of landslide movement have been considered at both coarse and fine scales using a range of field-based techniques. While terrestrial laser scanning can be used to explain the landslide processes across the whole cliff face, the landslide deformation is observed using more intensive field monitoring. Further, the underlying mechanisms of landslide movements have been explored using a set of laboratory tests.

The following summarises the key findings of the thesis:

1. Patterns of post-failure behaviour

The deformation behaviour of the reactivated landslide during the period of observation can be described as episodic, and can be divided into three types of movement, namely: 'accelerated movement' or reactivation (0.2 mm/hr – 6.27 mm/hr); 'slow movement' (< 0.2 mm/hr); and, negligible movements. The slow movement of the landslide can be referred to as the post-failure creep stage of landslide deformation. Slow movements only occurred during the initial stages of deformation, after which movements are either accelerated or ceased when deformation transits into periods of 'no movement'. Conversely, accelerated movements are referred to as a stage of 'reactivation'. This type of movement is characterised by increased displacement (from 13.39 to 309.67 mm) over a shorter period of time in response to increased groundwater fluctuations. Due to a rapid and continuous increase of the void ratio in relation to high groundwater levels and high fluctuations in groundwater change rate, the effective stress on the shear surface became particular low (Figure 7.11), leading to high rates of deformation of the landslide mass. These patterns of post-failure deformation are distinct from 'faster motion', 'slower motion' and 'cyclic motion' (Figure 2.10) that were observed by Massey et al. (2013) at the Utiku landslide, New Zealand. However, both sets of observed patterns are typically controlled by hydrological triggers, with an increase of pore water pressure leading to landslide reactivation.

2. Underlying mechanisms of reactiviation

A reactivated landslide is often associated with an increase in pore water pressure and the mobilized shear strength is closely related to the residual strength. This study indicates that plasticity is a key control underlying the deformation mechanisms of reactivated landsliding. An asymptotic trend in plots of 1/displacement rate against time (Δ-t space) (Petley et al., 2002) shows that reactivations of the landslide occur with either ductile or plastic deformation (Figure 7.9). The development of plastic deformation was based on the analysis of the PPR tests, which indicates that the soil behaviour was affected by large void ratio increments under a non-linear pore water pressure increase (Ng, 2007; Ng and Petley, 2009).

3. Patterns of hysteresis between displacement rate and groundwater

Two patterns of hysteresis relationship between displacement rate and groundwater were observed from the field monitoring data, namely, clockwise and anti-clockwise hysteresis loops. Most of the movement periods show a clockwise pattern of hysteresis, in which movement rate declines before groundwater levels start to decline. This pattern is also found elsewhere for clay materials (Van Asch et al., 2007; Massey et al., 2013).

Conversely, the anti-clockwise pattern of hysteresis, in which movement rates remain high as groundwater levels decline is occasionally observed when reactivated landslides are undergoing deformation as a response to hydrological influences. Commonly, the anti-clockwise behaviour can be found in brittle materials or weak rocks, such as fragments of broken rock or bedrock, as can be seen in the examples in Table 7.6 (i.e. Bertini et al., 1986; Corominas et al., 2005; Gonzalez et al., 2008 and Matsuura et al., 2008). However, such behaviour can also be observed in glacial till, despite being primarily composed of clay. This demonstrates that landslide displacement may reflect a progressive change in dominance from clockwise to anti-clockwise hysteresis, suggesting a change from a strain hardening to a strain softening process. Other than in-situ field monitoring, laboratory tests were also carried out using non-linear increase in pore water pressure (0.5, 1 and 2 kPa/hr). The laboratory results only revealed the clockwise pattern of hysteresis, which suggests that this pattern could be related to material properties. The clockwise pattern is a result of plastic or ductile deformation, particularly given that clays exhibit strain-hardening behaviour.

These results have important implications for understanding landslide movement patterns including the influences on landslide morphology, patterns of post failure, their mechanism and hysteresis relationship between displacement rate and groundwater. The results confirm that a combination of field monitoring and laboratory testing is a powerful approach to explore the controls on the nature and style of landslide movement.

8.2 Limitations of research

This research has sought to advance the understanding of landslide movement patterns and their mechanisms in shallow landslides. However, there exist certain research limitations in in-situ monitoring, data continuity and laboratory testing:

1. In terms of in-situ monitoring, there was only one extensometer that provided a significant continuous displacement record throughout the monitoring period. Linking extensometer data directly with that from the laser scanning may prove fruitful in future work linking local-scale deformation to wider-scale processes across the slope. Moreover, dGPS monitoring may be advantageous in providing specific and definitive coordinates of the extensometer position, in combination with the monitoring displacement across the extensometer to allow absolute movement to be measured.

2. Missing data was a problem during some monitoring periods due to two main problems, namely the movement range limits of the instruments and the weather conditions. During the initial phases of monitoring, the vibrating-wired extensometers provided excellent detection of small-scale magnitudes of movement (0.001 mm/record), but these sensors

only had a limited range (< 10 mm). This equipment was also not durable. Moreover, due to the design of the equipment, the maximum displacement that could be recorded was 5 cm, before the wire-rod needed to be re-zeroed, and as such the instrument range was less than the movement recorded during some monitoring epochs or single movement events. This led to data loss either because the equipment was not fixed in place or some timing errors were incurred due to the need for resetting the instruments. Subsequently, the vibrating-wired extensometers were replaced by the string extensometers, which provided more consistent displacement data. However, such extensometers cannot detect small displacements (< 0.3 mm/record), which resulted in 'noise' being recorded as significant during periods of monitoring, obscuring capture of the smallest movements. Therefore, the choice of equipment and monitoring system appropriate to the rate and magnitude of movement are of significant importance in investigating landslide movement. Additionally, the field site was visited at monthly intervals to carry out data capture via scanning and to download in-situ instrumentation. However, weather conditions such as fog, heavy rain or strong winds were the main causes of data loss in some periods due to visibility. Thus, for a manual monitoring system, revisiting the site more often may minimising data loss.

3. The displacement monitoring focused on the upper section of the cliff and described a landslide displacement pattern, which may not represent the whole landslide system. Similarly, laboratory results of both back pressure shear box (BPS) and pore pressure reinflation testing (PPR), which were undertaken on relatively small samples, and may not be representative of the entire field stress conditions. Moreover, due to time constraints, the laboratory testing program was limited, which resulted in a modest number of cases that can be referenced directly with field monitoring data. All results showed that the soil exhibited strain-hardening behaviour and this was consistent with most field monitoring results. However, some periods of accelerated movement showed a transition from strain-hardening to strain-softening behaviour. As such, the laboratory results may not reflect the potential variability of soil conditions, which may be significant in shaping the overall behaviour of the cliff. As a consequence, further testing should aim to explore ongoing deformation behaviours of soil, which change from strain-hardening to -softening behaviours. The test could be undertaken on pore water pressure cycles with a range of

pore water pressure change rates based on field monitoring data. Moreover, permeability tests could be undertaken in order to investigate further the effects of increasing pore water pressure.

8.3 Recommendations for further research

This research has provided an understanding of the mechanisms and processes operating in reactivated landslide complexes. Further research could be considered in order to advance the understanding of groundwater-induced landslide mechanisms. The PPR testing undertaken has been designed to replicate field conditions for groundwater-induced failure. The testing has successfully demonstrated the relationship between mean effective stress and time-dependent failure at a constant stress. It is clear that non-linear increases in pore water pressure as failure develops can be used to understand the behaviour of accelerated movement (reactivation). However, creep testing for slow movement does not replicate the cyclical patterns of increasing and decreasing pore water pressure within the landslide. As a consequence further testing through long periods of pore pressure reinflation on the back-pressured shear box samples would be beneficial to provide a more accurate simluation of these processes. Furthermore, as geochemistry and mineralogy directly influence geotechnical behaviour, these factors could be used to understand further aspects of soil composition reacting to an increasing groundwater. This would be beneficial for understanding the characteristics of soft soil sensitivity (i.e. glacial till) such as varying permeabilities due to changing liquid limit and void ratio.

The combined method of in-situ field monitoring and laboratory testing has provided a detailed understanding of landslide movement mechanisms. Therefore, detailed instrumentation and long-term monitoring would allow the consideration of important parameters such as characteristics of post failures, critical pore water pressure thresholds and hysteresis relationship between displacement rate and groundwater. These influences may be useful for developing a model that may predict landslide occurrences and movements. Additionally, similar material at different sites could be tested using the same method in order to facilitate investigation of a variety of soil deformation behaviours.

References

Agar, R. (1954) ‘Glacial and post-glacial geology of Middlesbrough and the Tees estuary’, *Proceedings of the Yorkshire Geological Society,* 29 (3): 237-253.

Allison, R. J., and Brunsden, D. (1990) ‘Some mudslide movement patterns’, *Earth Surface Processes and Landforms,* 15 (4): 297-311.

Anderson, S., and Sitar, N. (1995) ‘Analysis of rainfall-induced debris flows’, *Journal of Geotechnical Engineering,* 121 (7): 544-552.

Angeli, M., Gasparetto, P., Pasuto, A. and Silvano, S. (1989) ‘Examples of landslide instrumentation (Italy)’, Paper presented at Proc. XII ICSMFE, Rio de Janeiro.

Angeli, M.G., Gasparetto, P., Menotti, R.M., Pasuto, A. and Silvano, S. (1996) ‘A visco-plastic model for slope analysis applied to a mudslide in Cortina d'Ampezzo, Italy’, *Quarterly Journal of Engineering Geology and Hydrogeology,* 29(3): 233-240.

Angeli, M.-G., Pasuto, A. and Silvano, S. (2000) ‘A critical review of landslide monitoring experiences’, *Engineering Geology,* 55(3): 133-147.

Bell, F. G. (2002) ‘The geotechnical properties of some till deposits occurring along the coastal areas of eastern England’, *Engineering Geology,* 63(1-2): 49-68.

Bell, F. G., and Forster, A. (1991) ‘The geotechnical characteristics of the till deposits of Holderness’, *Geological Society, London, Engineering Geology Special Publications,* 7(1): 111-118.

Benson, C. H., Daniel, D.E. and Boutwell, G.P. (1999) ‘Field performance of compacted clay liners’, *Journal of Geotechnical and Geoenvironmental Engineering,* 125(5): 390-403.

Bertini, T., Cugusi, F., D’Elia, B. and Rossi-Doria, M. (1986) ‘Lenti movimenti di versante nell’Abruzzo Adriatico:caratteri e criteri di stabilizzazione, Paper presented at Proc. XVI Italian Geotechnical Congress, at Bologna.

Bishop, A. W., and Henkel, D.J. (1962) *The measurement of soil properties in the triaxial test* (2nd edition). London: E. Arnold.

Boulton, G. S., and Paul, M.A. (1976) ‘The influence of genetic processes on some geotechnical propeties of glacial tills’, *Engineering Geology,* 9: 159-194.

Brabb, E. (1991) ‘The world landslide problem’, *Episodes,* 14(1): 52-61.

Brand, E. W. (1981) 'Some thoughts on rain-induced slope failures', Paper presented at Proceedings of the 10th International Conference on Soil Mechanics and Foundation Engineering, Stockholm, 15-19 June.

British Standards Institution (BSI) (1981) 'Code of practice for site investigations', In *BS 5930: 1981*, 192.

British standards institution (BSI) (1990a) 'British standard methods of test for soils for civil engineering purposes. Part 1: General requirements and sample preparation', In *BS 1377: Part 1: 1990*, 28.

British Standards Institution (BSI) (1990b) 'British standard methods of test for soils for civil engineering purposes. Part 2: Classification tests', In *BS 1377: Part 2: 1990*, 61.

British Standards Institution (BSI) (1990c) 'British standard methods of test for soils for civil engineering purposes. Part 3: Chemical and electro-chemical tests', In *BS 1377: Part 3: 1990*.

British Standards Institution (BSI) (1990d) 'British standard methods of test for soils for civil engineering purposes. Part 8: Shear strength tests (effective stress)', In *BS 1377: Part 8: 1990*, 28.

Brooker, E. W., and Peck, R. B. (1993) 'Rational design treatment of slides in overconsolidated clays and clay shales', *Canadian Geotechnical Journal,* 30(3): 526-544.

Brown, S., Barton, M. and Nicholls, R. (2011) 'Coastal retreat and/or advance adjacent to defences in England and Wales', *Journal of Coastal Conservation,* 15(4): 659-670.

Brown, S., Barton, M. and Nicholls, R. (2012) 'The effect of coastal defences on cliff top retreat along the Holderness coastline', *Proceedings of the Yorkshire Geological Society,* 59: 1-13.

Brunsden, D., and Jones, D. K. C. (1980) 'Relative time scales and formative events in coastal landslide systems', *Zeitschrift für Geomorphologie, Supplementband, 34*: 1-19.

Brunsden, R. M. D. (1996) 'A physico-chemical mechanism of seasonal mudsliding', *Géotechnique*, 46(2): 259-278.

Carey, J. (2011) *The progressive development and post-failure behaviour of deep-seated landslide complexes*. Unpublished PhD Thesis, University of Durham.

Cascini, L., Bonnard, C.H., Corominas, J. Jibson, R. and Montero-Olarte, J. (2005) 'Landslide hazard and risk zoning for urban planning and development', In O. Hungr, R. Fell, R. Couture and E. Eberthardt (eds) *Landslide Risk Management*. London: Taylor and Francis, 199-235.

Catt, J. A. (2007) 'The Pleistocene glaciations of eastern Yorkshire: a review', Paper presented at Proceedings of the Yorkshire Geological and Polytechnic Society.

Chae, G. T., Yun, S.T., Kim, D.S., Kim, K.H. and Joo, Y. (2010) 'Time-series analysis of three years of groundwater level data (Seoul, South Korea) to characterize urban groundwater recharge', *Quarterly Journal of Engineering Geology and Hydrogeology,* 43: 117-127.

Chae, G.-T., Yun, S.T. Kim, D.S., Kim, K.H. and Joo, Y. (2010) 'Time-series analysis of three years of groundwater level data (Seoul, South Korea) to characterize urban groundwater recharge', *Quarterly Journal of Engineering Geology and Hydrogeology,* 43(1): 117-127.

Clark, A., and Guest, S. (1991) 'The Whitby cliff stabilisation and coast protection scheme', Paper presented at Slope stability engineering: developments and applications; Proceedings of the International Conference on Slope Stability, Isle of Wight, 15-18 April 1991.

Clarke, B. G., Chen, C.C. and Aflaki, E. (1998) 'Intrinsic compression and swelling properties of a glacial till', *Quarterly Journal of Engineering Geology and Hydrogeology,* 31(3): 235-246.

Clarke, B. G., Hughes, D. B., and Hashemi. S. (2008) 'Physical characteristics of subglacial tills', *Géotechnique,* 58: 67-76.

Corominas, J., Moya, J., Ledesma, A., Lloret, A. and Gili, J. (2005) 'Prediction of ground displacements and velocities from groundwater level changes at the Vallcebre landslide (Eastern Pyrenees, Spain)', *Landslides,* 2(2): 83-96.

Corominas, J., Moya, J. Lloret, A., Gili, J. A, Angeli, M. G., Pasuto, A. and Silvano. S. (2000) 'Measurement of landslide displacements using a wire extensometer', *Engineering Geology,* 55(3): 149-166.

Craig, R. F. (2004) *Craig's soil mechanics* (7th edition). London: Spon Press.

Cristescu, N., Cazacu, O. and Cristescu, C. (2002) 'A model for slow motion of natural slopes', *Canadian Geotechnical Journal,* 39(4): 924-937.

Cruden, D., and Varnes, D. (1996) 'Landslide Types and Processes', In S. R. Turner (ed) *Landslides Investigation and Mitigation*. Transportation research board national research council. Spec Rep 247, 36–75.

D'Elia, B., Picarelli, L. Leroueil, S. and Vaunat, I. (1986) 'Geotechnical characterisation of slope movements in structurally complex clay soils and stiff jointed', *Rivista Italiana di Geotecnica,* 32(3): 5-47.

Dai, F., Lee, C.F. and Wang, S. (1999) 'Analysis of rainstorm-induced slide-debris flows on natural terrain of Lantau Island, Hong Kong', *Engineering Geology,* 51(4): 279-290.

Elsbury, B. R., Daniel, D. E., Sraders, G. A. and Anderson, D. C. (1990) 'Lessons learned from compacted clay liner', *Journal of Geotechnical Engineering,* 116(11): 1641-1660.

Fell, R., Hungr, O., Leroueil, S. and Riemer, W. (2000) 'Geotechnical engineering of the stability of natural slopes, and cuts and fills in soil', Keynote Lecture presented at GeoEng2000 International Conference on Geotechnical and Geological Engineering, Melbourne*,* 1: 21-120.

Fenelli, G. B., and Plcarelli. L. (1990) 'The pore pressure field built up in a rapidly eroded soil mass', *Canadian Geotechnical Journal,* 27(3): 387-392.

Ferrari, A., Ledesma, A. González, D. and Corominas, J. (2011) 'Effects of the foot evolution on the behaviour of slow-moving landslides', *Engineering Geology,* 117(3): 217-228.

Gabet, E. J., and Mudd, S.M. (2006) 'The mobilization of debris flows from shallow landslides', *Geomorphology,* 74(1–4): 207-218.

Gass, A. A. (1961) 'General discussion on till', Paper presented at Proceedings of the Fourteenth Canadian Conference on Soil Mechanics, National Research Council, Ottawa.

González, D. A., Ledesma, A. and Corominas, J. (2008) 'The viscous component in slow moving landslides: A practical case', *Proceedings of the Tenth International Symposium on Landslides and Engineered Slopes, 1*: 237-242.

Gujarati, D. N. (1995) *Basic Econometrics* (3rd edition). Singapore: McGraw-Hill, Inc.

Head, K. (1988) *Manual of soil laboratory testing (Volume 2): Permeability, shear strength and compressibility tests*. London: Pentech Press.

Hemingway, J. E., and Riddler, G.P. (1980) 'Glacially transported Liassic rafts at Upgang, Near Whitby', *Proceedings of the Yorkshire Geological and Polytechnic Society,* 43(2): 183-189. Geological Society of London.

Hobbs, P., Gibson, A. Jones, L. Pennington, C. Jenkins, G., Pearson, S. and Freeborough, K. (2010) 'Monitoring coastal change using terrestrial LiDAR', *Geological Society, London, Special Publications,* 345(1): 117-127.

Hobbs, P. R. N., Humphreys, B., Rees, J.G., Tragheim, D.G., Jones, L.D.,Gibson, A., Rowlands, K., Hunter, G. and Airey, R. (2002) 'Monitoring the role of landslides in 'soft cliff'coastal recession', In R.G. McInnes and J. Jakeways (eds) *Instability: Planning and Management*, *Seeking Sustainable Solutions to Ground Movement Problems*. London: Thomas Telford, 589-600.

Hodge, R., Brasington, J. and Richards, K. (2009) 'In situ characterization of grain-scale fluvial morphology using Terrestrial Laser Scanning', *Earth Surface Processes and Landforms,* 34(7): 954-968.

Hodge, R. A. (2010) 'Using simulated Terrestrial Laser Scanning to analyse errors in high-resolution scan data of irregular surfaces', *ISPRS Journal of Photogrammetry and Remote Sensing,* 65(2): 227-240.

Hossain, D. (1996) 'Direct and indirect permeability of fissured tills', *ASTM Geotechnical Testing Journal,* 19(2): 191-202.

Hungr, O., Corominas, J. and Eberhardt, E. (2005) 'Estimating landslide motion mechanism, travel distance and velocity', In Landslide Risk Management, O. Hungr, R. Fell, R. Couture and E. Eberthardt (eds). London: Taylor and Francis, 99-128.

Iverson, R. M. (1985) 'A constitutive equation for mass-movement behavior', *The Journal of Geology,* 93: 143-160.

Iverson, R. M. (2005) 'Regulation of landslide motion by dilatancy and pore pressure feedback', *Journal of Geophysical Research - Earth Surface,* 110: 1-16.

Jakob, M., and Hungr, O. (2005) *Debris-flow hazards and related phenomena*. Berlin: Springer.

Jungerius, P. D. and De Jong, J. H. (1989) 'Variability of water repellence in the dunes along the Dutch coast', *Catena,* 16(4/5): 491-497.

Kasperski, J., Delacourt, C. Allemand, P., Potherat, P., Jaud, M. and Varrel, E. (2010) 'Application of a terrestrial laser scanner (TLS) to the study of the Séchilienne Landslide (Isère, France)', *Remote Sensing,* 2(12): 2785-2802.

Kilburn, C. R. J., and Petley, D.N. (2003) 'Forecasting giant, catastrophic slope collapse: lessons from Vajont, Northern Italy', *Geomorphology,* 54(1–2): 21-32.

Lee, J.Y., and Lee, K.K. (2000) 'Use of hydrologic time series data for identification of recharge mechanism in a fractured bedrock aquifer system', *Journal of Hydrology,* 229(3): 190-201.

Lee. M, and Clark. A. (2002) *Investigation and Management of Soft Rock Cliffs*: Thomas Telford Ltd.

Leroueil, S., Locat, J., Vaunat, J., Picarelli, L. and Faure, R. (1996) 'Geotechnical characterisation of slope movements', Paper presented at the Seventh International Symposium on Landslides at Norway, Balkema, Rotterdam.

Lim, M. (2006) *Coastal cliff evolution with reference to Staithes, North Yorkshire*. Unpublished PhD Thesis, University of Durham.

Lim, M., Petley, D.N., Rosser, N.J., Allison, R.J., Long, A.J. and Pybus, D. (2005) 'Combined Digital Photogrammetry and Time-of-Flight Laser Scanning for Monitoring Cliff Evolution', *The Photogrammetric Record,* 20(110): 109-129.

Long, J. S. (1997) *Regression models for categorical and limited dependent variables*. Vol. 7. Thousand Oaks: Sage Publications.

Mair, A., and Fares, A. (2011) 'Time series analysis of daily rainfall and streamflow in a volcanic dike-intruded aquifer system, O 'ahu, Hawai 'i, USA', *Hydrogeology Journal,* 19(4): 929-944.

Massey, C. (2010) *The dynamics of reactivated landslides: Utiku and Taihape, North Island, New Zealand*, Unpublished PhD Thesis, University of Durham.

Massey, C., Petley, D.N. and McSaveney, M.J. (2013) 'Patterns of movement in reactivated landslides', *Engineering Geology,* 159: 1-19.

Matsuura, S., Asano, S. and Okamoto, T. (2008) 'Relationship between rain and/or meltwater, pore-water pressure and displacement of a reactivated landslide', *Engineering Geology,* 101(1-2): 49-59.

Metoffice. 2013. Met Office surface data users guide [Online]. Accessed 1st August 2012, from http://badc.nerc.ac.uk/view/badc.nerc.ac.uk/ukmo-midas.

Moeyersons, J. (1989) 'A possible causal relationship between creep and sliding on Rwaza Hill, Southern Rwanda', *Earth Surface Processes and Landforms,* 14: 597-614.

Moon, S.-K., Woo, N.C. and Lee, K.S. (2004) 'Statistical analysis of hydrographs and water-table fluctuation to estimate groundwater recharge', *Journal of Hydrology,* 292(1): 198-209.

Moore, R. (1991) 'The chemical and mineralogical controls upon the residual strength of pure and natural clays', *Géotechnique,* 41: 35-47.

Moore, R., and Brunsden, D. (1996) 'Physico-chemical effects on the behaviour of a coastal mudslide', *Geotechnique,* 46(2): 259-278.

Morgenstern, N. (1995) ‘The role of analysis in the evaluation of slope stability’, *In Proceedings of the Sixth International Symposium on Landslides, Christchurch,* 3: 1615-1629.

Murray, E., Rix, D. and Humphrey, R. (1992) ‘Clay linings to landfill sites’, *Quarterly Journal of Engineering Geology and Hydrogeology,* 25(4): 371-376.

Ng, K., and Petley, D.N. (2009) ‘The use of pore pressure reinflation testing in landslide management in Hong Kong’, *Quarterly Journal of Engineering Geology and Hydrogeology,* 42(4): 487-498.

Ng, K. Y. (2007) *Mechanisms of Shallow Rainfall-induced Landslides in Residuali Soils in Humid Tropical Environments*, Unpublished PhD Thesis, University of Durham.

Norman, E. (2012) *Microseismic Monitoring of the Controls on Coastal Rock Cliff Erosion*, Unpublished PhD Thesis, University of Durham.

Parker, R. (2010) *Controls on the distribution of landslides triggered by the 2008 Wenchuan earthquake, Sichuan Province, China*, Unpublished M.Sc Dessertation, University of Durham.

Petley, D.N. (2012) ‘Global patterns of loss of life from landslides’, *Geology,* 40(10): 927-930.

Petley, D. N., and Allison, R.J. (1997) ‘The mechanics of deep-seated landslides’, *Earth Surface Processes and Landforms,* 22(8): 747-758.

Petley, D. N., Bulmer, M.H. and Murphy, W. (2002) ‘Patterns of movement in rotational and translational landslides’, *Geology,* 3(8): 719-722.

Petley, D. N., Higuchi, T., Petley, D.J., Bulmer, M.H. and Carey, J. (2005a) ‘Development of progressive landslide failure in cohesive materials’, *Geology,* 33(3): 201-204.

Petley, D. N., Mantovani, F., Bulmer, M.H.K. and Zannoni, F. (2005b) ‘The use of surface monitoring data for the interpretation of landslide movement patterns’, *Geomorphology,* 66(1-4): 133-147.

Picarelli, L. (2007) ‘Considerations about the Mechanics of Slow Active Landslides in Clay’, In K. Sassa, H. Fukuoka, F. Wang and G. Wang (eds) *Progress in Landslide Science*. Berlin; New York: Springer, 27-45.

Poulton, C. V., Lee, J., Hobbs, P., Jones, L. and Hall, M. (2006) ‘Preliminary investigation into monitoring coastal erosion using terrestrial laser scanning: case study at Happisburgh, Norfolk’, *Bulletin of the Geological Society of Norfolk,* 56: 45-64.

Prévost, J.H., and Höeg, K. (1975) ‘Soil mechanics and plasticity analysis of strain softening’, *Géotechnique,* 25: 279-297.

Quinn, J., Philip, L. and Murphy, W. (2009) ‘Understanding the recession of the Holderness Coast, east Yorkshire, UK: a new presentation of temporal and spatial patterns’, *Quarterly Journal of Engineering Geology and Hydrogeology,* 42(2): 165-178.

Quinn, J. D., Rosser, N.J., Murphy, W. and Lawrence, J. A. (2010) ‘Identifying the behavioural characteristics of clay cliffs using intensive monitoring and geotechnical numerical modelling’, *Geomorphology,* 120(3–4): 107-122.

Reid, M., Baum, R., LaHusen, R. and Ellis, W. (2008) ‘Capturing landslide dynamics and hydrologic triggers using near-real-time monitoring’, In Chen et al. (eds) *Landslides and Engineered Slopes: from the Past to the Future, Proceedings of the tenth International Symposium on Landslides and Engineered Slopes, 30 June-4 July, 2008, Xi'an, China.* Boca Raton: CRC Press, 179-191.

Roberts, D. H., Evans, D. J. A., Lodwick, J. and Cox N.J. (2013) ‘The subglacial and ice-marginal signature of the North Sea Lobe of the British–Irish Ice Sheet during the Last Glacial Maximum at Upgang, North Yorkshire, UK’, *Proceedings of the Geologists' Association,* 124(3): 503-519.

Rogerson, P. (2001) *Statistical methods for geography*. London: Sage.

Rosser, N. J., Petley, D. N., Lim, M., Dunning, S.A. and Allison, R.J. (2005) ‘Terrestrial laser scanning for monitoring the process of hard rock coastal cliff erosion’, *Quarterly Journal of Engineering Geology and Hydrogeology,* 38: 363-375.

Rosser, N. J., Lim, M., Petley, D.N., Dunning, S.A. and Allison, R.J. (2007) ‘Patterns of precursory rockfall prior to slope failure’, *Journal of Geophysical Research: Earth Surface (2003–2012),* 112(F4): 1-14.

Saito, M. (1965) ‘Forecasting the time of occurrence of a slope failure’, *Proceedings of the 6th International Conference on Soil Mechanics and Foundation Engineering*, 537-541.

Salt, G. A. (1985) ‘Aspectsof landslide mobility’, Paper presented at Proceedings of the 11th International Conference on Soil Mechanics and Foundation Engineering, San Francisco.

Selby, M. E. (1993) *Hillslope materials and processes*. Oxford: Oxford University Press.

Shimokawa, E. (1980) ‘Creep deformation of cohesive soils and its relationship to landslide’, *Mem. Fac. Agr. Kagoshima Univ,* 16: 129-156.

Shuzui, H. (2001) 'Process of slip-surface development and formation of slip-surface clay in landslides in Tertiary volcanic rocks, Japan', *Engineering Geology,* 61: 199-220.

Sidle, R. C., and Ochiai, H. (2006) *Landslides: Processes, Prediction, and Land Use*. Vol. 18: American Geophysical Union.

Skempton, A. W. (1985) 'Residual strength of clays in landslides, folded strata and the laboratory', *Géotechnique,* 35: 3-18.

Skempton A.W. and DeLory, F.A. (1957) 'Stability of natural slopes in London clay', *In: Proceedings 4th international conference on Soil Mechíanics and Foundation Engineering*, 2: 378-391.

Skempton, A. W. and Hutchinson, J.N. (1969) 'Stability of natural slopes and embankmentfoundations, state-of-the-art report', In *Proceedings of the 7th International Conference on Soil Mechanics and Foundation Engineering*, 4: 291-340.

Sturzenegger, M., Yan, M., Stead, D. and Elmo, D. (2007) 'Application and limitations of ground-based laser scanning in rock slope characterization', In E. Eberhardt, D. Stead and T. Morrison (eds) *Rock Mechanics: Meeting Society's Challenges and Demands, Proceedings of the 1st Canada-US Rock Mechanics Symposium, Vancouver, Canada, 27-31 May 2007*. London: Taylor & Francis, 29-36.

Summerfield, M. A. (1991) *Global Geomorphology*: *An Introduction to the Study of Landforms*. Harlow, Essex, England: Longman Scientific & Technical.

Terlien, M. T. J. (1998) 'The determination of statistical and deterministic hydrological landslide-triggering thresholds', *Environmental Geology,* 35(2-3): 124-130.

Terzaghi, K. (1950) 'Mechanism of landslides', In Geological Society of America (ed), *Application of Geology to Engineering Practice: Berkley Volume*. New York: Geological Society of America, 83-123.

Terzaghi, K., Peck, R.B. and Mesri, G. (1996) *Soil Mechanics in Engineering Practice*. New York: John Wiley and Sons.

Trenter, N. A. (1999) *Engineering in glacial tills*. London: CIRIA Construction Industry Research and Information Association.

Urciuoli, G., Picarelli, L. and Leroueil, S. (2007) 'Local soil failure before general slope failure', *Geotechnical and Geological Engineering,* 25(1): 103-122.

Van Asch, T. W. J. (1984) 'Creep processes in landslides', *Earth Surface Processes and Landforms,* 9(6): 573-583.

Varnes, D. J. (1978) *Slope movement types and processes*, *Landslides: Analysis and Control*. Chicago: Highway Research Board Special Report.

Varnes, D. J. (1983) 'Time-deformation relations in creep to failure of earth materials', *Proceedings of the 7th Southeast Asian Geotechnical Conference, 2, Southeast Asian Geotechnical Society, Bangkok,* 107-130.

Wright, S., Walden, P., Sangha, C. and Langdon, N. (1996) 'Observations on soil permeability, moulding moisture content and dry density relationships', *Quarterly Journal of Engineering Geology and Hydrogeology,* 29(3): 249-255.

Zhu, J.H. and Anderson, S.A. (1998) 'Determination of shear strength of Hawaiian residual soil subjected to rainfall-induced landslides', *Géotechnique,* 48: 73-82.

Appendix A: Monitoring data

This appendix includes monitoring results for the 21 movement periods observed. The three graphs in each movement period represent landslide movements, groundwater and rainfall, which are all the same on each page. Note that axes ranges differ markedly between plots.

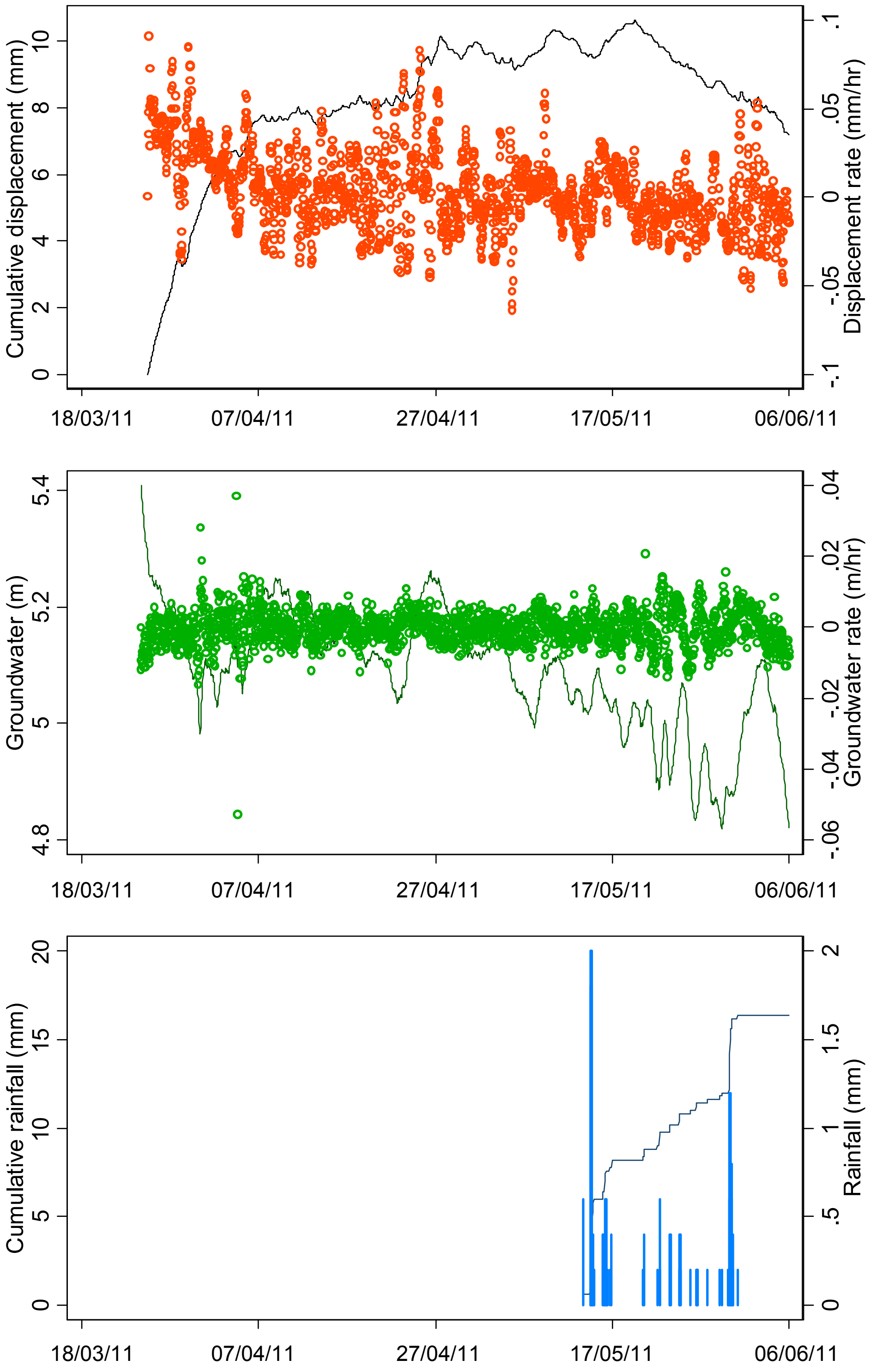

Figure A.1 Monitoring results at the Upgang Landslide (Period 1). Slow movement between 24th March and 05th June 2011 shows about 10.63 mm in cumulative displacement with a maximum displacement rate of 0.1 mm/hr. Groundwater fluctuated between 4.82 and 5.41 m with a low groundwater rate of 0.04 m/hr. The total rainfall was 16.4mm with a maximum rate of 2 mm/hr during a 39-hour wet period.

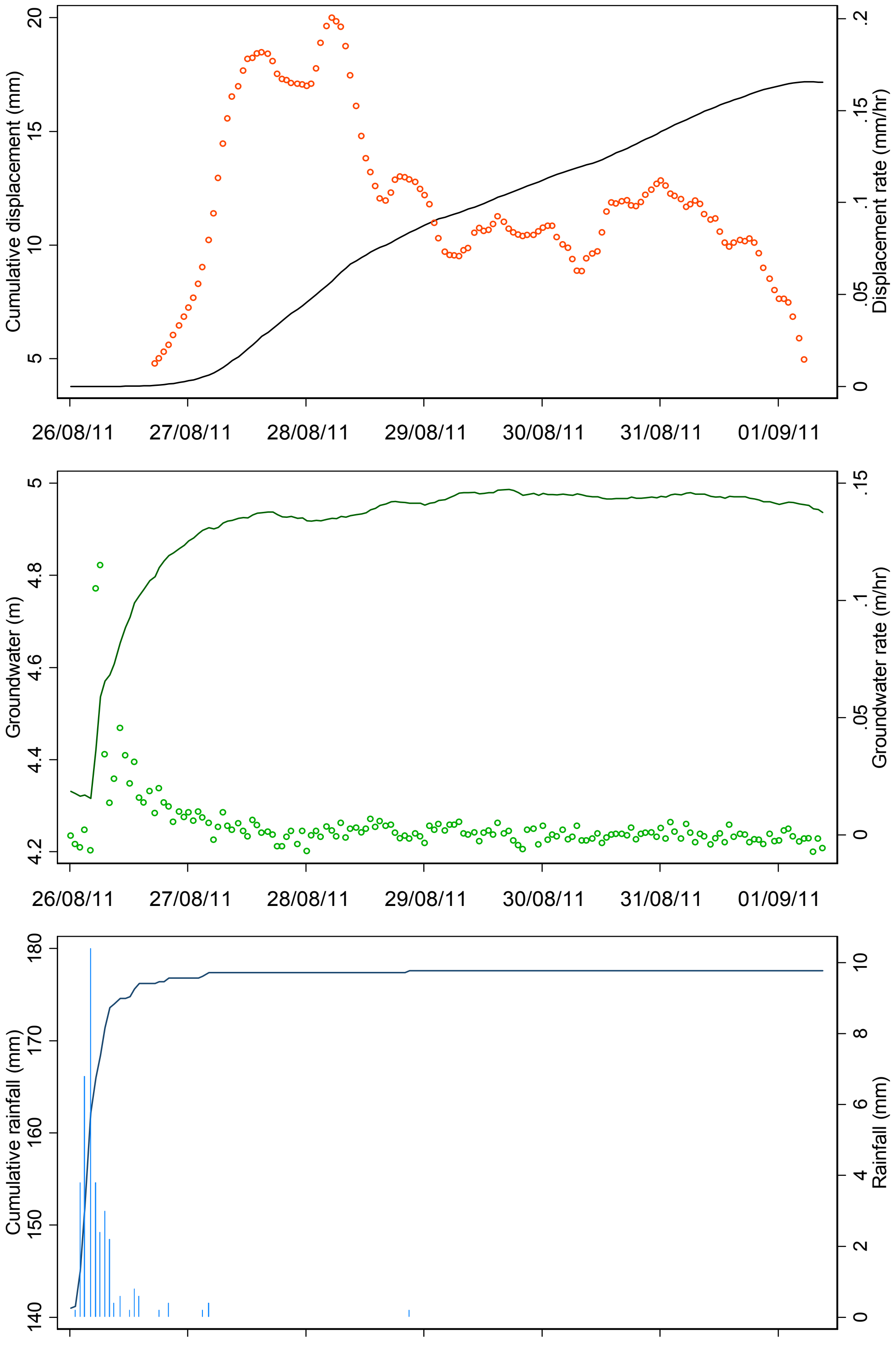

Figure A.2 Monitoring results at the Upgang Landslide (Period 2). Accelerated movement between 26th August and 01st September 2011 shows about 13.40 mm in cumulative displacement with a maximum displacement rate of 0.2 mm/hr. Groundwater fluctuated between 4.32 and 4.99 m with a moderate groundwater rate of 0.1 m/hr. The total rainfall was 36.60mm with a maximum rate of 10.40 mm/hr during a 18-hour wet period.

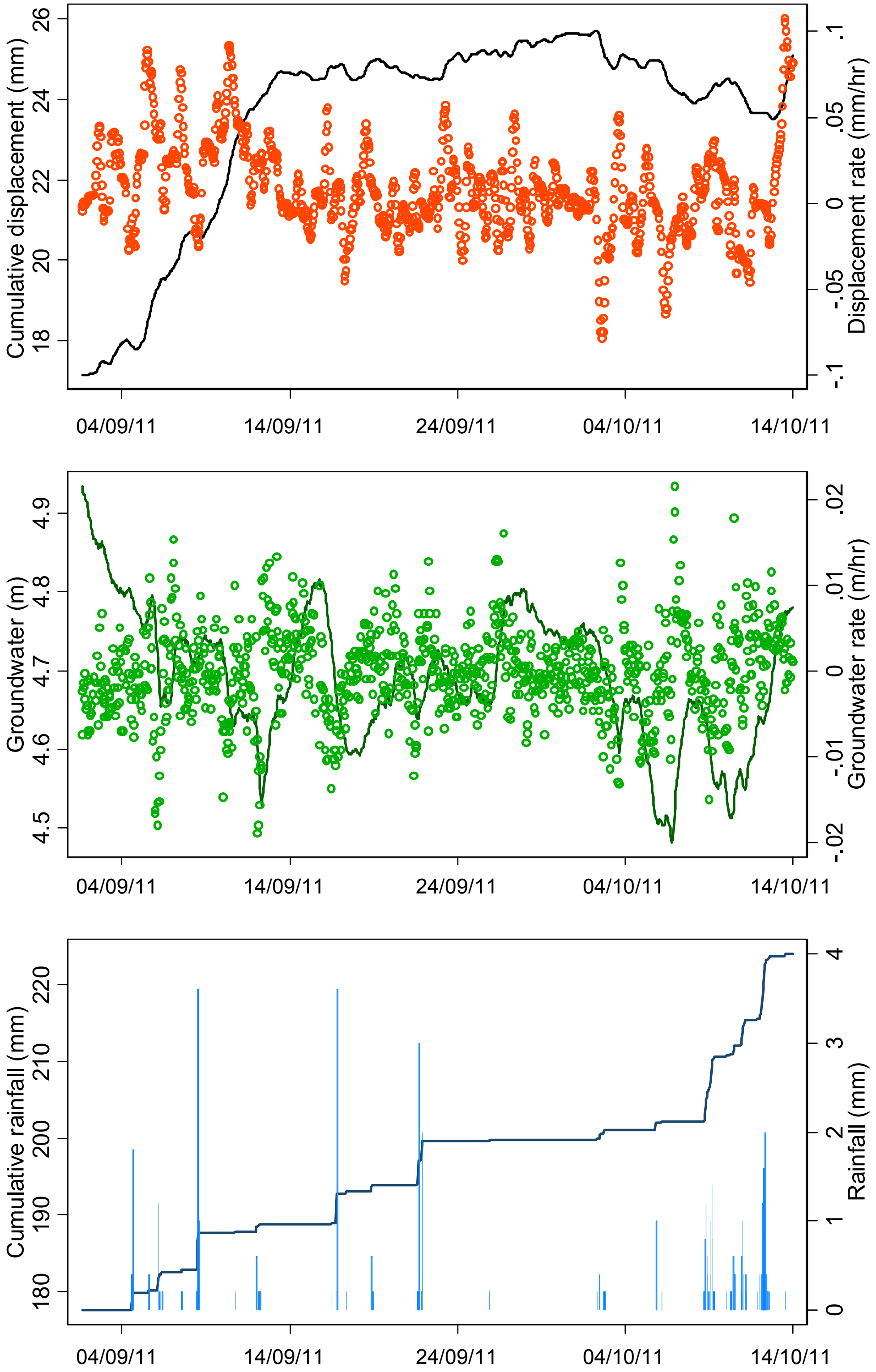

Figure A.3 Monitoring results at the Upgang Landslide (Period 3). Slow movement between 01st September and 14th October 2011 shows about 8.55 mm in cumulative displacement with a maximum displacement rate of 0.1 mm/hr. Groundwater fluctuated between 4.48 and 4.93 m with a low groundwater rate of 0.02 m/hr. The total rainfall was 77mm with a maximum rate of 3.6 mm/hr during a 77-hour wet period.

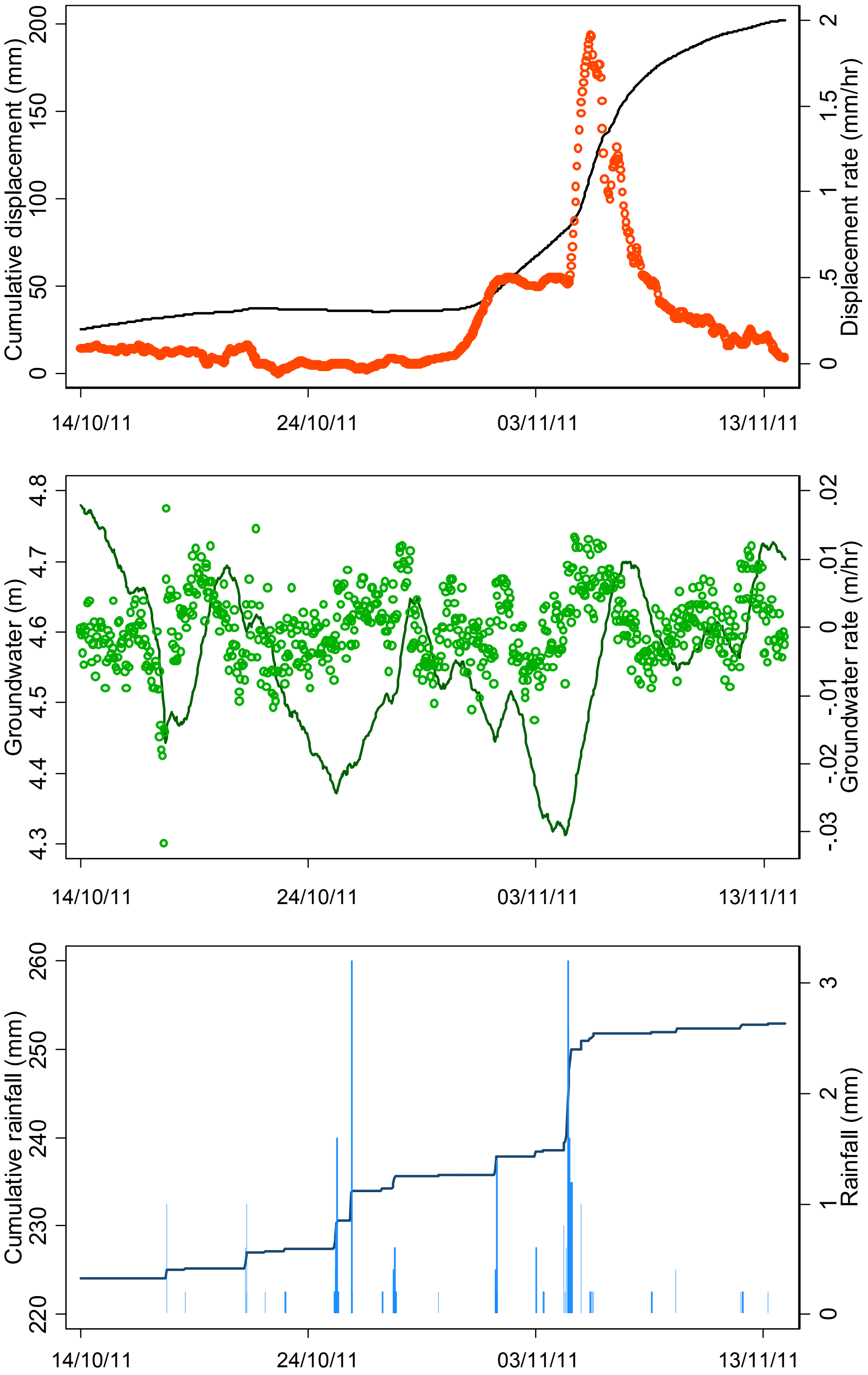

Figure A.4 Monitoring results at the Upgang Landslide (Period 4). Accelerated movement between 29th October and 14th November 2011 shows about 176.57 mm in cumulative displacement with a maximum displacement rate of 1.91 mm/hr. Groundwater fluctuated between 4.31 and 4.73 m with a low groundwater rate of 0.01 m/hr. The total rainfall was 29 mm with a maximum rate of 3.2 mm/hr during a 43-hour wet period.

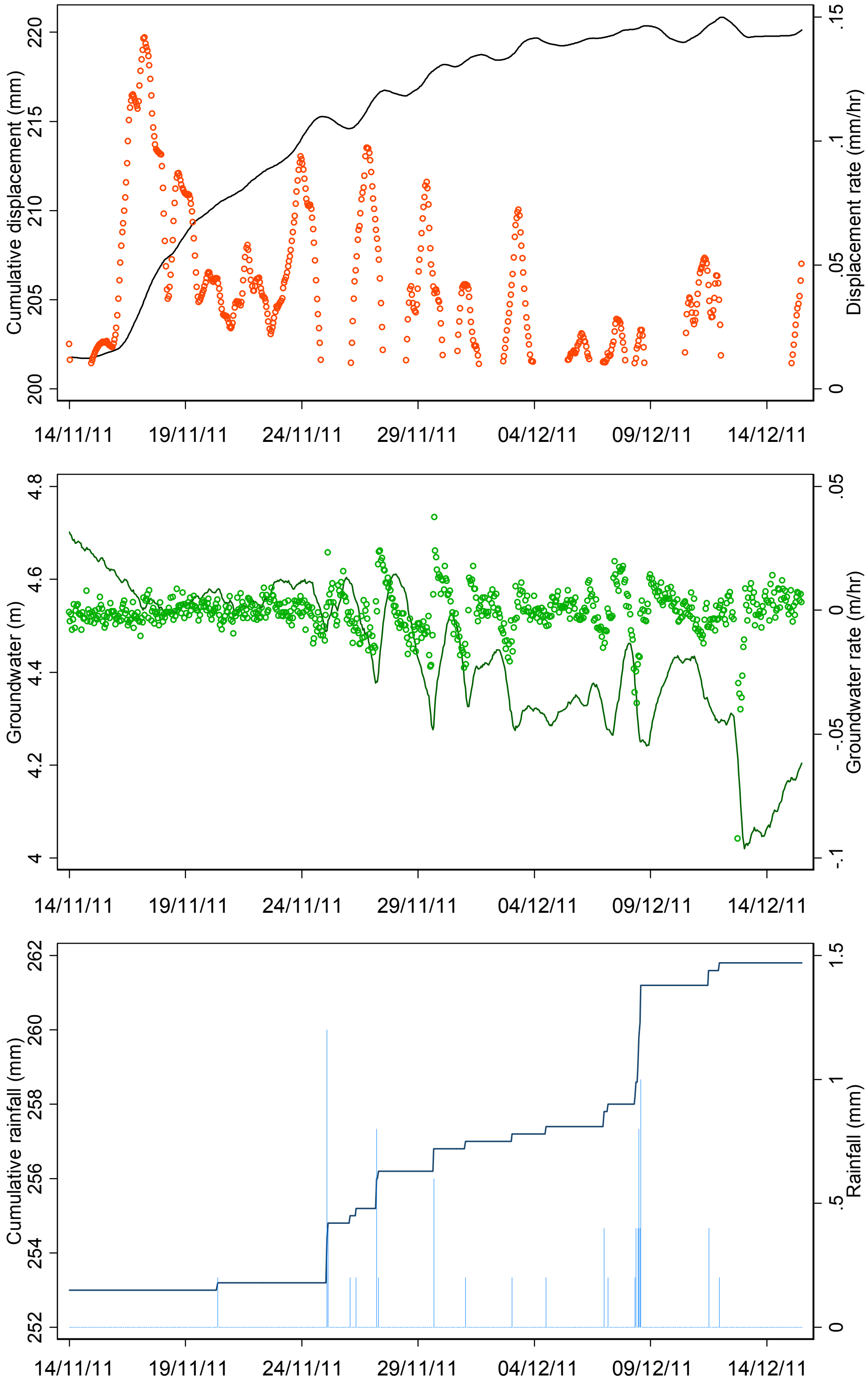

Figure A.5 Monitoring results at the Upgang Landslide (Period 5). Slow movement between 14th November and 15th December 2011 shows about 19 mm in cumulative displacement with a maximum displacement rate of 0.142 mm/hr. Groundwater fluctuated between 4.02 and 4.70 m with a low groundwater rate of 0.03 m/hr. The total rainfall was 8.8 mm with a maximum rate of 1.2 mm/hr during a 21-hour wet period.

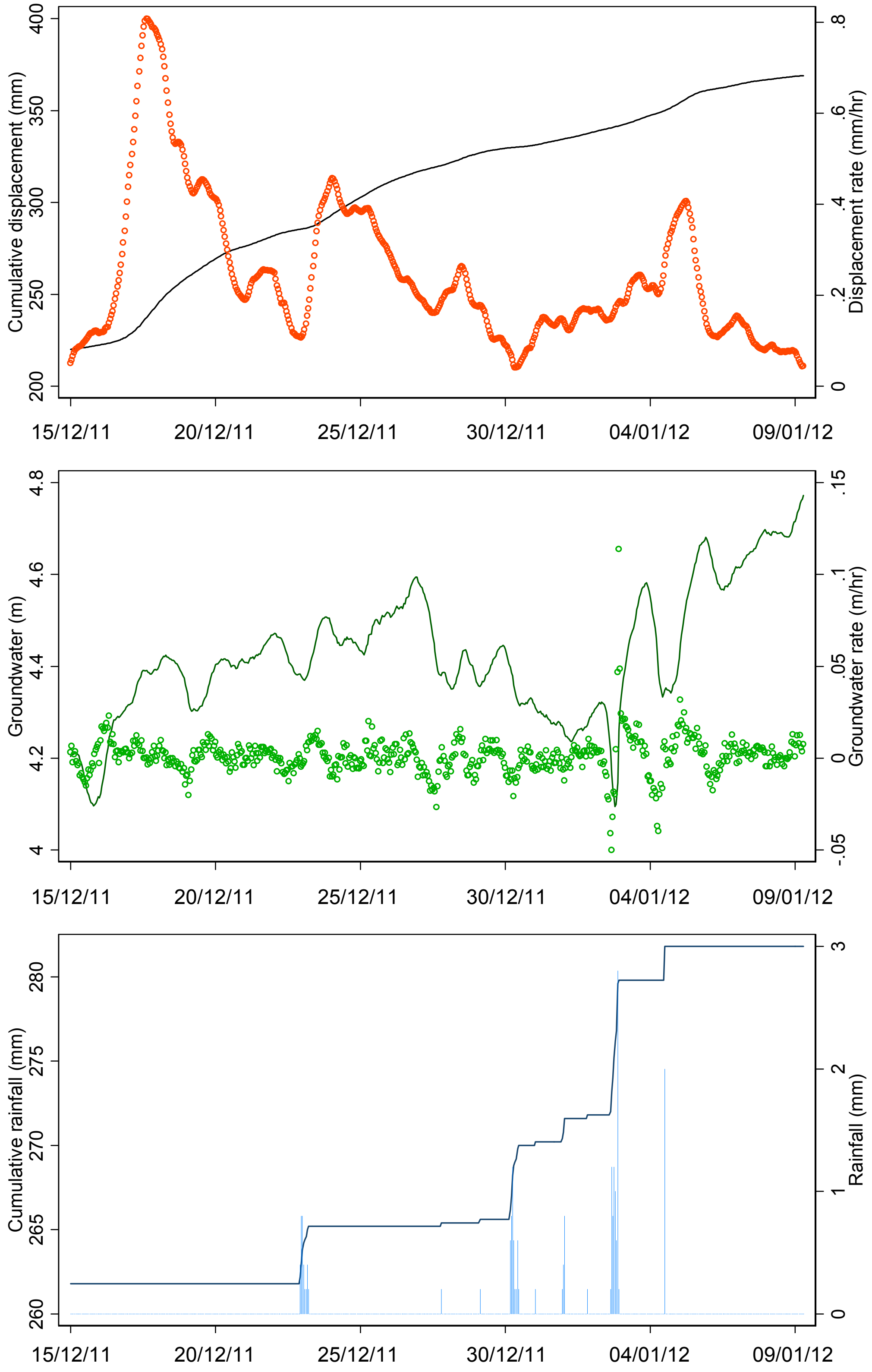

Figure A.6 Monitoring results at the Upgang Landslide (Period 6). Accelerated movement between 15th December 2011 and 09th January 2012 shows about 149 mm in cumulative displacement with a maximum displacement rate of 0.80 mm/hr. Groundwater fluctuated between 4.1 and 4.77 m with a moderate groundwater rate of 0.1 m/hr. The total rainfall was 20 mm with a maximum rate of 2.8 mm/hr during a 32-hour wet period.

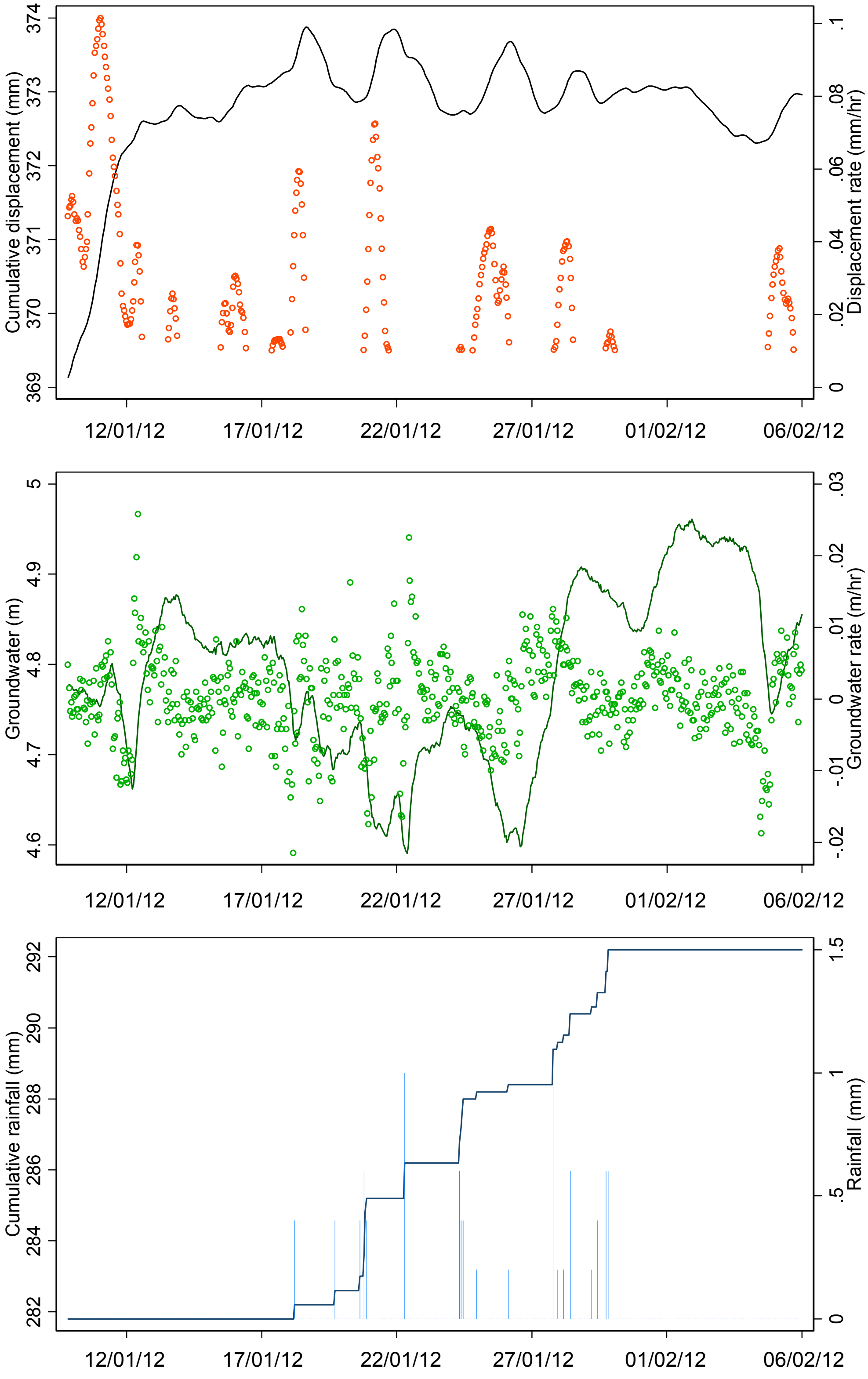

Figure A.7 Monitoring results at the Upgang Landslide (Period 7). Slow movement between 09th January and 06th February 2012 shows about 5 mm in cumulative displacement with a maximum displacement rate of 0.1 mm/hr. Groundwater fluctuated between 4.59 and 4.96m with a low groundwater rate of 0.02m/hr. The total rainfall was 10.4mm with a maximum rate of 1.2 mm/hr during a 21-hour wet period.

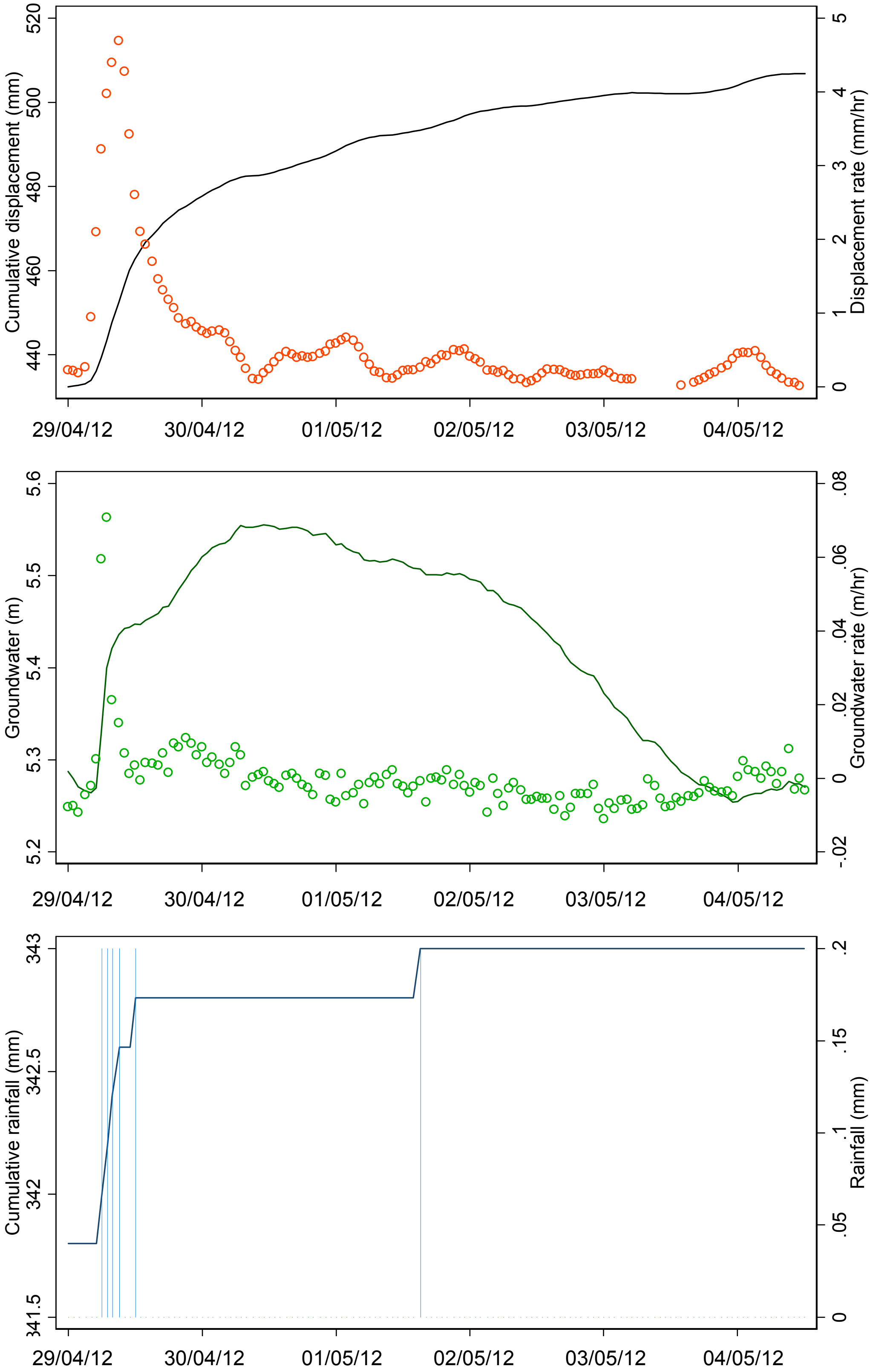

Figure A. 8 Monitoring results at the Upgang Landslide (Period 8). Accelerated movement between 29th April and 05th May 2012 shows about 74.46 mm in cumulative displacement with a maximum displacement rate of 4.7 mm/hr. Groundwater fluctuated between 5.25 and 5.55m with a low groundwater rate of 0.07m/hr. The total rainfall was 1.2 mm with a maximum rate of 0.2 mm/hr during a 6-hour wet period.

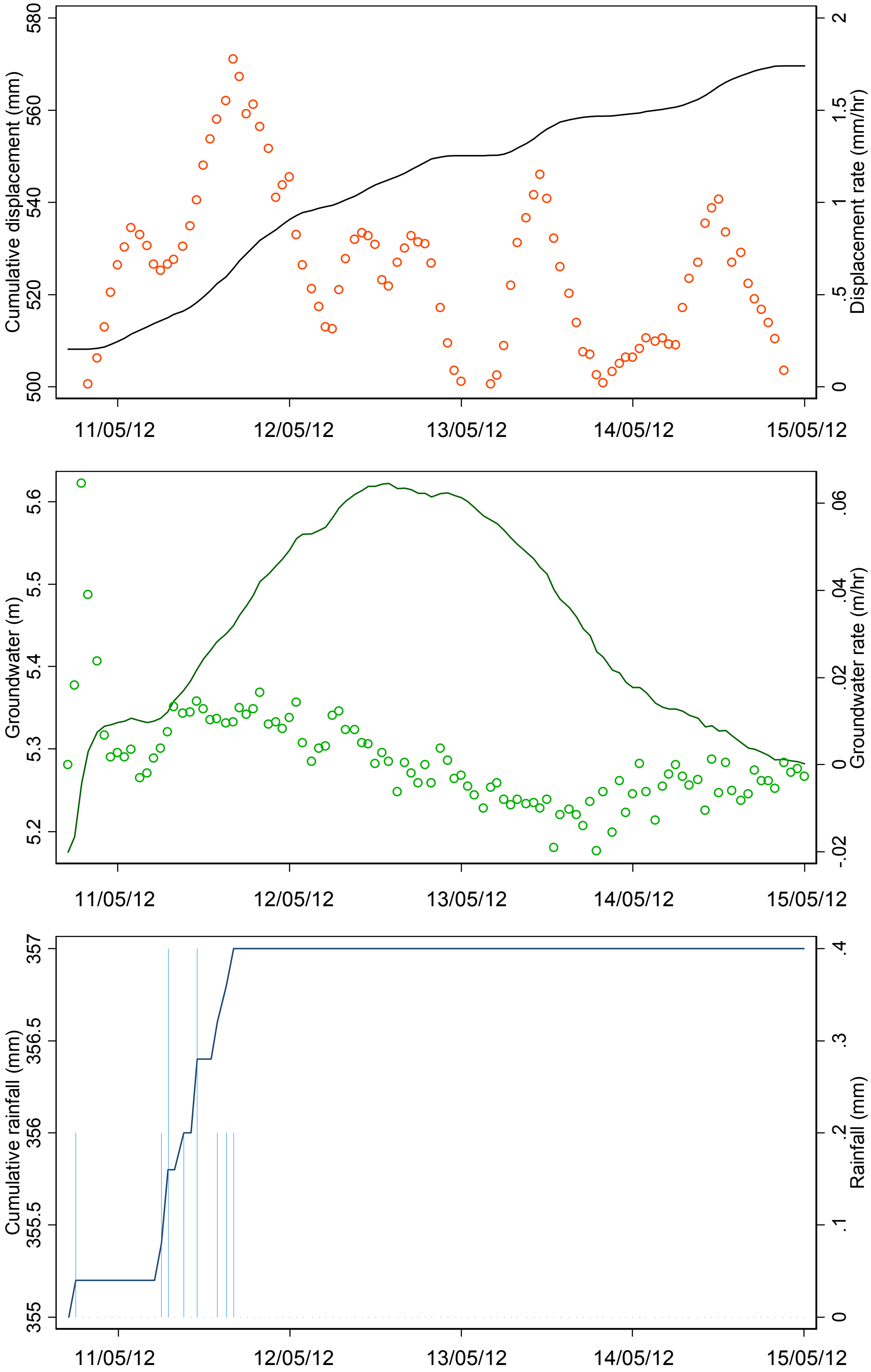

Figure A.9 Monitoring results at the Upgang Landslide (Period 9). Accelerated movement between 10th and 15th May 2012 shows about 61 mm in cumulative displacement with a maximum displacement rate of 1.78 mm/hr. Groundwater fluctuated between 5.17 and 5.62 m with a low groundwater rate of 0.06 m/hr. The total rainfall was 2mm with a maximum rate of 0.4mm/hr during a 8-hour wet period.

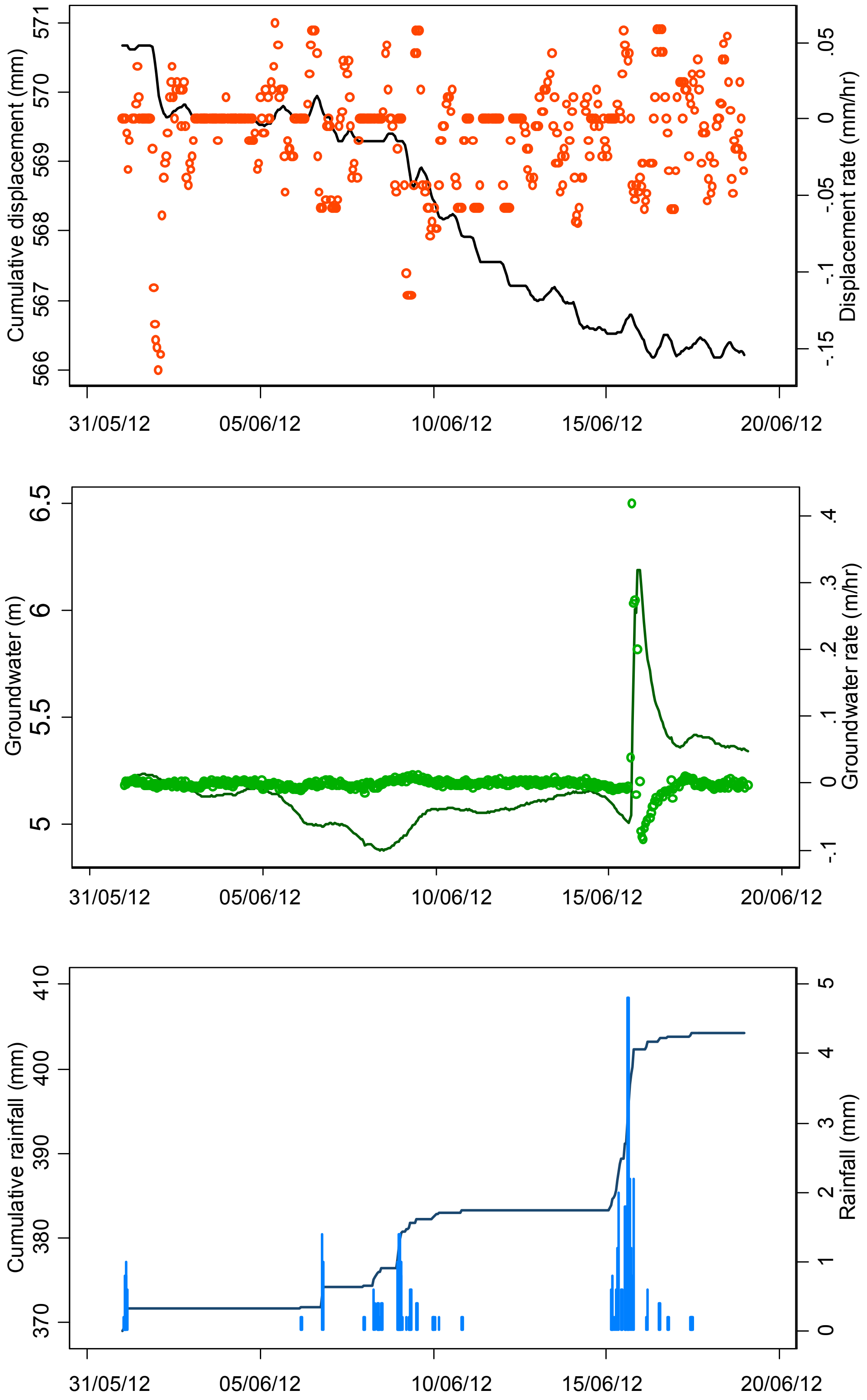

Figure A.10 Monitoring results at the Upgang Landslide (Period 10). No movement between 01st and 19th June 2012 shows about -4 mm in cumulative displacement with a maximum displacement rate of 0.06mm/hr. Groundwater fluctuated between 4.88 and 6.19m with a high groundwater rate of 0.42 m/hr. The total rainfall was 47mm with a maximum rate of 4.8mm/hr during a 35-hour wet period.

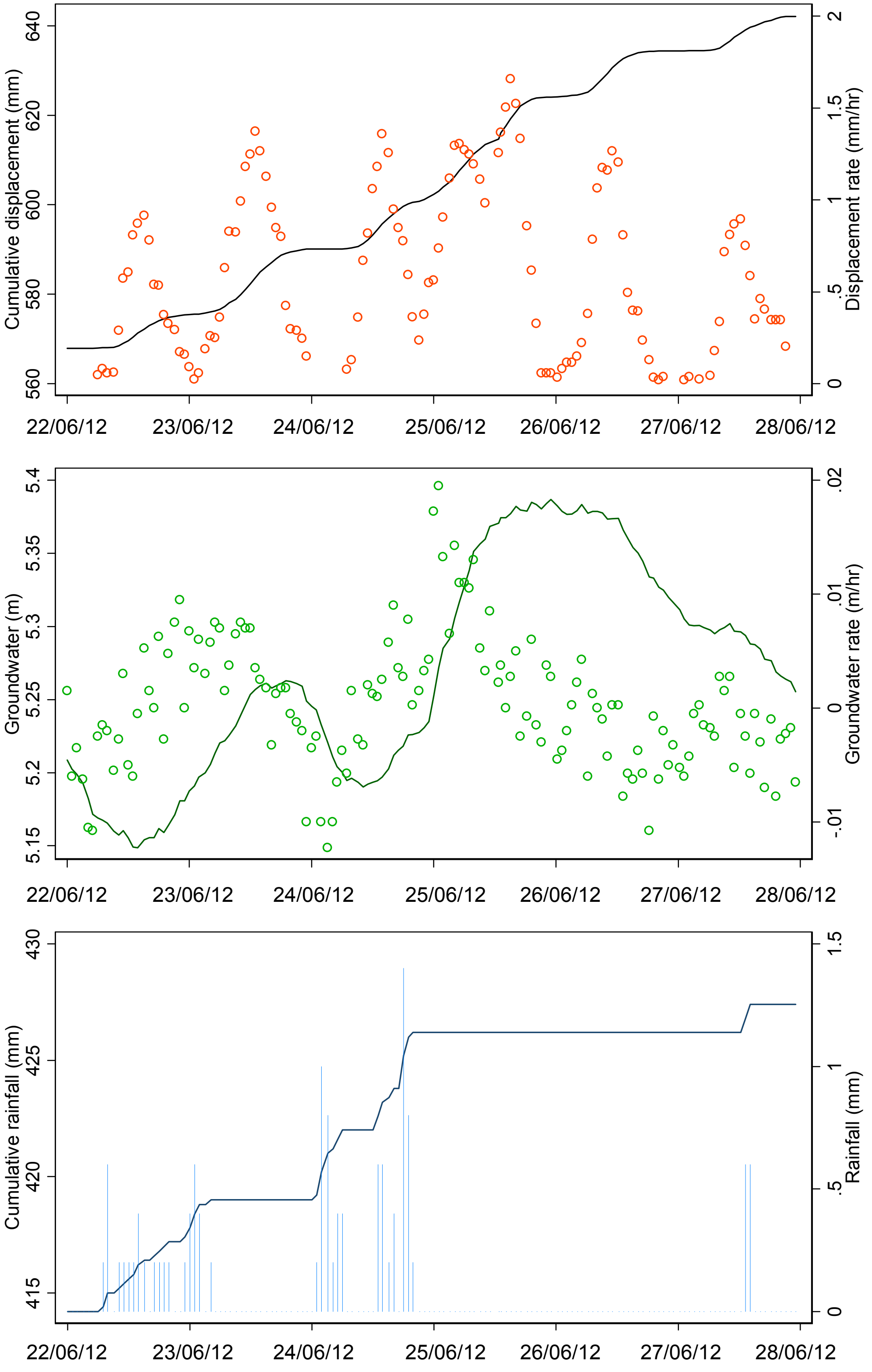

Figure A.11 Monitoring results at the Upgang Landslide (Period 11). Accelerated movement between 22nd and 28th June 2012 shows about 74.22 mm in cumulative displacement with a maximum displacement rate of 1.66mm/hr. Groundwater fluctuated between 5.15 and 5.38m with a low groundwater rate of 0.01m/hr. The total rainfall was 13.2 mm with a maximum rate of 1.4 mm/hr during a 32-hour wet period.

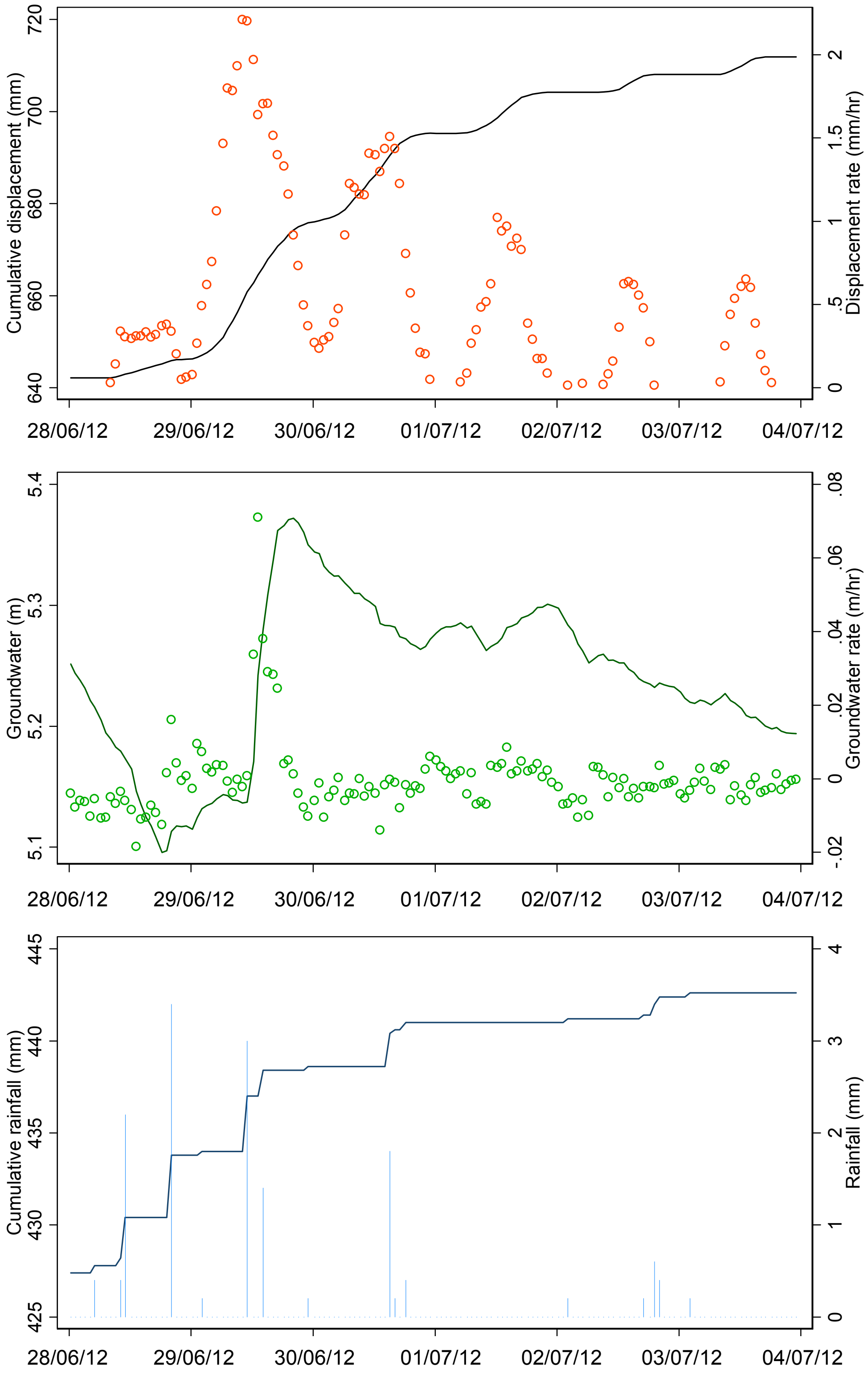

Figure A.12 Monitoring results at the Upgang Landslide (Period 12). Accelerated movement between 28th June and 04th July 2012 shows about 69.74 mm in cumulative displacement with a maximum displacement rate of 2.21 mm/hr. Groundwater fluctuated between 5.09 and 5.37m with a low groundwater rate of 0.07 m/hr. The total rainfall was 15.2mm with a maximum rate of 3.4mm/hr during a 16-hour wet period.

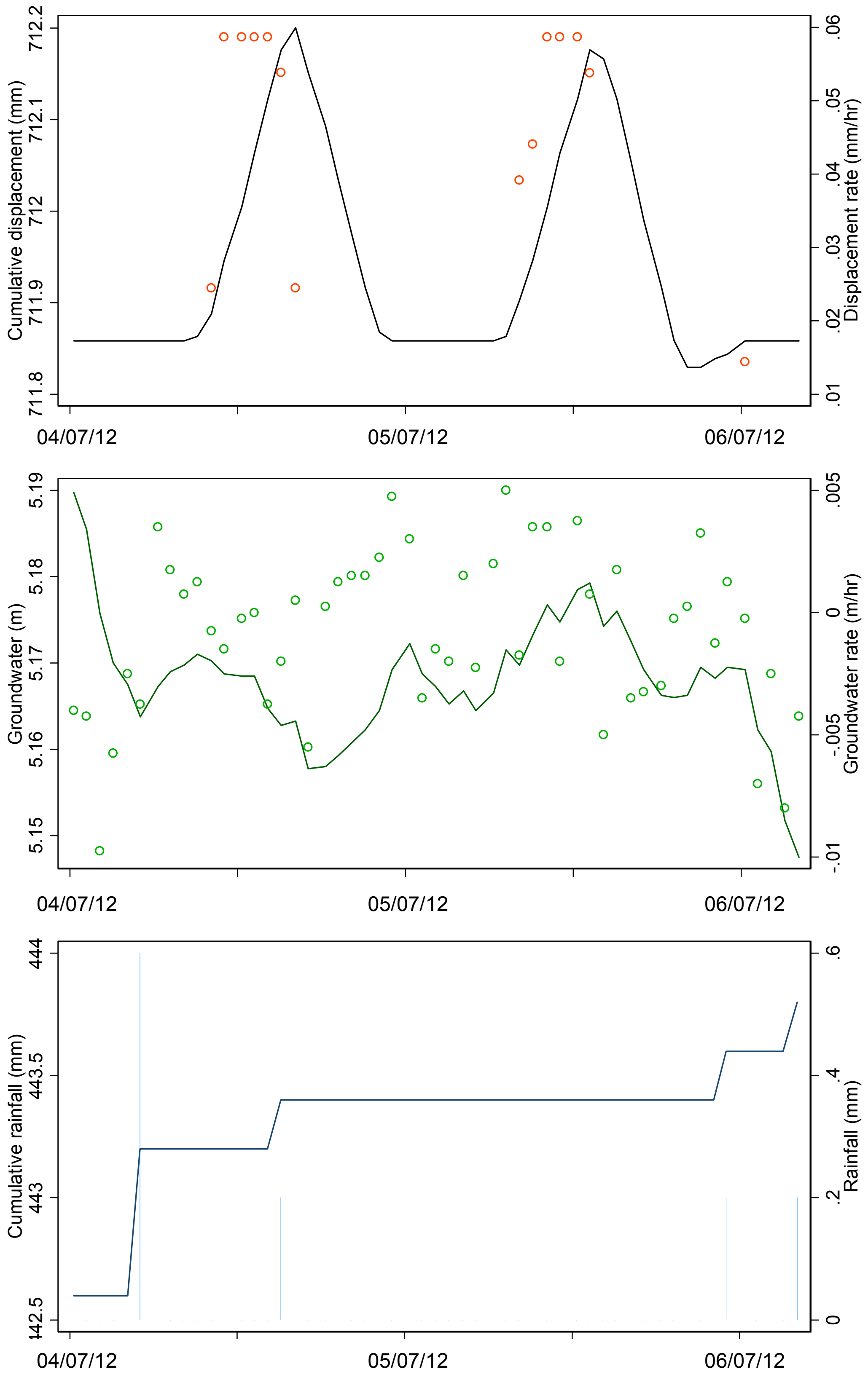

Figure A.13 Monitoring results at the Upgang Landslide (Period No.13). No movement between 04th and 06th July 2012 shows about 0.37mm in cumulative displacement with a maximum displacement rate of 0.059 mm/hr. Groundwater fluctuated between 5.15 and 5.19m with a very low groundwater rate of 0.005 m/hr. The total rainfall was 1.2 mm with a maximum rate of 0.6 mm/hr during a 4-hour wet period.

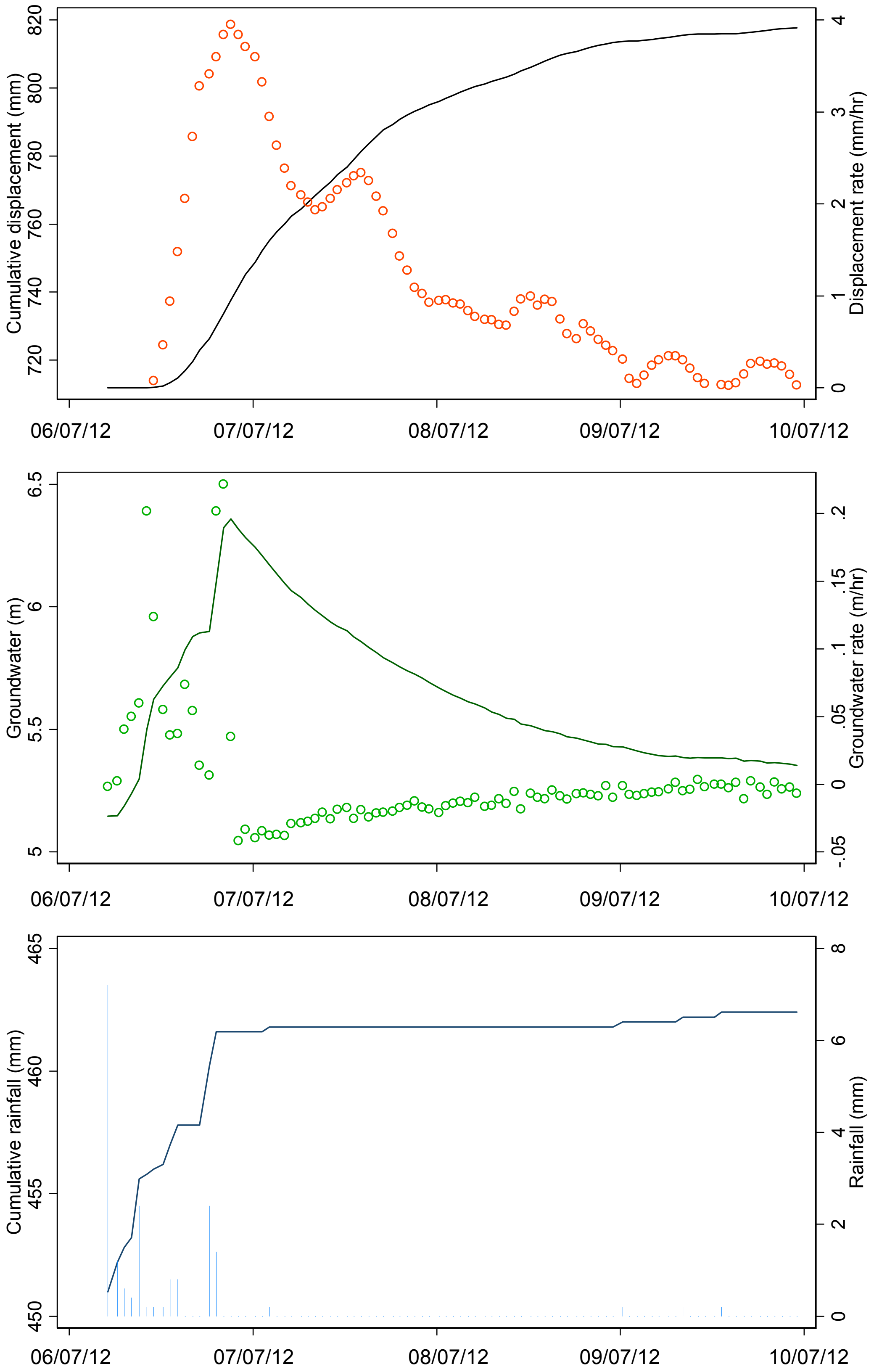

Figure A.14 Monitoring results at the Upgang Landslide (Period No.14). Accelerated movement between 06th and 10th July 2012 shows about 105.80 mm in cumulative displacement with a maximum displacement rate of 3.95 mm/hr. Groundwater fluctuated between 5.15 and 6.36 m with a high groundwater rate of 0.22 m/hr. The total rainfall was 11.4mm with a maximum rate of 7.2 mm/hr during a 16-hour wet period.

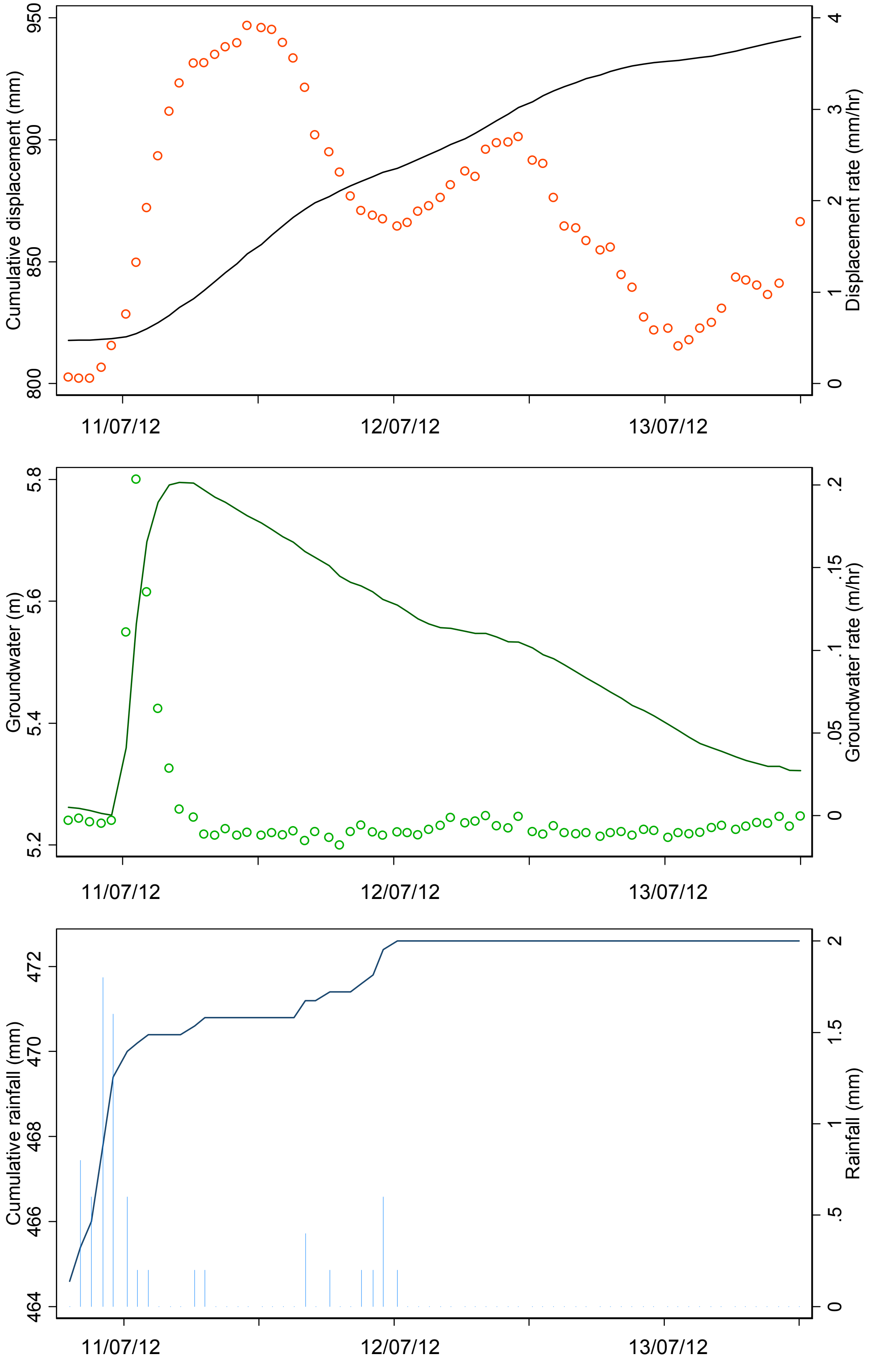

Figure A.15 Monitoring results at the Upgang Landslide (Period No.15). Accelerated movement during 10th – 13th July 2012 shows about 124.77 mm in cumulative displacement with a maximum displacement rate of 3.91 mm/hr. Groundwater fluctuated between 5.25 and 5.80 m with a high groundwater rate of 0.20 m/hr. The total rainfall was 10.2 mm with a maximum rate of 1.8 mm/hr during a 15-hour wet period.

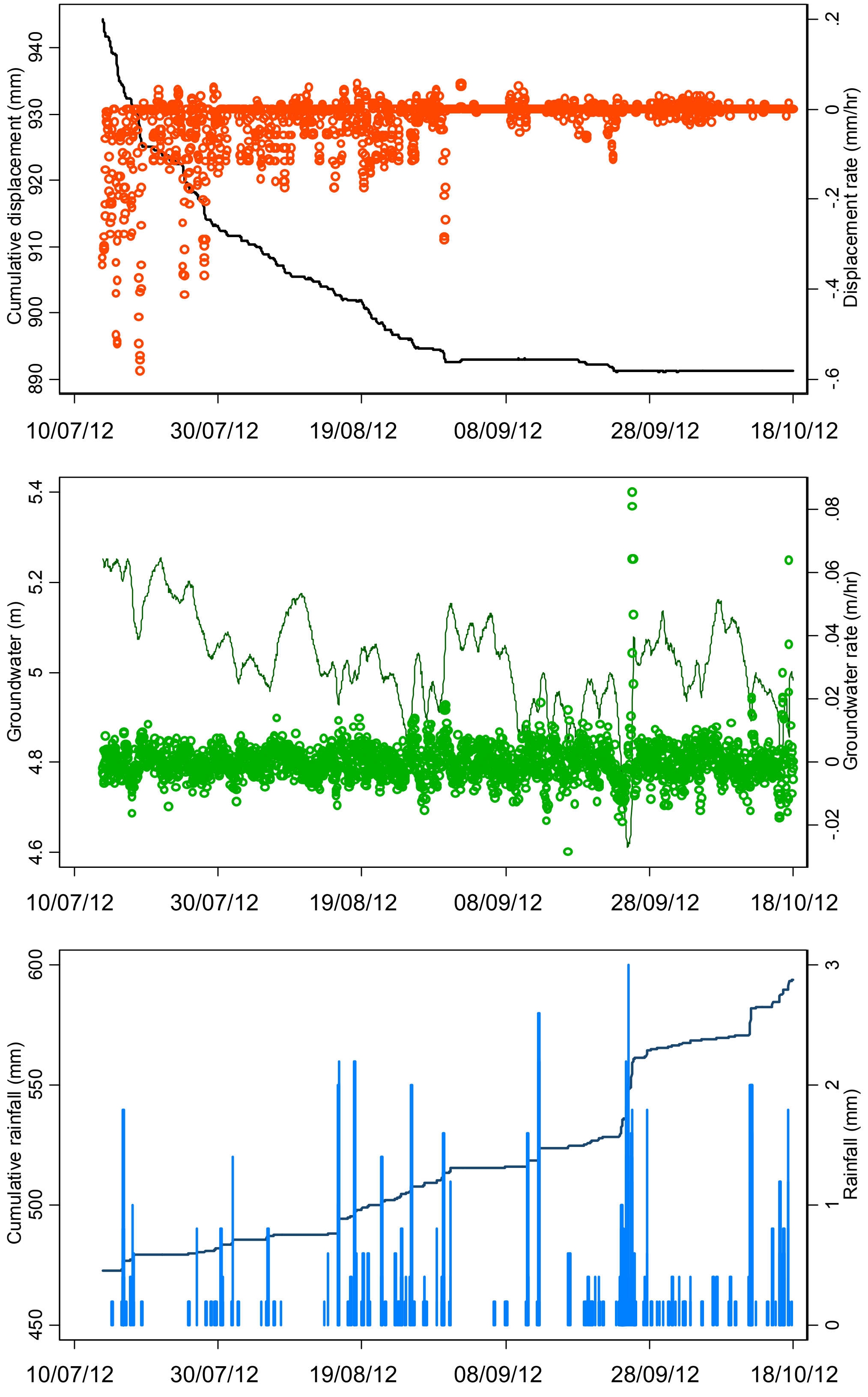

Figure A. 16 Monitoring results at the Upgang Landslide (Period No.16). No movement during 14th July- 18th October 2012 shows about -52.89 mm in cumulative displacement with a maximum displacement rate of 0.06 mm/hr. Groundwater fluctuated between 4.61 and 5.27 m with a low groundwater rate of 0.09 m/hr. The total rainfall was 121.2 mm with a maximum rate of 3 mm/hr during a 217-hour wet period.

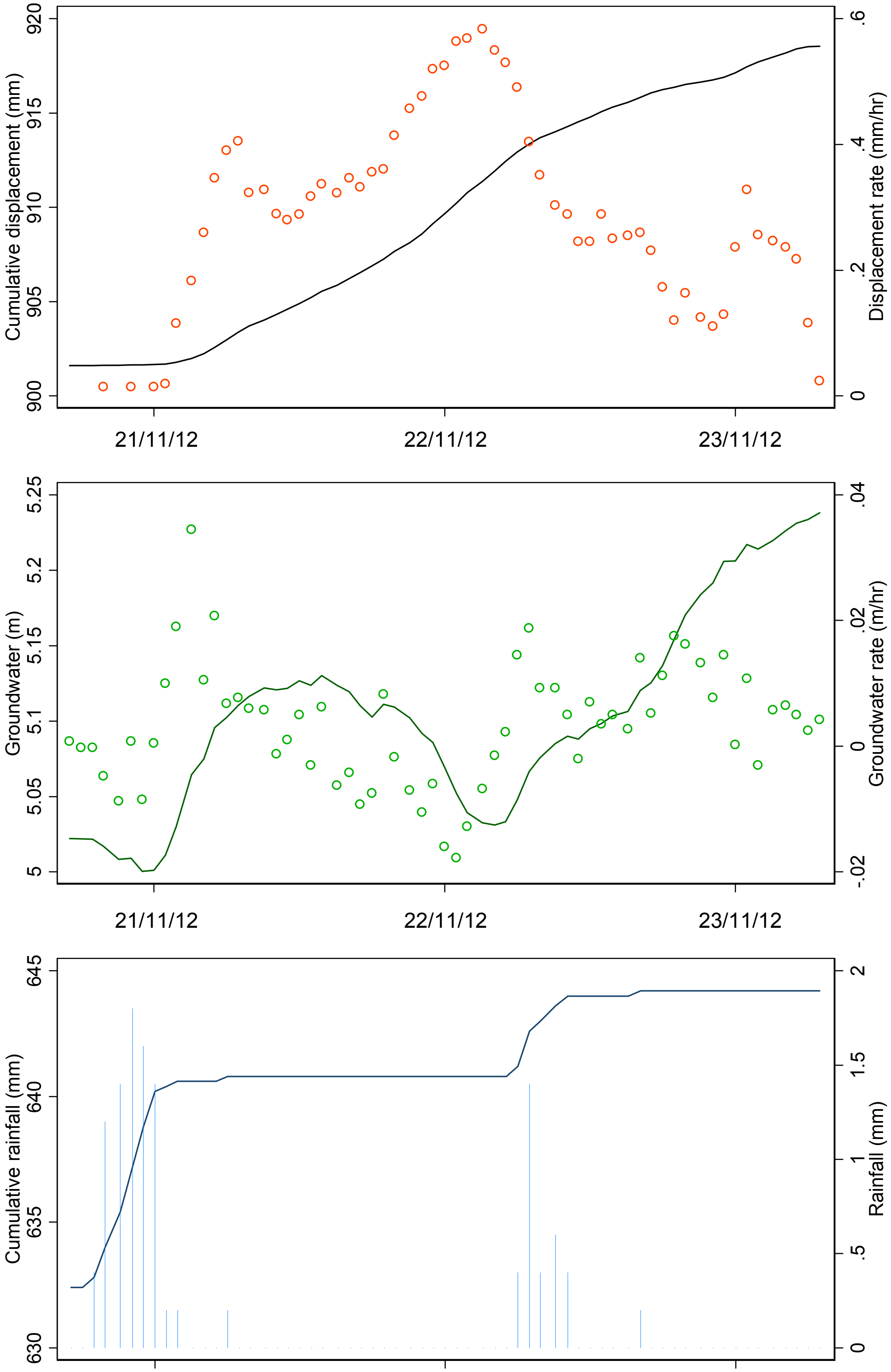

Figure A.17 Monitoring results at the Upgang Landslide (Period No.17). Accelerated movement during 21st – 23rd November 2012 shows about 17 mm in cumulative displacement with a maximum displacement rate of 0.58 mm/hr. Groundwater fluctuated between 5 and 5.24 m with a low groundwater rate of0.03 m/hr. The total rainfall was 11.8 mm with a maximum rate of 1.8 mm/hr during a 15-hour wet period.

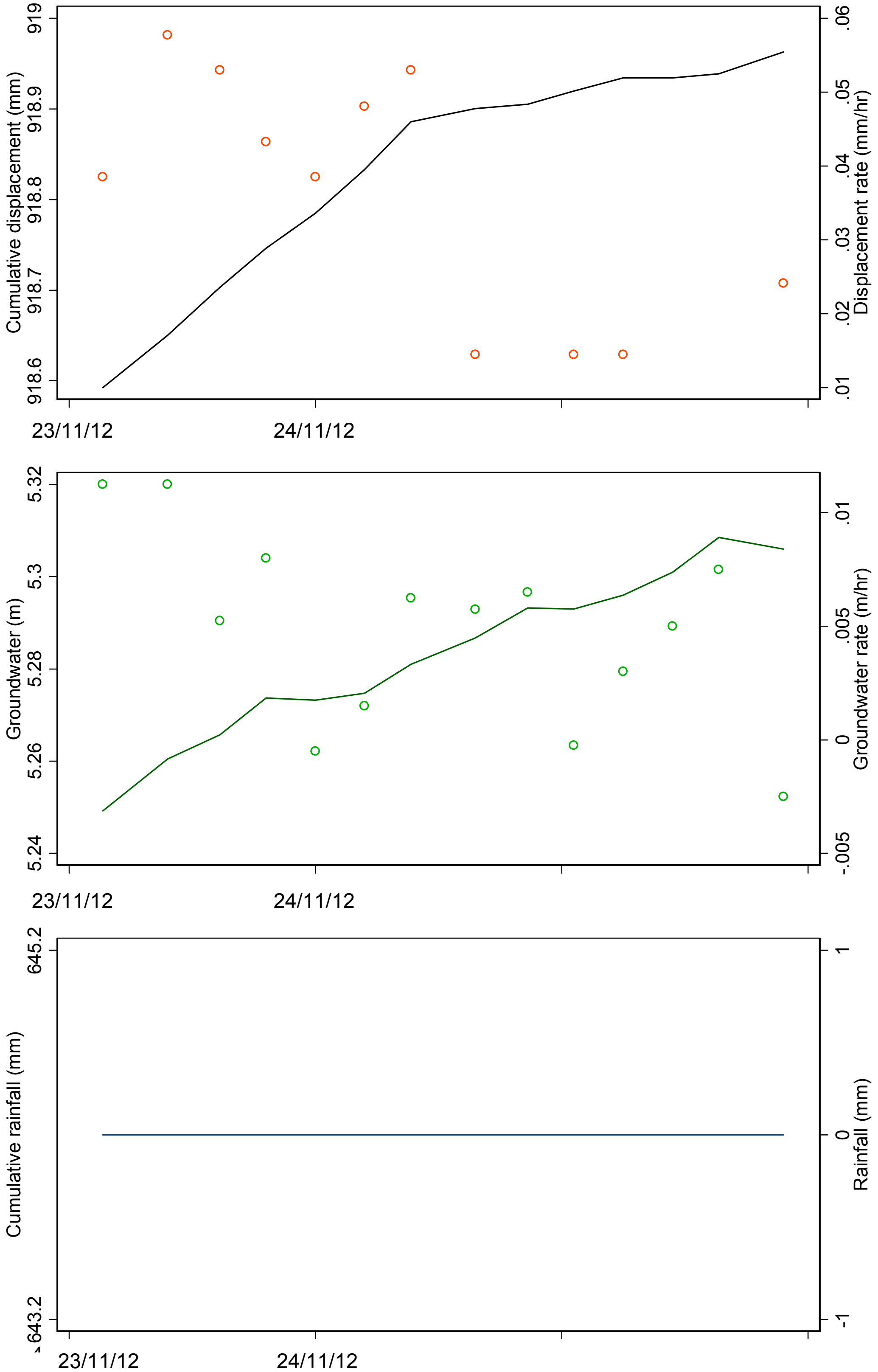

Figure A.18 Monitoring results at the Upgang Landslide (Period No.18). No movement between 23rd and 24th November 2012 shows about 0.37mm in cumulative displacement with a maximum displacement rate of 0.058 mm/hr. Groundwater fluctuated between 5.25 and 5.30 m with a low groundwater rate of 0.01 m/hr. No rainfall in this period.

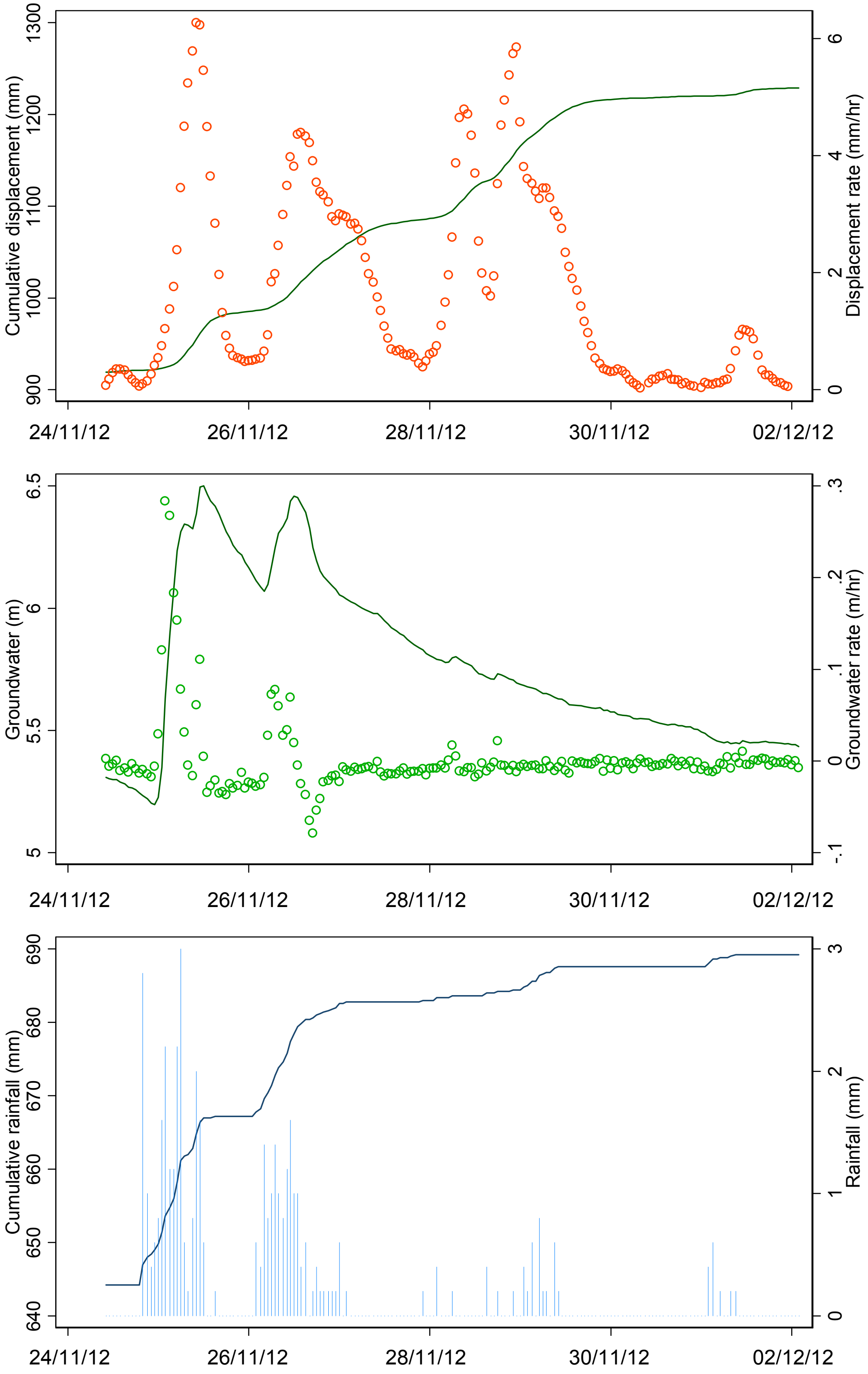

Figure A.19 Monitoring results at the Upgang Landslide (Period No.19). Accelerated movement between 24th November and 02nd December 2012 shows about 309.6 mm in cumulative displacement with a maximum displacement rate of 6.272 mm/hr. Groundwater fluctuated between 5.2 and 6.5 m with a high groundwater rate of 0.28 m/hr. The total rainfall was 45 mm with a maximum rate of 3 mm/hr during a 60-hour wet period.

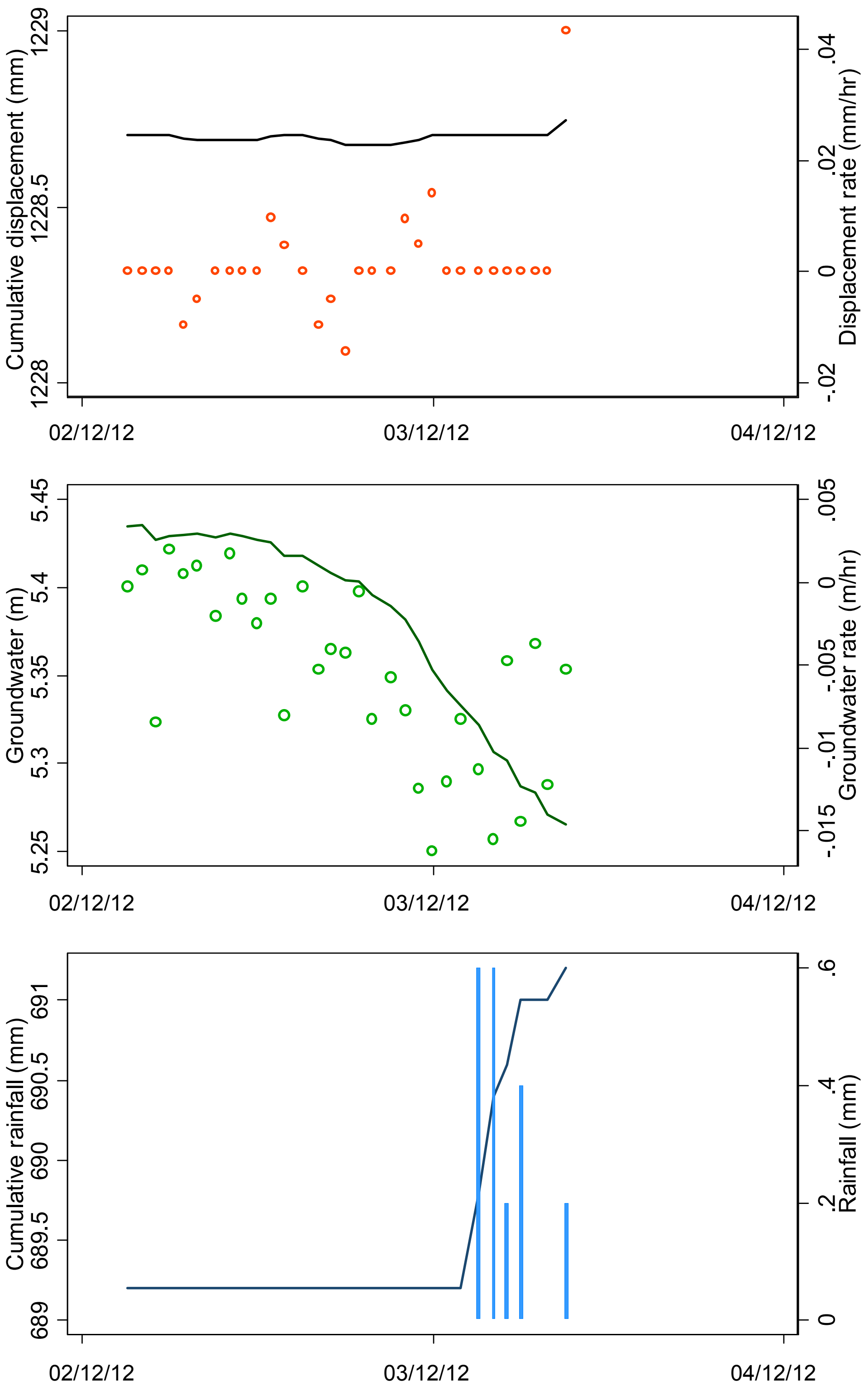

Figure A.20 Monitoring results at the Upgang Landslide (Period No.20). No movement between 02nd and 03nd December 2012 shows about 0.072 mm in cumulative displacement with a maximum displacement rate of 0.043 mm/hr. Groundwater fluctuated between 5.26 and 5.44m with a very low groundwater rate of 0.008 m/hr. The total rainfall was 2 mm with a maximum rate of 0.6 mm/hr during a 5-hour wet period.

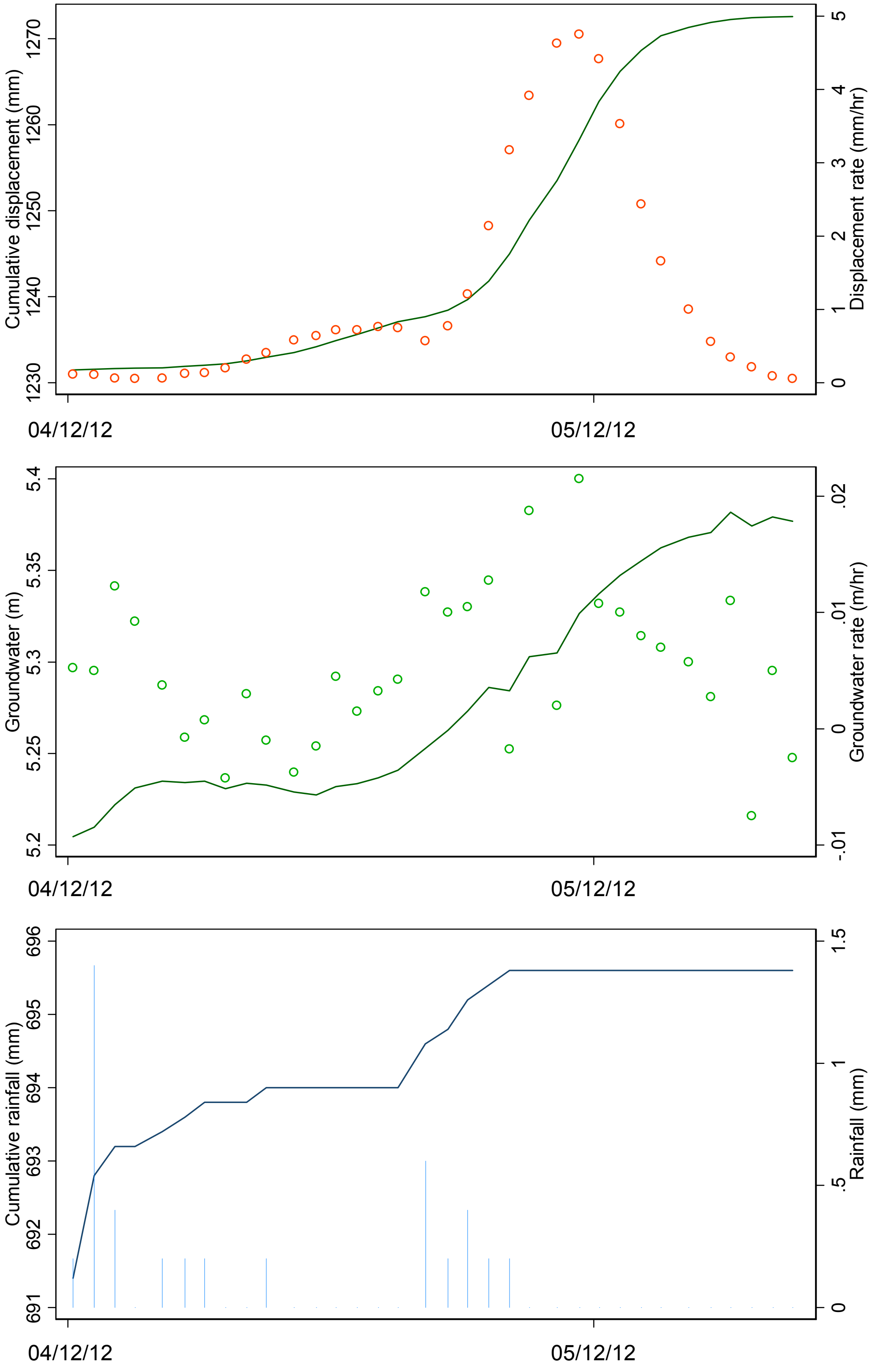

Figure A.21 Monitoring results at the Upgang Landslide (Period 21). Accelerated movement between 03nd and 06th December 2012 shows about 41 mm in cumulative displacement with a maximum displacement rate of4.75 mm/hr. Groundwater fluctuated between 5.2 and 5.38 m with a low groundwater rate of 0.02 m/hr. The total rainfall was 4.2 mm with a maximum rate of 1.4 mm/hr during a 12-hour wet period.